The influence of irradiation on structural and transport properties of graphene

Chenxing Deng

UNIVERSITÉ PARIS-SUD

ÉCOLE DOCTORALE

Sciences et Technologies de l'Information des Télécommunications et des Systèmes (STITS)

THESE EFFECTUEE AU SEIN DE

L'Institut d'Électronique Fondamentale (IEF), Univ. Paris-Sud/CNRS UMR 8622

DISCIPLINE

PHYSIQUE

THÈSE DE DOCTORAT

Soutenue le 26 Mai 2015
Par

Chenxing Deng

L'influence de l'irradiation sur les propriétés structurelles et de transport du graphène

Composition du jury

Rapporteur	Henri HAPPY	Professeur, Université de Lille 1
Rapporteur	Fausto SIROTTI	Directeur de recherche, CNRS, Synchrotron SOLEIL
Examinateur	Philippe DOLLFUS	Directeur de recherche, CNRS, IEF
Examinateur	Jinbo BAI	Directeur de Recherche, CNRS, Ecole Centrale de Paris
Directeur de thèse	Claude CHAPPERT	Directeur de recherche, CNRS
Co-directeur de thèse	Weisheng ZHAO	Chargé de recherche, CNRS

Abstract

Title: The influence of irradiation on structural and transport properties of graphene

Graphene is a single layer of honeycomb patterned carbon atoms. It has attracted much of interest in the past decade due to its excellent electronic, optical, and mechanical properties, etc., and shows broad application prospects in the future. Sometimes the properties of graphene need to be modulated to adapt for specific applications. For example, control of doping level provides a good way to modulate the electrical and magnetic properties of graphene, which is important to the design of graphene-based memory and logic devices. Also, the ability to tune the electrical conductance can be used to fabricate graphene transistor, and the chemical vapor deposition (CVD) method shows the possibility to make the preparation of graphene integrated into semiconductor manufacture processes. Both spin injection and irradiation are efficient and convenient method to tailor the transport properties of graphene. But due to the complicated fabrication process, it is hard to prepare graphene spin transport device successfully. The lithography and lift off processes which involve using photoresist will degenerate the transport properties of graphene. Moreover, the sensitivity of graphene to the H_2O and O_2 molecules when exposed to the air ambient will result in weak spin signal and noise background. Irradiation provides a clean method to modulate the electrical properties of graphene which does not involve chemical treatment. By ion or electron irradiation, the electronic band structure of graphene can be tuned and the lattice structure will be modulated as well. Moreover, the charged impurities and doping arising from irradiation can change the electronic properties of graphene such as electron-phonon scattering, mean free path and carrier density. As reported, graphene oxidization can be induced by exposure to oxygen plasma, and N-Doping of Graphene through thermal annealing in ammonia has been demonstrated. Furthermore, the strain in graphene can also be tailored by irradiation, which also contributes to the modification of transport properties of graphene. In conclusion, irradiation provides an efficient physical method to modulate the structural and transport properties of graphene, which can be applied in the graphene-based memory and logic devices, transistor, and integrated circuits (ICs).

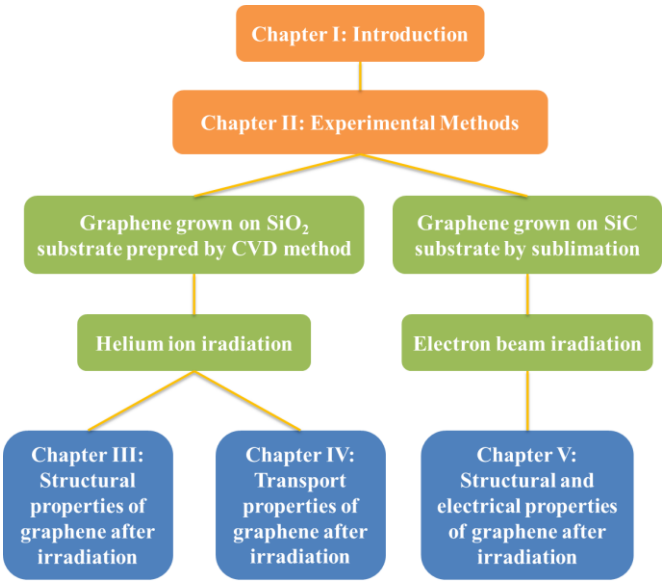

In this thesis, Helium ion irradiation was performed on graphene grown on SiO_2 substrate by CVD method, and the structural and transport properties were investigated. The charge transfer doping in graphene induced by irradiation results in a modification of these properties, which suggests a convenient method to tailor them. Moreover, electron beam irradiation was performed on graphene grown on SiC substrate. The local progressive amorphization, strain and electron doping contribute to the modification of structural and transport properties in graphene which can be observed. The organizations of the thesis are shown in the picture above. Chapter Ⅰ and II introduce the background of graphene and the experimental methods employed in our experiments respectively. Two types of graphene were used, the first one was graphene grown on Cu foils by CVD method and then transferred to SiO_2 substrate, while the other one was epitaxial graphene grown on SiC substrate by sublimation. Helium ion irradiation was performed on graphene prepared by CVD method, meanwhile vacuum annealing was used to restore the damage caused by irradiation. Due to the complicated situation of the crystal structure and chemical composition of graphene after irradiation arising from the PMMA residues, we paid lot of attention to analyze the structural modification which composed of chapter III. Transport properties of graphene after irradiation such as electrical conductance, electronic hysteresis and magnetoresistance were also studied and described in chapter IV. The electron beam irradiation was performed on graphene grown on SiC substrate. As there were no PMMA residues on graphene surface, the structural properties of graphene after irradiation were much easier to understand than graphene prepared by CVD method. Next, the electrical property of graphene

was also investigated. All the results were summarized in chapter V. The details of each chapter are shown below.

Chapter I introduces some basic knowledge about graphene. First, the crystal lattice structure band structure and electronic properties are presented. The recent studies about graphene use in spin transport are summarized. Then different methods about graphene fabrication are showed, such as exfoliation, chemical vapour deposition (CVD), epitaxial graphene from silicon carbide (SiC), and graphene grown on boron nitride (BN) substrate. The exfoliated graphene presents high crystal quality, while CVD method paves the way for mass production. Sublimation of SiC substrate is a commonly used and convenient method to prepare graphene, and the excellent electronic properties of graphene grown on BN substrate has proved this method can be used to gain record mobility and new physical phenomena. In the end, several methods about modulation of graphene properties are introduced.

Chapter II describes the experimental methods used in this thesis. Helium ion and electron beam irradiation were used to irradiate graphene films grown on SiO_2 by CVD method and epitaxial graphene grown on silicon carbide substrate. Raman spectroscopy was then used to characterize the modification of the structure of graphene, which revealed that defects and disorders were formed in graphene after irradiation. Commonly, the defects are referred to point defects: vacancies and interstitial defects. The chemical composition of graphene was characterized by X-ray photoelectron spectroscopy (XPS) and the surface topography was observed under Atomic force microscopy (AFM). Finally, the electrical properties and magnetoresistance of irradiated graphene were investigated on the transport measurement platform composed of Keithley 2400, SR 830 Lock-In Amplifier, HP3245A and HP 34902.

Chapter Ⅲ describes the observed reversible charge transfer doping effect in CVD graphene due to reactions with polymethyl methacrylate (PMMA) residues. The PMMA was used as the supporter during the Cu etching process, however, it is difficult to remove the PMMA film entirely even after repeated cleaning in acetone and annealing, and a small number of PMMA residues always remain on graphene surface. By Helium ion irradiation and vacuum annealing, reversible shifts in Raman G and 2D bands were observed as well as the change in the relative ratio 2D band intensity to the G band intensity. XPS results show that the composition ratios of sp^3 hybrid C–C (H), C−C=O and C−O−C (H) bonds in graphene increase after

irradiation while they decrease after annealing, which indicates that chemical bonds between functional groups in PMMA residues and graphene could be formed due to He^+ ion irradiation, and that the desorption of functional groups from graphene is dominant during the vacuum annealing process. Meanwhile, the PMMA residues on the graphene surface are mostly removed and the surface morphology becomes smooth after irradiation and annealing. Also the frequencies of G and 2D bands in Raman spectra show non-monotonic dependence on the irradiation dose which remains after annealing, indicating that the doping also involves irreversible effect.

Chapter IV shows the electrical and magnetic transport properties of CVD graphene after irradiation. The electrical conductance shows a non-monotonic dependence on the irradiation dose, and remains after annealing, which indicates that the doping involves irreversible effect as discussed in chapter three. The electronic hysteresis behaviors also show non-monotonic dependence on the dose density, which is due to the competitive effect of charging trapping and tunneling effect. By applying a perpendicular magnetic field, the electronic hysteresis behaviors of unirradiated graphene are enhanced while for irradiated graphene this effect is not significant. The Lorenz force and impurities or defects introduced by irradiation contribute to this phenomenon.

Chapter V describes the influence of electron beam irradiation on structural and transport properties of epitaxial graphene grown on silicon carbide. XPS results show that the crystal structure of graphene was broken after high dose irradiation. The frequencies of G and 2D bands in Raman spectra show a red-shift, and an increase of the bandwidth of the 2D peak was observed. This is mostly related to the local progressive amorphization and released strain after irradiation. The electron doping arising from electron beam irradiation can also result in the red-shift of 2D band. The electrical conductance of graphene shows a non-monotonic dependence on the irradiation dose, which is attributed to the competitive effect of local progressive amorphization, strain and electron doping. Our study helps better the understanding of the irradiation effects in graphene, which is efficient to tune the properties of graphene and applied in graphene-based memory and logic devices.

In conclusion, this work demonstrates that the reactions between polymer adsorption and graphene play an important role on charge-transfer doping in graphene grown on SiO_2 by CVD method, which involves both reversible and irreversible effects. The influence of electron beam

irradiation on epitaxial graphene grown on silicon carbide was also investigated. The effects of local progressive amorphization, strain and electron doping are discussed. These results indicate that irradiation is an efficient method to modulate the properties of graphene and paves a way for future application in graphene-based memory and logic devices, transistor and integrated circuits.

Keywords: Graphene, chemical vapor deposition (CVD), silicon carbide, charge-transfer doping, amorphization, Raman Spectroscopy, X-ray photoelectron spectroscopy, Atomic force microscopy, transport properties.

Résumé

Titre: L'influence de l'irradiation sur les propriétés structurelles et de transport du graphène

Le graphène est une simple couche de nid d'abeille motifs atomes de carbone. Il a suscité beaucoup d'intérêt dans la dernière décennie en raison de ses excellentes propriétés électroniques, optiques et mécaniques, etc., et montre larges perspectives d'applications dans le futur. Parfois, les propriétés du graphène doivent être modulées pour s'adapter à des applications spécifiques. Par exemple, le contrôle du niveau de dopage fournit un bon moyen de moduler les propriétés électriques et magnétiques de graphène, qui est important pour la conception de dispositifs de mémoire et de logique à base de graphène. En outre, la possibilité de régler la conductance électrique peut être utilisée pour fabriquer le transistor de graphène, et le dépôt chimique en phase vapeur (CVD) montre la possibilité d'effectuer la préparation de graphène intégrées dans les processus de fabrication de semi-conducteur. L'injection de spin et l'irradiation des méthodes efficaces et pratiques pour adapter les propriétés de transport du graphène. Mais en raison du processus de fabrication complexe, il est difficile de préparer le dispositif de transport de spin graphène succès. La lithographie et décoller les processus qui impliquent utilisant résine photosensible va dégénérer les propriétés de transport du graphène. En outre, la sensibilité du graphène aux molécules H_2O et O_2 lorsqu'il est exposé à l'air ambiant entraînera faible signal de rotation et le bruit de fond. L'irradiation fournit une méthode propre à moduler les propriétés électriques de graphène qui n'impliquent pas de traitement chimique. En ions ou irradiation d'électrons, la structure de bande électronique de graphène peut être réglée et la structure en treillis est modulée aussi bien. En outre, les impuretés chargées et dopage résultant de l'irradiation peuvent modifier les propriétés électroniques du graphène comme la diffusion électron-phonon, libre parcours moyen et la densité de charge. Comme indiqué, le graphène oxydé peut être induit par exposition à un plasma d'oxygène, et le N- dopage de graphène par recuit thermique dans de l'ammoniac a été démontré. En outre, la souche dans le graphène peut également être adaptée par irradiation, qui contribue également à la modification des propriétés de transport de graphène. En conclusion, l'irradiation fournit une méthode physique efficace pour moduler les propriétés

structurelles et de transport du graphène, qui peut être appliqués dans la mémoire à base de graphène et des dispositifs logiques, transistor, et des circuits intégrés.

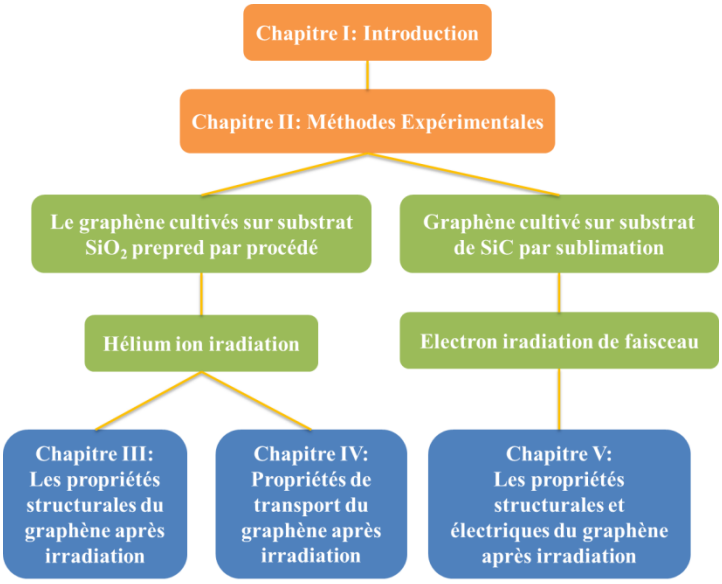

Dans cette thèse, l'irradiation d'ions hélium a été réalisée sur le graphène cultivé sur substrat SiO_2 par la méthode CVD, et les propriétés structurelles et de transport ont été étudiés. Le dopage de transfert de charge dans le graphène induite par les résultats d'irradiation dans une modification de ces propriétés, qui suggère une méthode pratique pour les adapter. En outre, l'irradiation par faisceau d'électrons a été effectuée sur graphène cultivé sur substrat de SiC. Les amorphisations progressives, contraintes et d'électrons dopage locales contribuent à la modification des propriétés structurelles et de transport dans le graphène qui peuvent être observés. Les organisations de la thèse sont présentées dans le tableau ci-dessus. Chapter Ⅰ and II introduisissent le fond de graphène et les méthodes expérimentales utilisées dans nos expériences, respectivement. Deux types de graphène ont été utilisés, le premier a été cultivé sur des feuilles de graphène Cu par la méthode de CVD, puis transféré sur un substrat de SiO_2, tandis que l'autre était graphène épitaxial développé sur un substrat de SiC par sublimation. Hélium ion irradiation a été effectuée sur le graphène préparé par procédé CVD, quant à vide recuit a été utilisé pour réparer les dommages causés par l'irradiation. En raison de la situation complexe de la structure cristalline et la composition chimique du graphène après l'irradiation provenant des résidus PMMA, nous avons payé beaucoup d'attention à analyser la modification structurelle qui composait du chapitre III. Propriétés de transport du graphène après irradiation tels que la conductance électrique, électronique et hystérésis magnétorésistance ont également été étudiées

et décrits dans le chapitre IV. L'irradiation par faisceau d'électrons a été effectuée sur graphène cultivé sur substrat de SiC. Comme il n'y avait pas de résidus de PMMA sur la surface du graphène, les propriétés structurelles du graphène après irradiation étaient beaucoup plus facile à comprendre que le graphène préparé par procédé CVD. Ensuite, la propriété électrique du graphène a également été étudiée. Tous les résultats ont été résumés dans le chapitre V. Les détails de chaque chapitre sont présentés ci-dessous.

Chapitre I introduit quelques connaissances de base sur le graphène. Premièrement, la structure de bande du réseau cristallin et des propriétés électroniques est présentée. Les études récentes sur l'utilisation du graphène dans le transport de spin sont résumées. Ensuite, les différentes méthodes de fabrication de graphène ont été montrées, comme exfoliation, le dépôt chimique en phase vapeur (CVD), le graphène épitaxiale de carbure de silicium (SiC), et graphène cultivé sur du nitrure de bore (BN) substrat. Le graphène exfolié présente de haute qualité de cristal, tout procédé CVD ouvre la voie à la production de masse. Sublimation du substrat SiC est une méthode couramment utilisée et pratique pour préparer le graphène, et les excellentes propriétés électroniques du graphène cultivés sur substrat BN ont prouvé que cette méthode peut être utilisée pour obtenir la mobilité d'enregistrement et de nouveaux phénomènes physiques. À la fin, plusieurs méthodes sur la modulation de propriétés de graphène sont introduites.

Chapitre II décrit les méthodes expérimentales utilisées dans cette thèse. Ions d'hélium et de l'irradiation par faisceau d'électrons ont été utilisés pour irradier des films de graphène cultivées sur SiO_2 par un procédé de CVD et graphène épitaxiale développée sur un substrat de carbure de silicium. La spectroscopie Raman a ensuite été utilisée pour caractériser la modification de la structure de graphène, qui a révélé que les défauts et désordres ont été formés dans le graphène après irradiation. Communément, les défauts sont appelés à signaler les défauts: les postes vacants et les défauts interstitiels. La composition chimique de graphène a été caractérisée par spectroscopie de photoélectrons X (XPS) et la topographie de surface a été observée sous microscopie à force atomique (AFM). Enfin, les propriétés électriques du graphène et magnétorésistance irradiée ont été étudiées sur la plate-forme de mesure de transport composé de Keithley 2400, SR 830 amplificateur lock-in, HP3245A et HP 34902.

Chapitre III décrit le transfert réversible de charge effet de dopant observée dans le graphène CVD en raison de réactions avec le polyméthacrylate de méthyle (PMMA) résidus. Le PMMA a été utilisé comme l'élément de support pendant le processus de gravure du Cu, cependant, il est difficile de retirer le film de PMMA entièrement répétée même après nettoyage dans de l'acétone et de recuit, et d'un petit nombre de résidus PMMA restent toujours sur la surface de graphène. Par de l'hélium irradiation ionique et recuit sous vide, des changements réversibles de Raman G et 2D bandes ont été observées ainsi que de la variation de l'intensité relative de la bande 2D rapport à l'intensité de la bande G. Résultats XPS montrent que les ratios des sp^3 hybride de la composition C-C(H), C-C=O et C-O-C(H) liaisons dans augmentation de graphène après irradiation pendant qu'ils diminuent après recuit , qui indique que les liaisons chimiques entre groupes fonctionnels de PMMA et graphène résidus peuvent être formés en raison de l'irradiation d'ions He^+, et que la désorption des groupes fonctionnels de graphène est dominant pendant le processus de recuit sous vide . Pendant ce temps, les résidus de PMMA sur la surface de graphène sont essentiellement éliminée et la morphologie de surface devient lisse après irradiation et recuit. De même, les fréquences des bandes G et 2D dans des spectres Raman montrent la dépendance non-monotone de la dose d'irradiation qui reste après le recuit, qui indique que le dopage comprend également un effet irréversible.

Chapitre IV montre les propriétés de transport électriques et magnétiques de graphène CVD après irradiation. La conductance électrique montre une dépendance non-monotone de la dose d'irradiation, et reste après recuit, qui indique que le dopage implique effet irréversible comme on le verra dans le chapitre trois. Les comportements d'hystérésis électroniques montrent également une dépendance non-monotone de la densité de dose, qui est due à l'effet concurrentiel de piégeage de charge et de l'effet tunnel. En appliquant un champ magnétique perpendiculaire, les comportements d'hystérésis électroniques du graphène non irradié sont renforcés tandis que cet effet n'est pas significatif pour le graphène irradié. La force de Lorenz et les impuretés ou défauts introduits par irradiation contribuent à ce phénomène.

Chapitre V décrit l'influence de l'irradiation par faisceau d'électrons sur les propriétés structurelles et de transport de graphène épitaxial développé sur carbure de silicium. XPS résultats montrent qu'un grand nombre de liaisons sp^2 C-C ont été brisées après irradiation et C-C formé (H) sp^3 et Si-C haute dose obligataire à la place, qui indique la modification de la structure

du graphène. Les fréquences des bandes G et 2D dans les spectres Raman montrent un décalage vers le rouge lorsque le graphène a été irradié à haute densité dose jusqu'à $10^{16}/cm^2$, et on a observé une augmentation de la bande passante du pic 2D. Cela est principalement lié à l'amorphisation progressive locale et libéré souche après irradiation. Le dopage d'électrons résultant d'une irradiation par faisceau d'électrons peut également résulter dans le décalage de rouge de bande 2D. Le ratio d'intensité de la 2D crête à crête et SiC conductance électrique du graphène montrent une dépendance non-monotone de la dose d'irradiation, qui est attribué à l'effet concurrentiel d'amorphisation progressive locale, la souche et le dopage d'électrons.

En conclusion, ce travail montre que les réactions entre l'adsorption de polymère et graphène jouent un rôle important sur le transfert de charge dopage dans le graphène cultivé sur SiO_2 par la méthode CVD, qui implique à la fois des effets réversibles et irréversibles. L'influence de l'irradiation par faisceau d'électrons sur le graphène épitaxial développé sur le carbure de silicium a été également étudiée. Les effets de l'amorphisation progressive locale, la souche et le dopage électronique sont discutées. Ces résultats indiquent que l'irradiation est une méthode efficace pour moduler les propriétés du graphène et ouvre un moyen pour application future dans la mémoire à base de graphène et les dispositifs logiques, le transistor et les circuits intégrés.

Mots-clés: Le graphène, dépôt chimique en phase vapeur (CVD), le carbure de silicium, le transfert de charge dopage, amorphisation, la spectroscopie Raman, spectroscopie photoélectronique des rayons X, la microscopie à force atomique, propriétés de transport.

Table of Contents

Chapter I. Introduction

1.1 Background

Since the first silicon transistor (Figure 1.1a) was invented in 1947 at Bell Telephone Laboratories by three American physicists John Bardeen, Walter Brattain, and William Shockley [1], a large number of modern electronic devices such as computer, radio, processor, smartphone have been developed based on this epochal invention. These novel products provided new experience for people and changed the human life dramatically, and then a new era called Digital revolution or the Third Industrial Revolution was opened [3]. In 1956, the Nobel Prize in Physics was awarded jointly to William Bradford Shockley, John Bardeen and Walter Houser Brattain *"for their researches on semiconductors and their discovery of the transistor effect"* [4].

More than 60 years passed, the size of the transistor has reduced exponentially and the number of transistors on one chip increased hugely (Moore's law), and promoted the high-speed development of the semiconductor industry during the past decades [5-6]. For example, billions of transistors are fabricated in one microprocessor and provide ultra-high-speed computing and processing ability. In 2012, Intel has announced the world's first 3-D transistors in mass production which used the 22 nm 3D tri-gate transistor technology. The Intel Core i7 and Core i5 processors which are widely used nowadays are fabricated by this technology. Recently, Apple's iPhone 6 and iPhone 6 plus have been introduced, the A8 processor used in these new generation smartphones is fabricated by the 20 nm process technology developed by TSMC. In August 11, 2014, Intel disclosed details of latest microarchitecture and 14 nm manufacturing process technical, 2nd generation 3D tri-gate transistors were used, and the SRAM cell size is almost half the area of that fabricated by 22 nm technology. As the International Technology Roadmap for Semiconductors (ITRS) predicts (Figure 1.1b), the successor of the 14 nm technology will be the 10 nm technology, and then scale down to 7 nm and 5 nm. As the chip becomes more and more complex, obstacles during the lithography processes will be present, such as multiple patterning and extreme ultraviolet lithography (EUV) [8].

In the past decades, the researchers were dedicated to find the replacement of traditional silicon material. Carbon nanotube field-effect transistor (CNTFET) was first demonstrated in 1998 at Delft University of Technology and IBM, and has great developments in the last 17 years [9-10]. Compared to conventional metal–oxide–semiconductor field-effect transistor (MOSFET), the CNTFET can operate even without dopants and are less influenced by the channel length. But

the mass production method for CNT with certain chirality is still not available at present which hinders its application in semiconductor industry [11].

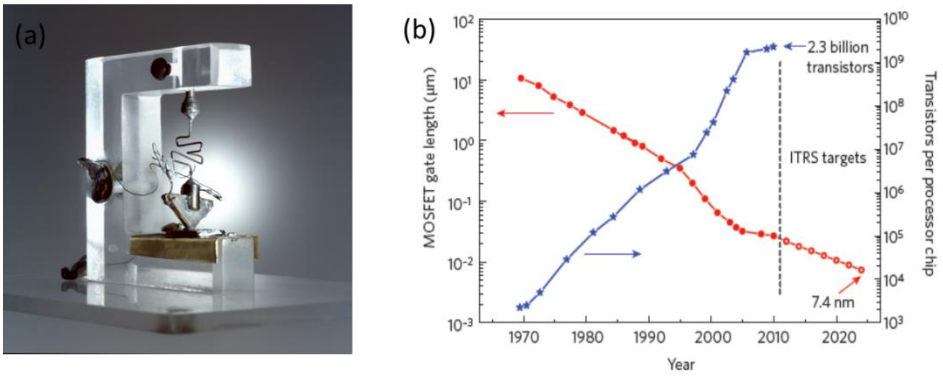

Figure 1.1 (a) Image of the first transistor invented by Bell Laboratories in 1947 [2] (b) International Technology Roadmap for Semiconductors [7].

Recently, two-dimensional (2D) materials have attracted much interest due to its unique structure and properties that could overcome the physical limitations during semiconductor fabrication processes. In 2004, the first 2D material graphene was fabricated by Andre Geim and Konstantin Novoselov at the University of Manchester. The particular honeycomb structure patterned with sp^2 bonded carbon atoms makes graphene have excellent electrical, optical, mechanical and thermal properties, etc. For example, the transport measurements show the mobility of graphene exceeds 15,000 $cm^2\ V^{-1}\ s^{-1}$ at the room temperature, which makes it a perfect candidate as the conductor in transistor or electronic circuits [12]. In 2011, the first integrated circuit (IC) based on a graphene transistor was built by IBM researchers. This circuit can be operated at 10 GHz, which is more than twice as fast as a silicon transistor of comparable dimensions [13]. Besides, due to the high density of states, high work function, and low dimensionality of graphene, graphene flash memory (GFM) has the potential to exceed the performance of current flash memory [14]. In 2010, the Nobel Prize in Physics was awarded jointly to Andre Geim and Konstantin Novoselov *"for groundbreaking experiments regarding the two-dimensional material graphene"* [15].

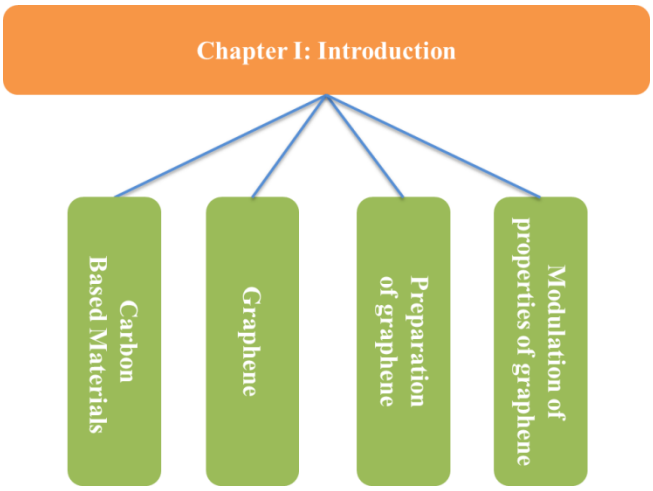

Figure 1.2 Organization of chapter I.

In this chapter, the basic knowledge of graphene was introduced and the organization of chapter one was shown in Figure 1.2. First, the carbon based materials which have been widely studied were present, such as diamond, graphite and fullerenes. Then the basic properties of graphene: crystal lattice structure, band structure and electronic properties and spin transport were exhibited. Next, several methods about preparation of graphene were introduced, for example, exfoliation, chemical vapour deposition, epitaxial graphene grown on silicon carbide substrate and graphene grown on boron nitride substrate. In the end, some common methods about modulation of properties of graphene were summarized, such as electric field, electrochemical, chemical doping, irradiation, and interface engineering.

1.2 Carbon Based Materials

Carbon is the chemical element symbolized with C and numbered six in periodic table. It locates in the 14^{th} group in periodic table, also called group IVA in semiconductor physics, followed by silicon (Si), germanium (Ge), tin (Sn) and lead (Pb) elements. The four electrons in the outermost valence shell of carbon atom can form a huge range of covalent bonds with other atoms, such as H, O, N, S, Cl, Br and P, etc., thus variety of compounds are formed based on these chemical bonds. Also, carbon can bond with itself in at least three different ways: single bond, double bonds, and triple bonds, and form three major allotropes of carbon--diamond, graphite, and fullerenes. In addition, carbon is one of the most abundant elements in the universe by mass, which occupies about 3.03% among all the elements, follows Hydrogen, Helium and

Oxygen. It is abundant in the stars, comets, and in the atmospheres of most planets [16]. Also carbon is the second abundant element in human body, which takes up about 18% and just less than oxygen. It forms the basic building block of virtually all organic chemistry and nearly 20 million known molecules, such as alkanes, alkenes, alcohols, amines, etc. In this situation, carbon is considered as the basis element of life on the earth.

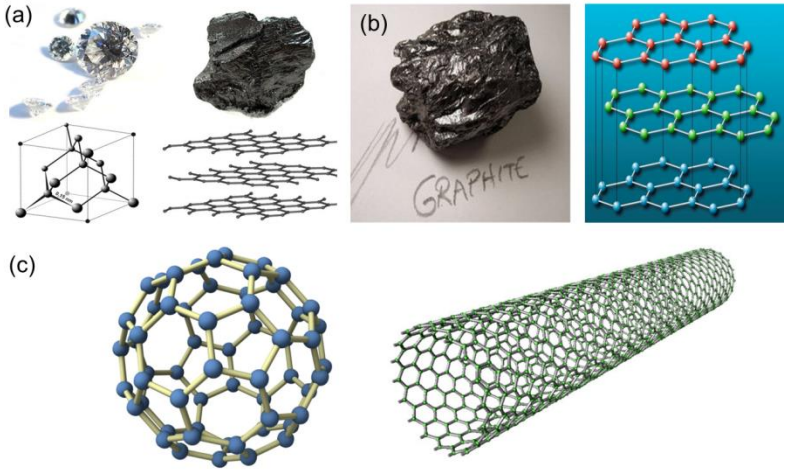

Figure 1.3 Three major allotropes of carbon based material (a) Diamond [18] (b) Graphite [19-20] (c) Fullerenes [21-22].

Diamond is one of the best known allotropes of carbon, which is considered as the hardest material in the world, see in Figure 1.3a. The carbon atoms in diamond are bonded by C-C sp^3 hybrid bonds to other four carbon atoms, it is difficult to break the carbon atoms apart or move them in relation to one another, and this provides an excellent strong structure and also gives rise to the other properties of diamond. This unique property makes it useful for industrial applications and jewelry. The high melting point (about 3550 ℃) also results from strong directional covalent C-C sp^3 hybrid bonds. Due to the electrons in diamond are localized in specific bonds, there is nearly no electrical conductivity in diamond. The exception is natural blue diamond, which contains boron impurities that also make it a semiconductor. Another interesting property is that the diamond shows insolubility in polar and non-polar solvents, this is because molecular bonds are stronger than any intermolecular forces [16-17].

Graphite, named by Abraham Gottlob Werner in 1789, is another common allotrope of carbon. In contrast to diamond, graphite is soft and brittle, although both are made up of carbon

atoms. The difference results from how the individual carbon atoms are arranged within the structure of diamond and graphite. Graphite is consisted of multilayers of carbon atoms arranged in honeycomb lattice structure (Figure 1.3b). Three valence electrons of carbon are bonded with the closest carbon atoms by C-C sp^2 hybrid bonds in six sided rings, and the other electron is delocalized in π-orbitals which is perpendicular from the plane of the carbon rings. The presence of π-orbitals allows for strong Van der waals forces that hold the layers together one by one and form the graphite in the end. Due to the delocalized electrons, the graphite has good conductivity, about 1×10^5 S/m at room temperature, which can be used as arc lamp electrodes [16]. What's more, due to the loose interlamellar coupling between layers in the structure of graphite, the sheets can easily slip against each other. Thus the graphite has an excellent lubrication effect, especially obvious under high temperature and pressure, and it can be used as dry lubricant in a wide range of areas, such as air compressors, railway track joints, food industry, open gear, ball bearings, machine-shop works, etc. Similar to diamond, graphite also has high melting point of about 3653 ℃, even higher than diamond which is due to the delocalized electron [16-17].

Fullerenes, also called buckminsterfullerene, is a family of carbon allotropes which are composed entirely of carbon atoms arranged in the form of hollow sphere, ellipsoid, or tube (Figure 1.3c). Fullerenes were first discovered in 1985 by a team of scientists from Rice University and the University of Sussex. Using laser irradiation to vaporize graphite in an atmosphere of helium stream, a super stable cluster composed of 60 carbon atoms (C60) was produced. The cluster is made of 60 vertices with 12 pentagonal and 20 hexagonal faces [23]. The fullerenes are named for the resemblance to geodesic domes structure invented by the American scientist and architect-Richard Buckminster Fuller. In 1996, three of them: Robert F. Curl Jr. and Richard E. Smalley from United States, Sir Harold W. Kroto from the United Kingdom, were jointly awarded the Nobel Prize in chemistry. The discovery of fullerenes greatly expands the family of carbon allotropes, and many different structures of fullerenes were found since 1985, such as buckyballs cluster, nanotube or cylindrical fullerenes, megatube, polymers, nano-onion, linked "ball-and-chain" dimers, and fullerene rings. Among them, buckyballs cluster and nanotube are two major types of fullerenes that have been investigated for many years. Buckyballs cluster is the smallest fullerene found in nature, most refers to C_{60} mentioned above. The tiniest buckyballs cluster is C_{20}, and another common one is C_{70}, in recent years, C_{72}, C_{76}, C_{84} and even C_{100} have also been successfully prepared. As for C60, each carbon atom is bonded

to three others atoms with two C-C and one C=C sp^2 hybrid bonds. Due to this special structure, C60 behaves as good electrical conductor, and has high tensile strength and heat conductivity [24]. Carbon nanotube is another important form of fullerenes, it was first discovered in the soot of arc discharge at NEC by Japanese researcher Sumio Iijima in 1991 [25], and the name comes from the 2D material with one layer atomic carbon atoms in honeycomb lattice structure, graphene. Nanotube looks like graphene sheet rolled-up continuous with unbroken hexagonal mesh and carbon molecules locate at the apexes of the hexagons. Classically, nanotube is divided in two types: single walled and multi walled nanotube, other related structures such as torus, nanobud, and graphenated carbon nanotubes (g-CNTs) have also been prepared. Similar to graphite, nanotubes are composed entirely of C-C sp^2 bonds, and naturally align themselves into "ropes" together by Van Der Waal Force. In this case, carbon nanotube shows high carrier mobility, excellent mechanical properties, and behaves as good thermal conductor, and can be applied in a huge range of areas: electronics industry, paper batteries, solar cells, textile and environmental remediation [26-27].

Although the carbon nanotube has been studied for many years, but it is difficult to prepare it on the substrate and the process variation is very large for integrated electronic circuits. The successful preparation of graphene and its excellent properties show a more convenient way to fabricate carbon based large scale electronic circuits [28].

1.3 Graphene

The structure of graphite was first figured out with using the powder diffraction in 1916 [29]. Then the details were studied by V. Kohlschütter and P. Haenni and described what they called graphite oxide paper in 1918 [30]. The theory of graphene was first discussed in 1946 by a Canadian physicist Philip Russell Wallace, where the graphite was treated as a stack of graphene sheets by neglecting the interactions between planes, and supposed the conduction only took place only in layers [31]. Since then, many researchers were dedicated to peel the graphene layer from graphite. In 1948, the first TEM pictures of thin layers of graphite were published by G. Ruess and F. Vogt [32]. Until 1970s monolayer of graphene was grown on top of other materials, but this epitaxial graphene contained a lot of charge from the substrate [33]. In 2004, few-layer graphene was exfoliated from the graphite bulk by scotch tape and deposited onto a thin layer of SiO_2/Si substrate, the peeled graphene shows ultra-high carrier mobility (about 10,000 $cm^2\ V^{-1}$

s^{-1}) and quantum hall effect at ultra-low temperature [12]. Many different kinds of graphene preparation methods have been invented from then, and various properties of graphene were discovered. The high application potential has also attracted the focus from the industry, one day the graphene will appear in our life in the form of multifarious devices [34].

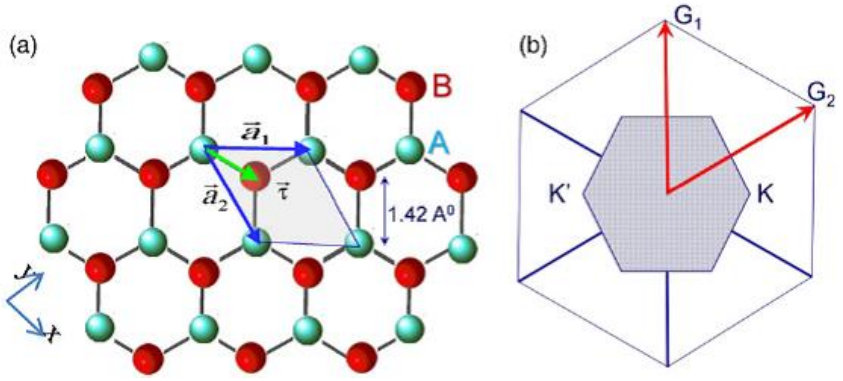

Figure 1.4 (a) The lattice structure of graphene. The two triangular sublattices are indicated by red and green colors. The primitive unit cell is shown by the grey area with lattice unit vectors $\vec{a}_1$ and $\vec{a}_2$. (b) Brillouin zone of graphene. $\vec{G}_1$ and $\vec{G}_2$are reciprocal lattice vectors [35].

1.3.1 Crystal Lattice Structure

The ideal single layer graphene is considered as one-atomic-thick planner sheet of carbon atoms that densely packed into honeycomb lattice (Figure 1.4a), it is the thinnest material ever found [35]. Each carbon atom in graphene is bonded to other three carbon atoms by C-C sp^2 hybrid bonds, and the fourth valence electron remains in the p_z-orbital which is perpendicular to the graphene plane. Every hexagon lattice contains two carbon atoms and the p_z-electrons from the two atoms form a weak bond by overlapping between each other. Similar to graphite, the electron delocalized in p_z-orbitals are responsible for the excellent transport properties of graphene. As shown in Figure 1.4a, the C-C bond length is 1.42 Å and the two adjacent bonds are aparted with angel of 120 º. The grey area presents the primitive unit cell of graphene with lattice unit vectors $\vec{a}_1$and $\vec{a}_2$, where $\vec{a}_1 = \frac{a}{2}(3, \sqrt{3})$, $\vec{a}_2 = \frac{a}{2}(3, -\sqrt{3})$, where a is the carbon-carbon distance. The Brillouin zone of graphene are shown in Figure 1.4b, and the reciprocal lattice vectors are $\vec{G}_1 = \frac{2\pi}{3a}(1, \sqrt{3})$ and $\vec{G}_2 = \frac{2\pi}{3a}(1, -\sqrt{3})$. More important are the two points K and K' at the corners of the first Brillouin zone (light blue hexagon area), which play important role on

graphene properties. In the momentum space, positions of these corners are given by $\vec{K} = \frac{2\pi}{3a}\left(1, \frac{1}{\sqrt{3}}\right)$ and $\overrightarrow{K'} = \frac{2\pi}{3a}\left(1, -\frac{1}{\sqrt{3}}\right)$ [35-36].

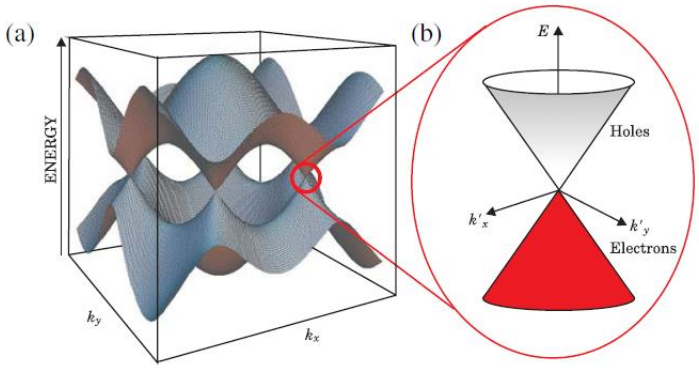

Figure 1.5 (a) Band structure of graphene. (b) Enlargement of the energy bands close to one of the Dirac points [37].

1.3.2 Band structure and Electronic properties

The energy band structure of graphene is shown in Figure 1.5a, the upper band corresponds to the conduction band while the lower band corresponds to the value band. Two p_z-electrons in each hexagon lattice completely fill the lower band, while the upper band is empty, and the electrons can be introduced from the lower band into the upper band by various methods [35-37]. Take the single layer graphene as example, the tight-binding Hamiltonian for electron states in graphene with considering the interaction between neighbor atoms is given by the form:

$$H = -t\sum_{|\vec{R}>}\left(\left|\vec{R}><\vec{R}+\vec{\tau}\right| + \left|\vec{R}><\vec{R}-\vec{a}_1+\vec{\tau}\right) + \left|\vec{R}><\vec{R}-\vec{a}_2+\vec{\tau}\right| + h.c. \quad (1)$$

Here $<\vec{r}|\vec{R}>= \Psi_{p_z}(\vec{R}-\vec{r})$ is a wave function of the p_z-orbital on atom in sublattice A, and $<\vec{r}|\vec{R}+\vec{\tau}>$ is the state on an atom of sublattice B, and t is the hopping integral from a state on one atom to a state on the neighbor atom. The value of t is about 2.7 eV, which can match the band structure near the ***K*** points obtained from first principle calculations [35-36]. Then the energy bands derived from this Hamiltonian approach can be described by the equation:

$$E_{\pm}(\boldsymbol{k}) = \pm t\sqrt{1+\cos^2\left(\frac{k_y a}{2}\right) + 4\cos\left(\frac{\sqrt{3}}{2}k_x a\right)\cos\frac{k_y a}{2}}, \quad (2)$$

Here the conduction band and value band are indicated by plus sign $E_+(\boldsymbol{k})$ and the minus sign $E_-(\boldsymbol{k})$ respectively. It is clear to see the energy band structure is symmetric near the area of zero energy [35-37].

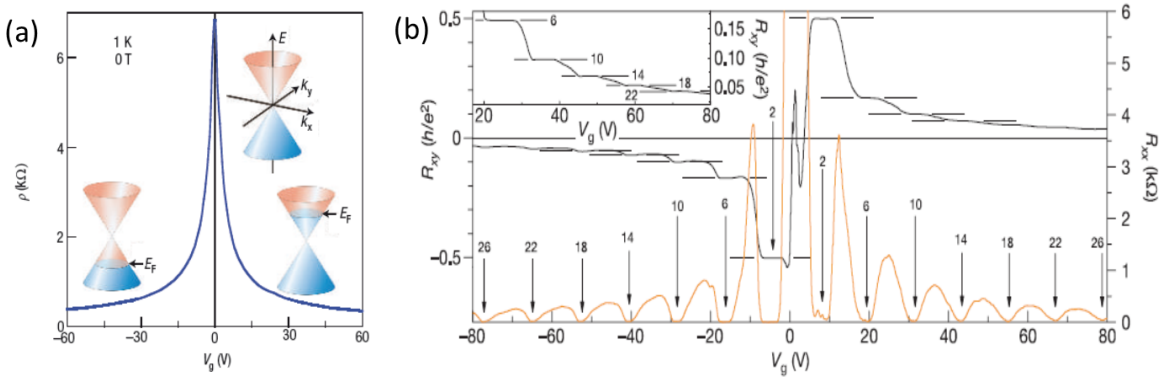

Figure 1.6 (a) Electric field effect of a graphene device [28]. (b) The Landau level density of states (DOS) and corresponding quantum Hall conductance (σ_{xy}) as a function of energy [40].

Also, the hexagon lattice can be considered as composed of two triangular sublattices A and B. The two sublattices A and B, which are equivalent and independent, lead to the formation of two new energy bands that meets at the ***K*** point, also called Dirac point. This special property of graphene band structure results in metallic behavior observed in experiments, and thus graphene can be considered as "semi-metal" or "zero-bandgap semiconductor". This structure is also responsible for another important characteristic of graphene energy band: the linear dispersion relationship between E_k and $\boldsymbol{k}$ near the Dirac point (Figure 1.5b), and the electron and hole can be treated as "massless particle". This relationship can be described by the equation:$E_{\pm}(k) = hFv_Fk$, here the velocity in graphene v_F is also called Fermi velocity, which is about 1/300 of the light (10^6 m/s). Due to this particular linear dispersion, carriers in graphene move in a different way compared to conventional metal or semiconductor, and result in some unique phenomena that are not observed in traditional materials [35-37]. From Figure 1.6a, it can be seen that the carrier density of graphene can be tuned by the gate voltage, while the V_g sweeps from minus voltage to the positive side, the Fermi level (E_F) increases from lower band to the Dirac point and in the end reaches the upper band. The carrier mobility μ measured is up to about 60,000 $cm^2\ V^{-1}\ s^{-1}$ even at low temperature of 4K [12]. The highest mobility reported is near 200,000 $cm^2\ V^{-1}\ s^{-1}$ (for carrier densities below 5×10^9 cm^{-2}) measured at low temperature on suspended graphene, which results from the ballistic transport mechanism [38]. The anomalous

half-integer quantum Hall Effect (QHE) was also observed in graphene, the quantization condition is shifted by a half-integer, which is different from the QEF observed in traditional 2D materials. This is also attributed to the topologically exceptional electronic structure of graphene, which presents the electron–hole degeneracy and massless carrier near the point of charge neutrality [39]. Moreover, the quantum Hall Effect was also observed at room temperature at Manchester University in 2007, which was measured at 300K under high magnetic field of 29T [40]. This will pave the way for novel graphene based quantum devices in the future.

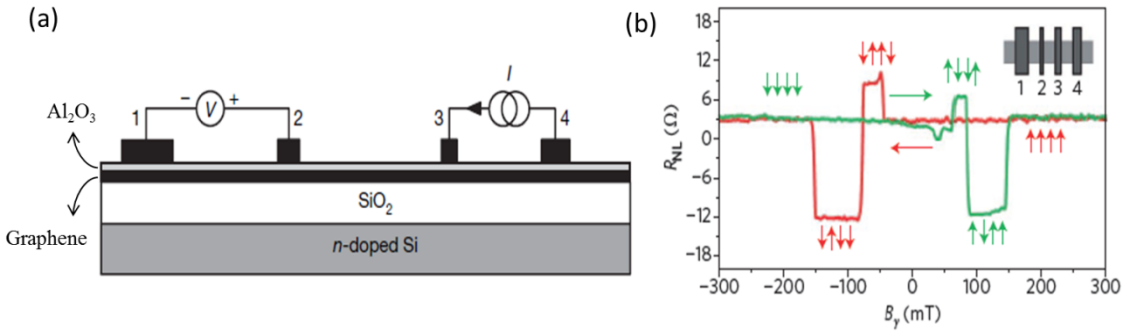

Figure 1.7 Spin transport in a spin-valve device. (a) Non-local spin transport measurement structure (b) Non-local spin signal detected on graphene with Al_2O_3 barrier at 4.2K. The magnetic field sweeping directions are indicated by the green and red arrows. The electron configuration is shown in the inset [42].

1.3.3 Spin Transport

Due to the special lattice and band structure of graphene, it is predicted to observe the anomalous magnetic properties such as half-metallic spin ordering and magnetized edges in graphene. And the weak spin-orbit coupling and hyperfine interactions could also lead to the long spin lifetime of the electron spins. Combined with the high carrier mobility in graphene, it is thought to have a long spin relaxation length in graphene based device. To perform spin signal measurement in graphene, the “non-local” geometry was used, as shown in Figure 1.7 (a). One layer Al_2O_3 was prepared on graphene, and the cobalt electrodes were prepared on oxide layer with four terminal contact configurations. The spin current is injected into graphene from electrode 3 and is extracted at electrode 4. The spin current will diffuse to electrode 4 mixed with charge current while the pure spin current moves towards the electrode 2. The spin signal is detected by the voltage between electrode 1 and 2. An in-plane magnetic field is applied along the y direction to generate the magnetized and anti-magnetized spin electrons between electrode 2

and 3 [42]. In 2007, the spin transport in graphene at room temperature was first observed by the Van Wees group at Zernike Institute for Advanced Materials (Figure 1.7b). The extracted spin relaxation length is between 1.5 μm and 2 μm at room temperature, and no significant change was found among the different measurement temperatures: 4.2K, 77K and room temperature [42]. In 2014, this group also fabricated mono layer graphene spin transport device on SiO_2 substrate covered by hexagonal boron nitride (BN), the measured spin relaxation times (τ_s) is up to about 2 ns and spin relaxation length (λ_s) exceeding 12 μm (highest reported) [43]. The longest spin life time of 6.2 ns was observed in bilayer graphene (BLG) spin device at 20K [44]. The non-local magneto-resistance (MR) and spin efficiency are two other parameters that characterize the spin injection effect. Using TiO_2 seeded MgO tunnel barrier, the largest non-local MR of 130 Ω was observed at room temperature by W. Han et al. in 2010. And the spin injection efficiency is calculated to be 26%-30%, which is higher than interface (between ferromagnetic electrode and graphene) using pinholes (2%-8%) and transparent contacts (1%) mode [45]. Recently, the spin transport in graphene-hBN heterostructure was also studied. The measurements performed at room temperature showed that the spin lifetime exceeded 2ns and spin diffusion length was over 10 μm, the carrier motilities was up to 20000 $cm^2 V^{-1} s^{-1}$ [46]. These results show high application potential paving the way to novel spintronic devices.

1.4 Preparation of graphene

Graphene has been prepared by various kinds of methods and on different substrates, such as exfoliation, chemical vapor deposition, epitaxy et al. Here some common methods will be introduced and discussed, about advantages, disadvantages and potential application areas.

1.4.1 Exfoliation

Mechanical exfoliation is one of the most used methods to fabricate graphene samples. Using the adhesive tape, thin layers of highly oriented pyrolytic graphite (HOPG) were cleaved off with repeated peeling process, and until get the single layer, bilayer or multilayer graphene samples needed. This method shows high reliability and can produce graphene up to 10 μm size, multilayer graphene (≥ 3nm) ranges to 100 μm has also been prepared successfully [12].

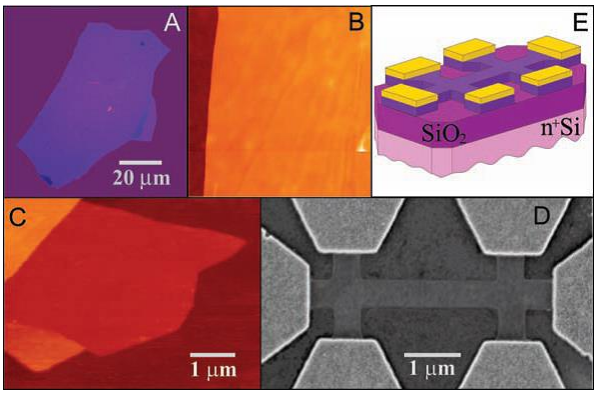

Figure 1.8 (a) Multilayer graphene on SiO_2/Si substrate (b) Atomic force microscopy (AFM) of graphene surface edge (c) AFM image of monolayer graphene (d) Scanning electron microscopy (SEM) image of multilayer graphene device (e) Schematic of the device show in D [12].

The first exfoliated graphene was prepared by K. S. Novoselov, A. K. Geim and other colleagues in 2004, as shown in Figure 1.8. The multilayer graphene in the size of 100 μm was prepared on the SiO_2/Si substrate, and the edge between graphene and the SiO_2 can be clearly observed in area of 2μm × 2 μm under AFM. The multilayer graphene device was fabricated (Figure 1.8d and 1.8e) to investigate the electronic properties, and carrier motilities up to about 10,000 cm^2/ V s was observed at room temperature [12]. Mechanical exfoliation is a method of low cost and no special equipment is needed. Meanwhile the exfoliated graphene shows high quality with few defects contained, which leads to extraordinary electronic properties for research. But on the other hand, it is hard to get a series of identical graphene films, which results from the remarkably difference in shape, size and thickness. These drawbacks limit this method for large-scale production. And according to this condition, many researchers have been focused on increasing the quality of graphene by exfoliation each time. In 2007, X.G. Liang et al. developed a new method involved using the pillars on a stamp to stick on and exfoliate graphene from graphite flakes. Then investigated the quality of graphene under SEM, if it is good, the graphene sheet would be transferred onto the active area of the substrate. This printed graphene sample has hole and electron mobility of 3,735 and 795 cm^2/V s, which is smaller than the exfoliated graphene prepared by scotch tape but still keep good conductivity [47]. In 2009, S. Li et al. used gold film as the transfer stamp to exfoliate graphene from HOPG, the printed graphene are identified made up of single-layer and multilayer graphene under Raman spectroscopy. These

studies improve the controllability (shape, size) of obtained graphene sheets, while the control of graphene layers still remains a problem [48].

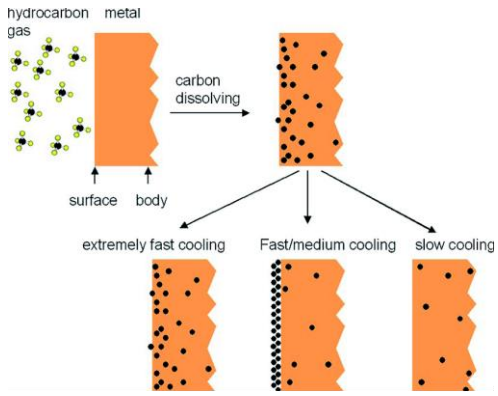

Figure 1.9 Schematic of carbon dissolution on the Ni surface [50].

1.4.2 Chemical vapor deposition

Chemical vapor deposition (CVD) has developed very fast during the past decades and become a vital technology to deposit varieties of high-purity, high density monocrystalline, polycrystalline and amorphous materials, such as carbon nanotubes, silicon carbide, silicon nitride, silicon oxide, gallium arsenide, indium gallium nitride, et al. It is the fundamental process that widely used in semiconductor, solar cell, and MEMS areas. During the typical CVD process, the precursors (in the form of vapor phase) are introduced into a reaction chamber at a certain temperature and pressure, after reaching the heated substrate, the reactions among the precursors result in the deposition of solid phase onto the substrate and then form the materials needed [49]. According to the operating pressure, the CVD method can be classified into three types: atmospheric pressure CVD (APCVD), low-pressure CVD (LPCVD) and ultrahigh vacuum CVD (UHVCVD). The first graphene prepared by CVD method was reported by Q.K. Yu et al. in 2008. As shown in Figure 1.9, the hydrocarbon gases were introduced into the chamber with the Ni foils placed inside. Then, the hydrocarbon molecules decomposed and carbon atoms dissolved into Ni substrate at high temperature (1000 ℃). Next, the samples were cooled down and lead to the carbon segregation from the Ni substrate. By controlling the cooling rates, the segregation effect is different. Extremely fast cooling (20 ℃/ s) results in reduced migration of the carbon atoms before they can diffuse on the substrate. While the slow cooling (0.1 ℃/ s) leads to most carbon atoms stay inside the substrate. Using the fast/medium cooling (10 ℃/ s),

one part of the carbon atoms segregate at the surface and form graphene on the substrate. In the end, graphene of 5×5 mm^2 grown on the Ni substrate was transferred to a glass plate with silicone rubber used as the media. The intensity ratio of 2D peak to G peak in Raman spectroscopy shows the graphene obtained is of few (four or less) layers [50]. In order to apply the graphene as transparent electrode, K.S. Kim et al. prepared large-scale (centimeter) graphene grown on nickel substrate by CVD in 2009. Meanwhile, two different transfer methods were presented: (1) put the graphene samples into 1M $FeCl_3$ aqueous solution to etch the nickel layers, and then transfer the graphene onto other substrates (2) use polydimethylsiloxane (PDMS) stamp to exfoliate graphene from Ni substrate and then stamping it to other substrates, also called dry-transfer process. The graphene prepared by this method shows high electron mobility larger than 3700 cm^2 V^{-1} s^{-1} and half-integer quantum Hall effect at low temperature, the optical transparency observed is up to 80% [51]. However, due to the pyrolysis of the precursor species, limited grain size, high carbon solubility and heterogeneous structure at the grain boundaries, it is hard to obtain uniform and continues graphene film grown on Ni substrate.

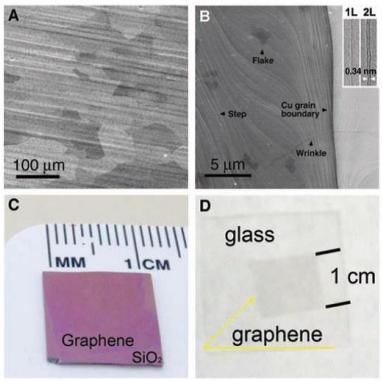

Figure 1.10 (a) SEM image of graphene on copper foils (b) High-resolution SEM image of graphene on Cu (c) and (d) Graphene films transferred onto SiO_2/Si substrate and glass plate [52].

In this case, the graphene grown on many kinds of metal substrates have been studied, such as: Co, Pt, Ru, Re, Ir and Pd, and present different catalytic effect during fabrication processes [52]. Specially, the graphene grown on Cu foils prepared by X.S. Li et al. exhibits highly continues at the grain boundaries, low solubility of carbon and good control of graphene layers. Using a mixture of methane and hydrogen, the graphene was prepared on copper foils at temperature up to 1000 ℃ by chemical vapor deposition. In Figure 1.10a and 1.10b, one can see that steps on Cu foils formed after thermal annealing, the wrinkles result from the different

thermal expansion coefficient was also observed under high-resolution SEM. Then, a process with the use of polymethyl methacrylate (PMMA) was employed to transfer graphene onto substrate and glass plate (Figure 1.10c and 1.10d). The electronic properties of graphene grown on SiO_2/Si substrates was measured by fabricating dual-gated field-effect transistor, electron mobility as high as 4,050 $cm^2 V^{-1} s^{-1}$ was observed at room temperature [53].

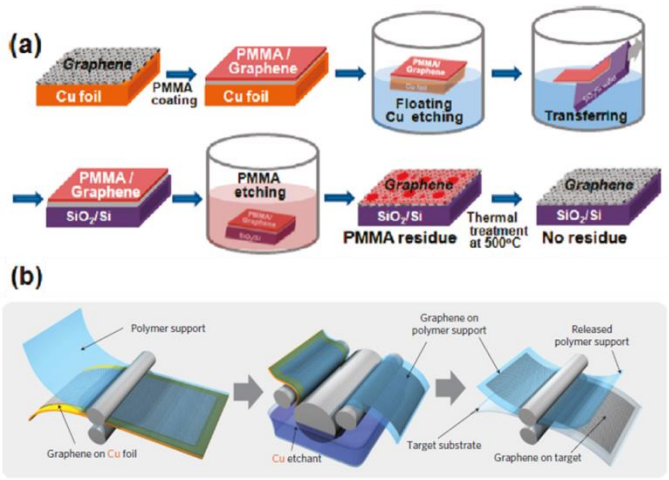

Figure 1.11 Schematic of (a) PMMA-mediated transfer method [54] (b) Roll to roll production of graphene films [55].

Typically there are two methods developed to transfer as-grown graphene on Cu foils onto target substrates, the PMMA-assisted transfer process is used to prepare small size (centimeter-scale) graphene, while the roll-to-roll transfer method can produce graphene in large size (up to 30 inches). A schematic illustration of PMMA-assisted transfer process is shown in Figure 1.11a. The graphene on copper foils was coated with PMMA and then float in aqueous solution, after the Cu foils were removed, the graphene was transferred onto the SiO_2/Si substrate. The PMMA remained on graphene surface was etched away by acetone, and a thermal treatment at 500 ℃ was used to further decompose the PMMA residues on graphene [54]. Based on the work of X.S. Li and his colleagues, S. Bae et al. reported a roll to roll method of producing 30-inch graphene in 2010. An 8-inch-wide tubular quartz reactor was used in the CVD system which allowed fabricating the graphene as large as 30 inches on a roll of Cu foil. Similar to the PMMA-assisted transfer process, a polymer film was adhered to the surface of graphene, and then put it into aqueous 0.1 M ammonium persulphate solution $(NH_4)_2S_2O_8$ to remove the copper foils. In the end, the polymer support was removed and graphene was transfer onto the target substrate.

The large-scale graphene exhibits high-quality with sheet resistance of about 125 Ω, 97.4% optical transmittance, and half-integer quantum Hall effect was also observed [55]. This work shows highly potential for commercial production of large-scale graphene electrodes. However, there are also some challenges need to be paid attention. As the Cu is less reactive than Ni, it maybe oxidized during the deposition process, thus lower base pressure and temperature is needed to offload the graphene sample. More importantly, the graphene grown on metals like Cu and Ni CVD still shows polycrystalline structure with many grain boundaries and different crystallographic orientations, this is due to these metal catalysts are difficult to form single crystalline even after annealing treatment [56]. Also, the PMMA residues on graphene surface are hard to be removed completely. This will lead to chemical doping in graphene and change its properties [57].

1.4.3 Epitaxial graphene on Silicon Carbide

The first study of graphite formed by decomposing silicon carbide was carried out by D.V. Badami et al. in 1965. After heating the SiC crystal to about 2280 ℃ for one hour and investigated its structure under X-ray diffraction, they found pseudomorphs which were made up of different stages of graphite lattice formed on the SiC [58]. Followed by this work, in 1975, Van Bommel and his colleagues revealed that the graphite layer formed on SiC (0001) substrate via $6\sqrt{3} \times 6\sqrt{3}R30$ structure with using low-energy electron diffraction (LEED) and Auger electron spectroscopy (AES) [59]. In 1998, I. Forbeaux et al. used angular-resolved inverse photoemission spectroscopy (KRIPES) to study the progressive formation of graphite on 6H-SiC (0001) substrate. The graphite of good single crystalline quality was observed in KRIPES after annealing SiC at 1400 ℃ [60]. In 2000, M. Kusunoki et al. heated the SiC at 1700 °C for half an hour in vacuum, and thin layer graphite (few layers graphene) sheet was found formed on the SiC substrate with the cross section high-resolution electron microscopy [61]. In 2004, ultrathin epitaxial graphite was prepared on 6H-SiC substrate by C. Berger et al. at Georgia Institute of Technology, the Shubnikov-de Haas oscillations observed suggested a potential new quantum Hall system [62]. In 2006, they also revealed the Dirac nature of the charge carriers in epitaxial graphene on SiC and found the mobilities exceeding 25,000 $cm^2 V^{-1}s^{-1}$ at 4K [63].

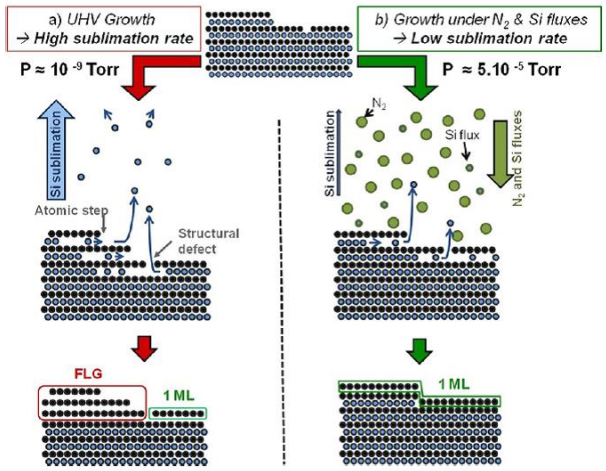

Figure 1.12 Epitaxial graphene grown on SiC under (a) UHV condition (b) N_2 and Si fluxes, exhibits a uniform single layer graphene [64].

As the graphene prepared by CVD can be greatly influenced during the transfer process, epitaxial graphene grown on silicon carbide provides a convenient method without transferring needed, thus the chemical contaminations will not be introduced into graphene. Epitaxial graphene can be easily formed on silicon carbide (SiC) by directly heating the SiC substrate to a high temperature in vacuum or in an inert gas atmosphere, then the silicon atoms will sublimate from the substrate and leave carbon atoms on the substrate, these remained carbon atoms can form the epitaxial graphene spontaneously on the SiC substrate surface (Figure 1.12) [64]. Single crystal 6H-SiC and 4H-SiC are both used to prepare graphene on the substrate surface. Traditionally, this method can be classified into two-types: graphene grown on Si face and graphene grown on C face. On the Si-terminated face, graphene shows good control of the thickness, high homogeneous and has good transport properties. But there is a buffer carbon layer between graphene and SiC, it has honeycomb lattice structure and is electrically inert. While on the C-terminated face, the graphene tend to form multilayer structure, and the layers are not homogeneous, the graphene domains are in the size of about 200 nm. And in contrast, no buffer layer is observed between graphene and SiC substrate [65-67]. Moreover, it is worth pointing out, the sublimation effect of on-axis and off axis SiC substrates lead to different quality of the graphene sheets. The on-axis SiC substrate exhibits lots of step bunching effect, and the formation of continuous graphene layers are prevented. These terraces and steps also influence the electronic properties of graphene grown on SiC substrate. As for the on-axis Si-terminated

SiC substrate, small domains (typically 30-200 nm in diameter) are observed in graphene after vacuum annealing. While for the on-axis C-terminated SiC substrate, a small amount of disorders are observed between the graphene sheets [64] [67-68]. Many works have been done to increase the quality of graphene grown on on-axis SiC substrate, K.V. Emtsev et al. heated the SiC substrate in argon atmosphere of about 1 bar, then larger domain size and improved quality of graphene films were obtained, the mobility reached about 2,000 $cm^2\ V^{-1}\ s^{-1}$ at 27 K [65]. R. M. Tromp and J. B. Hannon reported by controlling the sublimation rate with introduced external Si gas, the morphology of C-rich surface and epitaxial graphene were significantly improved [69]. On the other hand, the off-axis SiC substrate contains much less steps and the bunching effect is reduced, thus the number of disorder is not as significant as graphene on the on-axis substrate [64]. In 2012, A. Ouerghi et al. successfully prepared large area graphene up to hundreds of micrometers on off-axis Si-terminated SiC substrate under N_2 and Si mixture gas atmosphere, as shown in Figure 1.12b. The sublimation process was performed under N_2 gas with partial pressure of 2×10^5 Torr, and the Si deposition rate is 1 ML/min. High quality of uniform monolayer graphene with original surface morphology was observed under STM, LEED and low-energy electron microscopy (LEEM) [64]. Epitaxial graphene on SiC substrate shows highly potential for application in high-speed and high-frequency transistors, meanwhile the low cost due to this convenient method has also attracted many scientists and researchers to improve the quality of epitaxial graphene grown on SiC substrate.

1.4.4 Graphene on Boron nitride substrate

Graphene grown on SiO_2 substrate has been studied for a long time, but the roughness and charge traps on SiO_2 prevent increasing the electronic properties of graphene based devices. Recently, prepare graphene on hexagonal boron nitride (h-BN) substrate has attracted much interest due to the same structure and similar properties to graphene. The hexagonal boron nitride is an insulating isomorph of graphite and presents honeycomb lattice structure occupied with boron and nitrogen atoms, the lattice constant is 1.8% longer than that of graphene. The different energy of the boron and nitrogen atoms leads to large band gap of 5.97 eV and 1.7% mismatch with graphite. Furthermore, the ultra-flat surface of h-BN could suppress the rippling of graphene, and ionic bonding results in nearly free dangling bonds and charge traps, these unique properties make h-BN as an ideal substrate to support graphene [70-71].

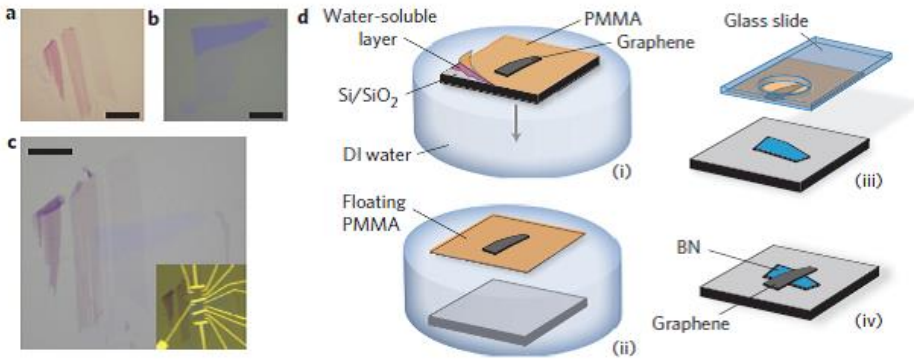

Figure 1.13 Image of (a) Graphene and h-BN substrate (b) before transfer (c) after transfer. Scale bar is 10 μm. The inset shows electrodes pattern on graphene (d) Schematic of process about transferring graphene onto h-BN substrate [70].

A mechanical transfer process was used by C. R. Dean et al. to prepare graphene on h-BN, as shown in Figure 1.13. The exfoliated graphene and h-BN substrate before transfer were observed under optical microscopy (Figure 1.13a and b). During the transfer process (Figure 1.13d), the graphene was first exfoliated onto the polymer film consisted of PMMA and water soluble layer, and then float the substrate on top of the deionized water. When the water soluble layer was dissolved, the Si/SiO_2 substrate dropped to the bottom of the water. Then the PMMA film was stick to a glass slide with graphene on the other side. Afterwards, located the position of graphene and accurately aligned to h-BN substrate with microscopy, the graphene and h-BN were then brought to touch with each other. In the end, heated the substrate at 110 ℃ to evaporate adsorbed water on the surface of graphene and h-BN, meanwhile increase the adhesion between PMMA and substrate. The PMMA was removed by acetone and the graphene grown on h-BN substrate was obtained. In order to remove the PMMA residues, the graphene on h-BN was annealed in H_2/Ar gas at 340 ℃ for 3.5 h. The electrodes were fabricated on graphene using standard electron beam lithography, see in Figure 1.13c. The electronic transport measurements showed the mobility reached up to 60,000 $cm^2 V^{-1} s^{-1}$ which is much higher than graphene on SiO_2, this indicated excellent quality of graphene. The Landau levels and Shubnikov–de Haas oscillations were also observed during the magneto-transport measurements [70]. In 2011, this group also studied the fractional quantum Hall effect (FQHE) in graphene on h-BN, and large energy gap between landau levels was observed. The Hall mobility at high density is about 30,000 $cm^2 V^{-1} s^{-1}$ at 300 mK, while the charged-impurity mobility, which plays the most

important role at low density, exceeds ultra-high value of 100,000 $cm^2 V^{-1} s^{-1}$ [72]. J. M. Xue et al. investigated the morphology of graphene on h-BN using scanning tunneling microscopy and spectroscopy, the electron-hole puddles were significantly reduced by two orders compared to graphene on SiO_2, which results in small charge fluctuations at the same level with suspended graphene [71]. The highest carrier mobility 500,000 $cm^2 V^{-1} s^{-1}$ of graphene on h-BN was obtained by A. K. Geim et al., and they found it is crucial not to expose graphene side that contact with h-BN to any solvents during the fabrication process [73]. In 2013, they reported the appearance of second generation Dirac points, and the anomalous fractional Quantum Hall Effect was also observed [74].

1.5 Modulation of Structural and Transport properties of graphene

The studies of modulation of graphene properties have attracted much more attention during last few years, which mainly focus on probing the fundamental properties of graphene and developing various functions for specific applications. Many kinds of methods have been employed, such as: electric field, electrochemical, chemical doping, irradiation, and interface engineering, et al. In 2007, J. Yan et al. observed tunable electron-phonon coupling in graphene by applying external electric field. The interactions of optical phonons with Dirac fermions were modified by gate voltage and result in band shifts in Raman spectra. These results prove the relationship between electric field and electron-phonon coupling and provide a convenient approach to investigate electronic properties of graphene [75]. Also, this method can be used to adjust the work function of graphene, which results from the modification of Fermi level by controlling the applied gate voltage. The work function ranges for SLG and BLG in ambient and dry conditions are 4.5-4.8 eV and 4.65-4.75 eV respectively. Moreover, with chemical functionalization, the range can be further enlarged and makes graphene as a good candidate for low barrier contact electrodes [76].

Electrochemical is another useful method to modify the properties of graphene. R.S. Sundaram prepared palladium-decorated graphene using electrodeposition, which was carried out in ethanol with Na_2PdCl_4 and $LiClO_4$ as supporting electrolyte. Electrical measurement showed the maximum resistance of graphene covered by Pd particles decreased compared to the pristine graphene. And with higher density of Pd particles, the decrease was more significant. Meanwhile, in order to investigate the application probability as chemical sensor, the palladium-decorated

graphene was measured in different gas atmospheres. While exposed the modified graphene to hydrogen, the resistance maximum showed a remarkably shift to the negative gate voltage. This can be related to hydrogen decomposed and dissociated on Pd particles, thus results in the reduction of work function and more electrons moves onto the graphene surface. This method provides a valuable way to expand the application of graphene, and it is predicted that by using an array of metal particles to decorate the graphene surface, it may be able to observe the modification of the quantum interference phenomena [77].

Interface engineering is also frequently employed to tune the properties of graphene. R. Wang et al. investigated the interface effect on graphene prepared on four kinds of substrates: PMMA, SiO_2, SiO_2 modified with two different silanes-$(CF_3)(CF_2)_5(CH_2)_2Si(OC_2H5)_3$ (FTS) and $(NH_2)(CH_2)_3Si(OC_2H_5)_3$ (ATS), the electrical properties of suspended graphene was also measured. The Raman spectra displayed a significant variation in position, intensity and bandwidth, indicating modification of electronic properties. Also the Fermi level can be controlled in the range of -130 mV to 90 mV, while carrier concentration is up to 10^{12} cm^{-2} [78].

Chemical doping and irradiation are two other major methods to modulate the properties of graphene. In this thesis, ion irradiation induced chemical doping was observed in graphene on SiO_2 substrate prepared by CVD method, and the influence of electron beam irradiation on graphene grown on SiC substrate was also investigated. The modification of structural properties of graphene after irradiation and its relationship with the transport properties are demonstrated, which can be used to build up future graphene memory and logic integrated circuits.

References

(1) Shockley, W.; Pearson, G. L. Modulation of conductance of thin films of semi-conductors by surface charges. *Phys. Rev.* **1948**, *74*, 232.

(2) Source: Retrieved Feb 2, **2015**, from: http://www.beatriceco.com/bti/porticus/bell/belllabs_transistor.html.

(3) Digital Revolution. In Wikipedia, the free encyclopedia. January 30, **2015**. Retrieved February 2, **2015**, http://en.wikipedia.org/wiki/Digital_Revolution.

(4) "The Nobel Prize in Physics 1956". *Nobelprize.org*.

(5) Moore, G. E. Cramming more components onto integrated circuits. *Electronics Magazine.***1965**, *38*, 8.

(6) Thompson, S. E, Parthasarathy, S. Moore's law: the future of Si microelectronics. *Mater. Today.* **2006**, *9*(6), 20.

(7) Schwierz, F. Graphene transistors. *Nat nanotechnol.* **2010**, *5*(7), 487.

(8) The International Technology Roadmap for Semiconductors, **2013**, Lithography.

(9) Tans, S. J.; Verschueren, A. R. M.; Dekker, C. Room-temperature transistor based on a single carbon nanotube. *Nature.* **1998**, *393*, 49.

(10) Martel, R.; Schmidt, T.; Shea, H. R.; Hertel, T.; Avouris, Ph. Single- and multi-wall carbon nanotube field-effect transistors. *Appl. Phys. Lett.* **1998**, *73*, 2447.

(11) Cao, Q.; Rogers, J. A. Ultrathin Films of Single-Walled Carbon Nanotubes for Electronics and Sensors: A Review of Fundamental and Applied Aspects. *Adv. Mater.* **2009**, *21*(1), 29.

(12) Novoselov, K. S.; Geim, A. K.; Morozov, S. V.; Jiang, D.; Zhang, Y.; Dubonos, S. V.; Grigorieva, I. V.; Firsov, A. A. Electric field effect in atomically thin carbon films. *Science.* **2004**, *306*, 666.

(13) Lin, Y. M.; Valdes-Garcia, Alberto.; Han, Shu-Jen,; Farmer, D. B.; Meric, I.; Sun Y. N.; Wu Y. Q.; Dimitrakopoulos, C.; Grill, A.; Avouris P.; Jenkins, K. A. Wafer-Scale Graphene Integrated Circuit. *Science*. **2011**, *332*, 1294.

(14) Hong, A. J.; Song, E. B.; Yu, H. S.; Allen, M. J.; Kim, J.; Fowler, J. D.; Wang, K. L. Graphene flash memory. *ACS nano*, **2011**, *5*(10), 7812.

(15) "The Nobel Prize in Physics 2010". *Nobelprize.org*.

(16) Pierson, H. O. Handbook of carbon, graphite, diamonds and fullerenes: processing, properties and applications. *William Andrew.* **1994**.

(17) Burchell, T. D. (Ed.). Carbon materials for advanced technologies. *Elsevier.* **1999**.

(18) Source: Retrieved Feb 1, **2015**, from: http://en.wikipedia.org/wiki/Diamond.

(19) Source: Retrieved Feb 1, **2015**, from: http://powerlisting.wikia.com/wiki/Graphite_Manipulation.

(20) Source: Retrieved Feb 2, **2015**, from: http://orientallinkholding.com/GRAPHITE.php.

(21) Source: Retrieved Feb 2, **2015**, from: http://nanotechnologyuniverse.com/buckyballs-the-molecular-structure-of-our-future/.

(22) Source: Retrieved Feb 2, **2015**, from: http://www.gaia3d.co.uk/3d-models/3d-chemistry/carbon-nanotube/.

(23) Kroto, H. W.; Heath, J. R.; Obrien, S. C.; Curl, R. F.; Smalley, R. E. C_{60}: Buckminsterfullerene. *Nature.* **1985**, *318*,162.

(24) Dresselhaus, M. S.; Dresselhaus, G.; Eklund, P. C. Science of fullerenes and carbon nanotubes: their properties and applications. *Academic press.* **1996**

(25) Iijima, S. Helical microtubules of graphitic carbon. *Nature.* **1991**, *354*, 56.

(26) Baughman, R. H.; Zakhidov, A. A.; de Heer, W. A. Carbon nanotubes--the route toward applications. *Science.* **2002**, *297*, 787.

(27) De Volder, M. F.; Tawfick, S. H.; Baughman, R. H.; Hart, A. J. Carbon nanotubes: present and future commercial applications. *Science.* **2013**, *339*, 535.

(28) Geim, A. K.; Novoselov, K. S. The rise of graphene. *Nat. Mater.* **2007**, *6*(3), 183.

(29) Debije, P; Scherrer, P. Interferenz an regellos orientierten Teilchen im Röntgenlicht I. *Phy. Z.* **1916**, *17*, 277.

(30) Kohlschütter, V.; Haenni, P. Zur Kenntnis des Graphitischen Kohlenstoffs und der Graphitsäure. *Zeitschrift für anorganische und allgemeine Chemie.* **1919**, *105*(1), 121.

(31) Wallace, P. R. The band theory of graphite. *Phys. Rev.* **1947**, *71*(9), 622.

(32) Ruess, G.; Vogt, F. Höchstlamellarer Kohlenstoff aus Graphitoxyhydroxyd. *Monatshefte für Chemie/Chemical Monthly.* **1948**, *78*(3), 222.

(33) Oshima, C.; Nagashima, A. Ultra-thin epitaxial films of graphite and hexagonal boron nitride on solid surfaces. *J. Phys.: Condens. Matter.* **1997**, *9*(1), 1.

(34) Novoselov, K. S.; Fal, V. I.; Colombo, L.; Gellert, P. R.; Schwab, M. G.; Kim, K. A roadmap for graphene. *Nature.* **2012**, *490*(7419), 192.

(35) Andrei, E. Y.; Guohong, L.; Xu, D. Electronic properties of graphene: a perspective from scanning tunneling microscopy and magnetotransport. *Rep. Prog. Phys.* **2012**, *75*,056501.

(36) Neto, A. C.; Guinea, F.; Peres, N. M. R.; Novoselov, K. S.; Geim, A. K. The electronic properties of graphene. *Rev. Mod. Phys.* **2009**, *81*(1), 109.

(37) Sarma, S. D.; Adam, S.; Hwang, E. H.; Rossi, E. Electronic transport in two-dimensional graphene. *Rev. Mod. Phys.* **2011**, *83*(2), 407.

(38) Du, X.; Skachko, I.; Barker, A.; Andrei, E. Y. Approaching ballistic transport in suspended graphene. *Nat. Nano.* **2008**, *3*(8), 491.

(39) Zhang, Y.; Tan, Y. W.; Stormer, H. L.; Kim, P. Experimental observation of the quantum Hall effect and Berry's phase in graphene. *Nature.* **2005**, *438*, 201.

(40) Novoselov, K. S.; Jiang, Z.; Zhang, Y.; Morozov, S. V.; Stormer, H. L.; Zeitler, U.; Geim, A. K. Room-temperature quantum Hall effect in graphene. *Science.* **2007**, *315*, 1379.

(41) Han, W.; Kawakami, R. K.; Gmitra M.; Fabian J. Graphene spintronics. *Nat. Nano.* **2014**, *9*, 794.

(42) Tombros, N.; Jozsa, C.; Popinciuc, M.; Jonkman, H. T.; Van Wees, B. J. Electronic spin transport and spin precession in single graphene layers at room temperature. *Nature.* **2007**, *448*, 571.

(43) Guimarães, M. H. D.; Zomer, P. J.; Ingla-Aynés, J.; Brant, J. C.; Tombros, N.; Van Wees, B. J. Controlling spin relaxation in hexagonal bn-encapsulated graphene with a transverse electric field. *Phys. Rev. Lett.* **2014**, *113*(8), 086602.

(44) Han, W.; Kawakami, R. K. Spin relaxation in single-layer and bilayer graphene. *Phys. Rev. Lett.* **2011**, *107*(4), 047207.

(45) Han, W.; Pi, K.; McCreary, K. M.; Li, Y.; Wong, J. J.; Swartz, A. G.; Kawakami, R. K. Tunneling spin injection into single layer graphene. *Phys. Rev. Lett.* **2010**, *105*(16), 167202.

(46) Drögeler, M.; Volmer, F.; Wolter, M.; Terrés, B.; Watanabe, K.; Taniguchi, T.; Beschoten, B. Nanosecond spin lifetimes in single-and few-layer graphene–hBN heterostructures at room temperature. *Nano Lett.* **2014**, *14*(11), 6050.

(47) Liang, X.; Fu, Z.; Chou, S. Y. Graphene transistors fabricated via transfer-printing in device active-areas on large wafer. *Nano Lett.* **2007**, *7*(12), 3840.

(48) Song, L.; Ci, L.; Gao, W.; Ajayan, P. M. Transfer printing of graphene using gold film. *ACS nano.* **2009**, *3*(6), 1353.

(49) Park, J. H.; Sudarshan, T. S. (Eds.). Chemical vapor deposition (Vol. 2). *ASM international.* **2001**.

(50) Yu, Q.; Lian, J.; Siriponglert, S.; Li, H.; Chen, Y. P.; Pei, S. S. Graphene segregated on Ni surfaces and transferred to insulators. *Appl. Phys. Lett.* **2008**, *93*(11), 113103.

(51) Kim, K. S.; Zhao, Y.; Jang, H.; Lee, S. Y.; Kim, J. M.; Kim, K. S.; Hong, B. H. Large-scale pattern growth of graphene films for stretchable transparent electrodes. *Nature*, **2009**, *457*(7230), 706.

(52) Zhang, Y.; Zhang, L.; Zhou, C. Review of chemical vapor deposition of graphene and related applications. *Acc. Chem. Res.* **2013**, *46*(10), 2329.

(53) Li, X. S.; Cai, W.; An, J.; Kim, S.; Nah, J.; Yang, D.; Ruoff, R. S. Large-area synthesis of high-quality and uniform graphene films on copper foils. *Science.* **2009**, *324*, 1312.

(54) Lee, W. H.; Park, J.; Sim, S. H.; Lim, S.; Kim, K. S.; Hong, B. H.; Cho, K. Surface-directed molecular assembly of pentacene on monolayer graphene for high-performance organic transistors. *J. Am. Chem. Soc.* **2011**, *133*(12), 4447.

(55) Bae, S.; Kim, H.; Lee, Y.; Xu, X.; Park, J. S.; Zheng, Y.; Iijima, S. Roll-to-roll production of 30-inch graphene films for transparent electrodes. *Nat. Nano.* **2010**, *5*(8), 574.

(56) Mikhailov, S. Physics and Applications of Graphene-Experiments. *Tech. Janeza. Trdine. Rijeka. Croatia*. **2011**.

(57) Lin, Y. C.; Lu, C. C.; Yeh, C. H.; Jin, C.; Suenaga, K.; Chiu, P. W. Graphene annealing: how clean can it be? *Nano Lett.* **2011**, *12*(1), 414.

(58) Badami, D. V. X-ray studies of graphite formed by decomposing silicon carbide *carbon. Carbon.* **1965**, *3*(1), 53.

(59) Van Bommel, A. J.; Crombeen, J. E.; Van Tooren, A. LEED and Auger electron observations of the SiC (0001) surface. *Surface Science.* **1975**, *48*(2), 463.

(60) Forbeaux, I.; Themlin, J. M.; Debever, J. M. Heteroepitaxial graphite on 6H-SiC (0001): Interface formation through conduction-band electronic structure. *Phys. Rev. B: Condens. Matter Mater. Phys.* **1998**, *58*(24), 16396.

(61) Kusunoki, M.; Suzuki, T.; Hirayama, T.; Shibata, N.; Kaneko, K. A formation mechanism of carbon nanotube films on SiC (0001). *Appl. Phys. Lett.* **2000**, *77*(4), 531.

(62) Berger, C.; Song, Z.; Li, T.; Li, X.; Ogbazghi, A. Y.; Feng, R.; De Heer, W. A. Ultrathin epitaxial graphite: 2D electron gas properties and a route toward graphene-based nanoelectronics. *J. Phys. Chem. B.* **2004**, *108*(52), 19912.

(63) Berger, C.; Song, Z.; Li, X.; Wu, X.; Brown, N.; Naud, C.; De Heer, W. A. Electronic confinement and coherence in patterned epitaxial graphene. *Science.* **2006**, *312*, 1191.

(64) Ouerghi, A.; Silly, M. G.; Marangolo, M.; Mathieu, C.; Eddrief, M.; Picher, M.; Belkhou, R. Large-area and high-quality epitaxial graphene on off-axis SiC wafers. *Acs Nano.* **2012**, *6*(7), 6075.

(65) Norimatsu, W.; Kusunoki, M. Structural features of epitaxial graphene on SiC {0001} surfaces. *J. Phys. D: Appl. Phys.* **2014**, *47*(9), 094017.

(66) Norimatsu, W.; Kusunoki, M. Epitaxial graphene on SiC {0001}: advances and perspectives. *Phys. Chem. Chem. Phys.* **2014**, *16*(8), 3501.

(67) Emtsev, K. V.; Bostwick, A.; Horn, K.; Jobst, J.; Kellogg, G. L.; Ley, L.; Seyller, T. Towards wafer-size graphene layers by atmospheric pressure graphitization of silicon carbide. *Nat. Mater.* **2009**, *8*(3), 203.

(68) Borysiuk, J.; Grodecki, K.; Wysmołek, A.; Strupinski, W.; Stepniewski, R.; Baranowski, J. M. Transmission electron microscopy investigations of epitaxial graphene on C-terminated 4H-SiC. *J. Appl. Phys.* **2010**, *108*(1), 013518.

(69) Tromp, R. M.; Hannon, J. B. Thermodynamics and kinetics of graphene growth on SiC (0001). *Phys. Rev. Lett.* **2009**, *102*(10), 106104.

(70) Dean, C. R.; Young, A. F.; Meric, I.; Lee, C.; Wang, L.; Sorgenfrei, S.; Hone, J. Boron nitride substrates for high-quality graphene electronics. *Nat. Nano.* **2010**, *5*(10), 722.

(71) Xue, J.; Sanchez-Yamagishi, J.; Bulmash, D.; Jacquod, P.; Deshpande, A.; Watanabe, K.; LeRoy, B. J. Scanning tunnelling microscopy and spectroscopy of ultra-flat graphene on hexagonal boron nitride. *Nat. Mater.* **2011**, *10*(4), 282.

(72) Dean, C. R.; Young, A. F.; Cadden-Zimansky, P.; Wang, L.; Ren, H.; Watanabe, K.; Shepard, K. L. Multicomponent fractional quantum Hall effect in graphene. *Nat. Phys.* **2011**, *7*(9), 693.

(73) Mayorov, A. S.; Gorbachev, R. V.; Morozov, S. V.; Britnell, L.; Jalil, R.; Ponomarenko, L. A.; Geim, A. K. Micrometer-scale ballistic transport in encapsulated graphene at room temperature. *Nano Lett.* **2011**, *11*(6), 2396.

(74) Ponomarenko, L. A.; Gorbachev, R. V.; Yu, G. L.; Elias, D. C.; Jalil, R.; Patel, A. A.; Geim, A. K. Cloning of Dirac fermions in graphene superlattices. *Nature.* **2013**, *497*(7451), 594.

(75) Yan, J.; Zhang, Y.; Kim, P.; Pinczuk, A. Electric field effect tuning of electron-phonon coupling in graphene. *Phys. Rev. Lett.* **2007**, *98*(16), 166802.

(76) Yu, Y. J.; Zhao, Y.; Ryu, S.; Brus, L. E.; Kim, K. S.; Kim, P. Tuning the graphene work function by electric field effect. *Nano Lett.* **2009**, *9*(10), 3430.

(77) Sundaram, R. S.; Gómez-Navarro, C.; Balasubramanian, K.; Burghard, M.; Kern, K. Electrochemical modification of graphene. *Adv. Mater.* **2008**, *20*(16), 3050.

(78) Wang, R.; Wang, S.; Zhang, D.; Li, Z.; Fang, Y.; Qiu, X. Control of carrier type and density in exfoliated graphene by interface engineering. *ACS nano*, **2010**, *5*(1), 408.

Chapter II Experimental Methods

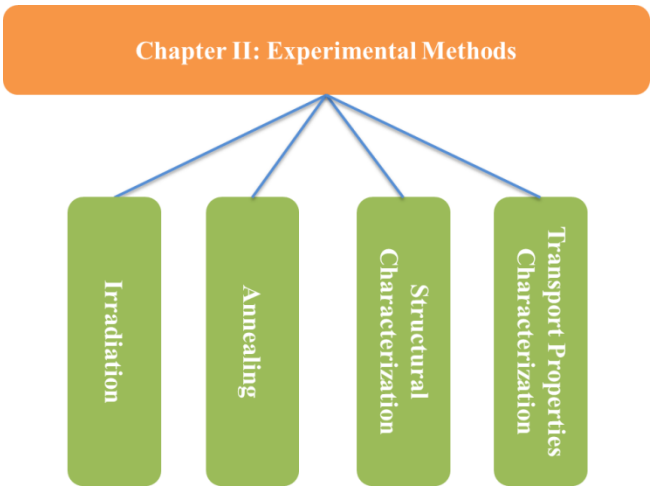

Figure 2.1 Organization of chapter II.

In this chapter, all the experimental techniques involved in this thesis were introduced. The Organization of chapter II was shown in figure 2.1. First, the irradiation technology employed to modify the properties of graphene was exhibited, two major irradiation types used in this thesis: ion irradiation, electron beam irradiation were introduced. Annealing was also presented as an important approach to restore the surface and structure of graphene. Then structural analysis of irradiated graphene was performed using Raman spectroscopy, X-ray photoelectron spectroscopy (XPS), atomic force microscopy (AFM). In the end, the transport properties were measured to study the transport properties of graphene after irradiation.

2.1 Irradiation

Irradiation involves the process that energetic particles interact with the target materials, which results in the modification of structure, and further modulates the electrical, chemical, optical and other properties [1-6]. It provides a useful tool to study basic properties or decorate the surface of target materials [1-4]. Meanwhile this method can be used to develop various kinds of functions for particular applications. According to the energy level and source type, the effect of irradiation is different and can be applied in different areas [1-6]. In this thesis, the modulation of structural and transport properties of graphene were investigated by ion and electron irradiation, meanwhile annealing provides a convenient method to restore these properties. The results observed indicate highly potential application in graphene based memory and logic devices, transistors, and integrated circuits.

Ion implantation is one type of ion irradiation which using accelerated ions to bombard the target materials at high energy [7-8]. This method is mostly used to introduce controllable doping in a substrate and modulate the electronic properties. Compared to chemical deposition, ion implantation is an ultra-clean process operated in high vacuum, it offers precise and fast control of the amount of the doping impurities, the doping profile is easily to be tailored, and the doping uniformity is also excellent [7-8]. A large number of elements such as boron, indium, nitrogen, hydrogen and helium, etc. have been used as the dopant source, and result in different doping effect in silicon ICs [9]. The first patent for ion implantation technology was proposed by William Shockley in 1954, but it was not until 1970s that ion implantation was applied in mass production, and nowadays ion implantation has become a vital process during the modern semiconductor fabrication [7-9]. Plasma source ion implantation (PSII) was invented by Professor John Conrad at the University of Wisconsin – Madison in 1980s [10], which was first applied to modify the surface of materials, such as metals, plastics, and ceramics, etc. In conventional ion implantation, the ion beam is extracted from the ion source, while in PSII technique, the target material is directly put in the plasma source and applied high voltage negative pulses, thus reducing the cost of ion implantation [10]. Nowadays, this technology has been used in a wide range of area such as industrial cutting tools, aerospace components and thin-film transistors, etc.

Food irradiation is a technology that widely used to reduce or destroy pathogenic microorganisms, bacteria and insects, and thus improving the quality and increasing the shelf life of the foods [5]. This method was first described in the patent proposed by J. Appleby and A.J. Miller in 1905. The most common source for irradiating food is Gamma rays emitted from radioactive cobalt (Cobalt 60) or cesium (Cesium 137), X-rays and Electron beam are also usually used [5] [11]. Food irradiation has been used for more than 50 years in European Union. National Aeronautics and Space Administration (NASA) also uses irradiation to sterilize the foods to avoid acquiring foodborne illnesses when the astronauts eat them in space. In agriculture, irradiation helps develop new products and improve the production of crop. X-rays, ultra-violet light, and gamma ray are always used to bombard the crops and seeds, which lead to varieties of mutations that have special properties, such as disease resistance, well adapted and higher nutritional value [13-15]. These crops offer safer and better quality for the life of human beings.

In medicine area, irradiation is used for diagnosis, radiation therapy and sterilization. X-ray and CT scan are frequently employed to diagnose the disease or damage in the body by using X-ray pass through specific position and form images of internal organs [16]. Radiation therapy is mostly used for cancer treatment which causes damage to the cancerous cells and reduces the surviving risk of surrounding healthy tissues [17]. Similar to food and agriculture, irradiation is also employed for sterilization by killing the germs and bacteria on the medical instruments [18].

2.1.1 Ion Irradiation

Ion irradiation is one of mostly used technology to modify the properties of target material. Due to the various type of ions, such as H^+, He^+, Ga^+, and Ar^+ ions, the irradiation effect are different. For example, C ions irradiation in carbon based material leads to interaction between the target material and external irradiation ions, while the He^+ ions irradiation only results in defects in the target material [4] [19]. According to the mass of ion, the ions used in irradiation are divided into two categories: heavy ions and light ions. Usually, the H, He and sometimes Li ions are considered as light ions, while the other ions of chemical element are classified as heavy ions, like C, N and Ne ions, etc. [4]. Another important factor that influences the irradiation effect is energy, normally the energy of ions below 30 keV is referred to low energy, while the energy higher than 30 keV and sometimes reach to MeV and even GeV is regarded as high energy. Also the dose plays a crucial role on irradiation effect. Low dose irradiation leads to a small amount of defects formed in the target material and makes a minor modification of the properties. The high dose irradiation means a number of ions strike the same area one time and results in major change of the structure of target material [4], for example, the Ar^+ irradiation over the dose density of 10^{15} Ar^+/cm^2 causes the full amorphization or partial sputtering of the graphene layer [20].

The first ion irradiation experiments on graphene have been carried out by L. Tapasztó et al. in 2008. Ar^+ ions irradiation was performed in mechanically exfoliated graphene layers prepared on SiO_2 substrate at 30 keV with a dose of 5×10^{11} ion/cm^2 [21]. Atomic resolution scanning tunneling microscopy and spectroscopy measurements showed that besides the well-known modification of the local on-site potential, the defects sites in graphene also induce disorder in the hopping amplitudes, which can substantially reduce the Fermi velocity [21]. Low energy 500 eV Ne and He ions irradiation effect on graphene transferred onto SiO_2 substrate was

also studied. A significant D band was observed in Raman spectroscopy which indicated defects formed in graphene. The defects result in a constant mobility, as well as the minimum conductivity dramatically decreases and the conductivity shows independent relationship on the temperature [22]. For high energy irradiation, 100 keV Ar^+ ions bombardment was performed on isotopically labeled single and bilayer graphene. The sample was prepared by subsequent transfer of CVD method fabricated ^{12}C and ^{13}C graphene onto SiO_2 substrate. Raman spectroscopy shows that the defects increase with the fluence in both bottom and top layer, while the final defect density of lower graphene layer is higher than top graphene layer. The amount of interstitials between substrate and bottom graphene is remarkably higher than that between two graphene layers. Self-annealing of defects presents an important method for 2D materials when using ion irradiation to tailor the graphene properties [23].

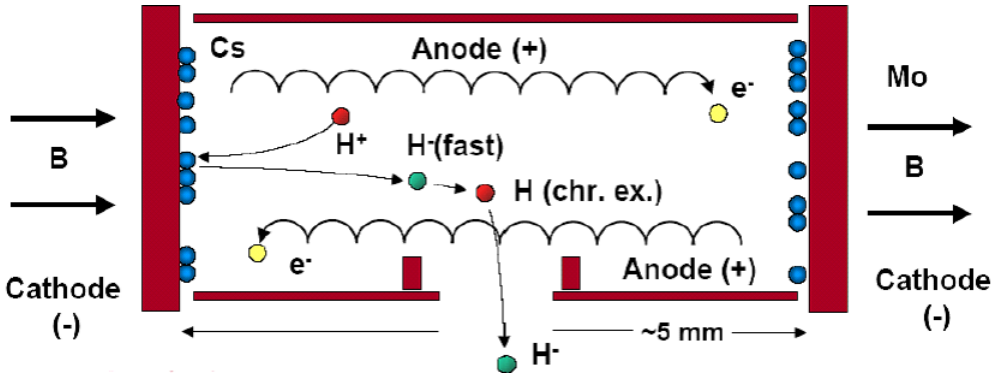

Figure 2.2 Illustration of Penning-ion source with lateral extraction [24].

In this thesis, low energy 5.4 keV He^+ ion irradiation was carried out to tailor the properties of graphene grown SiO_2 substrate by CVD method. The Penning or Philips Ionization Gauge (PIG) source was used to create He^+ ions in our experiments, as shown in Figure 2.2. Penning ionization is a fundamental atomic collision process which involves photochemical reaction between excited atom A^* (A adsorbed a photon) with target atom B, results in the formation of unexcited atom A, cation B^+ and an electron e^-. Meanwhile the process occurs in the condition that the energy of metastable atom A is higher than ionization energy of atom B [24-26].

$$A^* + B \rightarrow A + B^+ + e^- \qquad (3)$$

The process is named after the Dutch physicist Frans Michel Penning who first discovered it in1927 [26]. And before the invention of electron beam ion source (EBIS) and electron cyclotron

resonance ion source (ECRIS), Penning ion source is the only method to generate charged ions [24]. Typically, a Penning source is made up of annular cathode iron (or two cathodes facing each other), stainless steel anode, and samarium cobalt permanent magnet. The electrons emitted from the reaction process circumgyrate around the magnetic field lines and diffuse slowly along the anode. Meanwhile, the effective travel length of the electron in the reactive chamber is increased which results from the magnetic field. The material need to be ionized is situated in the anode and will be sputtered into the reactive area [24] [27]. The Penning source can be used to produce many kinds of charged ions and applied in a variety of area, such as electromagnetic separation of isotopes, controlled fusion, sealed-tube neutron generator, etc. [25].

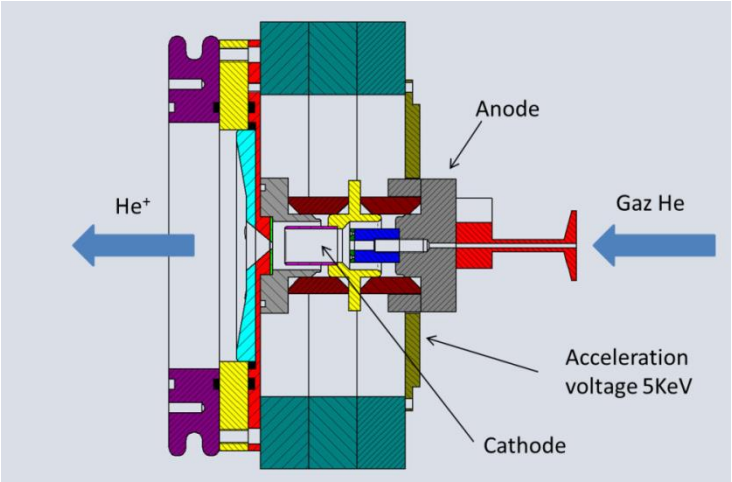

Figure 2.3 Sectional view of the Penning source setup [28].

Sectional view of the Penning source setup in our experiment is shown in Figure 2.3. It is composed of two electrodes, an anode and a cathode. The penning source is located inside the vacuum chamber and helium gas is injected directly into the source. A voltage of 2 kV is applied between the anode and cathode, which results in an oscillation of the charged particles. The presences of cylindrical magnets result in a magnetic field, and lead to the transfer of ions in a helical way, thereby the mean free path and the rate of ionization are both increased. An acceleration voltage range of 5-20 kV is applied between the source and the mass in the experiment. This voltage will accelerate the ions and pass through a hole in 2 mm diameter, and then the ions will be removed by a voltage of 5.4 kV through the extraction electrode which is grounded. It is worth to point out that when the gas is ionized (no longer electrical neutral), it contains ions, electrons and neutral molecules. Such a mixture is called plasma [28]. Figure 2.4

shows the photograph of the irradiation setup employed in this thesis. All voltages and currents are controlled on computer using programs written by LabVIEW language. In our experiments, the He^+ irradiation was performed under base pressure of 2×10^{-7} mbar and an operation pressure of 1×10^{-6} mbar, voltage applied on the anode was around 2.5 kV, the current in the anode was 0.1 mA, and with 20 μA ion beam currents.

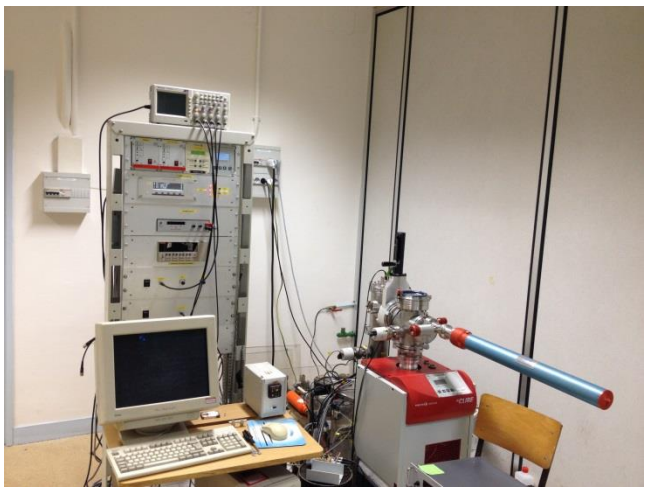

Figure 2.4 Photograph of the irradiation setup employed in this thesis.

2.1.2 Electron Irradiation

Electron irradiation is a process which involves accelerating electrons to certain energy and bombards the target material. As the mass of electron is much lighter than ion, the damage result from electron beam irradiation is less harmful than ion irradiation. Also, the electron irradiation will not lead to chemical doping in graphene compared to ion irradiation [4] [19]. For example, using NH_3 annealing after N^+ ion irradiation, the N-doping in graphene samples could be obtained [29]. Various approaches can be used to perform electron irradiation, such as transmission electron microscopy (TEM), scanning electron microscope (SEM) and specific high energy facilities, etc. [4]. Direct evidence for atomic defects in graphene layers have been observed by A. Hashimoto et al. under TEM in 2004. After several tens of seconds irradiation, the topological defects were formed in situ in graphene [30]. The high energy 1MeV electron beam irradiation on the graphene layers grown on 6H-SiC (0001) revealed the layered structure of graphene was destroyed and many small flakes and hillocks formed. The size of the hillocks increased with the e-beam irradiation fluence. XPS results also show the e-beam irradiation

induced oxidation of the graphene layer at room temperature in ambient condition [31]. Investigation of crystal lattice changes in the exfoliated graphene on SiO_2/Si substrate induced by the low and medium (5–20 keV) energy e-beam irradiation has also been reported. The strong disorder D band around 1345 cm^{-1} was appeared after the radiation, indicating damage to the graphene lattice structure. As the irradiation dose increases, the evolution of D and G peak follows the amorphization trajectory, which indicates graphene transform from crystalline to the nanocrystalline and in the end to amorphous form [32]. Recently, low energy (10 keV) e-beam irradiation performed by L. Tao et al. suggests disorder formed in graphene and the amount of disorder increases with the irradiation time, and these disorders can be partly recovered after annealing [33].

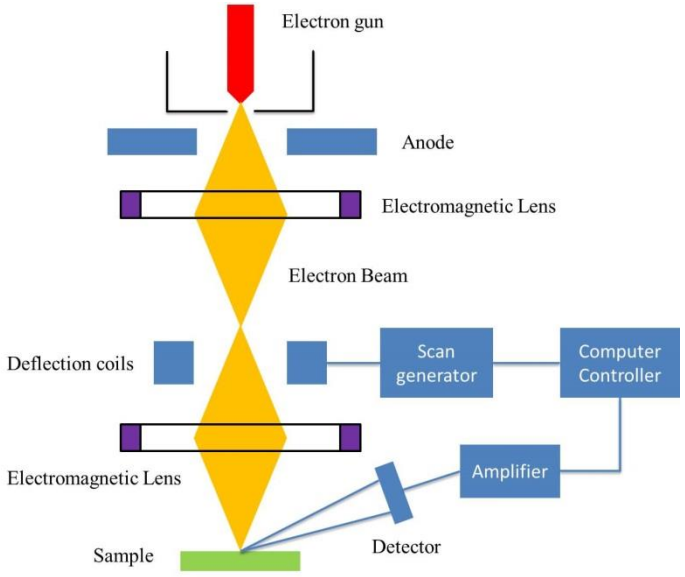

Figure 2.5 Schematic of basic components of a typical scanning electron microscope.

SEM is a convenient and cost-effective method to perform e-beam irradiation in graphene. It is mostly used to characterize the surface and cross-section morphology of material [34]. The concept and basic principle of SEM was described by Max Knoll et al. in the early 1930's [35], and in 1938 the first scanning transmission electron microscope (STEM) was constructed by Von Ardenne [36]. In 1942, SEM was first used to characterize the surface of bulk material by Zworykin and his colleagues [37]. But it was until 1965 that the first commercial SEM was fabricated by Cambridge Scientific Instrument Company. Nowadays, SEM has been widely employed in a wide range of areas such as Physics, Chemistry, Biology, Medicine, etc. A typical

component of SEM instrument is shown in figure 2.5. The primary electron beam is emitted from the electron gun, then electromagnetic lens and deflection coils is used to control the travelling path of electrons and reach the target material place on the sample stage. The secondary electrons, backscattered electrons, Auger electrons, X-rays and cathodo luminescence are generated after the interaction between incident electron beam and the sample. In the end, special detector such as secondary electrons detector, backscattered electron detector are placed in particular position to gather these excited electrons and form image on the computer [38].

In our experiments, the SEM FEG Philips XL30S Scanning Electron Microscope (SEM) was used to irradiate the epitaxial graphene grown on silicon carbide. A Schottky based field emission gun (FEG) is used and the sample is placed at where the magnetic field is maximum [38]. The different areas on the graphene surface were irradiated at a magnification of 36 × corresponding to an area of 3.4 × 2.6 mm^2 for 18 s to 40 min. More details about the irradiation processes will be presented in chapter five.

2.2 Annealing

Annealing refers to the heat treatment process which is aimed to relieve stress, increase ductility and softness, homogenization and recrystallization, etc. It is widely used in the metallurgy and materials science [40]. Typically, a full annealing process consists of three stages: heating the sample to desired temperature, and then holding at this temperature for enough time, in the end, cooling the sample to a certain temperature (usually room temperature). The heating rates, holding temperature, annealing time and cooling rates are the most important parameters that influence the annealing effect. To avoid the oxidation of sample surface results from annealing, the process is always performed in ultra-high vacuum, or in argon gas, hydrogen gas, nitrogen gas or a mixed gas atmosphere [39]. Rapid thermal annealing (RTA) is the process that consists of short annealing time, it is used to reduce the thermal redistribution at high temperature and manipulate the placement of the dopants. RTA technology was originally invented for ion implant during the semiconductor fabrication, but nowadays has been widely used in chemical vapor deposition, oxide growth, and silicidation [40].

Recently, annealing is commonly employed to eliminate the contamination and improve the cleanliness of graphene surface, meanwhile the strain between graphene and substrate can be modulated by this thermal treatment process [41-44]. High vacuum annealing above 300 ℃ was

performed in exfoliated graphene deposited on SiO_2 substrate and resist residues on graphene surface were effectively removed. The annealing effect at high temperature also results in close contact between graphene and substrate, thus giving rise to heavy hole doping and degradation of electrical properties of the graphene devices [41]. In 2012, the annealing effect in CVD graphene grown on SiO_2 substrate was investigated, and provides useful information for the large-scale graphene production. Air annealing was carried out in series of graphene samples for 1h and successively annealed in H_2/Ar atmosphere at 200 ℃, 250 ℃, and 300 ℃ respectively for another hour. A two-step scheme of the decomposition process of PMMA residue was revealed under TEM: the PMMA exposed to air has a low decomposition temperature, while the PMMA faced to graphene dissociates at high temperature. A super clean of graphene surface was obtained followed by this two-step annealing process, but it is difficult to remove the PMMA residue entirely even increase the annealing temperature (like 350 ℃ for 5h). And it is interesting to find that oxygen annealing lead to defects formation in graphene. An obvious blue-shift of the 2D band was also observed in the Rama spectra, indicating band structure modification after annealing [42]. Rapid high temperature (700 ℃-800 ℃) annealing in graphene grown on Cu foils by CVD method shows that the copper oxide was removed and the crystalline structure of copper around graphene was completely recovered, moreover, the graphene layer presents potential application for protecting the metal from oxidation. The partially reversible doping in CVD graphene resulted from the PMMA residue and hydrogen-functionalization was also observed while irreversible in the modification of strain between mechanically exfoliated graphene and substrate, this provides a useful method to modulate the properties of graphene [43]. Furthermore, the strain between graphene and SiC substrate can be tuned by thermal annealing, a compressive strain of 2.1 GPa was induced in graphene with SiO_2 top layer, and the defects formed during deposition process were greatly reduced after annealing [44].

In this thesis, high vacuum annealing was employed to reduce the PMMA residues on graphene surface after irradiation. The graphene sample was placed on one steel plate, while another one was pushing down and forming a small gap between the two steel plates, thus a constant thermal region was established. The graphene was exposed to air after annealing, which may lead to adsorption of O_2 and H_2O molecules on the surface and result in unintentional doping in graphene.

2.3 Structural Characterization

Structural characterization involves in using various kinds of techniques to investigate the structural properties, elemental composition, and surface morphology of the material. It is important to understand the fundamental properties of graphene and then modify its electrical, optical or magnetic properties, etc. In this thesis, Raman spectroscopy was used to analyse the structure of graphene, X-ray photoelectron spectroscopy (XPS) was used to study the element composition of graphene and surface, and Atomic Force Microscopy (AFM) was employed to study the surface morphology and roughness.

2.3.1 Raman Spectroscopy

Raman spectroscopy is a spectroscopic technology based on inelastic scattering or Raman Effect, and commonly used to investigate the molecular motions, especially the vibrational, rotational and other low frequency transitions [45]. When a beam of monochromatic light (usually laser) irradiates the sample, the light will be scattered in all directions. Most of the scattered light is of the same frequency with the incident light, while a small proportion of the reemitted light is different from the original light. This process related to interaction between photons and molecules which result in frequency change of the incident light is called inelastic scattering or Raman Effect [45-47]. The inelastic scattering was first predicted by A. Smekel in 1923 [48], but it was not until 1928 that this scattering process was observed in experiments by C.V. Raman and K.S. Krishnan [49]. Independently, G. Landsberg and L. Mandelstam also monitored unexpected frequency shifts in scattering from quartz while published their results months later than C.V. Raman [50]. In 1930, the Nobel Prize in Physics was awarded to Sir C.V. Raman "for his work on the scattering of light and for the discovery of the effect named after him" [51].

The incident light can be considered as consisted of a number of photons, when the photons interact with the molecules, the energy transformation will happen and result in oscillating dipoles, then the remitted light of three different frequencies will be induced by Rayleigh scattering, Stokes scattering and Anti-stoke scattering (Figure 2.6). The molecule without Raman-active mode adsorbs a photon of frequency υ_0 and is excited to the higher energy state, then when it returns to the ground state, a light of the same frequency υ_0 is emitted, and this elastic scattering process is called Rayleigh scattering. In another case, the Raman-active

molecule at the ground state vibrational level adsorbs one photon of frequency υ₀ and transfers part of the energy to Raman-active mode, then results in the reduction of frequency and energy of the emitted light, this inelastic process of photon energy loss is called Stokes scattering. The last situation is that the Raman-active molecule at the excited vibrational state adsorbs a photon, then when it returns the basic vibrational state, the released energy is transferred to the photon and leads to an emitted light of higher frequency and energy, this inelastic process is called Anti-Stokes scattering [45-47]. Most of the reemitted lights result from Rayleigh scattering, while only about 0.001% come from the Stokes and Anti-Stokes scattering, and the Raman spectra are formed by measuring these inelastic scattering signals. In this case, it is important to reduce the intensity of Rayleigh scattering so that inelastic scattering is more easily to be detected. The instruments such as tuneable filters, laser stop apertures, double and triple spectrometric systems have been developed to obtain high quality Raman spectra [45-47] [52].

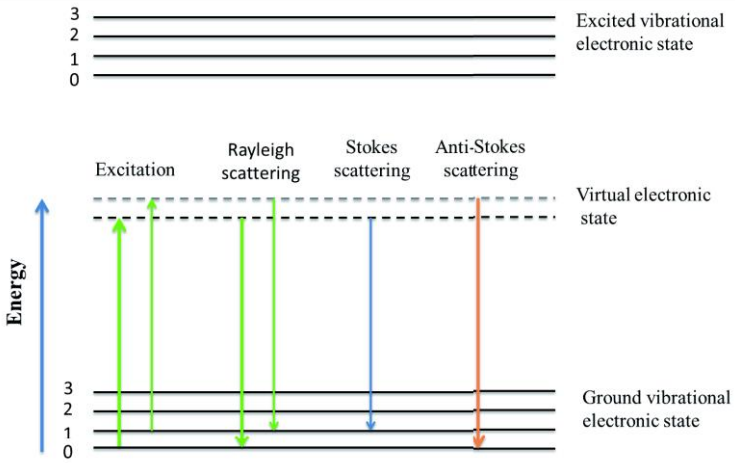

Figure 2.6 Illustration of the scattering process induced by interaction between photons and molecules.

Typically, a Raman system is made up of four major components: light source (laser), irradiation system and light collection optics, emission filter or spectrophotometer, and detector (Charge Coupled Device (CCD) or Photomultiplier (PMT)). A laser beam passes through the excitation filter and is objective to irradiate the sample, the scattered light will be reflected to the objective again and then reach the emission filter, in then end the scattered light will be detected by the CCD or PMT and form Raman spectra on the computer. The most prominent advantage of Raman spectroscopy is the fast response and non-destructive to the sample, the measurement can be performed at high temperature and the low wavenumber (100 cm^{-1}) region detection is

available. But Raman measurement cannot be used for metals and alloys, the Raman Effect is very weak and can be influenced by impurities, also the laser irradiation can damage the sample [45-47] [52]. In 1960, the invention of laser made the Raman spectroscopy instruments simplifier and the sensitivity was enhanced. Nowadays, a number of variations of Raman spectroscopy have emerged, such as Surface-enhanced Raman scattering (SERS), Stimulated Raman spectroscopy, and Resonance Raman spectroscopy, Coherent anti-Stokes Raman spectroscopy (CARS), etc. [52.]

In graphene, Raman spectroscopy is usually used to investigate the quality of the graphene sample, such as number and orientation of the layers, defects and edge type. More important, Raman spectroscopy presents a powerful tool to understand the effect of electrical and magnetic field, irradiation, chemical doping, and strain in graphene, and provides information about how to modulate the properties of graphene [53-55]. The most prominent feature of Raman spectra of pristine graphene is the G and 2D peak, for the graphene with defects, the D peak and sometimes D' peak are observed in Raman spectra. The G band which is around 1580 cm^{-1}, results from the in-plane vibration of sp^2 bonded C atoms and doubly degenerate (E_{2g}) phonon mode at the Brillouin zone center. The D peak (around 1350 cm^{-1}) is related to the breathing modes of six-atom rings and is activated by defect in graphene. It comes from the phonon around the K point of the Brillouin zone and is activated by double resonance. When an incident laser irradiates the graphene, an electron-hole pair is excited, and then the electron scatters with the phonon and exchanges the momentum. The phonon undergoes a defect-assisted intravalley scattering and leads to the recombination of electron and hole. Meanwhile, double resonance can also happen due to the intravalley process. Meanwhile, this process gives rise to the D' peak around 1620 cm^{-1} in graphite and sometimes observed in graphene. The 2D band (around 2700 cm^{-1}) is the second order of D peak, results from the intravalley scattering of two phonons in opposite momentum, and the frequency is twice of the defect-assisted intervalley one-phonon D peak. Different from the D peak, no activation is needed to induce the 2D peak, and it can be observed in the absence of defects [53-54]. In this thesis, Raman spectra was performed at room temperature in ambient condition to investigate the irradiation effect on both graphene on SiO_2 prepared by CVD method and graphene on SiC, the defect was appeared and the intensity increased with the dose density. More interesting, a red-shift in Raman spectra of graphene after annealing was observed which may result from the chemical doping from PMMA.

2.3.2 X-ray photoelectron spectroscopy

X-ray photoelectron spectroscopy (XPS), also known as Electron Spectroscopy for Chemical Analysis (ESCA), is a widely used surface analysis technique to investigate the elemental composition and chemical state on the material surface. A beam of light irradiates on the sample surface and interacts with the atom can give rise to three different situations: (a) the photon passes through the atom without interaction (b) the photon undergoes scattering after strike the orbital electron and loses energy, then the scattered photon has a lower frequency and longer wavelength, this process is called Compton scattering (c) the photon interacts with the orbital electron and transfers the energy to electron, then results in the emission of the orbital electron from atom, this process is called photoelectric emission and XPS technique is based on this effect [56-58]. The photoelectric effect was first observed by Heinrich Rudolf Hertz in 1887, but it was not until 1905 that Albert Einstein gave a reasonable explanation for this effect [59]. Due to this excellent work, Einstein was awarded the Nobel Prize in Physics in 1921. The significant improvement of XPS instrument was developed in the mid-1960's by Kai M. Siegbahn and his research group at the University of Uppsala, Sweden [57] [60]. This technique was first known as ESCA, and the commercial fabrication of XPS instrument was accomplished in 1969 by engineers from Hewlett-Packard in the USA, then XPS becomes a popular instrument used in Laboratories throughout the world. In 1981, Kai M. Siegbahn was awarded the Nobel Prize in Physics "for his contribution to the development of high-resolution electron spectroscopy" [61].

Typically, the photoelectric effect can be classified into two types: outer photoelectric effect and inner photoelectric effect. The outer photoelectric effect refers to the incident photon with energy higher than the work function (ϕ) interacts with the valence electron (outermost electron) and leads to ejection of photoelectron. Thus the maximum Kinetic Energy of photoelectron is described as: $KE_{max} = h\upsilon - \phi$, where h is the Plank constant, υ is the frequency of incident photon. This process usually observed in metal materials, due to the conduction band is full of electrons and value band is empty. The inner photoelectric effect originates from the emission of core electron, the high energy photon results in the excitation of core electron from the value band to the conduction band and then into the free state (vacuum), the Kinetic Energy of photoelectron is: $KE = h\upsilon - BE - \phi$, BE is the binding energy which is determined by the

attraction between nuclei and core electron, and indicates the energy required to excite the core electron to the conduction band (Figure 2.7). The binding energy for each element is different and in this way the various elements and the concentration can be identified by XPS.

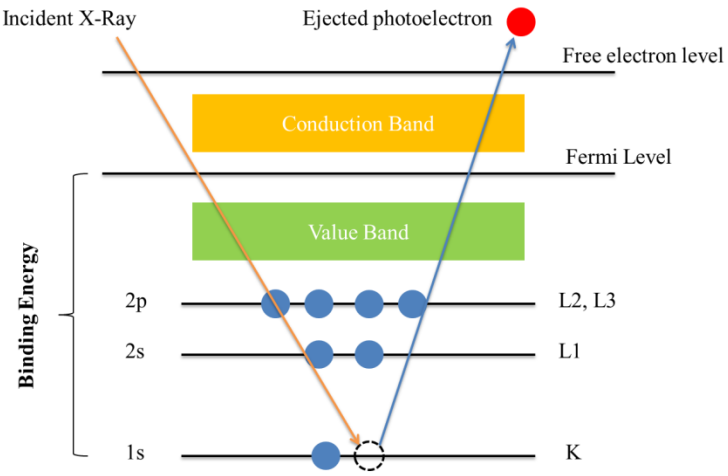

Figure 2.7 Schematic of photoelectron ejection process by X-Ray.

In addition, chemical shift (the change of binding energy before photoelectron ejection and after this process) is related to the local environment of the atom, this also provides information of the elemental chemical state on sample surface. Following this process, the atom can also release energy by the emission of a photon or Auger Electron. It is important to explain the difference between the ejection of valence electron and core electron. The valence electron is on the outermost orbit of atom, it is far from the nuclei and moving in all directions, thus the valence electron carries little information about the nuclei. The core electron is close to the nuclei and has binding energy characteristic of the particular element, the detection of ejected core electron can provide fruitful information of the atom. The XPS spectra lines are labeled by the shell from which the electron is ejected, such as 1s, 2p, 2s, etc. Especially, the core electron shows higher probability to match the energies of Al Kα (1486.6eV) and Mg Kα (1254.6eV) rays, which are usually used as the X-ray source in XPS. Normally, the sample will be radiated with photons of a single energy (Mg Kα or Al Kα) which is known as a mono-energetic X-Ray beam [56-58]. The X-ray irradiation on graphene surface results in inner photoelectric ejection of core electrons in carbon atom and oxygen atom, the oxygen element comes from the PMMA or adsorbed O_2 [62]. This inner photoelectric effect can also be observed in various kinds of semiconductor materials [63].

A commercial XPS instrument is usually composed of X-ray source, sample introduction chamber, ultra-high vacuum (UHV) system, electron collection lens, energy analyzer, electron detector system, computer controlled system and other additional components. As the XPS technique is sensitive to the sample surface, the UHV ($<10^{-7}$ Pa) is needed to eliminate the external contamination and make an accurate analysis of the elemental chemical state on sample surface. The X-ray often goes through the depth on the order of one micrometer, while the useful photoelectrons are detected from the depth of around 10 to 100 Å to the surface [56-58]. Nowadays, XPS has been employed in many areas such as polymer surface, electronics packaging, thin film structure analysis and catalyst, etc. In this thesis, XPS was used to investigate the elemental composition of graphene prepared by CVD and that after irradiation and annealing, the concentration change of carbon and oxygen element on graphene surface provided powerful evidence for irradiation induced chemical doping and then reduced by annealing.

2.3.3 Atomic force microscopy

Atomic force microscopy is one type of scanning probe microscopy (SPM) that used to form a three-dimensional surface (3D) topographical image and determine the roughness of the surface. This technique makes use of the atomic force between probe tip and sample and shape the atomic resolution image of the sample surface [64]. The AFM instrument was invented in 1986 by Gerd Binnig, Calvin Quate and Christoph Gerber [65], and the first atomic resolution image was obtained on graphite one year later by this group [66]. Then in 1989, the commercially AFM instrument was fabricated, and in 2007 it was the first time that AFM was carried by the NASA's Phoenix Martian Lander to investigate the soil on the Mars [67], this shows the importance of AFM as surface analysis tool. Before the advent of AFM, Gerd Binnig and Heinrich Rohrer had also already developed scanning tunneling microscope (STM) in 1981 at IBM Research-Zurich, which involves the measurement of tunneling currents between a probing tip and sample [68]. And they were jointly awarded the Nobel Prize Physics in 1986 this excellent invention. But the conductivity of sample is required which can guarantee the detection of tunneling currents, this limitation of STM prohibits its application in insulators. According to this problem, the AFM was invented which makes the investigation of conductors, semiconductors and insulators on an atomic scale possible [65]. The theory of measuring interaction between tip and sample surface also results in varieties kinds of other SPM such as

magnetic force microscope (MFM), the dipping force microscope (DFM), and chemical force microscope (CFM), etc. [69].

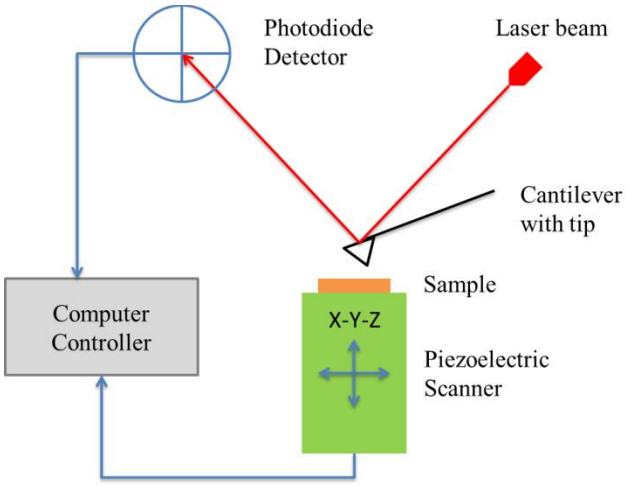

Figure 2.8 Schematic of AFM components and working principle.

Typically, an AFM instrument is composed of laser beam, cantilever, tip, piezoelectronic scanner, photodiode detector and computer controller, see in Figure 2.8. The probe tip is placed on the end of a cantilever, and the force between the sharp tip and sample surface leads to the deflection of cantilever. Thus the measured force is determined by the spring constant of the cantilever and distance between the tip and sample surface. The force can be described using Hooke's Law: $F = -kx$, where k is the spring constant, and x represents the cantilever deflection. Typical spring constant of cantilever ranges from 0.001 to 100 N/m and the force between tip and the sample is from 10^{-11} to 10^{-6} N. Usually, the tip is made from Si_3N_4 or Si, and the different material, dimension and shape of cantilever result in varied spring constants and resonant frequencies. When the tip is moving across the sample surface, a laser beam irradiates on the cantilever and is bounced off to the photodiode detector, the position-sensitive detector will analyze the reflected laser and generate a 3D map of the surface topography. Typically, the deflection of cantilever between microns and 0.1 Å can be measured by the photodiode detector. The sample position can be moved by the piezoelectric scanner which is used to adjust the distance between tip and sample surface, and the typical resolution of x, y, z dimension is 1 nm, 1 nm and 0.1 nm, respectively [64] [70-71]. The dominant interaction between tip and sample surface in short distance (nanometers) is Van der Waals force. The long distance interactions such as electrostatic, capillary and magnetic force are significantly far away from the sample

surface. The AFM operations are mainly divided into three types: contact mode, non-contact mode and tapping mode. In contact mode, the tip drags through the sample surface and experiences repulsive Van der Waals force. This continues contact with sample result in high resolution image while also cause damage to the sample. The contact mode is usually used for hard material, and the operation is accomplished in air or liquid. Opposite to contact mode, the non-contact mode means the tip does not touch the sample surface and oscillates near its resonant frequency. Then the attractive Van der Waals force plays the dominant role in this mode, and the distance between tip and surface usually ranges from 1 nm-10 nm. A low resolution image is obtained in this mode and no damage to the sample. The non-contact mode is commonly used for soft materials such as thin film, and ultra-high vacuum is needed to obtain the image of best quality. The tapping mode combined the contact mode and non-contact mode. The cantilever made of piezoelectric element touches the surface with the oscillation at its resonant frequency, and the amplitude ranges from 10 nm to 200nm. What's more, an electronic servo is used to maintain constant oscillation amplitude and keep the interaction between tip and sample surface. In this mode, the image of better resolution than non-contact mode and less damage to sample than contact mode is acquired. It is often used for biological samples and operated in air or liquid environment [64] [70-71].

The AFM technique is a powerful tool to obtain high resolution (comparable to STM and TEM) image on sample surface, and usually high vacuum system is not required which can reduce the cost of production. Compared to SEM, which provides two-dimensional image of surface morphology, three-dimensional image can be formed in AFM. Also, due to the small size of AFM instrument, it can be combined with other microscopes or instruments. But the single scan image size on the order of hundred micrometers is much lower than millimeter image observed in SEM. Moreover, the relatively slow scan time can result in thermal drift on the sample. Nowadays, AFM have been applied in many areas, like life science, materials and surface science, nanolithography, astronomy and medicine, etc. [64]. In this thesis, AFM in tapping mode was performed in pristine, irradiated graphene and that after annealing, the roughness obtained shows the graphene becomes cleaner after irradiation and annealing.

2.4 Transport Properties

The ion or electron irradiation can cause modification of electronic structure and reduction of Fermi velocity [21], and further change the charge carrier density and mobility [22]. The ferromagnetism can also be induced in graphene based materials by irradiation [72]. These results indicate that irradiation provides a fast and convenient method to modulate the transport properties of graphene. In this thesis, the transport properties were measured to investigate the effect of irradiation on electrical properties and magnetoresistance of graphene.

2.4.1 Electrical Properties

The electrical properties of graphene after irradiation were measured by Keithley 2400 connected to a micromanipulator probe station, and two-probe method was employed during the measurements. The drain-source voltage (V_{ds}) was supplied by Keithley 2400 and applied on graphene through the probes. All the measurements were performed at room temperature in ambient condition.

2.4.2 Magnetoresistance

The magnetoresistance of irradiated graphene was also measured to investigate the magnetic properties of graphene. The schematic of the experimental platform for magnetoresistance measurements is shown in Figure 2.10. The sample carrier is placed on top of the base, and two electromagnets are located beside the carrier. The design of the base makes sure that the sample carrier is located in the center of the two electromagnets, where a continuous and transverse magnetic can be obtained. By changing the direction of the sample carrier, perpendicular and in-plane magnetic field can be applied on graphene samples. The electromagnets are supplied by the power which is under control of SR830 lock-in amplifier in the DC output mode. The current or voltage applied on the sample is accomplished through the inner wires which are connected to the connector used as interface. The Keithley 2400 is used to input current or voltage signals through the input ports on the connector. With a hall sensor placed on the center of the electromagnet, the magnetic field generated can be measured by HP 34902 voltmeter which is connected to the base. In this thesis, the magnetoresistance of graphene was measured by applying various drain to source current (I_{ds}).

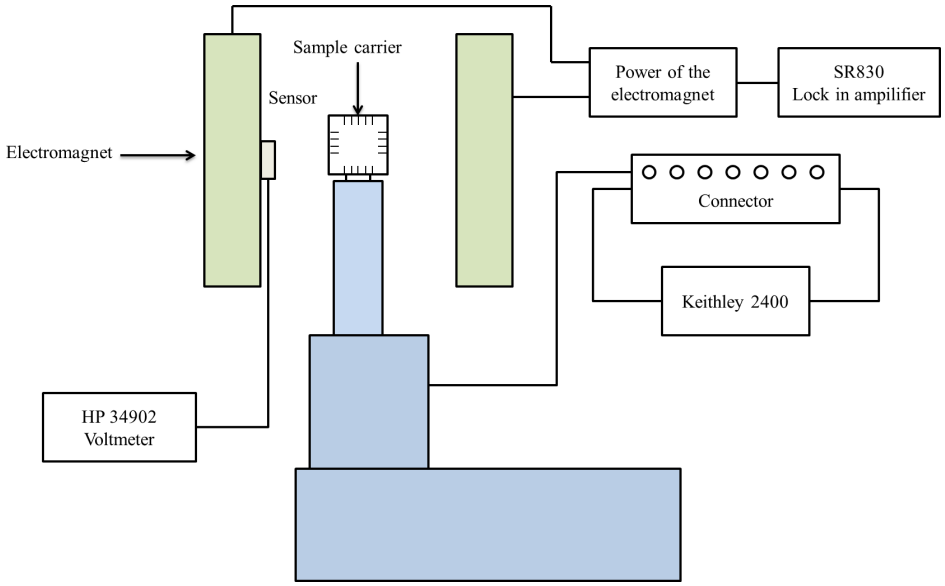

Figure 2.10 Schematic of the experimental platform magnetoresistance measurement.

References

(1) Li, J.; Stein, D.; McMullan, C.; Branton, D.; Aziz, M. J.; Golovchenko, J. A. Ion-beam sculpting at nanometre length scales. *Nature.* **2001**, *412*(6843), 166.

(2) Chappert, C.; Bernas, H.; Ferré, J.; Kottler, V.; Jamet, J. P.; Chen, Y.; Launois, H. Planar patterned magnetic media obtained by ion irradiation. *Science.* **1998**, *280*(5371), 1919.

(3) Hennig, G. R. Decoration of graphite surfaces for electron microscopy. *Appl. Phys. Lett.* **1964**, *4*(3), 52.

(4) Krasheninnikov, A. V.; Nordlund, K. Ion and electron irradiation-induced effects in nanostructured materials. *J. Appl. Phys.* **2010**, *107*(7), 071301.

(5) Farkas, J. Irradiation as a method for decontaminating food: a review. *Int. J. Food. Microbiol.* **1998**, *44*(3), 189.

(6) Wu, D.; Shu, Q.; Wang, Z.; Xia, Y. Effect of gamma irradiation on starch viscosity and physicochemical properties of different rice. *Radiat. Phys. Chem.* **2002**, *65*(1), 79.

(7) Ziegler, J. F. (Ed.). *Ion Implantation Science and Technology 2e*. Elsevier. **2012**.

(8) Schmidt, B.; Wetzig, K. *Ion beams in materials processing and analysis*. Springer. **2012**.

(9) Rubin, L.; Poate, J. Ion implantation in silicon technology. *Ind. Phys.* **2003**, *9*(3), 12.

(10) Conrad, J. R.; Radtke, J. L.; Dodd, R. A.; Worzala, F. J.; Tran, N. C. Plasma source ion-implantation technique for surface modification of materials. *J. Appl. Phys.* **1987**, *62*(11), 4591.

(11) Farkas, J.; Mohácsi-Farkas, C. History and future of food irradiation. *Trends. Food. Sci. Tech.* **2011**, *22*(2), 121.

(12) Davies, C. R. Effects of gamma irradiation on growth and yield of agricultural crops—I: Spring sown wheat. *Radiation Botany.* **1968**, *8*(1), 17.

(13) Issa, P.; Mehdi, B.; Abolfazl, T.; Mehdi, J. The use of gamma irradiation in agriculture. *Afr. J. Microbiol. Res. 5*(32), **2011**, 5806.

(14) Weindorf, D. C.; Zhu, Y.; Chakraborty, S.; Bakr, N.; Huang, B. Use of portable X-ray fluorescence spectrometry for environmental quality assessment of peri-urban agriculture. *Environ. Monit. Assess.* **2012**, *184*(1), 217.

(15) Lou, Y. S.; Huang, Y.; Li, Y. X.; Zhang, J.; Cao, C.; Zhu, T. T.; Kang, H. J. Effect of Enhanced Ultraviolet-B Radiation on Physiological Properties of Different Cultivars of Barley. *Journal of Ecology and Rural E.* **2011**, *4*, 010.

(16) Paunesku, T.; Vogt, S.; Maser, J.; Lai, B.; Woloschak, G. X-ray fluorescence microprobe imaging in biology and medicine. *J. Cell. Biochem.* **2006**, *99*(6), 1489.

(17) Potters, L.; Raince, J.; Chou, H.; Kapur, A.; Bulanowski, D.; Stanzione, R.; Lee, L. Development, implementation, and compliance of treatment pathways in radiation medicine. *Front. Oncol.* **2013**, *3*.

(18) Nguyen, H.; Morgan, D. A.; Forwood, M. R. Validation of 11 kGy as a radiation sterilization dose for frozen bone allografts. *J. Arthroplasty.* **2011**, *26*(2), 303.

(19) Banhart, F. Irradiation effects in carbon nanostructures. *Rep. Prog. Phys. 62*(8), **1999**, 1181.

(20) Lucchese, M. M.; Stavale, F.; Ferreira, E. H.; Vilani, C.; Moutinho, M. V. O.; Capaz, R. B.; Achete, C. A.; Jorio, A. Quantifying ion-induced defects and Raman relaxation length in graphene. *Carbon.* **2010**, *48*, 1592.

(21) Tapaszto, L.; Dobrik, G.; Nemes-Incze, P.; Vertesy, G.; Lambin, P.; Biró, L. P. Tuning the electronic structure of graphene by ion irradiation. *Phys. Rev. B.* **2008**, *78*(23), 233407.

(22) Chen, J. H.; Cullen, W. G.; Jang, C.; Fuhrer, M. S.; Williams, E. D. Defect scattering in graphene. *Phys. Rev. Lett.* **2009**, *102*, 680501.

(23) Kalbac, M.; Lehtinen, O.; Krasheninnikov, A. V.; Keinonen, J. Ion-Irradiation-Induced Defects in Isotopically-Labeled Two Layered Graphene: Enhanced In-Situ Annealing of the Damage. *Adv. Mater.* **2013**, *25*(7), 1004.

(24) Wolf, B. *Handbook of ion sources*. CRC press. **1995**.

(25) Shaw, M. J. Penning ionization. *Contemp. Phys.* **1974**, *15*(5), 445.

(26) Siska, P. E. Molecular-beam studies of Penning ionization. *Rev. Mod. Phys.* **1993**, *65*(2), 337.

(27) Rovey, J. L.; Ruzic, B. P.; Houlahan, T. J. Simple Penning ion source for laboratory research and development applications. *Rev. Sci. Instrum.* **2007**, *78*(10), 106101.

(28) *Beigne, C.* Effets d'irradiation par des ions légers sur les alliages ferromagnétiques. Le DIPLÔME D'INGÉNIEUR C.N.A.M. **2003**.

(29) Wang, X.; Li, X.; Zhang, L.; Yoon, Y.; Weber, P. K.; Wang, H.; Guo, J.; Dai, H. N-doping of graphene through electrothermal reactions with ammonia. *Science.* **2009**, *324*, 768.

(30) Hashimoto, A.; Suenaga, K.; Gloter, A.; Urita, K.; Iijima, S. Direct evidence for atomic defects in graphene layers. *Nature.* **2004**, *430*(7002), 870.

(31) Kim, K. J.; Choi, J.; Lee, H.; Lee, H. K.; Kang, T. H.; Han, Y. H.; Kim, B. Effects of 1 MeV electron beam irradiation on multilayer graphene grown on 6H-SiC (0001). *J. Phys. Chem. C.* **2008**, *112*(34), 13062.

(32) Teweldebrhan, D.; Balandin, A. A. Modification of graphene properties due to electron-beam irradiation. *Appl. Phys. Lett.* **2009,** *94*(1), 013101.

(33) Tao, L.; Qiu, C.; Yu, F.; Yang, H.; Chen, M.; Wang, G.; Sun, L. Modification on single-layer graphene induced by low-energy electron-beam irradiation. *J. Phys. Chem. C.* **2013**, *117*(19), 10079.

(34) Goldstein, J. I.; Newbury, D. E.; Echlin, P.; Joy, D. C.; Fiori, C.; Lifshin, E. Scanning electron microscopy and X-ray microanalysis. A text for biologists, materials scientists, and geologists. *Plenum Publishing Corporation.* **1981**.

(35) Knoll, M.; Ruska, E. Das elektronenmikroskop. *Z. Physik.* **1932**, *78*(5-6), 318.

(36) Von Ardenne, M. Das Elektronen-Rastermikroskop. *Z. Physik.* **1938**, *109*(9-10), 553.

(37) Zworykin, V. K. The Scanning Electron Microscope. *Sci. Am.* **1942**, *167*, 111.

(38) Flegler, S. L.; Heckman, J. W.; Klomparens, K. L. Scanning and transmission electron microscopy: an introduction. *New York: WH Freeman.* **1993**.

(39) Rollett, A.; Humphreys, F. J.; Rohrer, G. S.; Hatherly, M. Recrystallization and related annealing phenomena. *Elsevier.* **2004**.

(40) Fair, R. B. (Ed.). Rapid thermal processing: science and technology. *Academic Press.* **1993**.

(41) Cheng, Z.; Zhou, Q.; Wang, C.; Li, Q.; Wang, C.; Fang, Y. Toward intrinsic graphene surfaces: a systematic study on thermal annealing and wet-chemical treatment of SiO2-supported graphene devices. *Nano Lett.* **2011**, *11*(2), 767.

(42) Lin, Y. C., Lu, C. C., Yeh, C. H., Jin, C., Suenaga, K., & Chiu, P. W. Graphene annealing: how clean can it be? *Nano Lett.* **2011**, *12*(1), 414.

(43) Cho, J.; Gao, L.; Tian, J.; Cao, H.; Wu, W.; Yu, Q.; Guisinger, N. P. Atomic-scale investigation of graphene grown on Cu foil and the effects of thermal annealing. *ACS nano*, **2011**, *5*(5), 3607.

(44) Ni, Z. H.; Wang, H. M.; Ma, Y.; Kasim, J.; Wu, Y. H.; Shen, Z. X. Tunable stress and controlled thickness modification in graphene by annealing. *ACS nano*, *2*(5), **2008**, 1033.

(45) Colthup, N. B.; Daly, L. H.; Wiberley, S. E. Introduction to infrared and Raman spectroscopy. *Elsevier*. **1990**.

(46) Larkin, P. Infrared and Raman spectroscopy; principles and spectral interpretation. *Elsevier*. **2011**.

(47) Gardiner, D. J. Introduction to Raman scattering. In *Practical Raman spectroscopy* . *Springer Berlin Heidelberg.* **1989**, 1.

(48) Smekal, A. Zur Quantentheorie der Dispersion. *Naturwissenschaften*. **1923**, *11*(43), 873.

(49) Raman, C. V.; Krishnan, K. S. A new type of secondary radiation. *Nature.* **1928**, *121*(3048), 501.

(50) Landsberg, G.; Mandelstam, L. Über die Lichtzerstreuung in Kristallen. *Z. Physik.* **1928**, *50*(11-12), 769.

(51) "The Nobel Prize in Physics 1930". Nobelprize.org.

(52) Smith, E.; Dent, G. Modern Raman Spectroscopy-A Practical Approach. *John Wiley & Sons. Ltd.* **2005**.

(53) Ferrari, A. C.; Meyer, J. C.; Scardaci, V.; Casiraghi, C.; Lazzeri, M.; Mauri, F.; Piscanec, S.; Jiang, D.; Novoselov, K. S.; Roth, S.; et al. Raman spectrum of graphene and graphene layers. *Phys. Rev. Lett.* **2006**, *97*, 187401.

(54) Basko, D. M.; Piscanec, S.; Ferrari, A. C. Electron-electron interactions and doping dependence of the two-phonon Raman intensity in graphene. *Phys. Rev. B.* **2009**, *80*(16), 165413.

(55) Ferrari, A. C. Raman spectroscopy of graphene and graphite: disorder, electron–phonon coupling, doping and nonadiabatic effects. *Solid State Commun.* **2007**, *143*, 47.

(56) Stickle, W. F.; Sobol, P. E.; Bomben, K. D. Handbook of X-ray photoelectron spectroscopy (Vol. 40). *Eden Prairie, MN: Perkin Elmer.* **1992**.

(57) Van der Heide, P. X-ray photoelectron spectroscopy: an introduction to principles and practices. *John Wiley & Sons.* **2011**.

(58) Watts, J. F.; Wolstenholme, J. An introduction to surface analysis by XPS and AES. *Wiley-VCH*, **2003**.

(59) Einstein, A. Über einen die Erzeugung und Verwandlung des Lichtes betreffenden heuristischen Gesichtspunkt. **1905**, *Annalen der Physik. 17*(6), 132.

(60) Siegbahn, K.; Nordling, C. ESCA, atomic, molecular and solid state structure studied by means of electron spectroscopy. *Nov. Act. Uppsaliensis*. **1967**.

(61) "The Nobel Prize in Physics 1981". *Nobelprize.org.*

(62) Yang, D.; Velamakanni, A.; Bozoklu, G.; Park, S., Stoller, M.; Piner, R. D.; Ruoff, R. S. Chemical analysis of graphene oxide films after heat and chemical treatments by X-ray photoelectron and Micro-Raman spectroscopy. *Carbon.* **2009**, *47*(1), 145.

(63) Schroder, D. K. Semiconductor material and device characterization. John Wiley & Sons. **2006**.

(64) Eaton, P. J.; West, P. Atomic force microscopy (Vol. 10). Oxford: Oxford University Press. **2010**.

(65) Binnig, G.; Quate, C. F.; Gerber, C. Atomic force microscope. *Phys. Rev. Lett.* **1986**, *56*(9), 930.

(66) Binnig, G.; Gerber, C.; Stoll, E.; Albrecht, T. R.; Quate, C. F. Atomic resolution with atomic force microscope. *Europhys. Lett.* **1987**, *3*(12), 1281.

(67) Vijendran, S.; Sykulska, H.; Pike, W. T. AFM investigation of Martian soil simulants on micromachined Si substrates. *J. Microsc.* **2007**, *227*(3), 236.

(68) Binnig, G.; Rohrer, H.; Gerber, C.; Weibel, E. Tunneling through a controllable vacuum gap. *Appl. Phys. Lett.* **1982**, *40*(2), 178.

(69) Bonnell, D. A. (Ed.). *Scanning probe microscopy and spectroscopy: theory, techniques, and applications* (Vol. 2). *New York: Wiley-vch.* **2001**.

(70) Giessibl, F. J. Advances in atomic force microscopy. *Rev. Mod. Phys.* **2003**, *75*(3), 949.

(71) Cappella, B.; Dietler, G. Force-distance curves by atomic force microscopy. *Surf. Sci. Rep.* **1999**, *34*(1), 1.

(72) Yazyev, O. V. Magnetism in disordered graphene and irradiated graphite. *Phys. Rev. Lett.* **2008**, *101*(3), 037203.

Chapter III. Influence of Low Energy Helium Ion Irradiation on Structural Properties of Graphene prepared by CVD method

3.1 Introduction

Ion irradiation is one of the efficient methods to modify the material structure, which has been widely used in carbon-based structures and recently in graphene [1]. By irradiation in graphene, the energy of ions (or electrons) dissipates through the interaction with the lattices, which induces the displacement of atoms from the lattice. As a result, the amount of defects and charged impurities increases, and further influences the crystal lattice structure, electronic band structure, and other properties of graphene [2-6]. Moreover, the lattice distortion after irradiation may induce strain in graphene and influence the coupling with the substrate, which also leads to the change of the structural properties and morphology of graphene [5].

In recent years, chemical doping has also attracted much attention and several methods have been used for chemical doping in graphene [7-13]. Graphene oxidization can be induced by heating graphene in O_2 atmosphere [7] [9] [11] or exposure to oxygen plasma [15-16]. N-Doping of Graphene through thermal annealing in ammonia has been reported [14]. On the other hand, besides exposure to hydrogen plasma [17], hydrogenation of graphene can be also induced by the reaction of electron beam irradiated polymer films such as hydrogen silsesquioxane (HSQ) [7] and polymethyl methacrylate (PMMA) [18] coated on the graphene sample. Recently, charge-transfer doping effect due to polymer molecules adsorbed on graphene surface has attracted much attention [7] [16] [19-26]. For example, PMMA is the most popular solution used during the transfer process of chemical vapor deposited (CVD) graphene on the substrate [16] [19-28] and e-beam lithography [18]. However, PMMA is hard to be removed completely even with repeated cleaning process, and a small number of PMMA residues always remain on graphene surface [16] [19-26]. The C, H and O atoms in PMMA residues unit and the C atoms in graphene will interact with each other and forms new C-C, C-H and C-O bonds at the interface between PMMA residues and graphene, then the lattice structure of graphene can be changed, which leads to a series of modification of graphene properties [20-26].

In this chapter, He^+ ions irradiation was used to induce chemical doping in graphene grown on SiO_2/Si substrate by CVD method. The organization of chapter III was shown in Figure 3.1. The optical micrograph of unirraidated graphene was observed under microscope. Then the experimental detail of low energy He^+ ion irradiation was presented. X-ray photoelectron spectroscopy, Raman spectroscopy and Atomic force microscopy were used to characterize the

structural modification of irradiated graphene samples. According to these experimental results, a reversible charge transfer doping in graphene was observed and provide a convenient method to modify the electrical properties of graphene, which can be applied in graphene based memory and logic devices, transistors and integrated circuits.

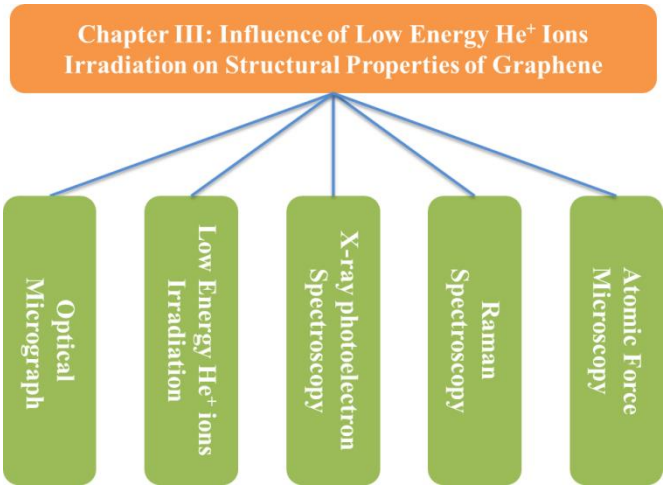

Figure 3.1 Organization of chapter III.

3.2 Optical micrograph

The studied samples are commercial single layer graphene grown on Cu foils by CVD method and transferred using PMMA onto silicon wafer capped by 300 nm thick SiO_2 layer [27-28]. Figure 3.2 shows the optical micrograph of the PMMA-transferred graphene, the PMMA residues (blue) on the graphene surface can be observed. Although the graphene samples were cleaned by annealing in H_2 and Ar gas, there is still amount of PMMA residues left on the graphene surface which is hard to be removed entirely [19-26].

3.3 Low Energy He^+ ions irradiation

Schematic of He^+ ion irradiation in graphene with PMMA residues is shown in Figure 3.3. The low energy He^+ ions irradiation was carried out in the graphene samples at room temperature (RT) in an high vacuum system with a base pressure of 2×10^{-7} mbar and an operation pressure of 1×10^{-6} mbar. The irradiation is of high homogeneity and low divergence in a 2×2 cm^2 area.

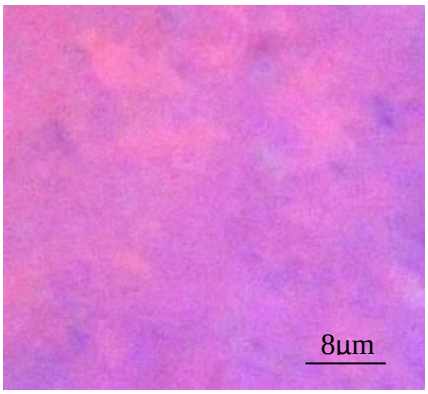

Figure 3.2 Optical micrograph of PMMA-transferred CVD graphene on Si/SiO_2 substrate.

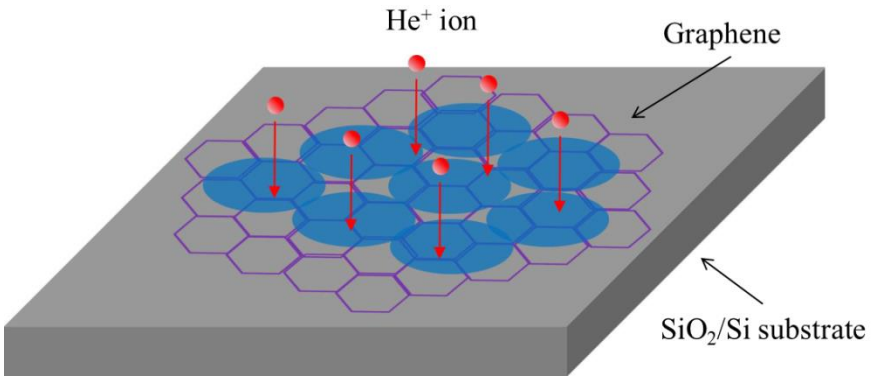

Figure 3.3 Schematic of He^+ ion irradiation in graphene with PMMA residues.

A wafer of graphene was cut to several pieces in 5 mm × 5 mm size. They were irradiated with He^+ ion energy of 5.4 keV and dose density ranging from 4×10^{12} He^+/cm^2 to 2.5×10^{13} He^+/cm^2. The irradiation duration is about 1 s for the dosage of 10^{13} He^+/cm^2.

3.4 X-ray Photoelectron Spectroscopy

As graphene is made up of carbon atoms, it is very sensitive to the O_2, H_2O, and H2 molecules in the air, these molecules can adsorb on the graphene surface and interact with the carbon atoms in graphene [23-24] [29]. In our experiment, the graphene samples were prepared by CVD method and some PMMA residues remained on the surface, as the PMMA is a polymer formed by C, H and O atoms, it can directly interact with the carbon atoms in graphene and in the end change the properties of graphene. By irradiation, some PMMA residues will decompose and many new bonds (C-C, C-H, etc.) will be formed between PMMA and graphene surface, which will promote the modification of the structural properties of graphene [23-24] [29] [32].

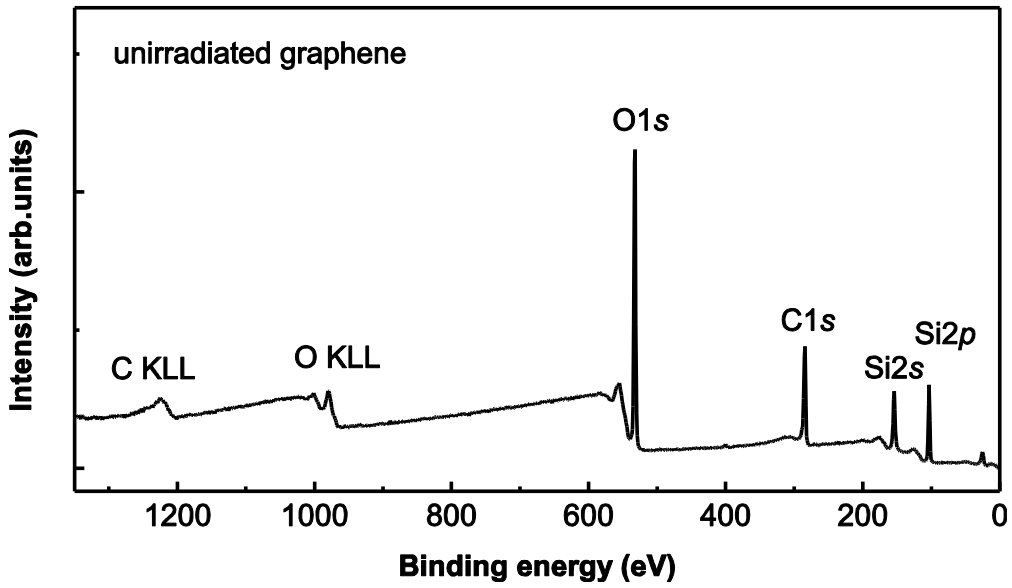

Figure 3.4 X-ray photoelectron spectroscopy survey of the unirradiated graphene sample.

X-ray photoelectron spectroscopy (XPS) is a powerful and widely used spectroscopic technique to measure the elemental composition and chemical bonds in graphene, which helps us have a deeper understanding of the doping effect in graphene after irradiation. The graphene samples were characterized by XPS with Al Kα radiation (1486.6 eV) at ambient temperature. The spot diameter was 400 μm and more than two positions in each sample were measured. The hemispherical analyzer was operated in constant analyzer energy (CAE) mode with the pass energy of 200 eV and the scan step of 1 eV for the survey spectra, as well as the pass energy of 50 eV and the scan step of 0.1 eV for the core-level spectra. A "dual beam" flood gun was used to neutralize the charge build-up. To avoid additional surface contamination, all samples were cleaned by acetone and dried before the XPS measurement. XPS is sensitive within the depth of 3-10 nm from the sample surface.

3.4.1 Unirradiated graphene

Figure 3.4 shows the X-ray photoelectron spectroscopy survey of the unirradiated graphene sample. The C1s, O1s, Si2s and Si2p peaks were observed in the XPS, and no impurities peaks were detected, which show the high quality of the graphene sample. The C1s peak comes from graphene and PMMA residues, O1s peak is from SiO_x and PMMA residues, and the Si2s and Si2p peaks originated from th`1e SiO_2 substrate. Five spots on the unirradiated

sample were measured. Table 3.1 shows the atom ratio of Si, C and O in the unirradiated graphene samples detected by XPS. The atom ratio was obtained from the peak areas divided by the Scofield sensitivity factors after subtracting a Shirley baseline. It can be seen that the content of O atoms is around 40.4%, higher than the C atoms and Si atoms, which are around 36% and 23.6% respectively, which originates from the SiO_x and PMMA residues [23] [29].

Table 3.1 Atom ratio of Si, C and O in the unirradiated graphene samples.

	Si atom ratio (%)	C atom ratio (%)	O atom ratio (%)
Unirradiated	23.6 ±0.3	36.0 ±0.1	40.4 ±0.2

Figure 3.5 shows the C 1s core-level spectra of the unirradiated graphene sample. The peak fitting was obtained using a Gaussian-Lorentzian (Voigt) formula after subtracting the Shirley baseline. The component of the C 1s spectrum around 284.3 ±0.1 eV corresponds to sp^2 hybrid of C–C bond (C1) and the component around 285.0 ±0.1 eV corresponds to sp^3 hybrid of C–C (H) bond (C2) in graphene and PMMA residues. The components with binding energy around 285.7 ±0.1 eV, 286.7 ±0.1 eV and 289.0 ±0.1 eV correspond to the species of PMMA or functional groups on graphene such as C−C=O (C3), C−O−C (H) (C4) and O−C=O (C5) bonds [23] [30-32]. Table 3.2 shows the components and bond ratio of C 1s spectra in unirradiated graphene. The proportion of C–C sp^2 hybrid bond and C-C (H) bond are around 51.0% and 19.3%, which occupy the mainly component in C 1s spectra. The other three bonds: C−C=O, C−O−C (H) and O−C=O occupy around 10.6%, 8.6% and 10.5% in C 1s spectra, respectively.

Table 3.2 Binding energy and area ratio of C 1s components in unirradiated graphene

Bond	**Binding energy (eV)**	**Ratio (%)**
C-C sp^2	284.6 ±0.1	53.2 ±2.1
C-C(H)	285.0 ±0.1	17.2 ±2.1
C-C=O	285.7 ±0.1	8.9 ±1.7
C-O-C(H)	286.7 ±0.1	10.5 ±1.9
O-C=O	289.1 ±0.1	10.2 ±0.3

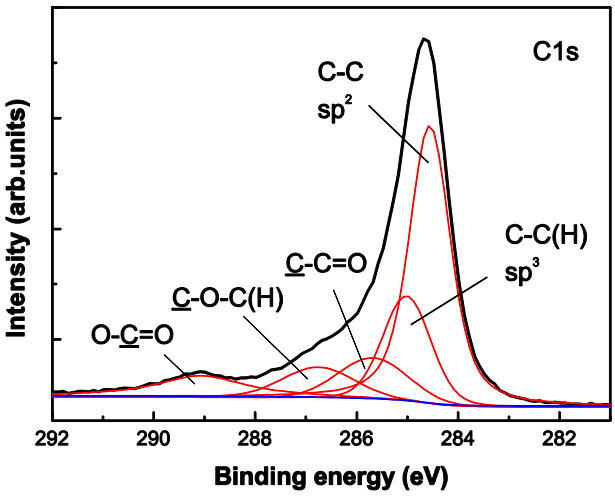

Figure 3.5 XPS C 1s spectra of PMMA-transferred unirradiated graphene. The red curves show the components fitted by a Gaussian/Lorentzian formula after subtracting a Shirley baseline (blue).

3.4.2 Irradiated graphene

Two graphene samples were irradiated under He^+ ions at the dose density of 1×10^{13} He^+/cm^2 and 2.5×10^{13} He^+/cm^2, then the X-ray photoelectron spectroscopy were measured to observe the variation of all the components in C 1s and O 1s spectra after irradiation.

Figure 3.6 shows the XPS C 1s core-level spectra of PMMA-transferred graphene unirradiated and irradiated at two different dose density: 1×10^{13} He^+/cm^2 and 2.5×10^{13} He^+/cm^2. It can be seen that the intensity of C-C sp^2 bond decreases with the dose density, while the intensity of C-C (H) bond increases with the dose density. Table 3.3 shows the binding energy and area ratio of C 1s components in the irradiated graphene samples. The area ratio of C-C sp^2 bond in C1s spectra is around 53.2% for uniradiated graphene, and after irradiated at the low dose density of 1×10^{13} He^+/cm^2, the value decreases to around 51.6%, but is still the mainly component of C 1s spectra. While continue to increase the dose density to 2.5×10^{13} He^+/cm^2, the area ratio of C-C sp^2 bond decreases dramatically to around 24.4% [23-24] [30-35]. For the C-C (H) bond, the area ratio increases from 17.2% in C 1s spectra of unirradiated graphene to 26.9% that of graphene irradiated at the dose density of 1×10^{13} He^+/cm^2, in then end the value increases to 29% at the dose density of 2.5×10^{13} He^+/cm^2, and becomes the most important component in C 1s spectra. The area ratio of C−C=O bond also shows an increase with the dose

density, the area ratio is around 17.2%, 26.9% and 29% for the C 1s spectra of unirradiated graphene, graphene irradiated at the dose density of 1×10^{13} He^+/cm^2 and 2.5×10^{13} He^+/cm^2, respectively. The area ratio of C−O−C (H) bond is around 10.5% and 8.1% for the C 1s spectra of unirradiated graphene and graphene irradiated at the dose density of 1×10^{13} He^+/cm^2, but at the dose density of 2.5×10^{13} He^+/cm^2, it increases to around 15%. While for the O−C=O bond, the area ratio shows a decrease with the dose density, from around 10.2% in C 1s spectra of unirradiated graphene to around 4.2% and 4.9% that of graphene irradiated at the dose density of 1×10^{13} He^+/cm^2 and 2.5×10^{13} He^+/cm^2.

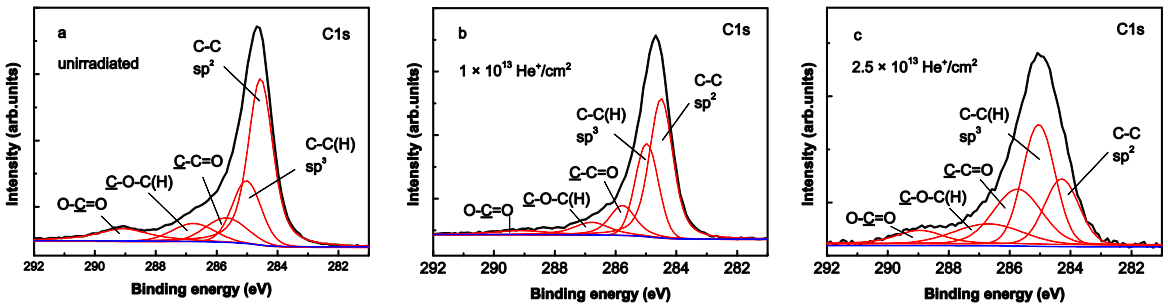

Figure 3.6 XPS C 1s core-level spectra of PMMA-transferred graphene (a) unirradiated and irradiated at two different dose density (b) 1×10^{13} He^+/cm^2 (c) 2.5×10^{13} He^+/cm^2.

Table 3.3 Binding energy and area ratio of C 1s components in the unirradiated and irradiated graphene.

		C1	**C2**	**C3**	**C4**	**C5**
unirradiated	binding energy (eV)	284.6±0.1	285.0±0.1	285.7±0.1	286.7±0.1	289.1±0.1
	area ratio (%)	53.2±2.1	17.2±2.1	8.9±1.7	10.5±1.9	10.2±0.3
1×10^{13} /cm^2	binding energy (eV)	284.5±0.1	285.0±0.1	285.8±0.1	287.0±0.1	289.2±0.1
	area ratio (%)	48.6±2.9	26.9±3.5	12.2±0.4	8.1±3.5	4.2±3.2
2.5×10^{13} /cm^2	binding energy (eV)	284.3±0.1	285.0±0.1	285.7±0.1	286.7±0.1	289.0±0.1
	area ratio (%)	24.4±3.8	29.0±6.3	26.7±1.7	14.9±2.6	4.9±1.9

These results indicates that irradiation leads to the oxidization of graphene from the functional groups in PMMA residues, which result in an increase of area ratio for sp^3 hybrid of C–C(H), C−C=O and C−O−C(H) bonds, and a decrease of area ratio for C-C sp^2 and O−C=O bonds [30-35].

3.4.3 Annealed after irradiation

After irradiation, the graphene sample irradiated at the dose density of 2.5×10^{13} /cm^2 was annealed at 300 °C for 1h in the vacuum of 2.5×10^{-6} mbar, and the XPS was measured to observe the modification of chemical bonds result from vacuum annealing. Figure 3.7 shows the XPS surveys of the unirradiated graphene sample, the graphene at the dose of 2.5×10^{13} He^+/cm^2, and that annealed after the dose of 2.5×10^{13} He^+/cm^2. Only the O1s, C1s, Si2s and Si2p peaks were detected in XPS surveys, which suggest that no other impurities were introduced in graphene during the irradiation and annealing processes. Table 3.6 shows the Atom ratio of Si, C and O in the unirradiated and irradiated graphene samples. The C atom ratio decreases from around 36.0% to 23.9 % after the irradiation, while both the atom ratios of Si and O increase. Similar behaviors are observed as the graphene samples were annealed after the irradiation, the C atom ratio decreases to around 10.5%, and the atom ratio of Si and O increase to around 33.4% and 56.1% respectively. It indicates the amount of PMMA residues on graphene surface decrease after both irradiation and annealing [23] [30-35].

Table 3.4 Atom ratios of Si, C and O in unirradiated graphene sample, the graphene irradiated at the dose of 2.5×10^{13} He^+/cm^2 and that annealed after the dose of 2.5×10^{13} He^+/cm^2.

	Si atom ratio (%)	C atom ratio (%)	O atom ratio (%)
Unirradiated	23.6 ±0.1	36.0 ±0.2	40.4 ±0.1
2.5×10^{13} /cm^2	27.2 ±2.9	23.9 ±3.6	48.9 ±2.8
Annealed	33.4 ±0.1	10.5 ±0.2	56.1 ±0.2

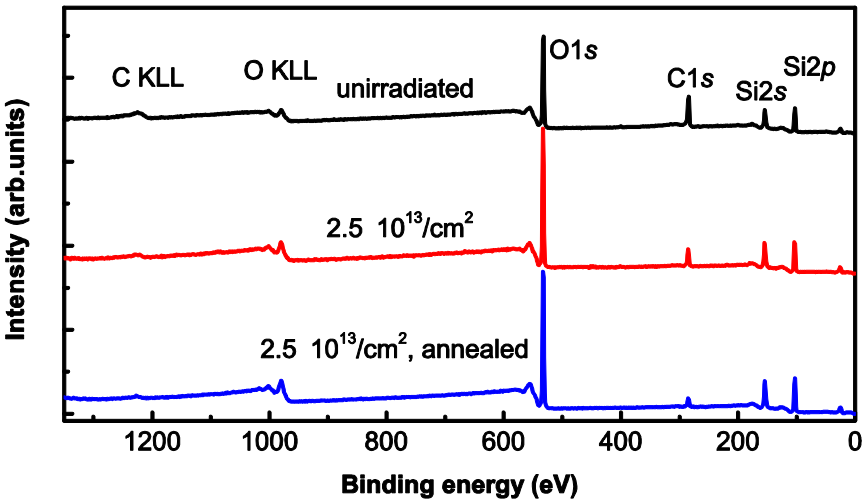

Figure 3.7 XPS surveys of the unirradiated graphene sample, the graphene irradiated at the dose of 2.5 × 10^{13} He^{+}/cm^{2} and that annealed after the dose of 2.5 ×10^{13} He^{+}/cm^{2}.

Figure 3.8 shows the C 1s core-level spectra of the unirradiated graphene, the graphene at the dose of 2.5 × 10^{13} He^{+}/cm^{2} and that annealed after the dose of 2.5 × 10^{13} He^{+}/cm^{2}. The intensity of C 1s spectra decreases and broadens after irradiation and annealing.

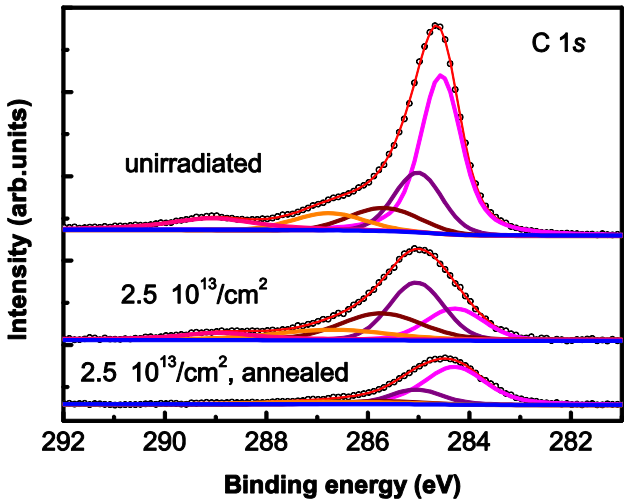

Figure 3.8 C 1s core-level spectra of the unirradiated graphene, the graphene at the dose of 2.5 ×10^{13} He^{+}/cm^{2} and that annealed after the dose of 2.5 ×10^{13} He^{+}/cm^{2}.

From Table 3.5, we can see that after annealing the irradiated graphene sample, the area ratio of sp^2 hybrid of C–C bond increases from around 24.4% to 64.1% compared to the irradiated one, the ratio is also larger than the unirradiated one. Meanwhile, the area ratio of C–C(H) sp^3 hybrid bond, C−C=O and C−O−C(H) groups decreases from around 29%, 26.7% and 14.9% to 20.8%, 6.3% and 8.8%, respectively. It suggests that the annealing leads to the reduction of oxidization in graphene which is induced by irradiation. The area ratio of O−C=O bond decreases after irradiation and almost vanishes after annealing, which may related to the decomposition of the methoxy and carboxyl functional groups in PMMA residues [23- 24] [30-35].

Table 3.5 Binding energy and area ratio of C 1s components in the unirradiated graphene, the graphene at the dose of 2.5×10^{13} He^+/cm^2 and that annealed after the dose of 2.5×10^{13} He^+/cm^2.

		C1	**C2**	**C3**	**C4**	**C5**
unirradiated	binding energy (eV)	284.6±0.1	285.0±0.1	285.7±0.1	286.7±0.1	289.1±0.1
	area ratio (%)	53.2±2.1	17.2±2.1	8.9±1.7	10.5±1.9	10.2±0.3
2.5×10^{13} $/cm^2$	binding energy (eV)	284.3±0.1	285.0±0.1	285.7±0.1	286.7±0.1	289.0±0.1
	area ratio (%)	24.4±3.8	29.0±6.3	26.7±1.7	14.9±2.6	4.9±1.9
2.5×10^{13} $/cm^2$ annealed	binding energy (eV)	284.3±0.1	285.0±0.1	285.7±0.1	286.7±0.1	
	area ratio (%)	64.1±2	20.8±2	6.3±0.6	8.8±0.3	

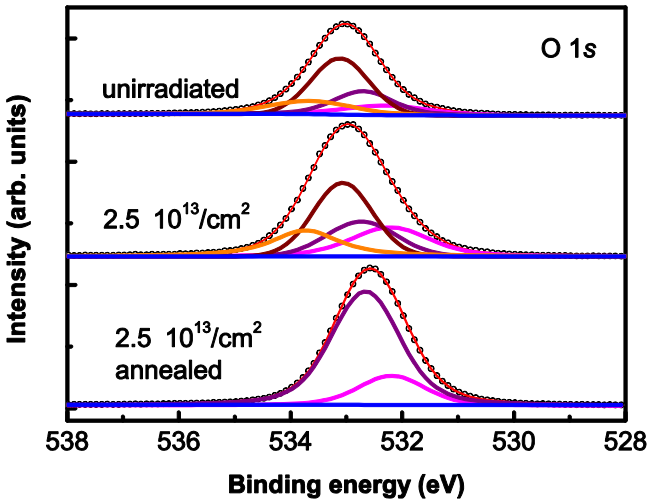

Figure 3.9 O 1s core-level spectra of the unirradiated graphene, the graphene at the dose of 2.5×10^{13} He^+/cm^2 and that annealed after the dose of 2.5×10^{13} He^+/cm^2.

Figure 3.9 shows the O 1s core-level spectra of the unirradiated graphene, the graphene at the dose of 2.5×10^{13} He^+/cm^2 and that annealed after the dose of 2.5×10^{13} He^+/cm^2. There are four components in the XPS O 1s spectra with binding energy around 532.3±0.1 eV, 532.7±0.1 eV, 533.0±0.1 eV and 533.7±0.1 eV, which are corresponding to the C=O (O1), Si−O (O2), C−O−C (H) (O3) and C−O−C=O (O4) bonds, respectively [23-24] [30-35]. It is observed that the intensity of O 1s signal increases after irradiation and annealing, this may results from SiO_x beneath the PMMA residues and graphene which also indicates the decrease of the amount of the PMMA residues.

3.5 Raman Spectroscopy

Raman spectroscopy is an efficient technique to probe the structural and electrical properties in graphene, which helps understand the mechanism of charge-transfer doping effect [36-44]. Electron doping in graphene causes blue-shift of Raman G band, and hole doping leads to blue-shifts in both G and 2D bands [36-43]. Either blue-shifts or red-shifts in G and 2D bands have been observed in PMMA-transferred graphene by irradiation or annealing, which is explained by several competitive effects related to chemical doping [16] [18-20] [22-26] [45].

However, few works show reversible chemical doping due to polymer adsorption by reversible shift in Raman band. In this chapter, the Raman spectroscopy was performed in ambient atmosphere at room temperature (RT) with a 100 × objective. The wavelength of excitation laser is 532 nm (2.33 eV in energy) and the spot diameter is 600 nm. Raman spectra were measured with the wavenumber resolution of 1.8 cm^{-1} in more than five positions of each graphene sample.

3.5.1 Unirradiated graphene

Figure 3.10 shows the Raman spectra of unirradiated graphene sample, five spots were measured in this sample. The intensity ratio of Raman 2D peak to G peak I_{2D}/I_G is 1.26±0.19, and the band width of G and 2D bands are 16±3 cm^{-1} and 37±3 cm^{-1}, respectively, indicating the presence of single layer graphene. The intravalley G band, corresponding to the E_{2g} phonon at the Brillouin-zone center, peaks at ~ 1590 cm^{-1} for the unirradiated graphene. The 2D band around ~ 2690 cm^{-1} is the second order of the D band, originating from an intervalley process where momentum conservation is satisfied by two phonons with opposite wave vectors. And the D peak (~1362 cm^{-1}) could be barely observed in the Raman spectra, which also provides a piece of evidence for the unirradiated graphene [36-38].

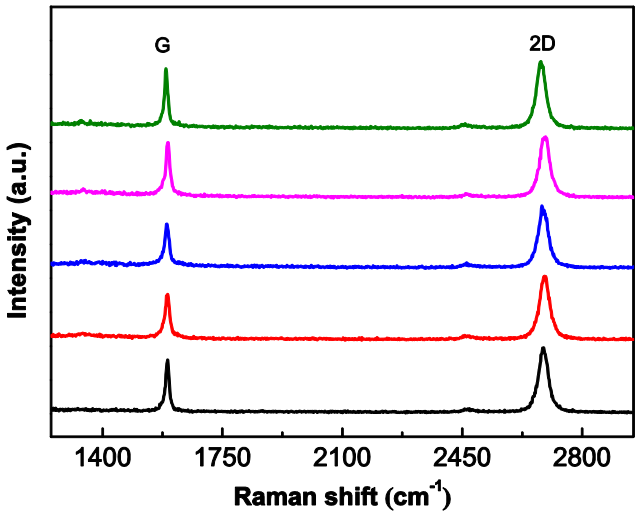

Figure 3.10 Raman spectroscopy of unirradiated graphene sample. The lines with different colors mean the sample was measured for five times.

In fact, we have performed Raman measurements on unirradiated graphene prepared by CVD method from Graphenea Company, Tsinghua University, and Graphene Supermarket. All of the samples are grown on the SiO_2 substrate. The Raman spectrum shows that the graphene prepared by Tsingua University contains a large number of defects. The XPS results also reveal that many Fe impurities remain on the graphene surface, which originate from the Fe $(NO_3)_3$ solutions used during fabrication processes. The Raman spectra of graphene fabricated by Graphene supermarket shows minor D peak, which indicates few defects formed in graphene. Moreover, the Raman spectra performed on different spots suggest the inhomogeneous distribution of the graphene sample. The Raman spectra of graphene from Graphenea Company shows high quality of the unirradiated graphene sample with nearly no defects contained. The Figure 3.10 above also shows the homogeneous distribution of the graphene sample.

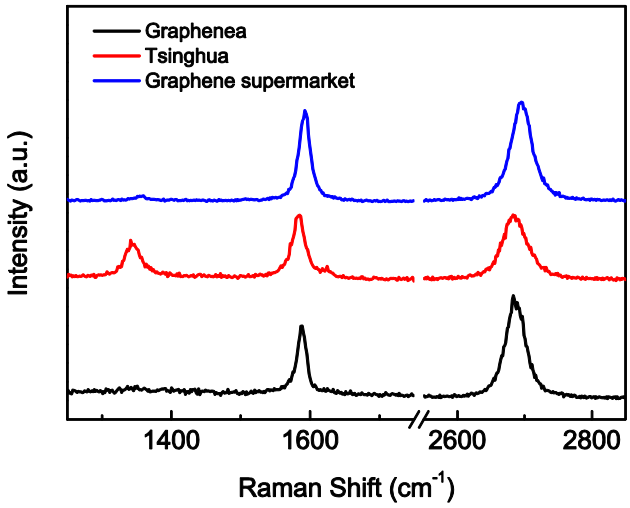

Figure 3.11 Raman spectra of unirradiated graphene prepared by CVD method from Graphenea Company, Tsinghua University and Graphene Supermarket.

3.5.2 Irradiated graphene

Three unirradiated graphene samples, each one about $0.5 \times 0.5 cm^2$, were irradiated at different dose densities: 4×10^{12} He^+/cm^2, 1.2×10^{13} He^+/cm^2 and 2.1×10^{13} He^+/cm^2 respectively, and another unirradiated graphene sample was chosen as reference.

Figure 3.12 shows the evolution of Raman spectra of unirradiated graphene and graphene irradiated with various dose densities. After irradiated the graphene sample at the lowest does density of 4 × 10^{12} He^{+}/cm^{2} (~ 1 He^{+} per 10^{3} carbon atoms), the D peak which is related to disorder appears at ~ 1362 cm^{-1}, and increases significantly for the dose density of 2.1 × 10^{13} He^{+}/cm^{2}. The D peak is due to the breathing modes of six-atom rings and requires a defect for its activation, which is intervalley one-phonon double resonance, this indicates some defects or disorder have formed in graphene after irradiation [36-38]. For the G peak, the intensity increases a lot after irradiation and the band width seems to broaden compared to the unirradiated graphene. While for the 2D peak, it is obvious that the band width broadens after irradiation, especially at the dose density of 1.16 × 10^{13} He^{+}/cm^{2}.

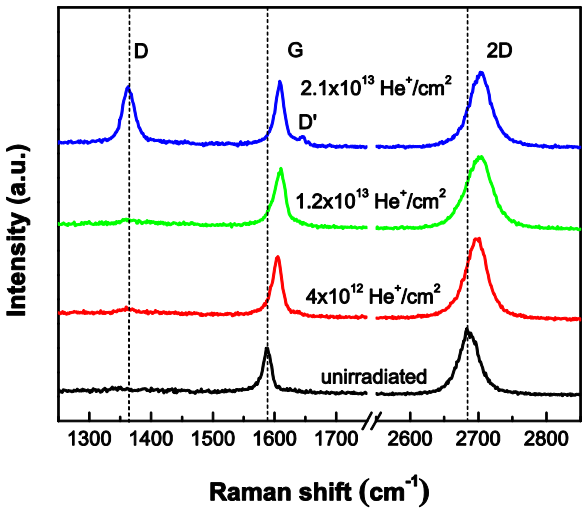

Figure 3.12 Evolution of Raman spectra of unirradiated graphene and irradiated graphene with various dose densities.

With the dash line, one can see that all the three peaks: D, G and 2D band, shift to higher frequency (blue-shifts), which is due to the charge-transfer doping in graphene induced by irradiation [37-43] and will be analyzed in the discussion section. A minor D' peak around 1640 cm^{-1} which is corresponded to a defect-assisted intravalley one-phonon process in graphene was observed in Raman spectra, and the intensity increases with the dose density which also results from the irradiation induced defects in graphene [36-38].

3.5.3 Annealed after irradiation

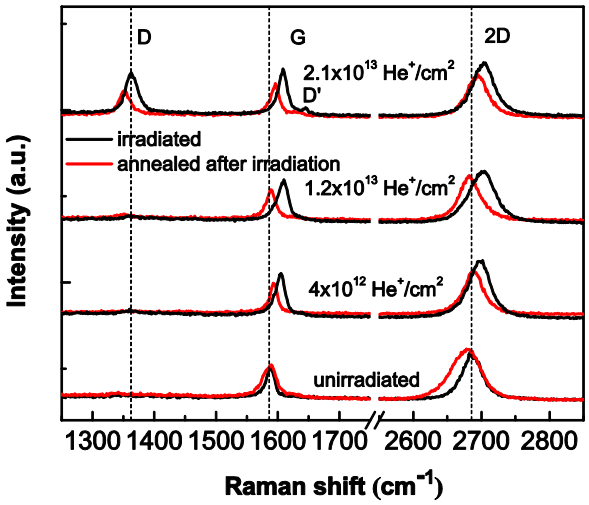

Figure 3.13 Evolution of Raman spectra of unirradiated graphene and irradiated graphene (black lines) with various dose densities after annealing (red lines).

After irradiation, a vacuum annealing process was carried out in the unirradiated and irradiated graphene samples at 300℃ for 1h in the vacuum of degree 2.5×10^{-6} mbar. Figure 3.13 shows the evolution of Raman spectra of unirradiated graphene and irradiated graphene with various dose densities after annealing. For the unirradiated graphene, the G peak broadens after annealing while the frequency and intensity remains on the original position and height level. The intensity of the 2D peak increases which results in a higher intensity ratio (about 1.6) of 2D peak to G peak compared to the unirradiated graphene, this indicates some PMMA residues are removed after annealing and the doping level decreases which leads to a better quality of graphene [23-24] [30-35] [46]. Meanwhile, a shift to lower frequency of 2D peak is observed and the band width broadens. For the irradiated graphene samples, the intensity of D peak decreases after annealing which means the defects or disorders are restored and the amount of PMMA residues reduces. More important, it is interesting to see that all the D, G and 2D bands shift to lower frequency (red-shifts) in the Raman spectra, which is also due to the decrease of doping level in graphene after a vacuum annealing [9] [22] [45].

3.5.4 Discussions

As mentioned before, more details of analysis of Raman Spectra data will be presented, such as the frequency as a function of the dose density, intensity ratio, band width, etc. These will help us better understand the charge-transfer doping processes induced by irradiation and annealing in graphene.

3.5.4.1 Dependence of Frequency on the Dose density

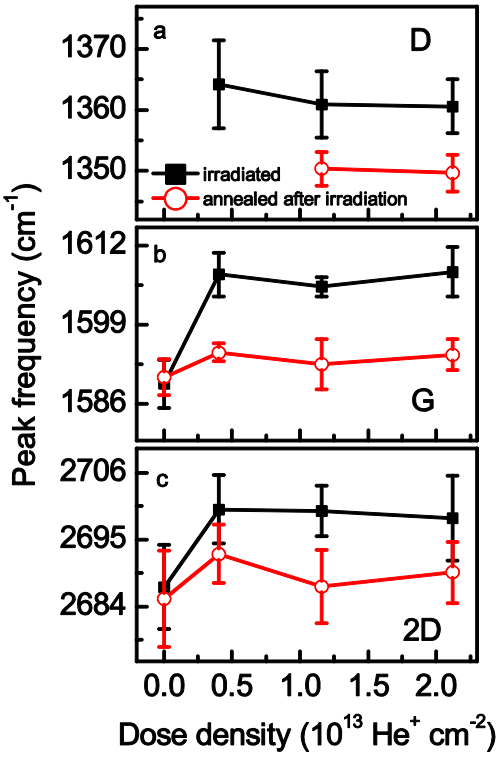

Figure 3.14 Dose density dependences of the frequencies of (a) D peak, (b) G peak and (c) 2D peak for the irradiated graphene (black solid) and the graphene annealed after irradiation (red open).

Figure 3.14 shows the frequencies of the D, G and 2D peaks as a function of dose density. The error bars are given by the results of several spot positions in each graphene sample, representing the spatial inhomogeneity of the Raman shift [41-42]. The D peak shows a small red-shift of about 4 cm^{-1} as the dose density increases from 4.0 $\times 10^{12}$ He^{+}/cm^{2} to 2.1 $\times 10^{13}$ He^{+}/cm^{2}. The G peak and the 2D peak show blue-shift of ~ 18 cm^{-1} and ~ 13 cm^{-1}, respectively, for the small dose density of 4.0 $\times 10^{12}$ He^{+}/cm^{2}. The variation of the shift is non-monotonic, which is similar to the results in Ref. 47. The blue-shift of G band can be due to both electron and

hole doping in graphene, while the blue-shift in 2D band can be caused only by hole doping [37-43]. It suggests that hole doping is an important contribution to the observed blue-shifts in both G and 2D bands due to electron-phonon coupling [15] [22-26]. Compared to the results of electric field-induced doping [43], the hole doping level in our case can be estimated to be $10^{13}/cm^2$. Note that blue-shifts of the G band have been observed in oxidized graphene [15] [22-26].

In our experiment, the irradiation was carried out in high-vacuum and He^+ ion itself cannot be doped in graphene. As shown in the XPS results, the residual carboxyl functional group from PMMA residues on the graphene surface can be the main source of hole doping [16] [19] [22-26]. The chemical bonds between functional groups from PMMA residues and graphene could be formed due to ion irradiation, which leads to hole doping in graphene. Moreover, because the Raman spectra were measured in atmosphere, the absorption of oxygen and H_2O in graphene after irradiation may has small contribution to hole doping [7] [9-11] [48].

After annealing the irradiated graphene, the D, G and 2D bands in the Raman spectra shift back to lower frequency, as shown in Figures 3.16(a)-3.16(c). For the graphene sample at the dose density of 4.0×10^{12} He^+/cm^2, the D peak is barely detectable after annealing. For the graphene samples irradiated at the dose density of 1.2×10^{13} He^+/cm^2 and 2.1×10^{13} He^+/cm^2, the D peak frequencies are around 1350 cm^{-1} after annealing, i.e. red-shift of about 10 cm^{-1} with respect to those before annealing. The frequencies of both G and 2D bands of the unirradiated graphene do not change much after annealing. The red-shifts of both the G and 2D bands of the irradiated graphene after annealing are related to the reduction of charge-transfer doping in graphene [9] [22] [45].

As shown in the XPS results, the annealing at temperature of $300\,^{\circ}C$ can result in the decomposition of the methoxy and carboxyl functional groups [23-24] [30-32]. It suggests that the irradiation induced bonds between functional groups from PMMA residues and graphene may be broken after irradiation and post-annealing [46]. The desorption of functional groups from graphene is dominant during the vacuum annealing process, which leads to the reduction of hole doping and red-shift in Raman bands [24]. It should be noticed that the non-monotonic behaviors for both the G and 2D band frequencies remain after annealing. It indicates that ion irradiation also leads to irreversible effect in graphene [11] [44], i.e. the doping effect is partially reversible.

In order to better clarify the transfer-doping processes in graphene, the diagram of the 2D peak frequency of irradiated graphene (black) and the graphene annealed after irradiation (red) as a function of the G peak frequency was depicted, as shown in Figure 3.15 [41]. It can be seen that the 2D peak frequency increases almost linearly with the G peak frequency. Irradiation causes blue-shift in both the G band and the decrease of the I_{2D}/I_G, however, annealing results in a recovery of the G peak frequency and the I_{2D}/I_G as shown in the diagram. This also indicates clearly a reversible effect of charge-transfer doping.

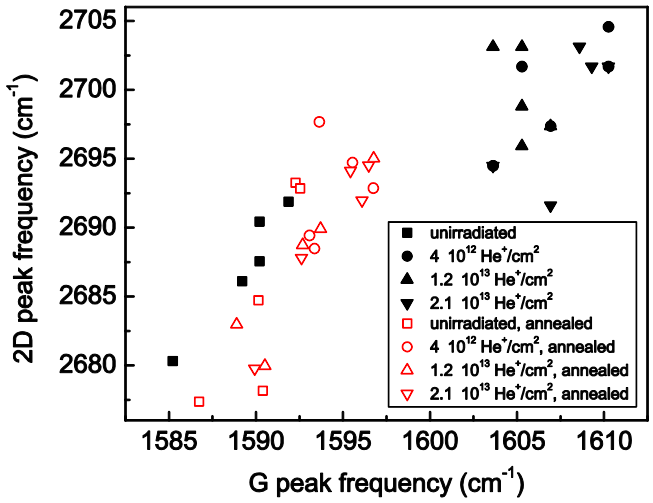

Figure 3.15 Diagram of 2D peak frequency vs G peak frequency for the irradiated graphene (black solid) and the graphene annealed after irradiation (red open).

3.5.4.2 Dependence of Intensity ratio on the Dose density

The intensity ratios of I_D/I_G and I_{2D}/I_G provide an important way to understand the amount of defects or disorders formed in graphene, and also the average interdefect distance can be calculated [36,37]. Figure 3.16 shows the intensity ratio of the D peak to the G peak (I_D/I_G) as a function of dose density for the irradiated graphene and the graphene annealed after irradiation. Before annealing, The I_D/I_G ratio is less than 0.1 as the dosage is lower than 1.2×10^{13} He^+/cm^2, indicating small amount of defects in graphene. The I_D/I_G ratio increases a lot as the dosage is more than 1.2×10^{13} He^+/cm^2, indicating the increase of the amount of defects [4-6] [36-37] [46] [49-51]. The average inter-defect distance can be considered similar to the size of in-plane crystallites L_a which is evaluated by the Tuinstra-Koenig relation [52-54], $L_a = (2.4 \times$

$10^{-10})\lambda_{\text{laser}}^4 \left(\frac{I_D}{I_G}\right)^{-1}$ (in unit of nm), where λ_{laser} is the laser excitation wavelength (532 nm in our case). The increase of the I_D/I_G ratio indicates the average inter-defect distance decreases. For the dose density of 2.1 × 10^{13} He^+/cm^2, the I_D/I_G ratio is about 0.87, and the average inter-defect distance is about 20 nm. After annealing, the I_D/I_G ratios of the irradiated graphene decreases. For the dose density of 2.1 × 10^{13} He^+/cm^2, the I_D/I_G ratio is about 0.72 after annealing, and the calculated average inter-defect distance is about 26.7 nm, which is larger than that before annealing. It indicates that the amount of defects decreases after annealing [26].

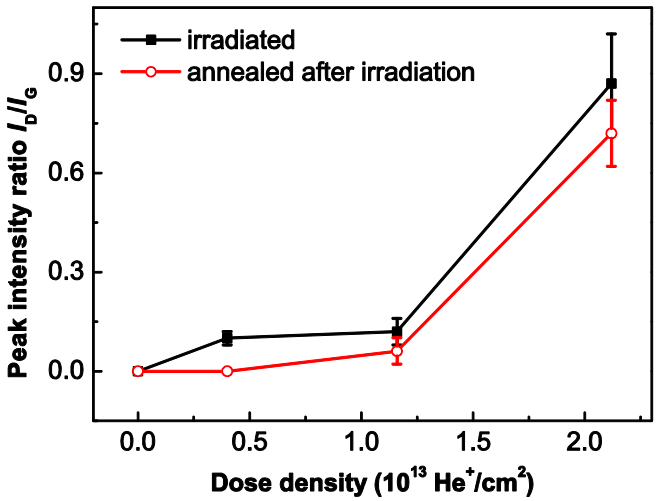

Figure 3.16 Dependences of the intensity ratio of the D peak to the G peak (I_D/I_G) on dose density of the irradiated graphene (black solid) and the graphene annealed after irradiation (red open).

As shown in Figure 3.17, the I_{2D}/I_G ratio decreases at the irradiation dose density of 4 × 10^{12} He^+/cm^2. The increase of disorder can lead to the decrease of the I_{2D}/I_G ratio [54]. However, we suggest that the observed decrease of the I_{2D}/I_G ratio is mainly related to ion irradiation induced hole doping [7] [15] [17] [43] [55]. Note that the I_{2D}/I_G ratio changes little of the dosages between 4.0 × 10^{12} He^+/cm^2 and 2.1 × 10^{13} He^+/cm^2, while the amount of defects increases a lot indicated by the I_D/I_G ratio.

It can be seen that the behavior of the I_{2D}/I_G ratio has a relation with that of the shifts of the G and 2D bands (shown in Figure 3.16). It indicates that low energy He^+ ion irradiation may induce charge-transfer doping in graphene before the formation of large amount of defects. It

should be noted that the spatial distributions of the bands shift and the intensity ratio are broad, which indicates the doping level in graphene is very inhomogeneous [42]. After annealing, the I_{2D}/I_G ratio increases nearly by 0.4 for each irradiation dose density, indicating the reduction of the charge-transfer doping level and the decrease of defects in graphene.

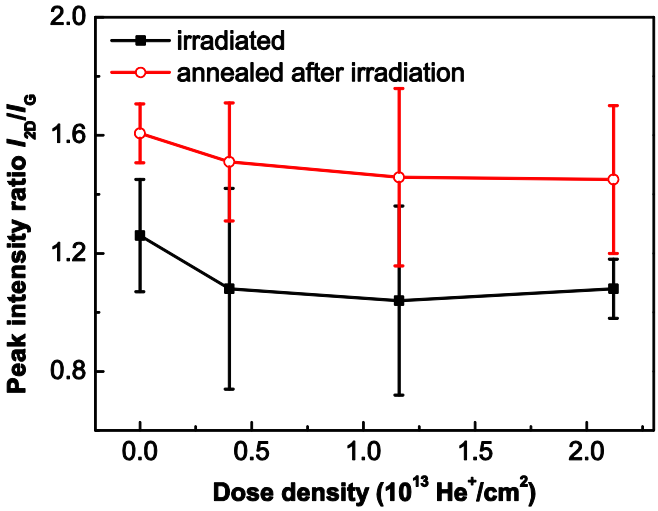

Figure 3.17 Dependences of the intensity ratio of the 2D peak to the G peak (I_{2D}/I_G) on dose density of the irradiated graphene (black solid) and the graphene annealed after irradiation (red open).

Figure 3.18 shows the I_{2D}/I_G ratio of the He^+ irradiation graphene (black) and the graphene annealed after irradiation (red) as a function of the he G peak frequency [41]. It can be seen that I_{2D}/I_G decreases almost linearly with the increase of the he G peak frequency. Irradiation leads to the blue-shift of the G band and the decrease of the I_{2D}/I_G, and annealing results in a recovery of the G peak frequency and the I_{2D}/I_G shown in the diagram. This also indicates clearly a reversible effect of charge-transfer doping.

3.5.4.3 Dependence of Band width on the Dose density

The dependences of the full width at half maximum (FWHM) of the D, G and 2D bands on dose density are shown in Figures 3.19(a)-3.19(c). The FWHM of the D band shows a small decrease by 4 cm^{-1} as the dose density increases from 4.0 $\times 10^{12}$ He^+/cm^2 to 2.1 $\times 10^{13}$ He^+/cm^2, which corresponds to the enhanced D band intensity at the larger dosage. However, the FWHM of the G and 2D bands increase by 6 cm^{-1} and 13 cm^{-1}, respectively, as the dose density increases

to 2.1 $\times 10^{13}$ He^{+}/cm^{2}, which could be related to hole doping and more disorder in graphene [15]. After annealing, the FWHM of the D band decreases slightly for the graphene with the dose density of 1.2 $\times 10^{13}$ He^{+}/cm^{2}. The G and 2D bands for the graphene annealed after irradiation are of similar FWHM to those for the unirradiated graphene, which is related to the reduction of doping level and less disorder after annealing. However, the FWHM of both the G and 2D bands for the unirradiated graphene after annealing are about 5 cm^{-1} and 6 cm^{-1} broader than those before annealing, respectively.

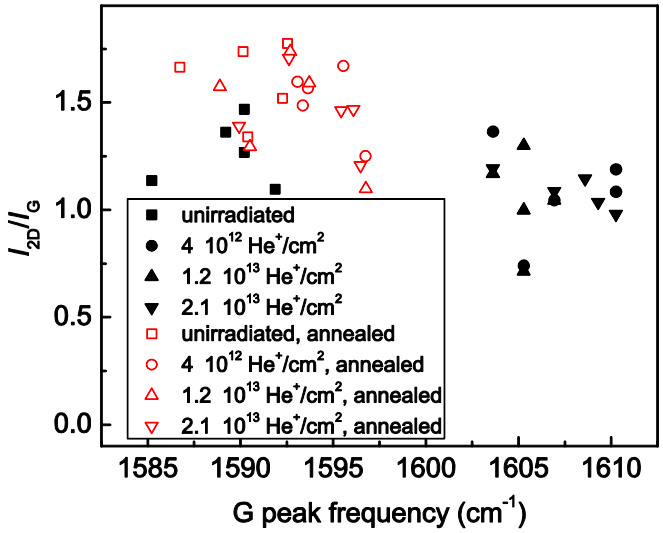

Figure 3.18 Diagram of I_{2D}/I_G vs the G peak frequency of the irradiated graphene (black solid) and the graphene annealed after irradiation (red open).

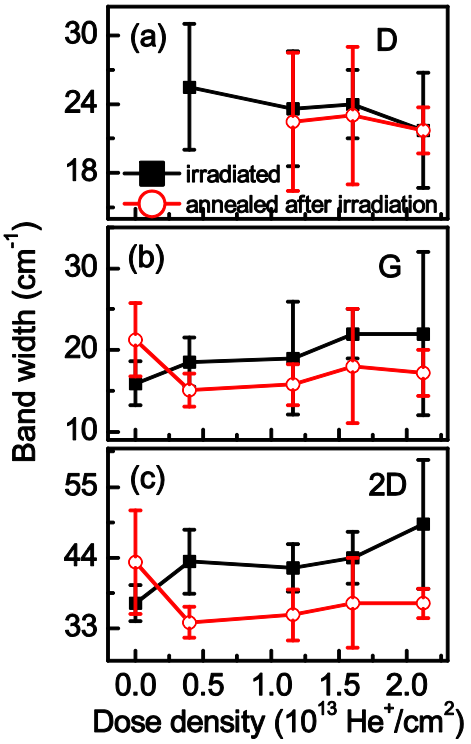

Figure 3.19 (a)-(c) Dose density dependences of the width (FWHM) of D band (a), G band (b) and 2D band (c) for the irradiated graphene (black solid) and the graphene annealed after irradiation (red open).

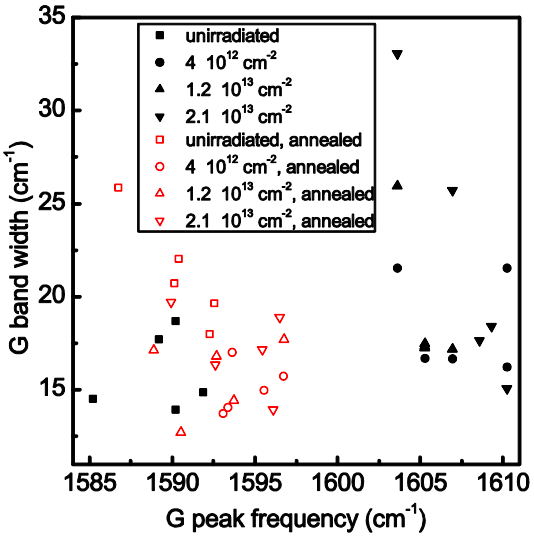

Figure 3.20 Diagram of G band width vs the G peak frequency for the irradiated graphene (black solid) and the graphene annealed after irradiation (red open).

Figure 3.20 shows the diagram of the FWHM of the G band vs the G peak frequency. Two branches could be seen in the diagram, the black one presents the irradiated graphene, while the red one gives the information about annealed graphene after irradiation. It is can be seen that for the irradiated graphene, the band width of G peak increases with the G peak frequency, and all the dots locate in two sides, one part is from 1585 cm^{-1}-1592 cm^{-1}, another part is from 1603 cm^{-1}-1611 cm^{-1}. For the annealed graphene after irradiation, a tendency of decrease with the dose density is observed, and all the dots distribute during 1586 cm^{-1}-1597 cm^{-1}. This also indicates that the reversible chemical doping behavior has happened during the irradiation and annealing processes [8] [41].

3.5.4.4 Irradiation after annealing

Here, the unirradiated graphene was cut into two pieces, each one is about $1 \times 0.5 cm^2$, the first one was annealed at 300 °C for 1h in the vacuum of degree 2.5×10^{-6} mbar and then irradiated at the dose density of 2.1×10^{13} He^+/cm^2, the second one was treated by a reversal process, irradiated at dose density of 2.1×10^{13} He^+/cm^2 and then annealed at 300 °C for 1h.

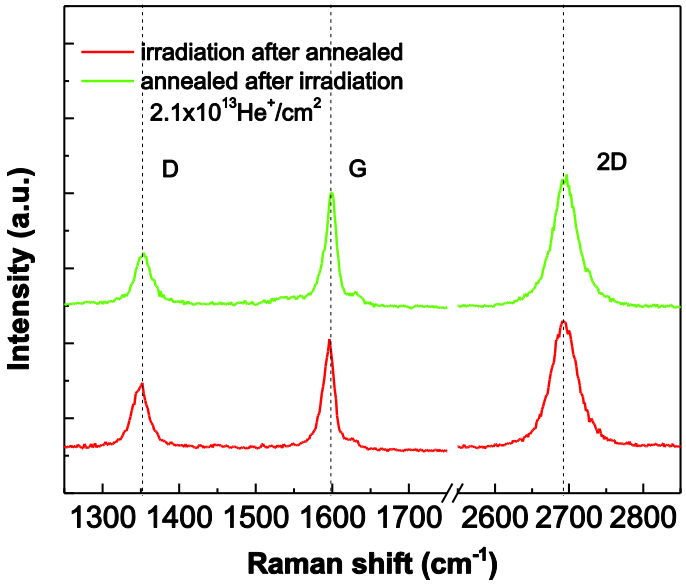

Figure 3.21 Raman spectra of graphene irradiation after annealed (red curve) and annealed after irradiation (green curve).

Figure 3.21, two similar Raman spectra curves was observed after the graphene samples were treated by the reverse processes. In the two cases, the frequencies of D, G and 2D peaks are all around 1351.9 cm^{-1}, 1596.3 cm^{-1} and 2692.4 cm^{-1}. For the graphene irradiated after annealing,

the I_D/I_G and I_{2D}/I_G ratio is about 0.6 and 1.16. While for the graphene annealed after irradiation, the I_D/I_G and I_{2D}/I_G ratio is about 0.51 and 1.12, respectively. This indicates the amount of defects and irradiation induced chemical doping from PMMA residues are on the same level after the reverse processes. The FWHM of D, G and 2D peaks for graphene irradiated after annealing is about 24.82, 16.17 and 40.96. And for the graphene annealed after irradiation, the FWHM is about 21.69, 15.63 and 38.49. There is also no significant difference between the two graphene samples. These results provide evidence that the irradiation and annealing effects have weak relationship with the processes.

3.5.4.5 Irradiation at high dose density

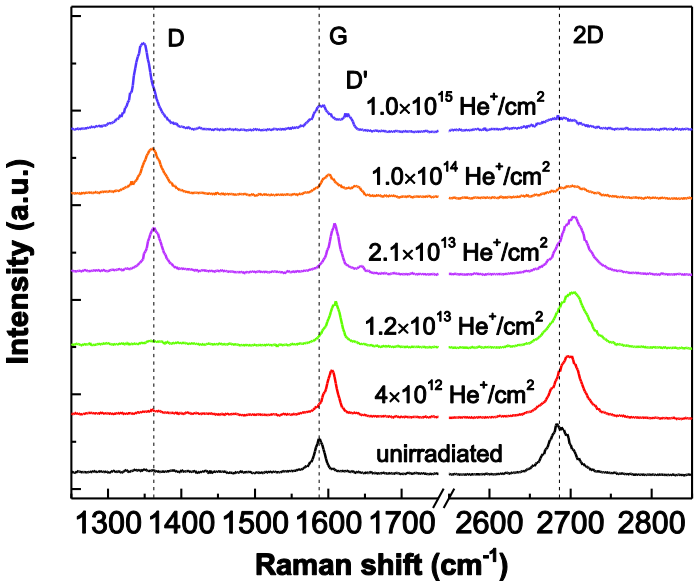

Figure 3.22 Raman spectra of graphene irradiated at high dose density.

In order to investigate the graphene irradiated high dose density, the unirradiated graphene samples were irradiated at the dose density of 1×10^{14} He^+/cm^2 and 1×10^{15} He^+/cm^2, respectively. As shown in Figure 3.22, the intensity of D peak increases significantly when the graphene irradiated at the dose density of 1×10^{14} He^+/cm^2 and 1×10^{15} He^+/cm^2, which means there are a large amount of defects formed in graphene. Furthermore, compared to the graphene irradiated at the dose density of 2.1×10^{13} He^+/cm^2, the frequency of D peak shows a red-shift of ~3 cm^{-1} and ~15 cm^{-1} after irradiated at dose density of 1×10^{14} He^+/cm^2 and 1×10^{15} He^+/cm^2, respectively. For the G peak, the intensity decreases obviously after irradiated at dose density of 1×10^{14} He^+/cm^2 and 1×10^{15} He^+/cm^2. While the frequency of graphene irradiated at dose density

of 1 × 10^{15} He^+/cm^2 shows a red-shift of ~17 cm^{-1} compared to graphene irradiated at the dose density of 2.1 × 10^{13} He^+/cm^2, but is near the frequency of unirradiated graphene. This may related to the strain effect results from the interaction between graphene and SiO_2/Si substrate [56]. The 2D peak nearly vanishes after irradiated at high dose density of 1 × 10^{14} He^+/cm^2 and 1 × 10^{15} He^+/cm^2, indicating full amorphization or partial sputtering of the graphene layer [6].

3.6 Atomic Force Microscopy

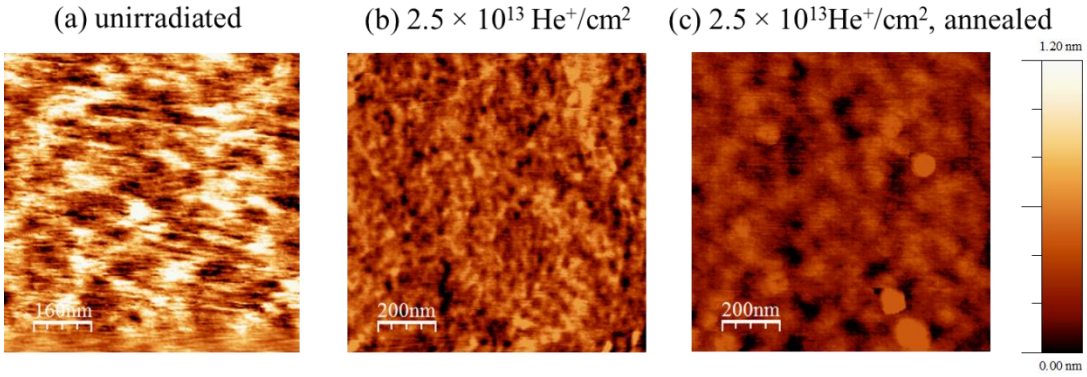

Figure 3.23 AFM images of the unirradiated graphene, the graphene at the dose of 2.5 × 10^{13} He^+/cm^2 and that annealed after the dose of 2.5 × 10^{13} He^+/cm^2.

AFM measurement was performed in tapping mode with a silicon tip in atmosphere at room temperature, and more than six positions in each sample were imaged. Figure 3.23(a)-3.23(c) shows AFM images of the unirradiated graphene, the graphene at the dosage of 2.5×10^{13} He^+/cm^2 and that annealed after the irradiation. The AFM image of the unirradiated sample (Figure 3.23(a)) shows some areas (white) with the large height of 1.2 nm, which corresponds to the presence of PMMA residues. The root mean square (RMS) roughness of the sample surface for the unirradiated graphene, the graphene at the dose of 2.5×10^{13} He^+/cm^2 and that annealed after the irradiation are 0.35 ± 0.17 nm, 0.20 ± 0.07 nm and 0.15 ± 0.05 nm, respectively. It indicates that irradiation does not cause the surface rough and the surface morphology becomes smooth after annealing. The black spot with zero height in AFM images of the irradiated and annealed graphene samples may indicate the presence of defects in graphene. In the light of the decrease of the amount of carbon in XPS, the AFM results confirm that the PMMA residues on the surface is mostly removed after the irradiation and annealing, which leads to smooth the

surface morphology. Ref. 16 shows similar behavior that the surface looks cleaner after plasma treatment.

AFM images on SiO_2 substrate for the unirradiated graphene, the graphene at the dosage of 2.5×10^{13} He^+/cm^2 and that annealed after the irradiation were also measured to observe irradiation and annealing effect on the substrate. As show in Figure 3.24, the RMS of the SiO_2 substrate surface for the unirradiated graphene, the graphene at the dose of 2.5×10^{13} He^+/cm^2 and that annealed after the irradiation are 0.10 ± 0.02 nm, 0.14 ± 0.03 nm and 0.18 ± 0.06 nm, respectively. Compared to the graphene, the RMS of SiO_2 substrate surface increases after irradiation and annealing. It indicates He^+ ions go through the graphene and bombard the SiO_2 substrate during the irradiation process, which make the SiO_2 substrate rougher. After annealing, the oxidization in graphene is reduced and more O atoms from the decomposed PMMA residues interact with the Si atoms in the substrate and further increase the roughness of SiO_2 substrate.

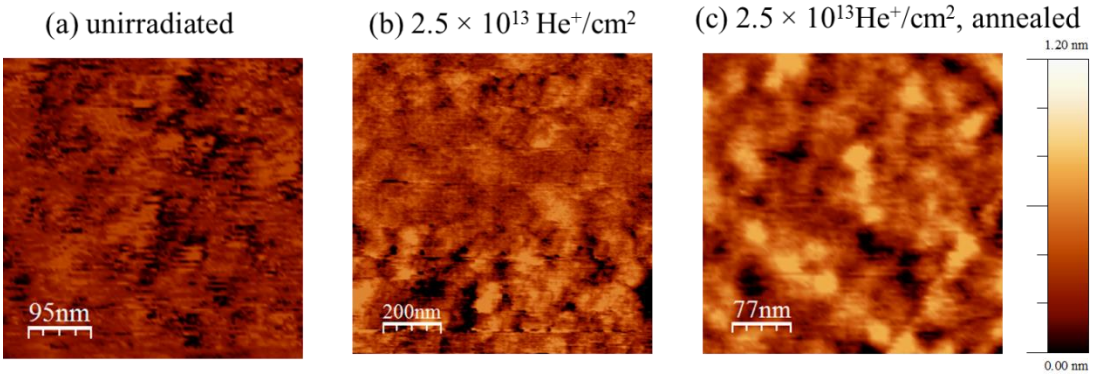

Figure 3.24 AFM images of the SiO_2 substrate for unirradiated graphene, the graphene at the dose of 2.5×10^{13} He^+/cm^2 and that annealed after the dose of 2.5×10^{13} He^+/cm^2.

3.7 Conclusion

In this chapter, a reversible charge-transfer doping effect was observed in graphene on Si/SiO_2 substrate by He^+ ion irradiation and vacuum annealing. For a small dose density of 4×10^{12} He^+/cm^2, both the G and 2D bands in the Raman spectra exhibit blue-shift and the intensity ratio of the 2D peak to the G peak decreases. The intensity ratio of the D peak to the G peak increases a lot as the dose density is larger than 1.2×10^{13} He^+/cm^2. It suggests that before the formation of large amount of defects, chemical bonds between functional groups from PMMA residues and graphene could be formed due to He^+ ion irradiation, which leads to hole doping in graphene. By annealing the irradiated graphene in vacuum, red-shift of the G and 2D bands and the increase of the intensity ratio of the 2D band to the G band were observed, indicating the charge-transfer doping can be partially restored. The desorption of functional groups from graphene is dominant during the vacuum annealing process, which leads to the reduction of hole doping. Meanwhile, the PMMA residue on the graphene surface is mostly removed and the surface morphology becomes smooth after irradiation and annealing.

This work demonstrates that the reaction between polymer adsorption and graphene plays an important role on charge-transfer doping in graphene, which involves both reversible and irreversible effects. Meanwhile, it also paves the way for a better understand of the modulation of transport properties of graphene, which shows high potential application in graphene based memory and logic devices, transistors, and integrated circuits.

References

(1) Krasheninnikov, A. V.; Nordlund, K. Ion and electron irradiation-induced effects in nanostructured materials. *J. Appl. Phys.* **2010**, *107*(7), 071301.

(2) Hashimoto, A.; Suenaga, K.; Gloter, A.; Urita, K.; Iijima, S. Direct evidence for atomic defects in graphene layers. *Nature.* **2004**, *430*(7002), 870.

(3) Tapasztó, L.; Dobrik, G.; Nemes-Incze, P.; Vertesy, G.; Lambin, Ph.; Biró, L. P. Tuning the electronic structure of graphene by ion irradiation. *Phys. Rev. B.* **2008**, *78*(23), 233407.

(4) Teweldebrhan, D.; Balandin, A. A. Modification of graphene properties due to electron-beam irradiation. *Appl. Phys. Lett.* **2009,** *94*(1),, 013101.

(5) Compagnini, G.; Giannazzo, F.; Sonde, S.; Raineri, V.; Rimini, E. Ion irradiation and defect formation in single layer graphene. *Carbon.* **2009**, *47*, 3201.

(6) Lucchese, M. M.; Stavale, F.; Ferreira, E. H.; Vilani, C.; Moutinho, M. V. O.; Capaz, R. B.; Achete, C. A.; Jorio, A. Quantifying ion-induced defects and Raman relaxation length in graphene. *Carbon.* **2010**, *48*, 1592.

(7) Liu, L.; Ryu, S.; Tomasik, M. R.; Stolyarova, E.; Jung, N.; Hybertsen, M. S.; Steigerwald, M. L.; Brus, L. E.; Flynn, G. W. Graphene oxidation: thickness-dependent etching and strong chemical doping. *Nano Lett*. **2008**, *8*, 1965.

(8) Ryu, S.; Han, M. Y.; Maultzsch, J.; Heinz, T. F.; Kim, P. Reversible basal plane hydrogenation of graphene. *Nano Lett.* **2008**, *8*, 4597.

(9) Abdula, D.; Ozel, T.; Kang, K.; Cahill, D. G.; Shim, M. Environment-induced effects on the temperature dependence of Raman spectra of single-layer graphene. *J. Phys. Chem. C* **2008**, *112*, 20131.

(10) Malard, L. M.; Moreira, R. L.; Elias, D. C.; Plentz, F.; Alves, E. S.; Pimenta, M. A. Thermal enhancement of chemical doping in graphene: a Raman spectroscopy study. *J. Phys.: Condens. Matter* **2010**, *22*, 334202.

(11) Ryu, S.; Liu, L.; Berciaud, S.; Yu, Y. J.; Liu, H.; Kim, P.; Flynn, G. W.; Brus, L. E. Atmospheric oxygen binding and hole doping in deformed graphene on a SiO_2 substrate. *Nano Lett.* **2010**, *10*, 4944.

(12) Song, S. M.; Cho, B. J. Investigation of interaction between graphene and dielectrics. *Nanotech.* **2010**, *21*, 335706.

(13) Kim, K. J.; Yang, S.; Park, Y.; Lee, M; Kim, B. S.; Lee, H. Annealing effects after nitrogen ion casting on monolayer and multilayer graphene. *J. Phys. Chem. C.* **2013**, *117*, 2129.

(14) Wang, X.; Li, X.; Zhang, L.; Yoon, Y.; Weber, P. K.; Wang, H.; Guo, J.; Dai, H. N-doping of graphene through electrothermal reactions with ammonia. *Science.* **2009**, *324*, 768.

(15) Childres, I.; Jauregui, L. A.; Tian, J.; Chen, Y. P. Effect of oxygen plasma etching on graphene studied using Raman spectroscopy and electronic transport measurements. *New J. Phys.* **2011**, *13*, 025008.

(16) Peltekis, N.; Kumar, S.; McEvoy, N.; Lee, K.; Weidlich, A.; Duesberg, G. S. The effect of downstream plasma treatments on graphene surfaces. *Carbon.* **2012**, *50*, 395.

(17) Elias, D. C. Nair, R. R.; Mohiuddin, T. M. G.; Morozov, S. V.; Blake, P.; Halsall, M. P.; Ferrari, A. C.; Boukhvalov, D. W.; Katsnelson, M. I.; Geim, A. K.; et al. Control of graphene's properties by reversible hydrogenation: Evidence for graphane. *Science.* **2009**, *323*, 610.

(18) Woo, S. O.; Teizer, W. The effect of electron induced hydrogenation of graphene on its electrical transport properties. *Appl. Phys. Lett.* **2013**, *103*, 041603.

(19) Pirkle, A.; Chan, J.; Venugopa, A.; Hinojos, D.; Magnuson, C. W.; McDonnell, S.; Colombo, L.; Vogel, E. M.; Ruoff, R. S.; Wallace, R. M. The effect of chemical residues on the physical and electrical properties of chemical vapor deposited graphene transferred to SiO_2. *Appl. Phys. Lett.* **2011**, *99*, 122108.

(20) Suk, J. W.; Lee, W. H.; Lee, J.; Chou, H.; Piner, R. D.; Hao, Y. Enhancement of the electrical properties of graphene grown by chemical vapor deposition via controlling the effects of polymer residue. *Nano Lett*. **2013**, *13*, 1462.

(21) Ryu, S.; Maultzsch, J.; Han, Y. H.; Kim, Ph.; Brus, L. E. Raman spectroscopy of lithographically patterned graphene nanoribbons. *ACS Nano* **2011**, *5*, 4123.

(22) Fan, J.; Michalik, J. M.; Casado L.; Roddaro, S., Ibarra, M. R.; De Teresa J. M. Investigation of the influence on graphene by using electron-beam and photo-lithography. *Solid State Commun.* **2011**, *151*, 1574.

(23) Lin, Y. C.; Lu, C. C.; Yeh, C. H.; Jin, C.; Suenaga, K.; Chiu, P. W. Graphene annealing: how clean can it be? *Nano Lett*. **2012**, *12*, 414.

(24) Ahn, Y.; Kim, H.; Kim, Y-H.; Yi, Y.; Kim, S-I. Procedure of removing polymer residues and its influences on electronic and structural characteristics of graphene. *Appl. Phys. Lett.* **2013**, *102*, 091602.

(25) Kim, J.-H.; Hwang, J.-H.; Suh, J.; Tongay, S.; Kwon, S.; Hwang, C. C.; Wu, J.; Park, J. Y. Work function engineering of single layer graphene by irradiation-induced defects. *Appl. Phys. Lett.* **2013,** *103*, 171604.

(26) Kumar, K.; Kim, Y.-S.; Yang, E.-H. The influence of thermal annealing to remove polymeric residue on the electronic doping and morphological characteristics of graphene. *Carbon.* **2013**, *65*, 35.

(27) Li, X. S.; Cai, W. W.; An, J. H.; Kim, S.; Nah, J.; Yang, D. X.; Piner, R.; Velamakanni, A.; Jung, I.; Tutuc, E.; et al. Large-area synthesis of high-quality and uniform graphene films on copper foils. *Science.* **2009**, *324*, 1312.

(28) Liang, X.; Sperling, B. A.; Calizo, I.; Cheng, G.; Hacker, C. A.; Zhang. Q.; Obeng, Y.; Yan, K.; Peng, H.; Li, Q.; et al. Toward clean and crackless transfer of graphene. *ACS Nano.* **2011**, *5*, 9144.

(29) Schedin, F.; Geim, A. K.; Morozov, S. V.; Hill, E.W.; Blake, P.; Katsnelson, M. I.; Novoselov, K. S. Detection of individual gas molecules adsorbed on graphene. *Nat. Mater.* **2007**, *6*, 652.

(30) Kashiwagi, T.; Inaba, A.; Brown, J. E.; Hatada, K.; Kitayama, T.; Masuda, E. Effects of weak linkages on thermal and oxidative degradation of PMMA. *Macromolecules* **1986**, *19*, 2160.

(31) Manring, L. E. Thermal degradation of poly (methy1 methacrylate). 4. Random side-group scission. *Macromolecules* **1991**, *24*, 3304.

(32) Ben Amor, S.; Baud, G.; Jacquet, M.; Nanse, G.; Fioux, P.; Nardin, M. XPS characterisation of plasma-treated and alumina-coated PMMA. *Appl. Sur. Sci*. **2000**, *153*, 172.

(33) D áz, J.; Paolicelli, G.; Ferrer, S.; Comin, F. Separation of the sp^3 and sp^2 components in the C 1*s* photoemission spectra of amorphous carbon films. *Phys. Rev. B.* **1996**, *54*, 8064.

(34) Du, J.; Zhu, J.; Wilkie, Ch. A.; Wang, J. Y. An XPS investigation of thermal degradation and charring on PMMA clay nanocomposites. *Polym. Degrad. Stab.* **2002**, *77*, 377.

(35) Guittet, M. J.; Crocombette, J. P.; Gautier-Soyer, M. Bonding and XPS chemical shifts in $ZrSiO_4$ versus SiO_2 and ZrO_2: Charge transfer and electrostatic effects. *Phys. Rev. B.* **2001**, *63*, 125117.

(36) Ferrari, A. C.; Meyer, J. C.; Scardaci, V.; Casiraghi, C.; Lazzeri, M.; Mauri, F.; Piscanec, S.; Jiang, D.; Novoselov, K. S.; Roth, S.; et al. Raman spectrum of graphene and graphene layers. *Phys. Rev. Lett.* **2006**, *97*, 187401.

(37) Ferrari, A. C. Raman spectroscopy of graphene and graphite: disorder, electron–phonon coupling, doping and nonadiabatic effects. *Solid State Commun.* **2007**, *143*, 47.

(38) Saito, R.; Hofmann, M.; Dresselhaus, G.; Jorio, A.; Dresselhaus, M. S. Raman spectroscopy of graphene and carbon nanotubes. *Adv. Phys.* **2011**, *60*, 413–550.

(39) Pisana, S.; Lazzeri, M.; Casiraghi, C.; Novoselov, K. S.; Geim, A. K.; Ferrari, A. C.; Mauri, F. Breakdown of the adiabatic Born-Oppenheimer approximation in graphene. *Nat. Mater.* **2007**, *6*, 198–201.

(40) Yan, J.; Zhang, Y.; Kim, Ph.; Pinczuk, A. Electric field effect tuning of electron-phonon coupling in graphene. *Phys. Rev. Lett.* **2007**, *98*, 233108.

(41) Casiraghi, C.; Pisana, S.; Novoselov, K. S.; Geim, A. K.; Ferrari, A. C. Raman fingerprint of charged impurities in graphene. *Appl. Phys. Lett.* **2007**, *91*, 032102.

(42) Stampfer, C.; Molitor, F.; Graf, D.; Ensslin, K.; Jungen, A.; Hierold, C.; Wirtz, L. Raman imaging of doping domains in graphene on SiO_2. *Appl. Phys. Lett.* **2007**, *91*, 241907.

(43) Das, A.; Pisana, S.; Chakraborty, B.; Piscanec, S.; Saha, S. K.; Waghmare, U. V.; Novoselov, K. S.; Krishnamurthy, H. R.; Geim, A. K.; Ferrari, A. C.; et al. Monitoring dopants by Raman scattering in an electrochemically top-gated graphene transistor. *Nat. Nanotech.* **2008**, *3*, 210.

(44) Tao, L.; Qiu, C.; Yu, F.; Yang, H.; Chen, M.; Wang, G.; Sun L. Modification on single-layer graphene induced by low-energy electron-beam irradiation. *J. Phys. Chem. C* **2013**, *117*, 10079.

(45) Gunho, J.; Minhyeok, C.; Chu-Young, C.; Jin, K. H.; Woojin, P.; Sangchul, L.; Woong-Ki, H.; Tae-Wook, K.; Seong-Ju, P.; Byung, H. H.; et al. Large-scale patterned multi-layer graphene films as transparent conducting electrodes for GaN light-emitting diodes. *Nanotechnology.* **2010**, *21*, 175201.

(46) Yang, X.; Tang, S.; Ding, G.; Xie, X.; Jiang, M.; Huang, F. Layer-by-layer thinning of graphene by plasma irradiation and post-annealing. *Nanotechnology.* **2012**, *23*, 025704.

(47) Liu, G.; Teweldebrhan, D.; Balandin, A. A. Tuning of graphene properties via controlled exposure to electron beams. *IEEE Trans. Nanotech.* **2011**, *10*, 865.

(48) Mitoma, N.; Nouchi, R.; Tanigaki, K. Photo-oxidation of graphene in the presence of water. *J. Phys. Chem. C* **2013**, *117*, 1453.

(49) Kalbac, M.; Lehtinen, O.; Krasheninnikov, A. V.; Keinonen, J. Ion-irradiation-induced defects in isotopically-labeled two layered graphene: Enhanced in-situ annealing of the damage. *Adv. Mater.* **2013**, *25*(7), 1004.

(50) Fox, D.; Zhou, Y. B.; O'Neill, A.; Kumar, S.; Wang, J. J.; Coleman, J. N.; Duesberg, G. S.; Donegan, J. F.; Zhang, H. Z. Helium ion microscopy of graphene: beam damage, image quality and edge contrast. *Nanotechnology.* **2013**, *24*, 335702.

(51) Hang, S.; Moktadir, Z.; Mizuta, H. Raman study of damage extent in graphene nanostructures carved by high energy helium ion beam. *Carbon* **2014**, *72*, 233.

(52) Tuinstra, F.; Koenig, J. L. Raman spectrum of graphite. *J. Chem. Phys.* **1970**, *53*, 1126.

(53) Cançado, L. G.; Takai, K.; Enoki, T.; Endo, M.; Kim, Y. A.; Mizusaki, H.; Jorio, A.; Coelho, L. N.; Magalhães-Paniago, R.; Pimenta, M. A. General equation for the determination of the crystallite size L_a of nanographite by Raman spectroscopy. *Appl. Phys. Lett.* **2006,** *88*, 163106.

(54) Martins Ferreira, E. H.; Moutinho, M. V. O.; Stavale, F.; Lucchese, M. M.; Capaz, R. B.; Achete, C. A.; Jorio, A. Evolution of the Raman spectra from single-, few-, and many-layer graphene with increasing disorder. *Phys. Rev. B.* **2010**, *82*, 125429.

(55) Guo, B.; Liu, Q.; Chen, E.; Zhu, H.; Fang, L.; Gong, J. R. Controllable N-doping of graphene. *Nano Lett.* **2010**, *10*, 4975.

(56) Ni, Z. H.; Yu, T.; Lu, Y. H.; Wang, Y. Y.; Feng, Y. P.; Shen, Z. X. Uniaxial strain on graphene: Raman spectroscopy study and band-gap opening. *ACS Nano*. **2008**, *2*(11), 2301.

Chapter IV. Influence of Low Energy Helium Ion Irradiation on Transport Properties of Graphene prepared by CVD method

4.1 Introduction

The electronic and magnetic properties of graphene are strongly related to the electron and hole concentrations and very sensitive to defects and charged impurities [1]. Due to the formation of defects and disorder, the electronic band structure, electron-phonon scattering, mean free path, carrier density will be changed [3-6]. Thus the modulation of defects and doping level in graphene is essential to the study of the transport properties of this attractive two-dimensional material. More important, the highly application potential for graphene based memory and logic devices also attracts much interest to modulate the electronic and magnetic properties of graphene by introducing defect, doping and strain engineering [2-17]. For example, the formation of structural defects may lead to the decrease of the charge carrier mobility and minimum conductivity of graphene by several orders of magnitude [2-14]. The shift of charge neutrality point as well as the mobility change can be induced by chemical doping such as H, N and O in graphene [14-19]. Quantum Hall effect in the hydrogenated graphene may disappear and can be partly restored by annealing [20]. Magnetism can be controlled in graphene by molecular doping [17], and tunable Kondo effect has been observed recently in graphene [11]. Moreover, the lattice distortion after irradiation may induce strain in graphene and influence the coupling with the substrate, which also leads to the change of the electronic properties in graphene [3] [6]. Graphene prepared by CVD method results in a small number of PMMA residues on the surface. Due to the formation of the bonds between PMMA unit and graphene, the mobility of graphene decreases and the neutrality point is shifted to high gate voltage [21-22]. The neutrality point at nearly zero gate voltage and the increase of the mobility has also been obtained in graphene with PMMA residues [23].

In this chapter, the modulation of electrical and magnetic properties of graphene is presented. The organization of chapter four was shown in Figure 4.1. First, the device structure used in the measurement was introduced. Then the electrical conductance, electronic hysteresis and magnetoresistance of irradiated graphene were measured and discussed. It can be seen that the electrical conductance shows a non-monotonic dependence on the dose density, which remains after annealing, indicating the doping also involves irreversible effect. The electronic hysteresis behaviors measurement results show the irradiation at larger dose density results in more obvious electronic hysteresis behavior. Moreover, the resistance hysteresis loops were measured under perpendicular and in-plane magnetic field, which suggests that the hysteresis behavior is enhanced at perpendicular magnetic field. In conclusion, the defects and doping in graphene result from

irradiation provide an efficient method to modulate the transport properties, which can be applied in graphene based memory and logic devices, transistors, and integrated circuits.

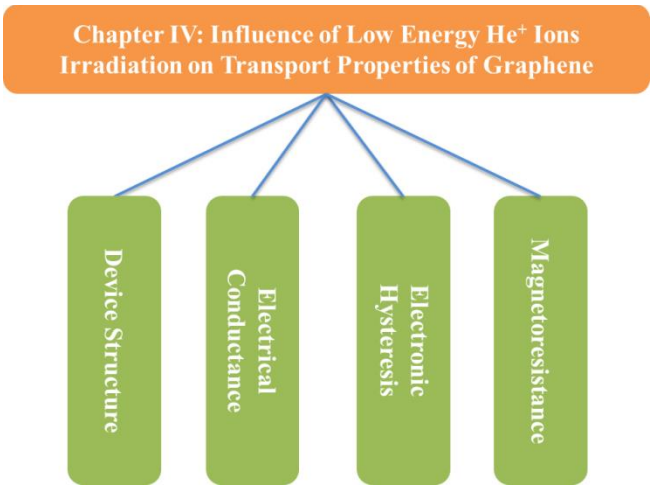

Figure 4.1 Organization of chapter IV.

4.2. Device Structure

The schematic of graphene device structure for measurements in our experiments is shown in Figure 4.2. The graphene sample was adhesive to the holder surface by double face adhesive tape. Two electrodes were prepared on graphene surface and the distance between them is 100 μm. Two rows of copper pads were located along the holder, one pad on the left (G4) was connected to one electrode on graphene via copper wire, and the other electrode was connected one pad (B2) on the right. Then the voltage and current can be applied on graphene through the two pads. The whole device was put into a larger sample carrier which connected to the transport measurements platform, as shown in chapter II.

4.3 Electrical Conductance

The electronic transport properties of graphene can be influenced strongly by the electron and hole concentrations [1]. To study the doping effect on the electronic properties, the electrical conductance was measured in the graphene samples irradiated with various dose densities and those annealed after irradiation. All the measurements were performed by Keithley 2400 at room temperature in ambient condition. And two-probe method was used during the measurements.

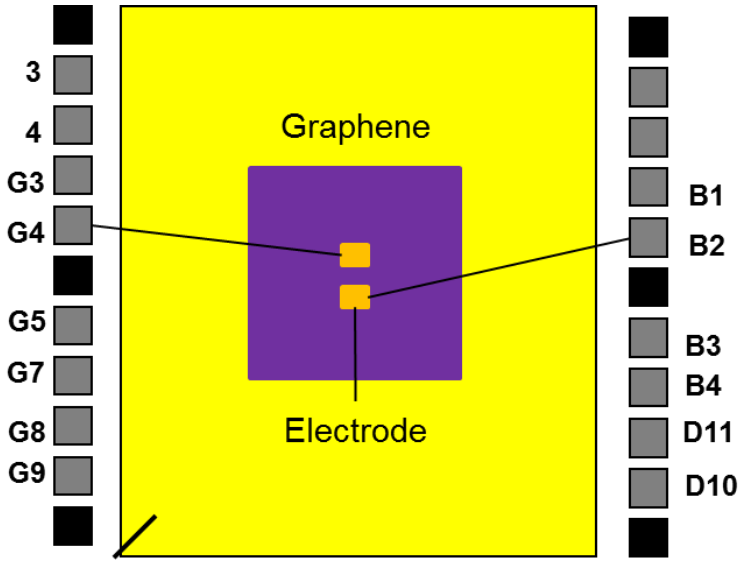

Figure 4.2 Schematic of graphene device structure for measurements.

As shown in Figure 4.3, the electrical conductance (G) of unirradiated graphene and irradiated graphene under a drain-source voltage of 0.1 V without gating were measured and a non-monotonic dependence on the dose density was observed. G at the dose density of 4.0×10^{12} He^+/cm^2 is 0.89 mS, one time larger than that of the unirradiated graphene which is 0.43 mS. While continue to increase the dose density, the conductance decreases gradually, and at the dose density of 1.2×10^{13} He^+/cm^2, G decreases to the minimum value of 0.13 mS, as small as 25% of that of the unirradiated graphene. For the dose density larger than 1.2×10^{13} He^+/cm^2, the conductance shows an increase behavior again, and at the dose density of 2.5×10^{13} He^+/cm^2, it increases to 0.4 mS. Note that similar non-monotonic dependence of the resistance on dose density is also shown in Ref. 13. After annealing, the conductance increases until the dose density irradiated on graphene increases to 4.0×10^{12} He^+/cm^2. With increase the dose density, the conductance decreases to 0.61 mS at the dose density of 1.2×10^{12} He^+/cm^2. While continue to increase the dose density to 2.1×10^{12} He^+/cm^2, the conductance remains on the same level 0.6 mS. It is interesting that the non-monotonic behavior remains after annealing. It is worth pointing out that there is the similarity between the non-monotonic behaviors in the electrical conductance and the shifts of the G and 2D bands (Figure 3.14). The electronic conductance in graphene is proportional to the carrier concentration and mobility which is related to the random electron-hole puddles [1].

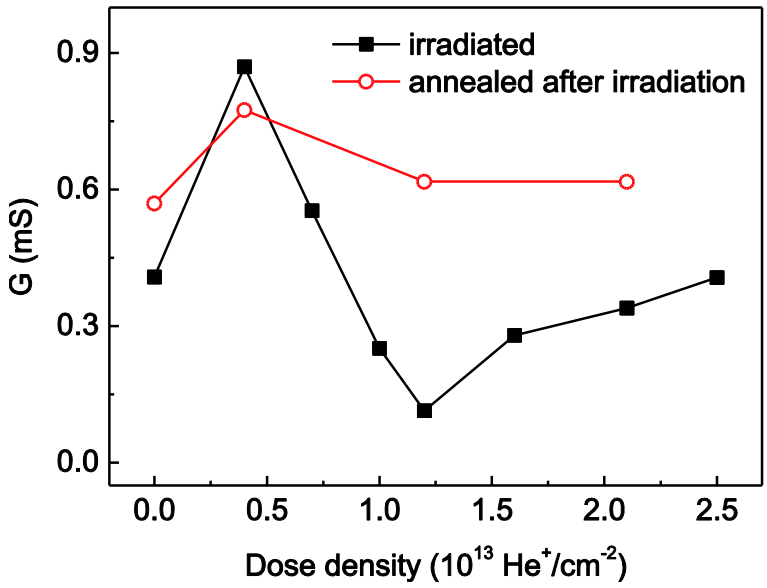

Figure 4.3 Dose density dependences of electrical conductance of irradiated graphene (solid squares) and those annealed after irradiation (open circles) under a drain-source voltage of 0.1 V without gating.

On one hand, doping changes the carrier concentration, the charge neutrality point and mobility [1]. The non-monotonic behavior in electrical conductance around zero gate voltage is related to the competitive effects of carrier concentration, mobility and defect scattering [1] [8] [14] [15] [43]. The He^+ ion irradiation cause the decomposition of PMMA residues and results in hole doping in graphene, which leads to the increase of conductance at the dose density of 4.0×10^{12} He^+/cm^2. By increasing the dose density to 1.2×10^{13} He^+/cm^2, the amount of defects and disorders formed in graphene increase, which lead to the decrease of mobility and enhanced defect scattering effect, this result in the decrease of the conductance of graphene. While continue to increase the dose density to 2.5×10^{13} He^+/cm^2, the hole doping in graphene becomes more prominent and results in the increase of conductance of graphene [1] [8] [14] [15] [43]. As shown in figure 3.14, the D peak increases significantly at the dose density of 2.1×10^{13} He^+/cm^2, this is related to more impurities such as O and H atoms were introduced in graphene through hole doping by irradiation. On the other hand, doping leads to the shifts in G and 2D bands due to electron-phonon coupling, this can be expressed in term of Fermi level shift [24]. Thus, the correlation between the electrical conductance and the shifts of the G and 2D bands demonstrates the modification of doping level and mobility by irradiation and annealing. These results indicate that the doping effect is partially reversible, which induces mark in graphene. More important,

this method shows efficient modification of the electrical conductance of graphene and can be applied in the graphene based memory and transistor.

4.4 Electronic Hysteresis

Hysteresis behaviour of graphene is a phenomenon that usually observed during electronic measurements [25-36]. Due to the charge trapping effect, capacitive charging effect, and interfacial redox reaction, the carrier density in graphene changes between the forward and backward sweeping direction, and the hysteresis behaviour is observed [25-37]. The charge trapping usually originates from the charge injection from graphene to the trapping sites at the graphene and substrate interface [26] [28]. The tunneling between the defects sites in graphene results from the fabrication processes and irradiation is also responsible for the hysteresis behaviour [31] [35]. Capacitive charging happens when nanoscale air gap appears between graphene and substrate, thus a capacitance is formed at the interface when external voltage applied [26] [28]. Moreover, the interfacial redox reaction comes from the interaction among O_2, H_2O and OH^- at the interface also contributes to the hysteresis phenomenon, it is usually induced by the adsorption of oxygen and water molecules on the graphene surface [29].

Here we investigated the electronic hysteresis behavior of unirradiated graphene and graphene irradiated at different dose densities, all the graphene devices were measured in at room temperature in ambient condition. The drain to source voltage (V_{ds}) was swept continuously from -5 V to 0 V, then to 5V and in the end back to -5 V, the sweeping step is 0.02 V and waiting time is 100 ms. As shown in Figure 4.4 (a), the conductance of unirradiated graphene decreases during the forward sweeping direction, from 0.496 mS at V_{ds} = -5V to the minimum 0.47 mS at V_{ds} = 1.9 V, increases to 0.479 mS when V_{ds} = 4.78 V. Then the G jumps to 0.48 mS at V_{ds} = 4.8 V and continues to increase to 0.482 mS when V_{ds} = 5 V. During the backward sweeping direction, the G shows a similar behavior compared to the forward sweeping direction, it decreases to about 0.48 mS at V_{ds} = -2.4 V and then increases to 0.5 mS when V_{ds} sweeps back to -5 V. For the graphene irradiated at the dose density of 1×10^{13} He^+/cm^2 and 1.6×10^{13} He^+/cm^2, the modification of conductance is not obvious between the forward and backward sweeping direction, which indicates the irradiation at low density does not result in a stronger electronic hysteresis. But it is worth pointing out that the conductance of graphene irradiated at the dose

density of 1 $\times 10^{13}$ He^{+}/cm^{2}, the G shows a nearly monotonic decrease and increase when the V_{ds} sweeps from -5 V to 5 V, and back from 5 V to -5 V respectively.

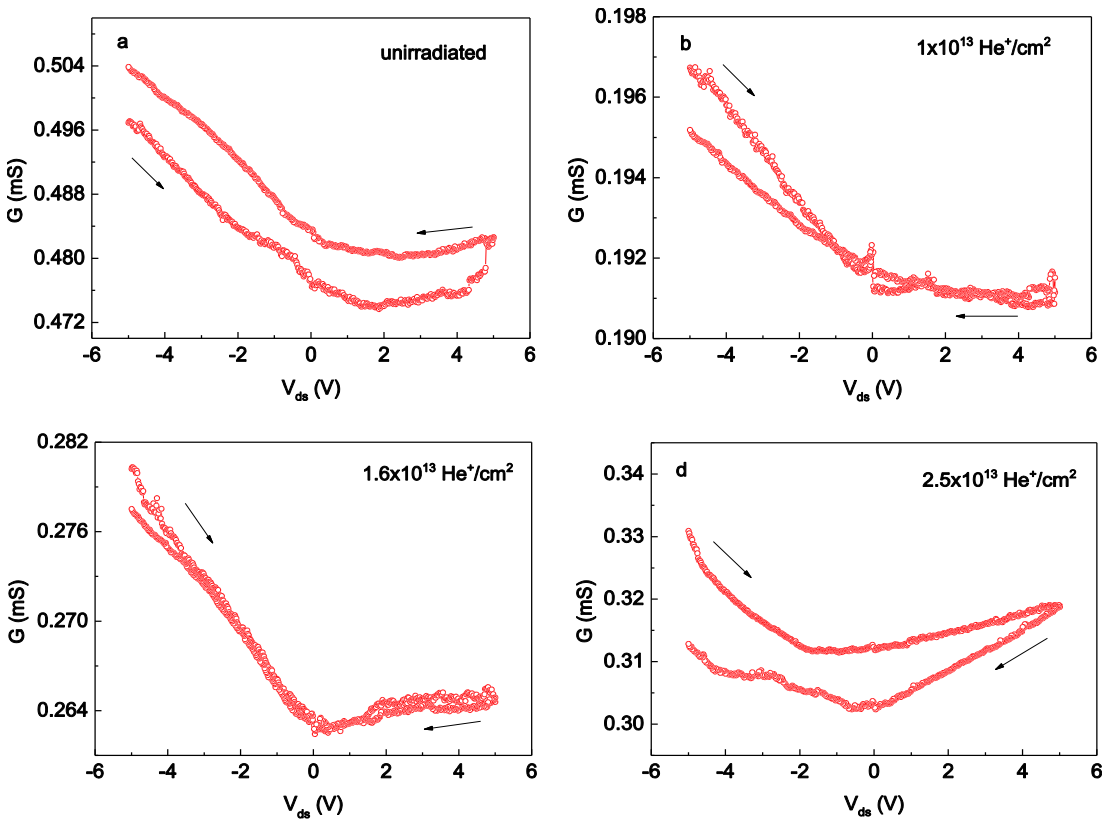

Figure 4.4 Conductance as a function of drain-source voltage (a) unirradiated graphene and graphene irradiated with different dose densities (b) 1 $\times 10^{13}$ He^{+}/cm^{2} (c) 1.6 $\times 10^{13}$ He^{+}/cm^{2} (d) 2.5 $\times 10^{13}$ He^{+}/cm^{2}.The forward and backward sweeping direction are indicated by the black arrows.

When the dose density for irradiation increases to 2.5 $\times$ 10^{13} He^{+}/cm^{2}, the electronic hysteresis behaviour of graphene becomes more significant. The conductance is 0.33 mS at V_{ds} = -5 V, it decreases to 0.31 mS at V_{ds}= -1.68 V, then increases to about 0.32 mS at V_{ds} = 5 V. During the backward sweeping direction, the G decreases to 0.3 mS at V_{ds} = -0.4 V, and in the end increases to about 0.31 mS at V_{ds} = -5 V. It can be concluded that the electronic hysteresis behavior weakened first and then increased, following the increasing of the dose density. For the unirradiated graphene, the charge trapping process occurring at the interface plays the most important role on the hysteresis behavior, while capacitive charging and interfacial redox reaction show much less contribution to this phenomenon than charge trapping [25-29] [37]. The tunneling can also happen due to the initial defects result from the fabricating process [35]. While

irradiate graphene at the dose density of 1×10^{13} He^+/cm^2 and 1.6×10^{13} He^+/cm^2, a small number of defects formed in graphene (Figure 3.13), and induce tunneling between the defects sites [31]. Meanwhile, the He^+ ion irradiation results in the decomposition of PMMA residues on graphene surface and induces chemical doping in graphene, which further increase the defects and impurity density, thus the tunneling effect becomes more pronounced [31]. The H and O atoms from PMMA residues can also contribute to the interfacial redox reaction. Under low dose irradiation, the major two mechanisms: tunneling effect and charge trapping compete with each other, resulting in weakened hysteresis behaviour. After increasing the dose density to 2.5×10^{13} He^+/cm^2, a large number of defects formed and more impurities doped in graphene, which makes the tunneling effect play a dominant role on the hysteresis behavior [31]. In this way, the influence of charge trapping is reduced, and more significant electronic hysteresis behaviour appears.

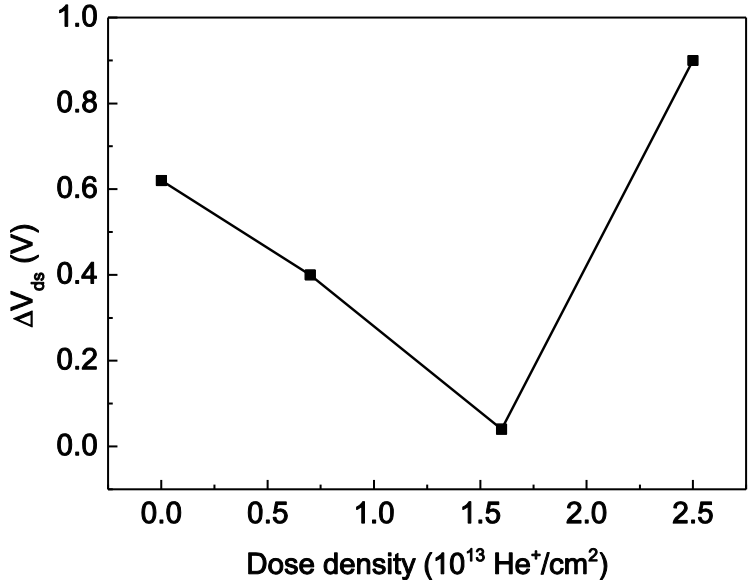

Figure 4.5 The dose density dependency on V_{ds} difference at minimum conductance of each sweeping direction for unirradiated graphene and graphene irradiated with various dose densities.

In order to further clarify the irradiation effect on electronic hysteresis behaviour of graphene, the drain to source voltage difference (ΔV_{ds}) at minimum conductance of each sweeping direction was plotted (Figure 4.5). It can be seen that as the behaviour of conductance, the ΔV_{ds} also shows a monotonic dependence on the dose density. The ΔV_{ds} decreases from 0.62 V for unirradiated graphene to 0.4 V at the dose density of 1×10^{13} He^+/cm^2 and 0.04 V at the

dose density of 1.6 $\times 10^{13}$ He^{+}/cm^{2}, then at the 2.5 $\times 10^{13}$ He^{+}/cm^{2}, the ΔV_{ds} increases to about 0.9 V. It is clearer to see that at low dose density, the hysteresis behaviour is weakened, and at higher dose density, the irradiation causes more defects or impurities in graphene and leads to a more significant hysteresis behaviour.

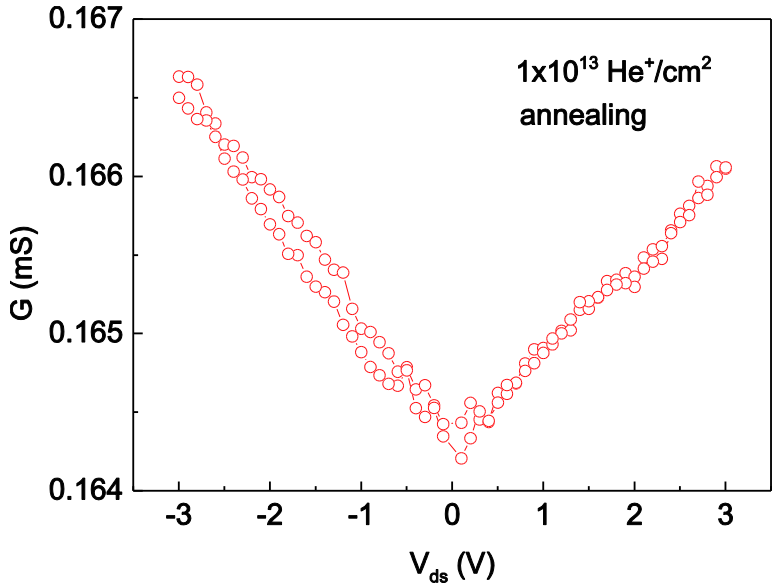

Figure 4.6 The conductance as a function of V_{ds} for the graphene annealed after irradiated at the dose density 1×10^{13} He^{+}/cm^{2}.

After annealing the graphene irradiated at the dose density of 1×10^{13} He^{+}/cm^{2} at 300℃ for 1h, suppressed electronic hysteresis behaviour of this graphene device was observed and the drain to source voltage difference at minimum conductance of each sweeping direction is nearly zero (see in Figure 4.6). This is related to the reduced doping level in graphene that originates from the decomposition of PMMA residues [26-27], meanwhile, annealing restore the crystal defects of graphene and reduces the charge traps on the SiO_2 substrate, thus suppressed electronic hysteresis behaviour in graphene was observed.

4.4.1 Sweeping Rate

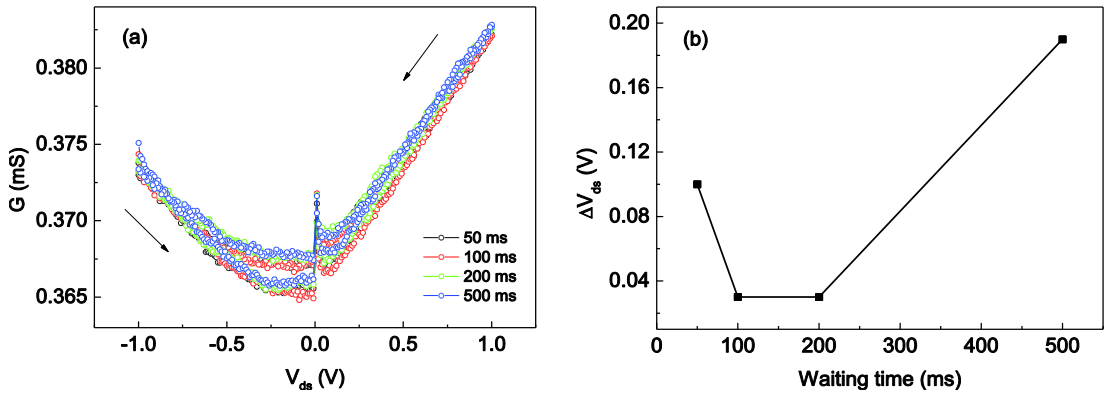

Figure 4.7 (a) The electronic hysteresis behaviour and (b) The V_{ds} difference at minimum conductance of each sweeping direction for the unirradiated graphene device under four different waiting time.

For the unirradiared graphene device, the electronic hysteresis behaviour under different voltage pulse waiting times were also measured, as shown in Figure 4.7 (a). The V_{ds} sweeps from -1 V to 1 V then back to 1 V, sweeping step is 0.01V. The waiting time between two impulse voltage increases from 50 ms to 100 ms, 200 ms and in then end to 500 ms, and the sweeping rate can be controlled. In Figure 4.6 (b), the V_{ds} difference at minimum conductance of each sweeping direction as a function of these four waiting time was plotted. It can be seen that similar to the V_{ds} difference dependence on dose density, the electronic hysteresis behavior also follows a trajectory of weakened and then enhanced with the waiting time increasing. Due to the small sweeping range -1 V to 1 V, the hysteresis behavior is not as obvious as the large sweeping range -5 V to 5 V. While at fast sweeping rate (short waiting time), the electronic hysteresis behavior is related to the charge trapping and tunneling effect. And due to the small number of defects in unirradiated graphene, charge trapping plays a more important role. While at lower sweeping rate (longer waiting time), the interfacial redox reaction becomes more significant [28-29] [35]. In this case, we suggest that when the waiting time is 50 ms, charge trapping and tunneling effect result in the hysteresis behavior with ΔV_{ds} of 0.1V, while increase the waiting time to 100 ms and 200 ms, the interfacial redox reaction compete with the charge trapping effect, and lead to a weaker hysteresis behavior, by continuing to increase the waiting time to 500 ms, the interfacial redox reaction shows more influence than the charge trapping and a more pronounced electronic hysteresis behavior appears.

4.4.2 The influence of Magnetic field

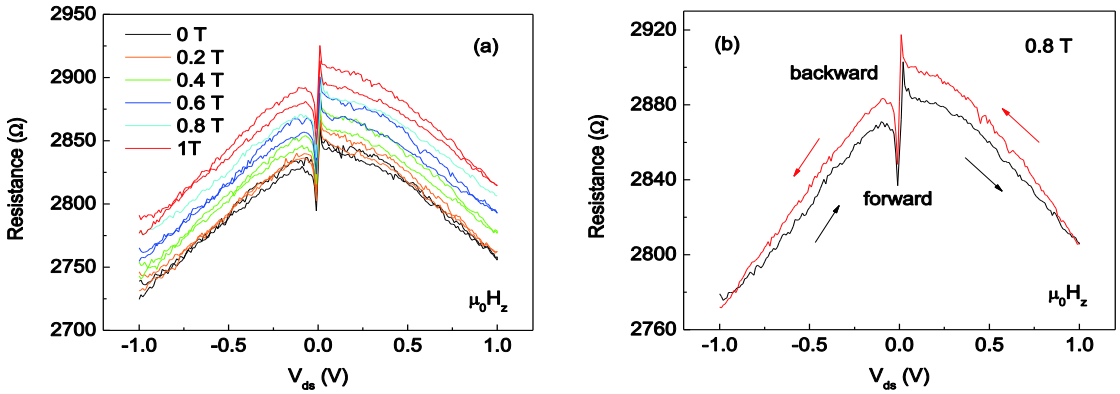

Figure 4.8 (a) The resistance hysteresis behavior of unirradiated graphene as a function of V_{ds} under different perpendicular magnetic fields (b) The detail of hysteresis behavior process of unirradiated graphene measured under 0.8 T perpendicular magnetic field.

Magnetism induced by defects in graphene has also attracted much attention [38-41]. The vacancies and adatoms are thought to carry magnetic-moment, which result in magnetism in graphene [39-41]. Here, in order to investigate the effect of external magnetic field on the defects or impurities in graphene, the electronic hysteresis of unirradiated graphene under different magnetic field was measured, as shown in Figure 4.8 (a). The V_{ds} sweeps from -1 V to 1 V and then back to -1 V, sweeping step is 0.01 V, external perpendicular magnetic field ($\mu_0 H_z$) of 0.2 T, 0.4 T, 0.6 T, 0.8 T and 1 T were applied on the unirradiated graphene device. It can be seen that the resistance of unirradiated graphene increases with the $\mu_0 H_z$, for example, at V_{ds} = -0.08 V, the resistance increases from 2827.3 Ω under zero $\mu_0 H_z$ to 2879.8 Ω while the external applying H_z = 1 T. The hysteresis behavior also becomes more obvious after applying the perpendicular magnetic field. In Figure 4.7b, the unirradiated graphene measured under 0.8 T perpendicular magnetic field shows the detail of the electronic hysteresis behaviour, the resistance increases from V_{ds}= -1 V and reaches the peak when V_{ds}= 0.02 V, then decreases until the V_{ds}= 1 V. The backward process is the reverse of the forward process, and the resistance of the forward branch is lower than the backward branch. The unirradiated graphene samples measured under other perpendicular magnetic fields present the same hysteretic process. The difference of maximum resistance (ΔR_{max}) in forward and backward V_{ds} sweeping direction in -1 V-0 V range as a function of $\mu_0 H_z$ was also plotted to get a better understand of this phenomenon. From Figure 4.9, it can be seen that the ΔR_{max} shows an increase tendency with the perpendicular magnetic field,

the ΔR_{max} at $\mu_0 H_z$ = 0 T is about 7 Ω, while at the $\mu_0 H_z$ = 0.2 T, 0.4 T, 0.6 T, 0.8 T and 1 T, the ΔR_{max} are 3.5 Ω, 7.8 Ω, 11.5 Ω, 12.5 Ω, and 11.4 Ω respectively, although there is an decrease at the $\mu_0 H_z$ = 0.2 T, but the overall trend of ΔR_{max} still has an increase relationship with the external perpendicular magnetic field. The electronic hysteresis behaviors measured under $\mu_0 H_z$ = 0.1 T, 0.3 T, 0.5 T, 0.7 T and 0.9 T respectively also follow this trend, and the maximum ΔR_{max} of 28.9 Ω was obtained when $\mu_0 H_z$ = 0.9 T. This may due to change of the motion direction of electrons or holes in graphene, which originates from the Lorenz force while an external perpendicular magnetic field is applied on the device, and results in the more obvious resistance hysteresis behavior in unirradiated graphene.

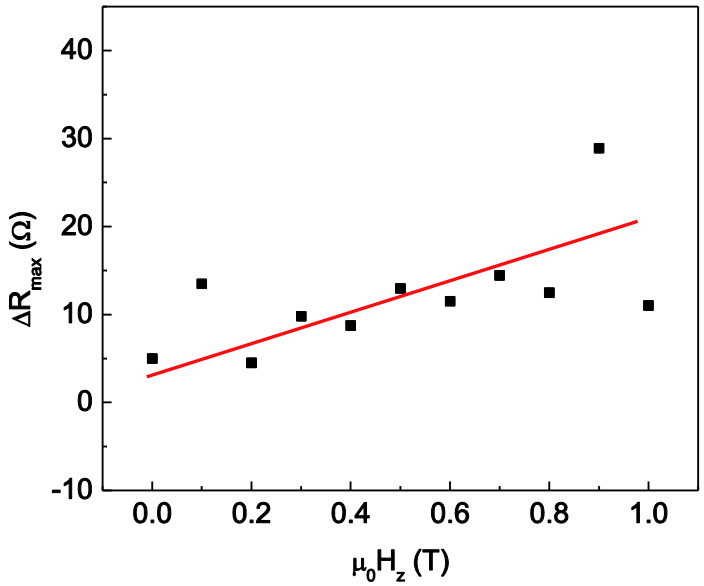

Figure 4.9 The difference of maximum resistance of forward and backward V_{ds} sweeping direction in -1 V-0 V range as a function of various perpendicular magnetic fields.

Furthermore, we also measured the V_{ds} dependence on resistance of unirradiated graphene under different in-plane magnetic field ($\mu_0 H_x$), as show in Figure 4.10 (a). Compare to the V_{ds} dependence on resistance measured under perpendicular magnetic field, the hysteresis behavior seems to become weaker, and the drift of resistance was not observed, all the five hysteresis loops locate in the same range, from 2730 Ω to 2852 Ω. In addition, the V_{ds} dependence on resistance under the same perpendicular magnetic field and in-plane magnetic field of 0.4 T was plotted, see in Figure 4.10 (b). It is clear to see that the hysteresis behavior becomes weaker when applying an in-plane magnetic field, the resistance loop have a ΔR_{max} of 8.7 Ω under perpendicular magnetic field, which is larger than that of under in-plane magnetic field, 5.4 Ω.

This may due to the same direction of in-plane magnetic field and the motion of the carrier, thus the Lorenz force is zero and has no influence on the carrier, and then leads to a weaker electronic hysteresis behavior.

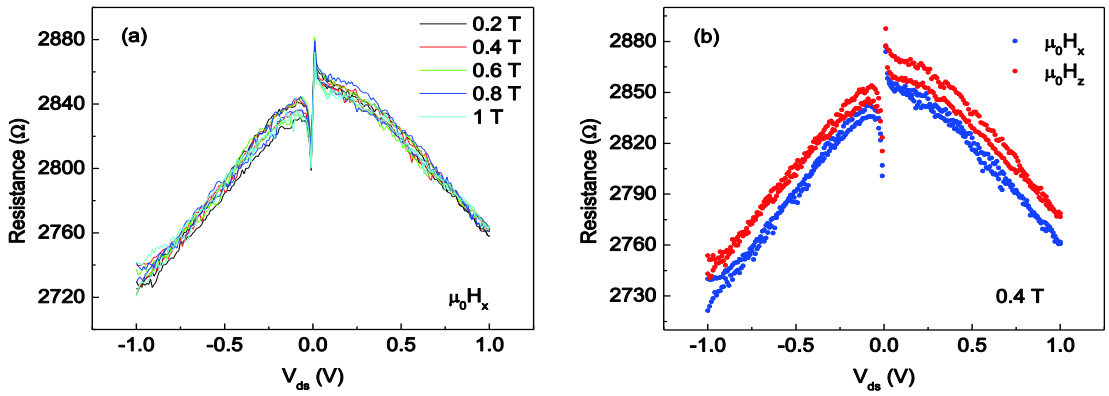

Figure 4.10 The resistance of unirradiated graphene as a function of V_{ds} (a) under different in-plane magnetic field and (b) under 0.4T perpendicular magnetic field (red curve) and in-plane magnetic field (blue curve) respectively.

The V_{ds} dependences on resistance of graphene irradiated at the dose density of 2×10^{13} He^+/cm^2 under different perpendicular magnetic fields were also measured, see in Figure 4.11. Three perpendicular magnetic fields 0.5 T, 1 T and -1 T were applied on the irradiated graphene device respectively. The V_{ds} sweeps from -20 V to 20 V then back to -20 V, and the sweeping step is 0.1 V. It can be seen that after irradiation, the hysteresis behaviors do not show significant change under $\mu_0 H_z$ = 0.5 T, 1 T and -1 T. But shape of the hysteresis loop is different from that of unirradiated graphene. The resistance follows a monotonic decrease with the V_{ds} sweeps from -20 V to 20 V, and then shows monotonic increase while the sweeps from 20 V back to -20 V. Due to this reason, we use the resistance difference of forward and backward sweeping direction near the zero V_{ds} to present the enhancement and weakening of the hysteresis loop. From Figure 4.12, one can see that the resistance difference has a minimum value of about 11 Ω at the $\mu_0 H_z$ = 0T. While at the $\mu_0 H_z$ = 0.5 T and 1 T, it increases to about 13 Ω, and at the $\mu_0 H_z$ = -1 T, the ΔR is about 12 Ω. This result confirms that the hysteresis behavior of irradiated graphene does not show obvious improvement after applying external perpendicular magnetic field. After performing irradiation on graphene, the C, H and O atoms come from decomposition of PMMA residues will interact with the C atoms in graphene, and then more defects and impurities will be formed in graphene, thus the tunneling effect becomes more important [31].

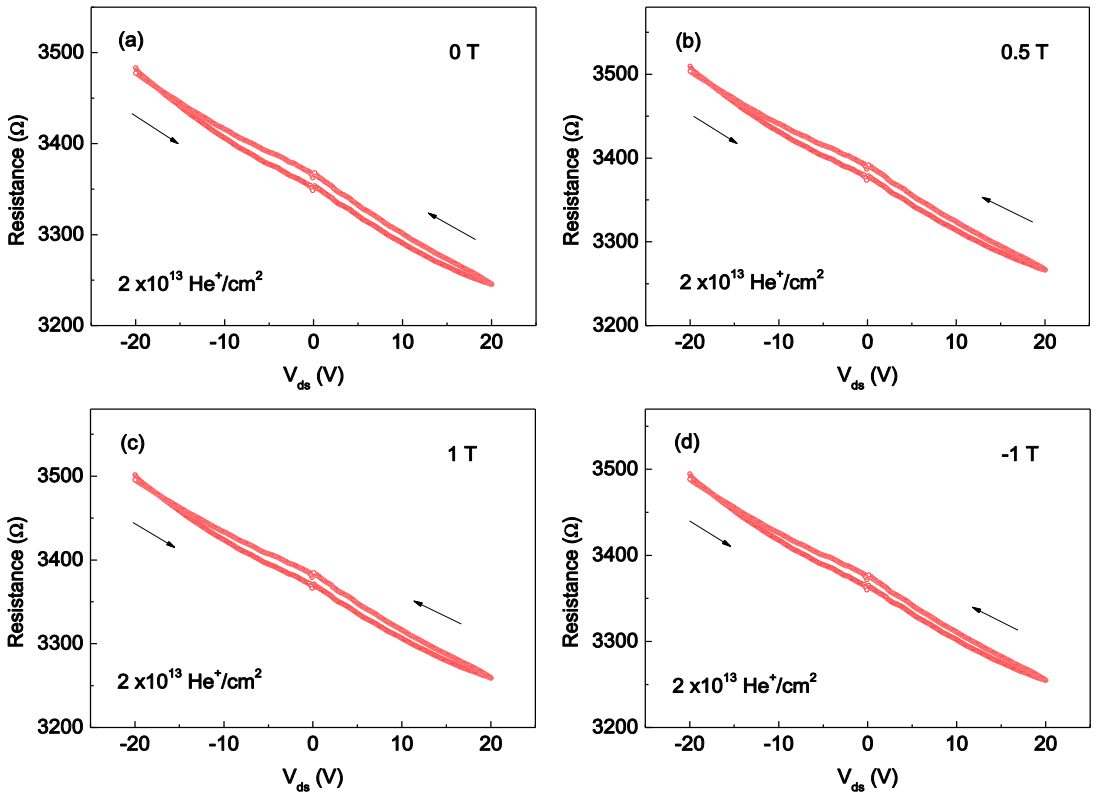

Figure 4.11 The hysteresis behaviour of graphene irradiated at the dose density of 2×10^{13} He^+/cm^2 as a function of V_{ds} under different perpendicular magnetic fields (a) 0 T (b) 0.5 T (c) 1T (d) -1 T.

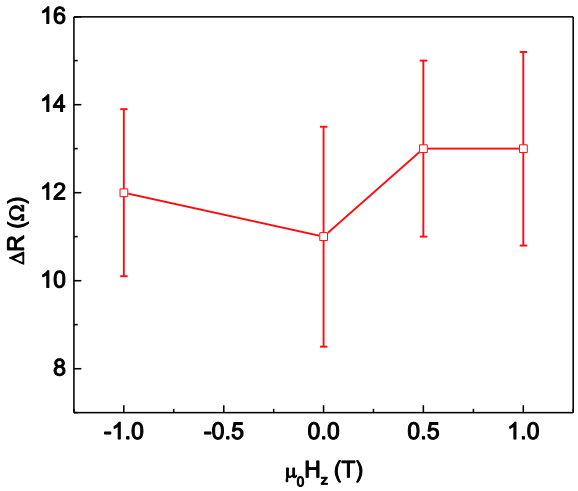

Figure 4.12 The resistance difference at V_{ds} of -0.4 V as a function of different perpendicular magnetic fields.

Although the external perpendicular magnetic field exerts Lorenz force on the carriers in graphene and changes the motion direction, while due to the large number of defects and

impurities, the influence of magnetic field is weakened and leads to electronic hysteresis behavior that does not show obvious changes when applying the perpendicular magnetic field.

4.5 Magnetoresistance

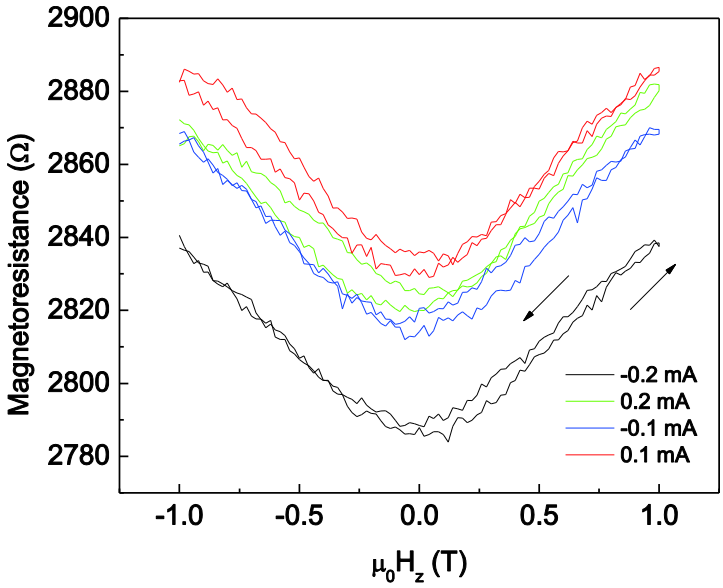

Figure 4.13 The magnetoresistance of unirradiated graphene as a function of perpendicular magnetic field under different drain to source current (I_{ds}).

Some works have reported that giant MR of ~ 400 % and 275 % was observed at 1.9 K and room temperature in single layer graphene with an applied field of 9 T, which is useful in practical application [42]. Here, the magnetoresistance (MR) of unirradiated graphene was investigated, and the measurements were manipulated at room temperature in ambient condition. Figure 4.13 shows the resistance of unirradiated graphene as a function of perpendicular magnetic field (H_z) under different drain to source current (I_{ds}), the magnetic field sweeps from -1 T to 1 T and back to -1 T, and the sweeping step is 0.02 T. It can be seen that the resistance shows an almost symmetric hysteresis loop by applying a perpendicular magnetic field, such as under the I_{ds} of -0.1 mA, the resistance decreases while the H_z sweeps from -1 T and reaches the minimum value of 2811.9 Ω at H_z= -0.06 T, then the resistance increases to 2838.5 Ω when the H_z sweeps to 1 T. The backward sweeping process shows the reverse dependence on the magnetic field, and the minimum resistance is 2788.1 Ω at H_z = 0.02 T.

To further understand the influence of I_{ds} on the resistance of unirradiated graphene, ratio of resistance difference (ΔR) (R_1 (H=1 T) - R_0 (H=0 T)) and R_0 (H=0 T) was plotted, as shown in

Figure 4.14. It is interesting to see that in the forward magnetic field sweeping direction, the $\Delta R/R_0$ ratio shows non-monotonic increasing dependence behavior on the I_{ds}, which may be related to the inhomogeneous charge distribution results from impurities [42]. For the forward magnetic field sweeping direction, the $\Delta R/R_0$ ratio is about 1.81 at I_{ds} = -0.2 mA, then it increases to about 1.96 at I_{ds} = -0.1 mA. While the $\Delta R/R_0$ ratio decreases to 1.85 at I_{ds} = -0.05 mA and 0.05 mA. In the end the $\Delta R/R_0$ ratio increases to 2 and 2.19 at I_{ds} = 0.1 mA and 0.2 mA. Overall, the $\Delta R/R_0$ ratios resulting from different I_{ds} are not very obvious, which suggest that the weak influence of perpendicular magnetic field ranges from -1 T to 1 T and modification of carrier density in graphene by applying various I_{ds} at the order of milliampere. This may be related to low inhomogeneous charge distribution in unirradiated graphene [42].

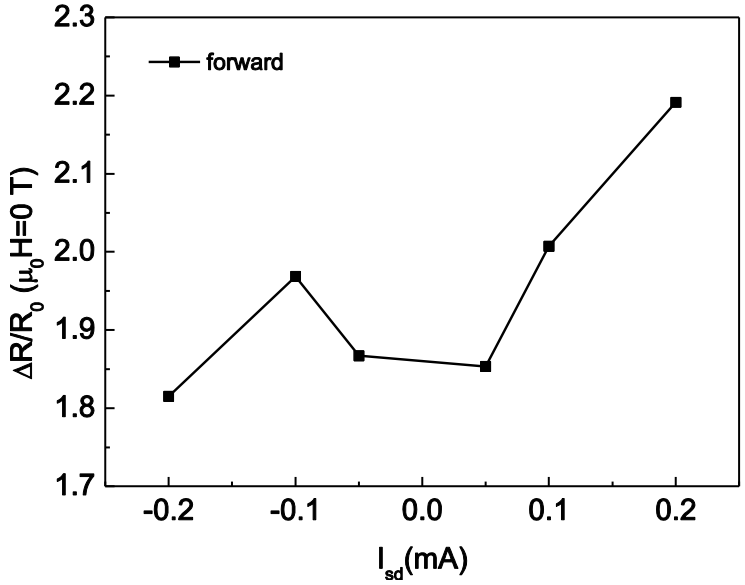

Figure 4.14 The ratio of ΔR and R_0 of unirradiated graphene measured under different I_{ds} during forward magnetic field sweeping direction.

4.6 Conclusion

In this chapter, ion irradiation and vacuum annealing were used to tune the local electron and hole concentrations in graphene, which leads to the modification of electronic and magnetic properties of graphene. The electrical conductance of graphene shows a similar non-monotonic dependence on the dose density as the Raman band shift, and the trend remains after annealing, which indicates the doping also involves irreversible effect. The electronic hysteresis behavior becomes more obvious when the graphene irradiated at larger dose density, which suggests the competitive influence of charge trapping and tunneling effect. The resistance hysteresis loops were also measured under perpendicular and in-plane magnetic field, which shows the higher perpendicular magnetic field can enhance the hysteresis behavior. These works provide us a better understand of the modulation of electrical and magnetic properties of graphene, which can be applied in graphene based memory and logic devices, transistors and integrated circuits.

References

(1) Sarma, S. D.; Adam, S.; Hwang, E. H.; Rossi, E. Electronic transport in two-dimensional graphene. *Rev. Mod. Phys.* **2011**, *83*, 407.

(2) Tapasztó, L.; Dobrik, G.; Nemes-Incze, P.; Vertesy, G.; Lambin, Ph.; Biró, L. P. Tuning the electronic structure of graphene by ion irradiation. *Phys. Rev. B.* **2008**, *78*, 233407.

(3) Compagnini, G.; Giannazzo, F.; Sonde, S.; Raineri, V.; Rimini, E. Ion irradiation and defect formation in single layer graphene. *Carbon.* **2009**, *47*, 3201.

(4) Lucchese, M. M.; Stavale, F.; Ferreira, E. H.; Vilani, C.; Moutinho, M. V. O.; Capaz, R. B.; Achete, C. A.; Jorio, A. Quantifying ion-induced defects and Raman relaxation length in graphene. *Carbon.* **2010**, *48*, 1592.

(5) Teweldebrhan, D.; Balandin, A. A. Modification of graphene properties due to electron-beam irradiation. *Appl. Phys. Lett.* **2009,** *94*, 013101.

(6) Fu, X. W.; Liao, Z. M.; Zhou, J. X.; Zhou, Y. B.; Wu, H. C.; Zhang, R.; Yu, D. Strain dependent resistance in chemical vapor deposition grown graphene. *Appl. Phys. Lett.* **2011**, *99*(21), 213107.

(7) Krauss, B.; Lohmann, T.; Chae, D.-H.; Haluska, M.; von Klitzing, K.; Smet, J. H. Laser-induced disassembly of a graphene single crystal into a nanocrystalline network. *Phys. Rev. B.* **2009**, *79*, 165428.

(8) Chen, J. H.; Cullen, W. G.; Jang, C.; Fuhrer, M. S.; Williams, E. D. Defect scattering in graphene. *Phys. Rev. Lett.* **2009**, *102*, 680501.

(9) Kim, D. C.; Jeon, D.-Y.; Chung, H.-J.; Woo, Y. S.; Shin, J. K.; Seo, S. The structural and electrical evolution of graphene by oxygen plasma-induced disorder. *Nanotechnology*. **2009**, *20*, 375703.

(10) Zhou, Y. B.; Liao, Z. M.; Wang, Y. F.; Duesberg, G. S.; Xu, J.; Fu, Q.; Wu, X. S.; Yu, D. P. Ion irradiation induced structural and electrical transition in graphene. *J. Chem. Phys.* **2010**, *133*, 234703.

(11) Chen, J. H.; Li, L.; Cullen, W. G.; Williams, E. D.; Fuhrer, S. M. Tunable Kondo effect in graphene with defects. *Nat. Phys.* **2011**, *7*, 535.

(12) Buchowicz, G.; Stone, P. R.; Robinson, J. T.; Cress, C. D.; Beeman, J. W.; Dubon, O. D. Correlation between structure and electrical transport in ion-irradiated graphene grown on Cu foils. *Appl. Phys. Lett.* **2011**, *98*, 032102.

(13) Liu, G.; Teweldebrhan, D.; Balandin, A. A. Tuning of graphene properties via controlled exposure to electron beams. *IEEE Trans. Nanotech.* **2011**, *10*, 865.

(14) Nakaharai, S.; Iijima, T.; Ogawa, S.; Suzuki, S.; Li, S.-L.; Tsukagoshi, K.; Sato, S.; Yokoyama, N. Conduction tuning of graphene based on defect-induced localization. *ACS Nano.* **2013**, *7*, 5694.

(15) Guo, B.; Liu, Q.; Chen, E.; Zhu, H.; Fang, L.; Gong, J. R. Controllable N-doping of graphene. *Nano Lett.* **2010**, *10*, 4975.

(16) Mitoma, N.; Nouchi, R.; Tanigaki, K. Photo-oxidation of graphene in the presence of water. *J. Phys. Chem. C* **2013**, *117*, 1453.

(17) Nair, R. R.; Tsai, I. L.; Sepioni, M.; Lehtinen, O.; Keinonen, J.; Krasheninnikov, A. V.; Castro Neto, A. H.; Geim, A. K.; Grigorieva, I. V. Dual origin of defect magnetism in graphene and its reversible switching by molecular doping. *Nat. Commun.* **2013**, *4*, 2010.

(18) Schedin, F.; Geim, A. K.; Morozov, S. V.; Hill, E.W.; Blake, P.; Katsnelson, M. I.; Novoselov, K. S. Detection of individual gas molecules adsorbed on graphene. *Nat. Mater.* **2007**, *6*, 652–655.

(19) Ryu, S.; Liu, L.; Berciaud, S.; Yu, Y. J.; Liu, H.; Kim, P.; Flynn, G. W.; Brus, L. E. Atmospheric oxygen binding and hole doping in deformed graphene on a SiO_2 substrate. *Nano Lett.* **2010**, *10*, 4944.

(20) Elias, D. C. Nair, R. R.; Mohiuddin, T. M. G.; Morozov, S. V.; Blake, P.; Halsall, M. P.; Ferrari, A. C.; Boukhvalov, D. W.; Katsnelson, M. I.; Geim, A. K.; et al. Control of graphene's properties by reversible hydrogenation: Evidence for graphane. *Science.* **2009**, *323*, 610.

(21) Pirkle, A.; Chan, J.; Venugopa, A.; Hinojos, D.; Magnuson, C. W.; McDonnell, S.; Colombo, L.; Vogel, E. M.; Ruoff, R. S.; Wallace, R. M. The effect of chemical residues on the physical and electrical properties of chemical vapor deposited graphene transferred to SiO_2. *Appl. Phys. Lett.* **2011**, *99*, 122108.

(22) Peltekis, N.; Kumar, S.; McEvoy, N.; Lee, K.; Weidlich, A.; Duesberg, G. S. The effect of downstream plasma treatments on graphene surfaces. *Carbon.* **2012**, *50*, 395.

(23) Suk, J. W.; Lee, W. H.; Lee, J.; Chou, H.; Piner, R. D.; Hao, Y. Enhancement of the electrical properties of graphene grown by chemical vapor deposition via controlling the effects of polymer residue. *Nano Lett*. **2013**, *13*, 1462.

(24) Ferrari, A. C. Raman spectroscopy of graphene and graphite: disorder, electron–phonon coupling, doping and nonadiabatic effects. *Solid State Commun.* **2007**, *143*, 47.

(25) Sabri, S. S.; Levesque, P. L.; Aguirre, C. M.; Guillemette, J.; Martel, R.; Szkopek, T. Graphene field effect transistors with parylene gate dielectric. *Appl. Phys. Lett. 95*(24), **2009**, 242104.

(26) Wang, H.; Wu, Y.; Cong, C.; Shang, J.; Yu, T. Hysteresis of electronic transport in graphene transistors. *ACS nano*, **2010**, *4*(12), 7221.

(27) Joshi, P.; Romero, H. E.; Neal, A. T.; Toutam, V. K.; Tadigadapa, S. A. Intrinsic doping and gate hysteresis in graphene field effect devices fabricated on SiO2 substrates. *J. Phys. Condens. Matter.* **2010**, *22*(33), 334214.

(28) Lee, Y. G.; Kang, C. G.; Jung, U. J.; Kim, J. J.; Hwang, H. J.; Chung, H. J.; Lee, B. H. Fast transient charging at the graphene/SiO_2 interface causing hysteretic device characteristics. *Appl. Phys. Lett.* **2011**, *98*(18), 183508.

(29) Lee, Y. G.; Kang, C. G.; Cho, C.; Kim, Y.; Hwang, H. J.; Lee, B. H. Quantitative analysis of hysteretic reactions at the interface of graphene and SiO_2 using the short pulse I–V method. *Carbon*, **2013**, *60*, 453.

(30) Sundararajan, A.; Boland, M. J.; Hunley, D. P.; Strachan, D. R. Doping and hysteretic switching of polymer-encapsulated graphene field effect devices. *Appl. Phys. Lett.* **2013**, *103*(25), 253505.

(31) Wang, Q.; Liu, S.; Ren, N. Manipulation of transport hysteresis on graphene field effect transistors with Ga ion irradiation. *Appl. Phys. Lett.* **2014**, *105*(13), 133506.

(32) Shin, Y. J.; Kwon, J. H.; Kalon, G.; Lam, K. T.; Bhatia, C. S.; Liang, G.; Yang, H. Ambipolar bistable switching effect of graphene. *Appl. Phys. Lett.* **2010**, *97*(26), 262105.

(33) Liao, Z. M.; Han, B. H.; Zhou, Y. B.; Yu, D. P. Hysteresis reversion in graphene field-effect transistors. *J. Chem. Phys.* **2010**, *133*(4), 044703.

(34) Wessely, P. J.; Schwalke, U. Insitu CCVD grown bilayer graphene transistors for applications in nanoelectronics. *Appl. Surf. Sci.* **2014**, *291*, 83.

(35) Cho, C.; Lee, Y. G.; Jung, U.; Kang, C. G.; Lim, S.; Hwang, H. J.; Lee, B. H. Correlation between the hysteresis and the initial defect density of graphene. *Appl. Phys. Lett.* **2013**, *103*(8), 083110.

(36) Xu, H.; Chen, Y.; Zhang, J.; Zhang, H. Investigating the mechanism of hysteresis effect in graphene electrical field device fabricated on SiO2 substrates using Raman spectroscopy. *Small.* **2012**, *8*(18), 2833.

(37) Kalon, G.; Shin, Y. J.; Truong, V. G.; Kalitsov, A.; Yang, H. The role of charge traps in inducing hysteresis: Capacitance–voltage measurements on top gated bilayer graphene. *Appl. Phys. Lett.* **2011**, *99*(8), 083109.

(38) Wang, Y.; Huang, Y.; Song, Y.; Zhang, X.; Ma, Y.; Liang, J.; Chen, Y. Room-temperature ferromagnetism of graphene. *Nano Lett.* **2008**, *9*(1), 220.

(39) Yazyev, O. V.; Helm, L. Defect-induced magnetism in graphene. *Phys. Rev. B.* **2007**, *75*(12), 125408.

(40) Nair, R. R.; Sepioni, M; Tsai, I. L.; Lehtinen, O.; Keinonen, J.; Krasheninnikov, A. V.; Grigorieva, I. V. Spin-half paramagnetism in graphene induced by point defects. *Nat. Phys. 8*(3), **2012**, 199.

(41) Nair, R. R.; Tsai, I. L.; Sepioni, M.; Lehtinen, O.; Keinonen, J.; Krasheninnikov, A. V.; Grigorieva, I. V. Dual origin of defect magnetism in graphene and its reversible switching by molecular doping. *Nat. Commun.* **2013**, *4*.

(42) Gopinadhan, K.; Shin, Y. J.; Yudhistira, I.; Niu, J.; Yang, H. Giant magnetoresistance in single-layer graphene flakes with a gate-voltage-tunable weak antilocalization. *Phys. Rev. B*. **2013**, *88*(19), 195429.

(43) Wang, X.; Li, X.; Zhang, L.; Yoon, Y.; Weber, P. K.; Wang, H.; Guo, J.; Dai, H. N-doping of graphene through electrothermal reactions with ammonia. *Science.* **2009**, *324*, 768.

Chapter V. Influence of Electron Beam Irradiation on Structural and Transport Properties of Graphene grown on SiC Substrate

5.1 Introduction

The epitaxial graphene obtained from sublimation of SiC substrate has been studied for many years [1-2]. Usually, 4H-SiC (0001) is used during the preparation due to the similar crystal structure to graphene, which guarantees the high quality of epitaxial graphene sample [1-3]. As the different growth mechanism between sublimation and CVD method, there are no PMMA residues remained on graphene surface prepared by sublimation of SiC substrate [1-2]. In this case, the modulations of structural and electronic properties of graphene are always accomplished by introducing external adsorptions, molecular doping and irradiation [4-10] [12-19]. Oxygen adsorption shows that the oxygen atoms interact with the free Si bonds and break some Si-C bonds at the interface, resulting in partially decoupled buffer layer and oxygen intercalation [4]. The strong electron acceptor tetrafluorotetracyanoquinodimethane (F4-TCNQ) deposited on graphene surface leads to charge neutrality in monolayer graphene, and the hole doping in bilayer graphene allows the Fermi level shifts into energy bandgap and increase its magnitude [6]. By performing Ar ions irradiation on graphene, the reduction of charge transfer doping from the SiC substrate to graphene has been achieved [12].

Compared to the methods mentioned above, electron beam irradiation is a cleaner method which can be used to modify the structural and electronic properties of graphene. The adsorption, molecular doping and ion irradiation will inevitably introduce external elements in graphene, which lead to more complicated situation of the graphene structure [4-10]. While the electron beam irradiation on the graphene surface only results in the formation of crystal defects or disorders in graphene, and changes the strain between graphene and SiC substrate [11]. It is a method that will not directly introduce chemical doping in graphene. But as mentioned in chapter II, the small size and light mass of electron can not result in the equal effect on graphene structure as ion irradiation at the same order of the dose level, which indicates higher electron beam energy or longer exposure time is needed to efficiently modify the properties of graphene [11].

In this chapter, electron beam irradiation was used to modulate the structural and electronic properties of graphene grown on SiC substrate. The organization of chapter five was shown in Figure 5.1. First, the experimental detail of electron beam irradiation was introduced. Then X-ray photoelectron spectroscopy and Raman spectroscopy were used to characterize the structural modification of irradiated graphene samples. The tuning of transport properties of

graphene by irradiation was also investigated. In the end, the irradiation influence on structural and transport properties of graphene grown on SiO_2 substrate prepared by CVD method and graphene grown on SiC substrate were compared. The XPS results show the crystal structure of graphene was broken after high dose irradiation. The frequencies of G and 2D peaks show red-shifts with increasing the dose density. And the electrical conductance measured shows a non-monotonic dependence on the dose density. The relationship between structural and transport properties of graphene are demonstrated and paves the way for future application in graphene based memory and transistor.

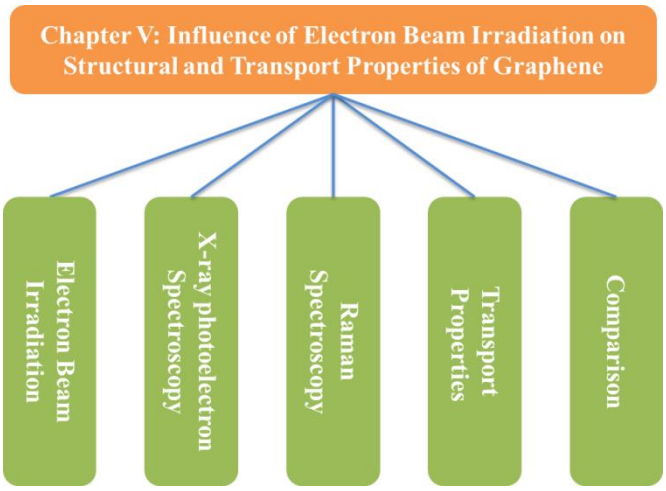

Figure 5.1 Organization of chapter V.

5.2 Electron Beam Irradiation

Schematic of e-beam irradiation in epitaxial graphene grown on SiC substrate is shown in Figure 5.2. The graphene was grown on the Si terminated 4H-SiC substrate, and the bottom and right border length of the SiC substrate are 10.37 mm and 7.68 mm respectively. After the sublimation of SiC substrate at high temperature, graphene was formed and distributed on the substrate. The electron irradiation was performed by Philips FEG SEM under vacuum degree of 8.6×10^{-6} mbar, the electron beam energy and current was 30 keV and 16 nA respectively. The magnification of 36 × was used, and led to the largest irradiated area of 3.4×2.6 mm^2. Four times of this area cover the most of graphene sample surface, and each area was irradiated with different dose density. Low and high dose irradiation were both performed on the graphene sample to investigate the dose dependence on irradiation as well as compare the irradiation effect

in chapter III. First, the four areas were irradiated at low dose densities: 2.04 $\times 10^{13}$ /cm^2, 4.07 $\times 10^{13}$ /cm^2, 6.11 $\times 10^{13}$ /cm^2, 8.15 $\times 10^{13}$ /cm^2, respectively. These dose densities were at the same level of the irradiation dose used in chapter III. Then, high dose irradiation was performed again in area 2 and 3, the irradiation times increased to 20 min and 40 min, and the corresponding dose densities were: 1.36 $\times 10^{15}$ /cm^2 and 2.71 $\times 10^{15}$ /cm^2.

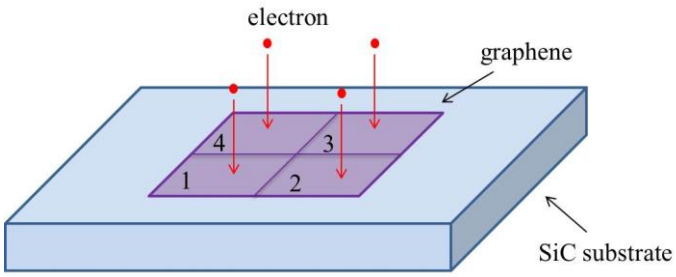

Figure 5.2 Schematic of e-beam irradiation in epitaxial graphene grown on SiC substrate.

5.3 X-ray Photoelectron Spectroscopy

The XPS measurements are in the same parameters with chapter III. The epitaxial graphene samples grown SiC substrate were characterized using a K Alpha model spectrometer from ThermoFisher equipped with a monochromatic Al Kα X-Ray source (1486.6 eV) at ambient temperature. The spot diameter was 100 μm and more than two positions in each area were measured. The hemispherical analyzer was operated in constant analyzer energy (CAE) mode with the pass energy of 200 eV and the scan step of 1 eV for the survey spectra, while the pass energy of 50 eV and the scan step of 0.1 eV for the core-level spectra.

5.3.1 Unirradiated graphene

Figure 5.3 shows the XPS surveys of the unirradiated graphene. Similar to Figure 3.3, C1s, O1s, Si2s and Si2p peaks were detected in XPS surveys of graphene on SiC substrate. But interestingly, F1s peak was also observed in the survey, this may due to the SiC substrate was cleaned by HF solution during the fabrication processes, and the remaining HF solution on SiC substrate resulted in the F1s peak in XPS surveys. The C1s peak originates from graphene and SiC substrate, and the Si2s and Si2p peaks come from the SiC substrate. Compared to Figure 3.3, the intensity of O1s peak is much lower than graphene prepared on SiO_2 substrate by CVD method, which is due to the H_2O and O_2 molecules adsorbed on the graphene surface exposed to air ambient.

Figure 5.4 shows the C 1s core-level spectra of the unirradiated graphene sample. The peak fitting was obtained using a sum of a Gaussian function convoluted with a Doniach-Sunjic lineshape. The component of the C 1s spectrum around 283.8 eV corresponds to SiC substrate (SiC), and the components around 284.5 eV and 285.4 eV correspond to graphene (G) and interlayer (IL) respectively [3] [20-23].

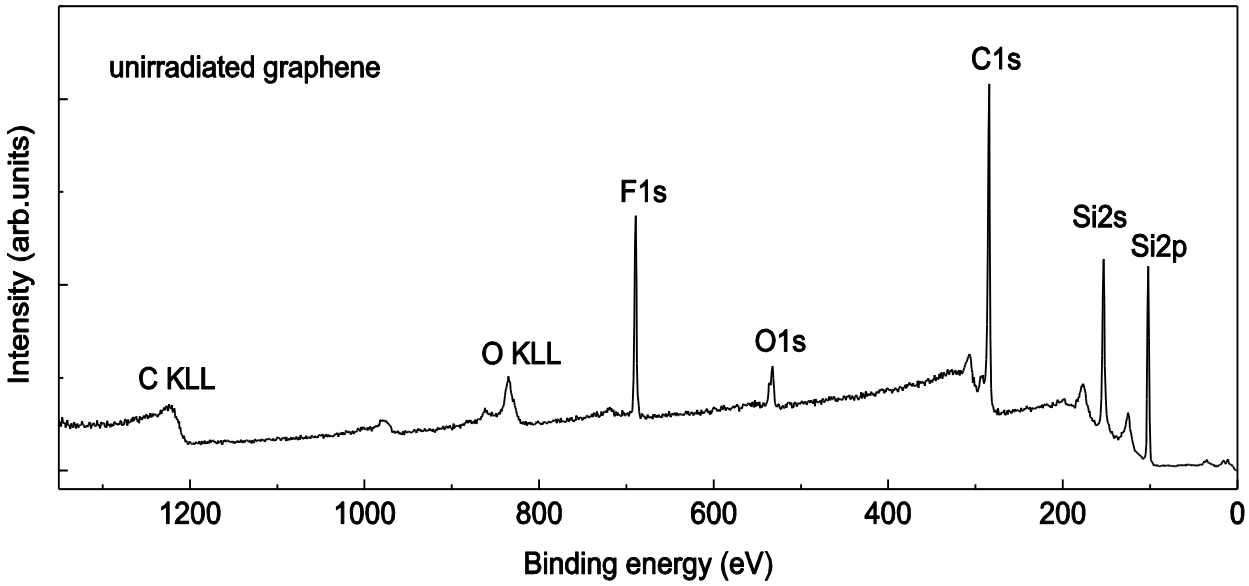

Figure 5.3 X-ray photoelectron spectroscopy survey of the unirradiated graphene sample.

Table 5.1 shows the components and bond ratio of C 1s spectra in unirradiated graphene. The proportion of graphene peak is around 55.4%, which occupy the mainly component in C 1s spectra. While the components of SiC and IL is respectively around 20.5% and 24.1%. Compared to Table 3.2, there are few contributions come from oxygen related components. This is related to different growth mechanism between sublimation and CVD method, and there are no PMMA residues remained on graphene surface prepared by sublimation of SiC substrate [1-2].

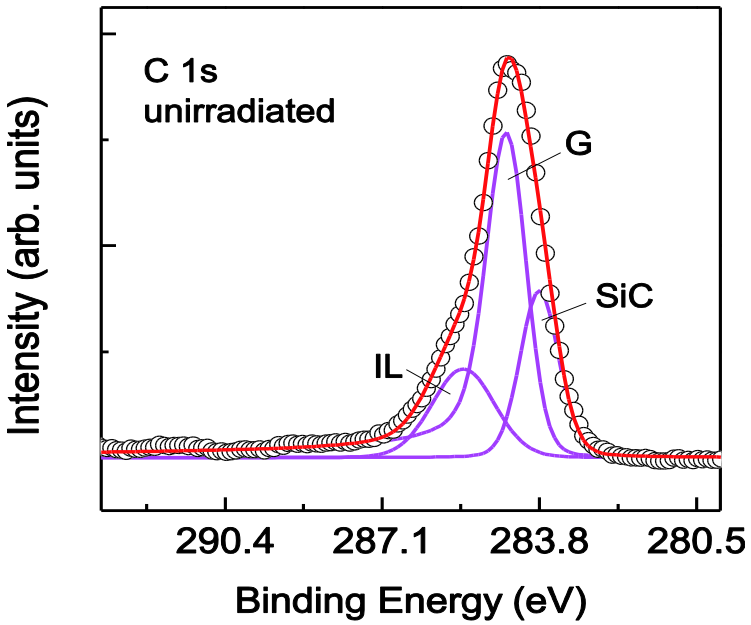

Figure 5.4 XPS C 1s spectra of unirradiated graphene on SiC substrate. The peak fitting was obtained using a sum of a Gaussian function convoluted with a Doniach-Sunjic lineshape.

Table 5.1 Binding energy and area ratio of C 1s components in the unirradiated graphene.

Component	Binding energy (eV)	Ratio (%)
SiC	283.8 ±0.1	20.5 ±1.8
G	284.4 ±0.1	55.4 ±3.2
IL	285.4 ±0.1	24.1 ±2.9

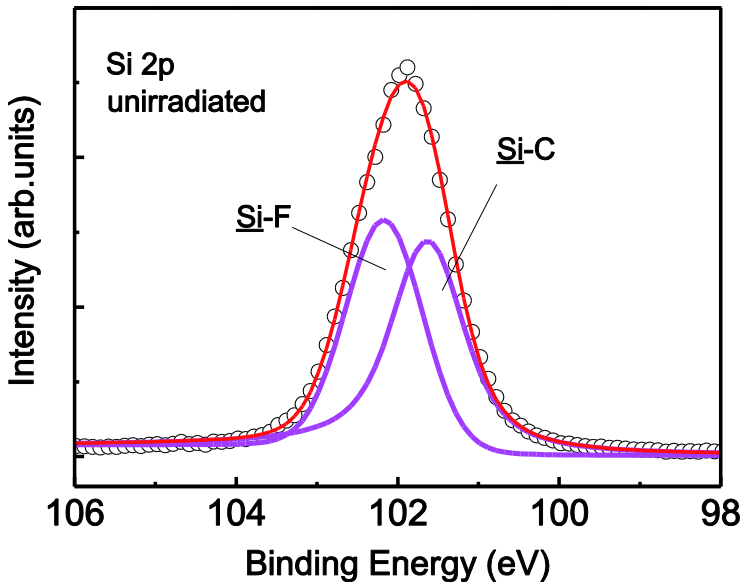

Figure 5.5 XPS O 1s spectra of unirradiated graphene on SiC substrate.

Figure 5.5 shows the Si 2p core-level spectra of the uniradiated graphene sample. There are two components in the XPS Si 2p spectra with binding energy around 101.6 eV, 102.2eV, which are corresponding to the Si-C (Si1) and Si-F (Si2), respectively [21-23]. Table 5.2 shows binding energy and area ratio of Si 2p components in the unirradiated graphene. The proportion of Si-C bond is 52.9%, which originates from the SiC substrate. And the area ratio of Si-F bond is around 47.1%, which indicates that a large number of F atoms interact with Si atoms in the substrate.

Table 5.2 Binding energy and area ratio of Si 2p components in the unirradiated graphene.

Component	Binding energy (eV)	Ratio (%)
Si-C	101.6±0.1	52.9±3.8
Si-F	102.2±0.1	47.1±2.1

5.3.2 Low dose irradiation

First, in order to compare the irradiation effect with the results in chapter III, the graphene on SiC substrate was irradiated at low dose density of 10^{13} /cm^2 magnitude, and the XPS results of graphene irradiated at the dose density of 2.04 × 10^{13} /cm^2 is present here. Figure 5.6 shows the XPS C 1s core-level spectra of graphene irradiated at the dose density of 2.04 × 10^{13} /cm^2. It

can be seen that the intensity of graphene and interlayer peak maintain at the same level compared to that of unirradiated graphene, while the intensity of SiC component decreases.

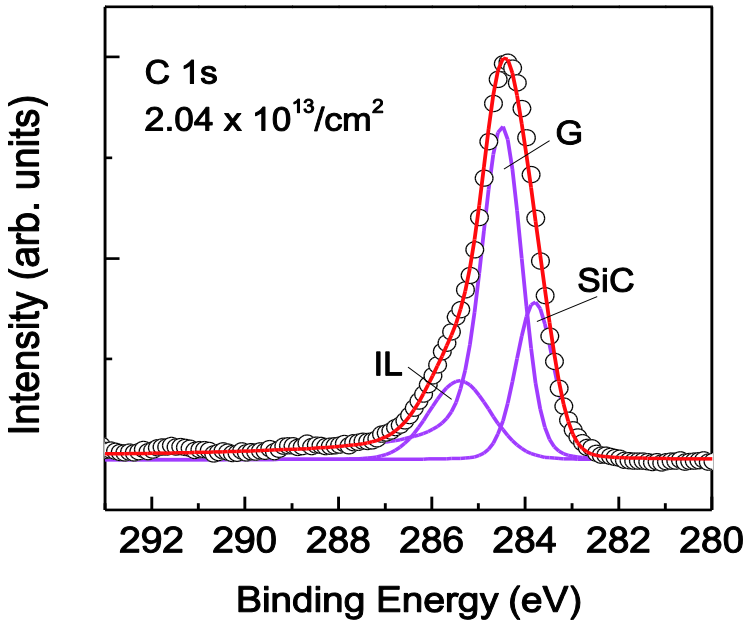

Figure 5.6 XPS C 1s core-level spectra of graphene irradiated at the dose density of 2.04 $\times 10^{13}$ /cm^2.

Table 5.3 Binding energy and area ratio of C 1s components in the unirradiated graphene and graphene irradiated at the dose density of 2.04 $\times 10^{13}$ /cm^2.

		SiC	G	IL
unirradiated	binding energy (eV)	283.8±0.1	284.4±0.1	285.4±0.1
	area ratio (%)	24.1±1.8	55.4±2.2	20.5±2.9
2.04 $\times 10^{13}$ /cm^2	binding energy (eV)	283.8±0.1	284.4±0.1	285.4±0.1
	area ratio (%)	23.3±2.2	58.0±2.7	18.7±2.3

Table 5.3 presents the binding energy and area ratio of C 1s components in the unirradiated graphene and graphene irradiated at the dose density of 2.04 $\times 10^{13}$ /cm^2. The area ratio of graphene component increases from around 55.4% to 58.0% after irradiation at dose density of 2.04 $\times 10^{13}$ /cm^2, while the area ratio of SiC and IL component decreases from around

24.1% and 20.5% to around 23.3% to 18.7%. This is related to the short duration electron beam irradiation plays as the annealing effect and leads to the recovery of graphene structure [34-35].

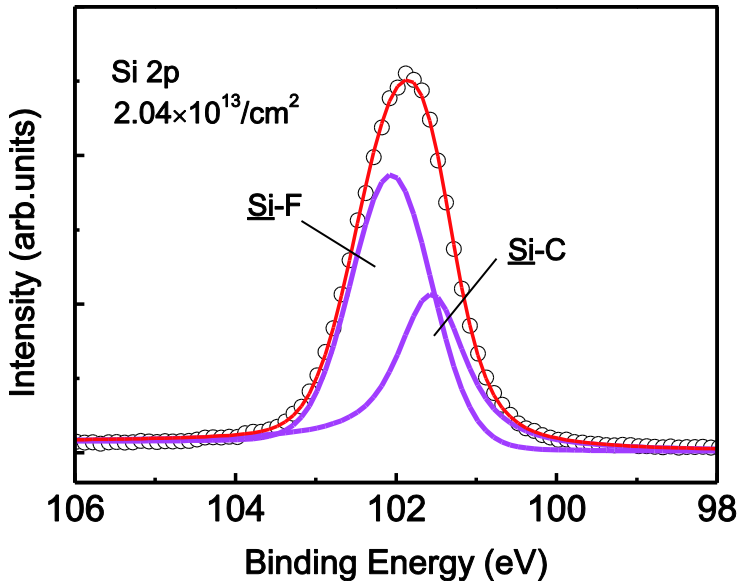

Figure 5.7 XPS Si 2p core-level spectra of graphene irradiated at the dose density of 2.04 $\times 10^{13}$ /cm^2.

Table 5.4 Binding energy and area ratio of Si 2p components in the unirradiated graphene and graphene irradiated at the dose density of 2.04 $\times 10^{13}$ /cm^2.

		Si1	Si2
unirradiated	binding energy (eV)	101.6 ±0.1	101.2 ±0.1
	area ratio (%)	52.9 ±3.8	47.1 ±2.1
2.04 $\times 10^{13}$ /cm^2	binding energy (eV)	101.6 ±0.1	102.0 ±0.1
	area ratio (%)	39.3 ±3.4	60.7 ±2.7

The Si 2p spectra (Figure 5.7) shows that the intensity of Si-C bond decreases while that of Si-F bond increases after irradiated at the dose density of 2.04 $\times 10^{13}$ /cm^2. Binding energy and area ratio of Si 2p components in the unirradiated graphene and graphene irradiated at the dose density of 2.04 $\times 10^{13}$ /cm^2 are shown in table 5.4. It can be seen that the area ratio of Si-C bond decreases dramatically from around 52.9% to 39.3%, and that of Si-F increases from around 47.1%

to 60.7%. This may be related to low dose electron irradiation which leads to more F atoms interact with the Si atoms in SiC substrate.

5.3.3 High dose irradiation

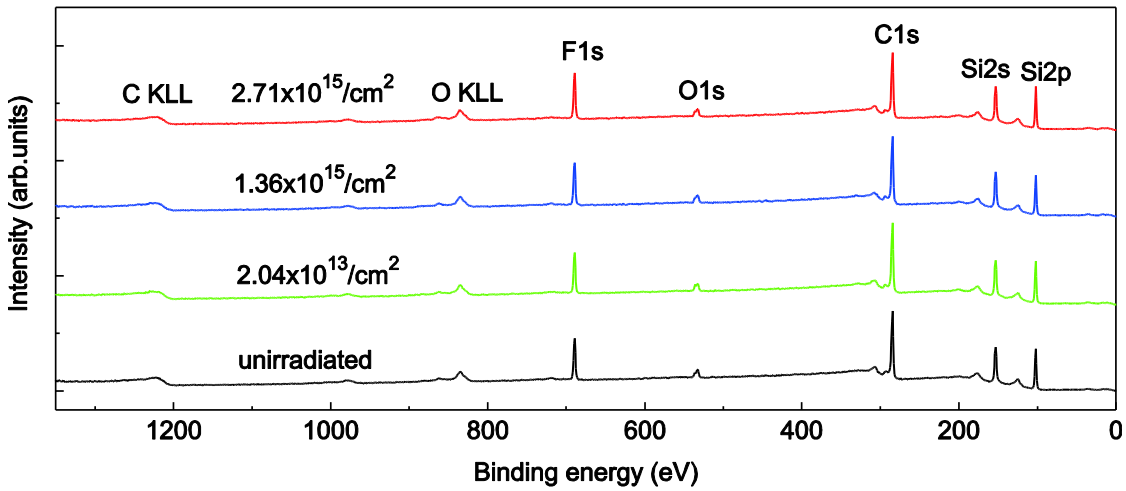

Figure 5.8 XPS surveys of unirradiated graphene, graphene irradiated at the dose of 2.04 $\times 10^{13}$ /cm^2, 1.36 $\times 10^{15}$ /cm^2 and 2.71 $\times 10^{15}$ /cm^2.

As mentioned in 5.2, area 2 and 3 were irradiated at high dose density of 1.36 $\times 10^{15}$ /cm^2 and 2.71 $\times 10^{15}$ /cm^2 after low dose electron irradiation, and the XPS results of these two areas are shown here. Figure 5.8 shows XPS surveys of unirradiated graphene, the graphene irradiated at the dose of 2.04 $\times 10^{13}$ /cm^2, 1.36 $\times 10^{15}$ / cm^2 and 2.71 $\times 10^{15}$ /cm^2. Similar to Figure 5.2, only the O1s, C1s, F1s, Si2s and Si2p peaks were detected in XPS surveys, which suggest that no other impurities were introduced in graphene during the irradiation processes. Table 5.6 shows the atom ratio of Si, C and O in the unirradiated and irradiated graphene samples. The ratios of these three atoms do not show significant change after low dose and high dose irradiation, which is due to that there were no PMMA residues and chemical doping was not induced e-beam by irradiation in graphene. The Si atoms and C atoms ratios remain around 30% and 60% respectively, while the O atom ratio shows a minor increase from around 8.8% to 10.1%, this may related to the O_2 and H_2O molecules adsorbed on graphene surface.

Table 5.6 Atom ratios of Si, C and O in the unirradiated and irradiated graphene samples.

	Si atom ratio (%)	C atom ratio (%)	O atom ratio (%)
unirradiated	30.3±0.2	60.9±0.3	8.8±0.1
2.04 ×10^{13} /cm^2	29.7±0.9	61.4±1.2	8.8±0.3
1.36 ×10^{15} /cm^2	29.1±2.1	61.4±2.7	9.5±0.3
2.71 ×10^{15} /cm^2	29.2±2.4	60.7±2.1	10.1±0.7

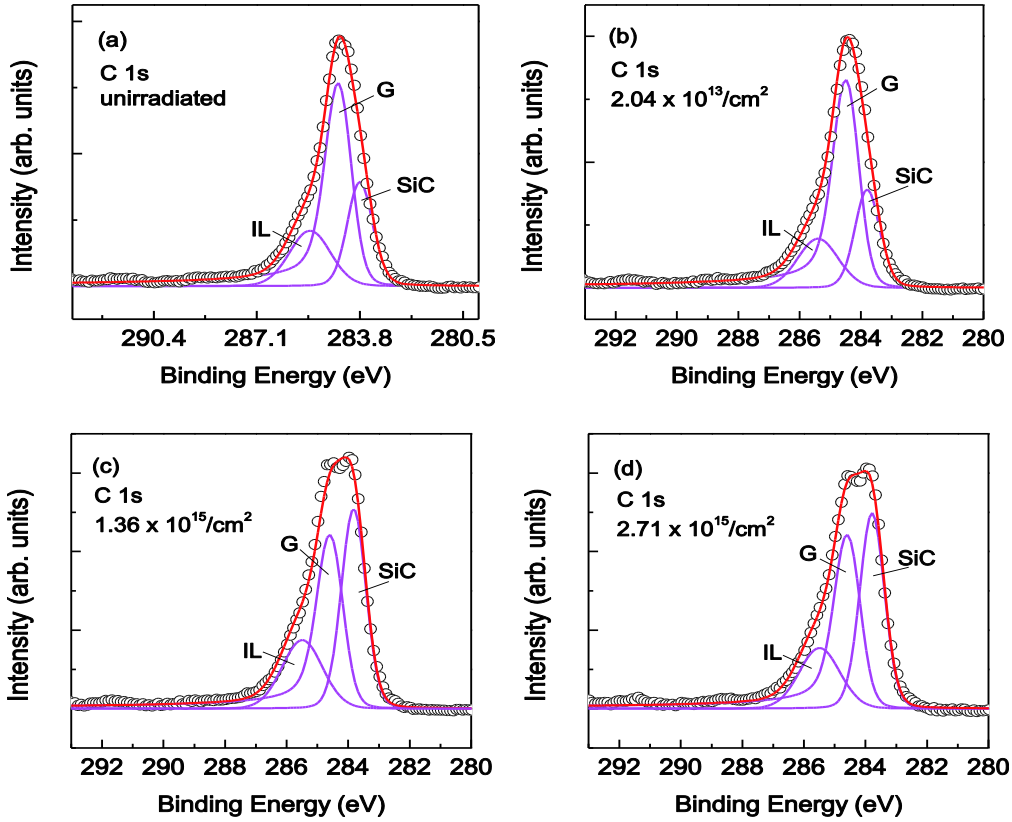

Figure 5.9 XPS C 1s core-level spectra of unirradiated graphene, graphene irradiated at the dose of 2.04 × 10^{13} /cm^2, 1.36 ×10^{15} /cm^2 and 2.71 ×10^{15} /cm^2.

Different from the results shown in chapter 3, as there are no PMMA residues remained on graphene surface, irradiation dose not result in complicated chemical reactions in graphene grown on SiC substrate [12-19]. Also, due to the use of the electron beam as the irradiation

source, the damage to the graphene is not as significant as He^+ ions [11]. The minor increase of O atoms ratio may be related to the adsorption of more O_2 and H_2O molecules when exposed to air ambient after irradiation.

Figure 5.9 shows the XPS C 1s core-level spectra of unirradiated graphene, graphene irradiated at the dose of 2.04×10^{13} /cm^2, 1.36×10^{15} / cm^2 and 2.71×10^{15} /cm^2. It can be seen that the intensity of G peak decreases obviously after high dose irradiation, while the intensities of SiC peak increases and IL peak shows minor change. This indicates that high dose irradiation leads to the break of the C-C sp^2 bond and induces a local amorphization and defects formed in graphene [15-19].

Table 5.7 shows the binding energy and area ratio of C 1s components in the unirradiated graphene and graphene irradiated at the dose density of 2.04×10^{13} /cm^2, 1.36×10^{15} / cm^2 and 2.71×10^{15} /cm^2. It is obvious that after high dose irradiation, the area ratio of G peak decreases from around 58.0% at the dose density of 2.04×10^{13} /cm^2 to around 39.8% and 40.8% at the dose density of 1.36×10^{15} / cm^2 and 2.71×10^{15} /cm^2 respectively. The area ratio of SiC component shows an increase with the dose density, growing from around 24.1% at the dose density of 2.04×10^{13} /cm^2 to around 38.8% and 39.2% at the dose density of 1.36×10^{15} / cm^2 and 2.71×10^{15} /cm^2 respectively. These results confirm that high dose irradiation breaks the crystal structure of graphene, the C-C sp^2 bonds are broken and amorphization/defects are induced [12-19]. It is interesting to note that the area ratio of G peak increases at the dose density of 2.04×10^{13} /cm^2, which is due to that low dose irradiation plays a role as annealing and leads to the recovery of graphene structure [34-35].

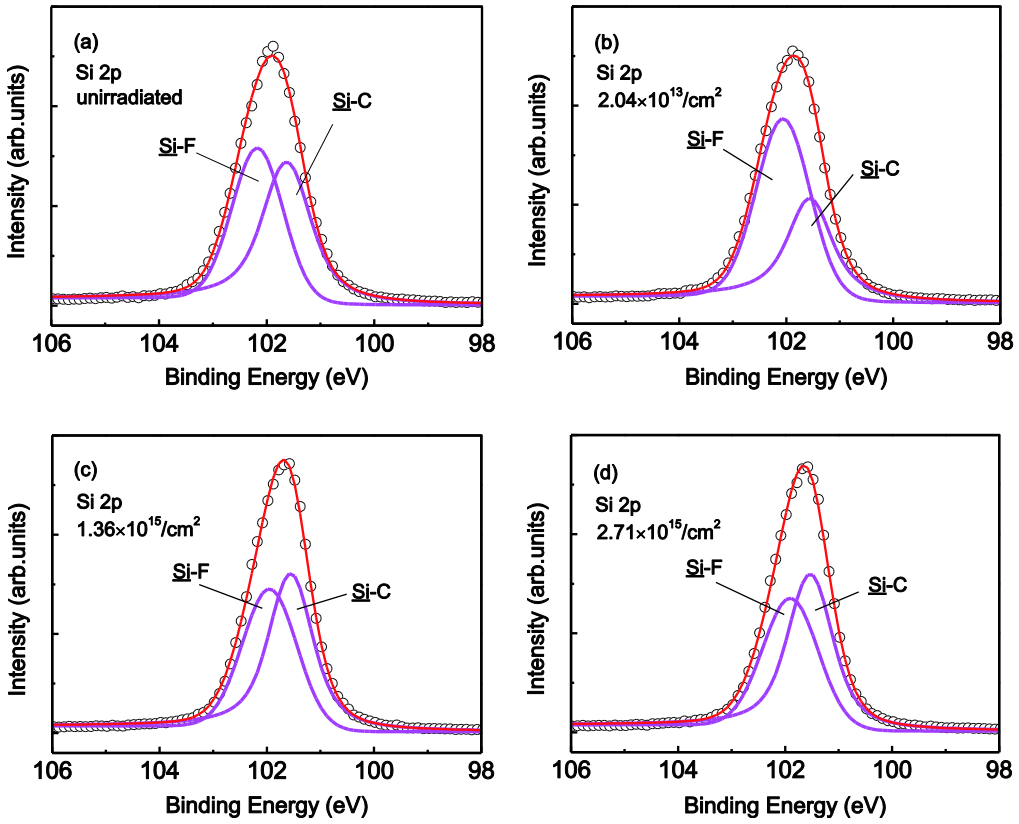

Figure 5.10 XPS Si 2p core-level spectra of unirradiated graphene, graphene irradiated at the dose of 2.04 $\times 10^{13}$ /cm^2, 1.36 $\times 10^{15}$ /cm^2 and 2.71 $\times 10^{15}$ /cm^2.

Figure 5.10 shows the Si 2p core-level spectra of unirradiated graphene, graphene irradiated at the dose of 2.04 $\times 10^{13}$ /cm^2, 1.36 $\times 10^{15}$ /cm^2 and 2.71 $\times 10^{15}$ /cm^2. The intensity of Si-C bond decreases after low dose irradiation, while it increases a lot after high dose irradiation of 1.36 $\times 10^{15}$ /cm^2 and 2.71 $\times 10^{15}$ /cm^2. The intensity of Si-F bond shows reverse dependence on the dose density, it increases after low dose irradiation and then decreases after high dose irradiation.

Table 5.7 Binding energy and area ratio of C 1s components in the unirradiated graphene and graphene irradiated at the dose density of 2.04×10^{13} /cm^2, 1.36×10^{15} /cm^2 and 2.71×10^{15} /cm^2.

		SiC	**G**	**IL**
unirradiated	binding energy (eV)	283.8±0.1	284.4±0.1	285.4±0.1
	area ratio (%)	24.1±1.8	55.4±2.2	20.5±2.9
2.04×10^{13} /cm^2	binding energy (eV)	283.8±0.1	284.4±0.1	285.4±0.1
	area ratio (%)	23.3±2.2	58.0±2.7	18.7±2.3
1.36×10^{15} /cm^2	binding energy (eV)	283.8±0.1	284.5±0.1	285.5±0.1
	area ratio (%)	38.8±3.1	39.8±3.4	21.4±3.1
2.71×10^{15} /cm^2	binding energy (eV)	283.8±0.1	284.5±0.1	285.5±0.1
	area ratio (%)	39.2±3.5	40.8±3.9	20.0±2.8

Table 5.8 Binding energy and area ratio of Si 2p components in the unirradiated graphene and graphene irradiated at the dose density of 2.04×10^{13} /cm^2, 1.36×10^{15} /cm^2 and 2.71×10^{15} /cm^2.

		Si1	**Si2**
unirradiated	binding energy (eV)	101.6±0.1	101.2±0.1
	area ratio (%)	52.9±3.8	47.1±2.1
2.04×10^{13} /cm^2	binding energy (eV)	101.6±0.1	102.0±0.1
	area ratio (%)	39.3±3.4	60.7±2.7
1.36×10^{15} /cm^2	binding energy (eV)	101. 6±0.1	101.9±0.1
	area ratio (%)	54.0±4.1	46.0±3.6
2.71×10^{15} /cm^2	binding energy (eV)	101. 5±0.1	101.9±0.1
	area ratio (%)	55.1±3.7	44.9±3.1

Table 5.8 shows binding energy and area ratio of Si 2p components in the unirradiated graphene, graphene irradiated at the dose of 2.04 $\times 10^{13}$ /cm^2, 1.36 $\times 10^{15}$ /cm^2 and 2.71 $\times 10^{15}$ /cm^2. The proportion of Si-C bond decreases significantly from around 52.9% to 39.3% after low dose irradiation, then it increases to around 54.0% and 55.1% at the dose of 1.36 $\times 10^{15}$ /cm^2 and 2.71 $\times 10^{15}$ /cm^2. And the area ratio of Si-F bond increases from around 47.1% to 60.7% follows the low dose irradiation, while at high dose density of 1.36 $\times 10^{15}$ /cm^2 and 2.71 $\times 10^{15}$ /cm^2, it decreases to around 46.0 and 44.9%. This indicates that a number of F atoms interact with Si atoms in the substrate after low dose irradiation. While at high dose irradiation, the interactions between F and Si atoms are suppressed, then more Si-C bonds are formed.

5.4 Raman Spectroscopy

The Raman measurements were performed to investigate the low dose and high dose irradiation on the graphene grown on SiC substrate. Figure 5.11 shows the evolution of Raman spectra of unirradiated graphene and graphene irradiated with various dose densities. For the unirradiated graphene, the G and 2D peaks are located around the 1595.7 cm^{-1} and 2727.3cm^{-1}.

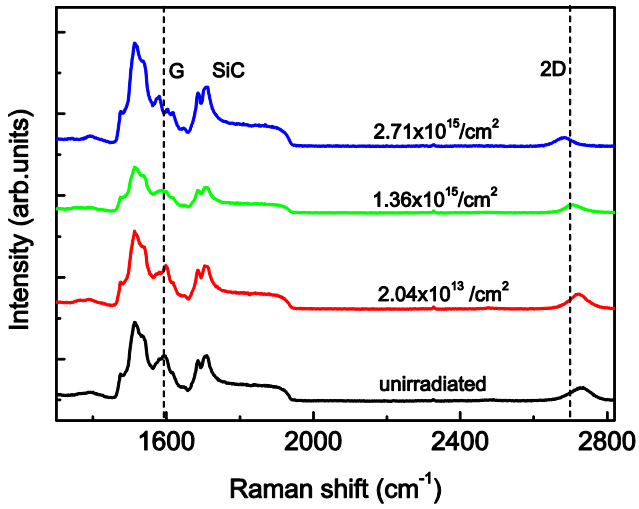

Figure 5.11 Evolution of Raman spectra of unirradiated graphene and irradiated graphene with various dose densities: 2.04 $\times 10^{13}$ /cm^2, 1.36 $\times 10^{15}$ /cm^2 and 2.71 $\times 10^{15}$ /cm^2.

It is worth pointing out that the 2D peak shows a high shift of ~40 cm^{-1} with respect to 2680 cm^{-1} of exfoliated graphene. This is related to uniform compressive strain in epitaxial graphene on SiC [14] [25]. The other two peaks which are around 1516.6 cm^{-1} and 1708.7 cm^{-1}

come from the SiC substrate [24]. These two SiC peaks have wide bandwidth and the positions are near to the G peak, thus overlapping of the three peaks observed in the Raman spectra. The buffer layer under the graphene film also contributes to the overlapping Raman curves [24-25]. Interestingly, it can be seen that the G and 2D peaks shift to lower frequency (red-shift) after both of the low dose and high dose irradiation. These results are different from the Raman spectra shown in chapter three, where irradiation induces blue shift for the G and 2D peaks in the Raman spectra of graphene grown on SiO_2 substrate prepared by CVD method. This may be related to the different irradiation influence on these two type graphene. For the graphene grown by CVD method, the chemical bonds between functional groups from PMMA residues and graphene could be formed due to ion irradiation, which leads to hole doping in graphene and results in blue-shift of G and 2D peaks. While for the epitaxial graphene grown on SiC (0001) substrate, the amorphization progress and defects play important role on the effect of irradiation in graphene [14] [24-25].

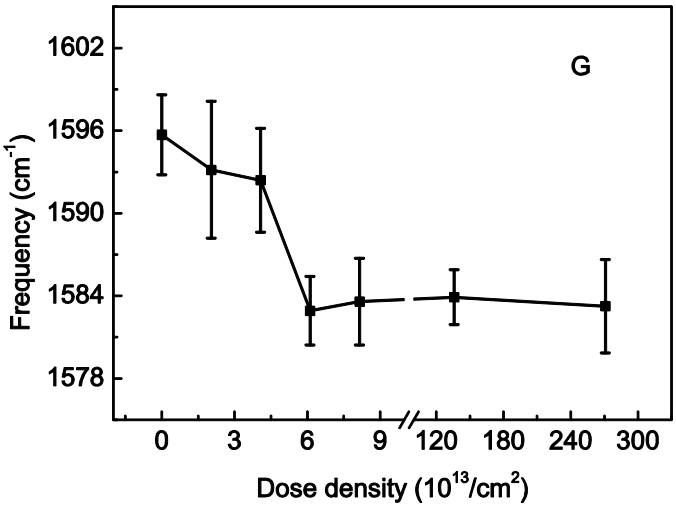

Figure 5.12 Dose density dependence of the frequency of G peak for the unirradiated graphene and graphene irradiated with various dose densities.

Meanwhile, the D peak which presents the amounts of defects or disorders in graphene is very weak in the Raman spectra, which is also different from the irradiation effect in CVD prepared graphene on SiO_2 substrate. This may be related that the electron beam irradiation only results in a small number of crystal defects formed in graphene, thus the D peak is hard to be

detected in Raman spectra. Moreover, it is interesting to see that the intensity of 2D peak decreases with increasing the dose density, which suggests local progressive amorphization of the graphene [14].

Figure 5.12 shows the dose density dependence of the frequency of G peak for the unirradiated graphene and graphene irradiated with low and high dose densities. The error bars are given by the results of several spot positions in each irradiated area, representing the spatial inhomogeneity of the Raman shift. For the unirradiated graphene, the frequency of G peak is around 1595.7 cm^{-1}, after irradiated at the low dose density of 2.04 $\times 10^{13}$ $/cm^2$ and 4.07 $\times 10^{13}$ $/cm^2$, G peak shows a red-shift of ~ 3 cm^{-1} and ~ 4 cm^{-1}, and reaches to around 1593.1 cm^{-1} and 1592.4 cm^{-1}, respectively. Then when the dose increases to 6.11 $\times 10^{13}$ $/cm^2$, the G peak suddenly shifts to around 1582.9 cm^{-1}. While continue to increase the irradiation dose density, the frequency of G peak remains around 1583 cm^{-1}. The position of G peak is around 1583.6 cm^{-1}, 1583.9 cm^{-1} and 1583.2 cm^{-1} at the dose density of 8.15 $\times 10^{13}$ $/cm^2$, 1.36 $\times 10^{15}$ $/cm^2$ and 2.71 $\times 10^{15}$ $/cm^2$, respectively. This red-shift behavior of G peak may be related to several mechanisms. As the G peak in Raman spectra originates from the in-plane vibration of sp^2 bonded C atoms and doubly degenerate (E_{2g}) phonon mode at the Brillouin zone center [26], electron beam irradiation breaks the C-C sp^2 bonds in graphene, and induces defects in the graphene layer, which contributes to the red-shift of G peak. Also, the local strain released after electron beam irradiation may also result in the downshift of G peak [33].

Figure 5.13 shows the dose density dependence of the frequency of 2D peak for the unirradiated graphene and graphene irradiated with low and high dose densities. The position of 2D peak for unirradiated graphene locates around the 2727.3 cm^{-1}. With increasing the dose density to 8.15 $\times 10^{13}$ $/cm^2$, the frequency of 2D follows a decrease process. The position of the 2D peak are around 2710.7 cm^{-1}, 2706.8 cm^{-1}, 2691.1 cm^{-1} and 2690.5 cm^{-1} at the dose density of 2.04 $\times 10^{13}$ $/cm^2$, 4.07 $\times 10^{13}$ $/cm^2$, 6.11 $\times 10^{13}$ $/cm^2$ and 8.15 $\times 10^{13}$ $/cm^2$, respectively. While continue to increase the dose density to 1.36 $\times 10^{15}$ $/cm^2$, the frequency of 2D peak suddenly increases to around 2703.4 cm^{-1}. And in the end when the dose density increases to 2.71 $\times 10^{15}$ $/cm^2$, the frequency of 2D peak further decreases to 2689.5 cm^{-1}. Except the dose density of 1.36 $\times 10^{15}$ $/cm^2$, the overall trend of the 2D peak frequency shows a red-shift dependence on the dose density. This may be related to the inhomogeneity of electron beam irradiation on graphene.

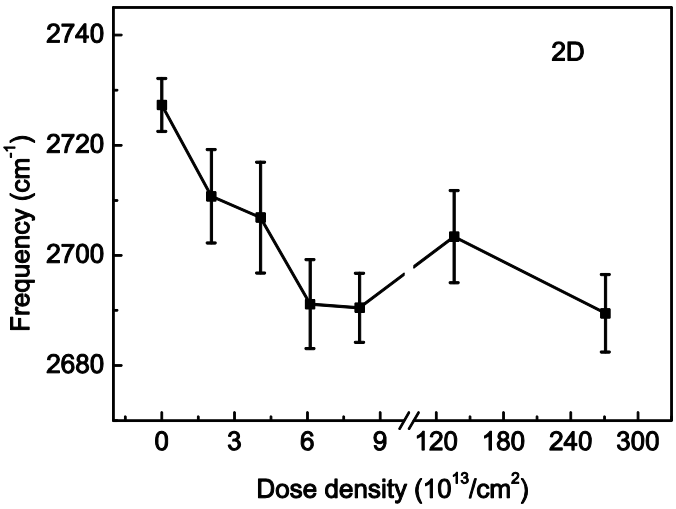

Figure 5.13 Dose density dependence of the frequency of 2D peak for the unirradiated graphene and graphene irradiated with various dose densities.

The 2D peak is the second order of D peak, while no defects are required for the activation of second order phonons [27]. The creation of local defects can release the strain in epitaxial graphene which may leads to 2D peak shifts to lower frequency [12-19]. The electron beam irradiation can also result in a modification of the n-type doping of graphene, which originates from charge transfer from SiC substrate to graphene or hole trapped at the SiC interface [12] [28]. With increasing the dose density, the n-doping effect becomes more prominent and results in the red-shift of the 2D peak [27]. Also, the local strain released after electron beam irradiation may also contribute to the downshift of 2D peak [14].

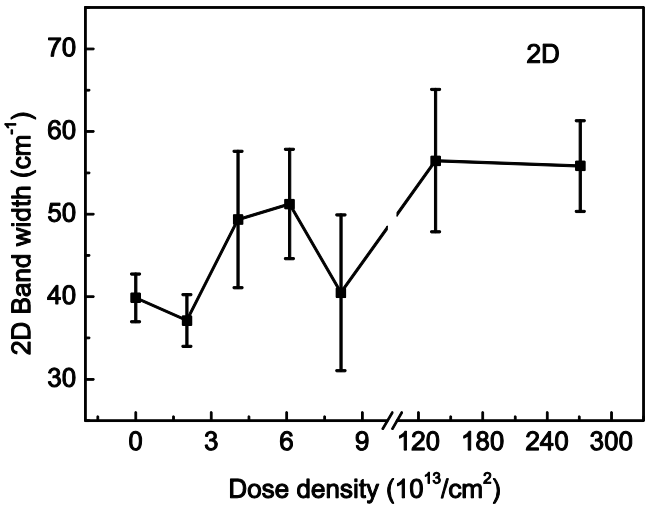

Figure 5.14 Dose dependences of the band width of 2D peak for unirradiated and irradiated graphene.

Figure 5.14 shows the dependences of 2D band width on dose density of unirradiated graphene and irradiated graphene. The 2D band width for unirradiated graphene is around 39.8 cm^{-1}. When irradiated the graphene at the dose density of 2.04×10^{13} $/cm^2$, the band width shows a minor decrease to around 37.1 cm^{-1}. Continue to increase the dose density to 4.07×10^{13} $/cm^2$ and 6.11×10^{13} $/cm^2$, the band width increases dramatically to around 49.3 cm^{-1} and 51.2 cm^{-1}. Then at the dose density of 8.15×10^{13} $/cm^2$, the 2D band width suddenly decreases to around 40.5 cm^{-1}. In the end, the 2D band width further increases to around 56.4 cm^{-1} and 55.8 cm^{-1} at the dose density of 1.36×10^{15} $/cm^2$ and 2.71×10^{15} $/cm^2$. Except the dose density of 8.15×10^{13} $/cm^2$, the 2D band width shows an increasing dependence on the dose density. This is related to the fact that the irradiation induces a progressive local amorphization of graphene. [14]. The strain released after irradiation may also contribute to this behaviour [14].

5.5 Transport Properties

The electrical properties of unirradiated and irradiated graphene grown on SiC substrate have also been investigated. All the measurements were performed by Keithley 2400 at room temperature in ambient condition. And two-probe method was used during the measurements. The conductance of unirradiated and graphene irradiated with various dose densities were measured and discussed here.

As shown in Figure 5.15, the electrical conductance G of unirradiated graphene and irradiated graphene under a drain-source voltage of 0.1 V without gating were measured. Similar to the results in chapter IV, a non-monotonic dependence of the conductance on the dose density was observed. The conductance for unirradiated graphene is about 0.87 mS, about 1.5 times larger than that of the graphene irradiated at the dose density of 8.15×10^{13} /cm^2 which is about 0.59 mS. While continue to increase the dose density, the conductance decreases significantly to about 0.14 mS at the dose density of 1.36×10^{15} /cm^2, which is minimum value observed, as small as 16% of that of the unirradiated graphene. For the dose density larger than 1.36×10^{15} /cm^2, the conductance shows an increase behavior again, and at the dose density of 2.71×10^{15} /cm^2, it increases to about 0.86 mS, which is at the same level with the unirradiated graphene.

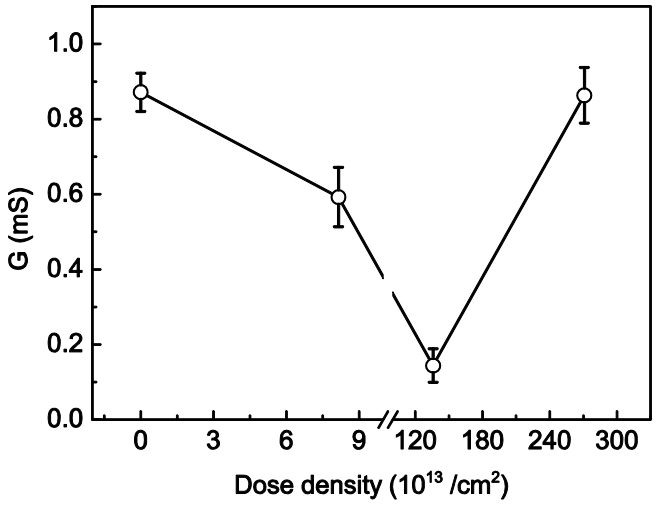

Figure 5.15 Dose density dependences of electrical conductance in unirradiated and irradiated graphene under a drain-source voltage of 0.1 V without gating.

As mentioned in chapter IV, the non-monotonic behavior in electrical conductance of graphene around zero gate voltage is related to the competitive effects of carrier concentration, mobility and defect scattering [11] [30] [31]. The strain in graphene results in the modification of structure and further influence the electrical conductance [32]. The modification of n-type doping results from the electron beam irradiation can change the carrier concentration and mobility [28] [29]. Meanwhile, the small amount of defects or disorders formed in graphene by irradiation lead to defect scattering [30]. At the dose density of 8.15×10^{13} /cm^2 and 1.36×10^{15} /cm^2, the strain

and defect scattering plays more important role and results in the decrease of the conductance. While continue to increase the dose density to 2.71 × 10^{15} /cm^2, the electron doping effect becomes more prominent and leads to the increase of the conductance. These different mechanisms work together and lead to the non-monotonic dependence of the electrical conductance on dose density, which can be applied in the design of novel graphene based memory and logic devices.

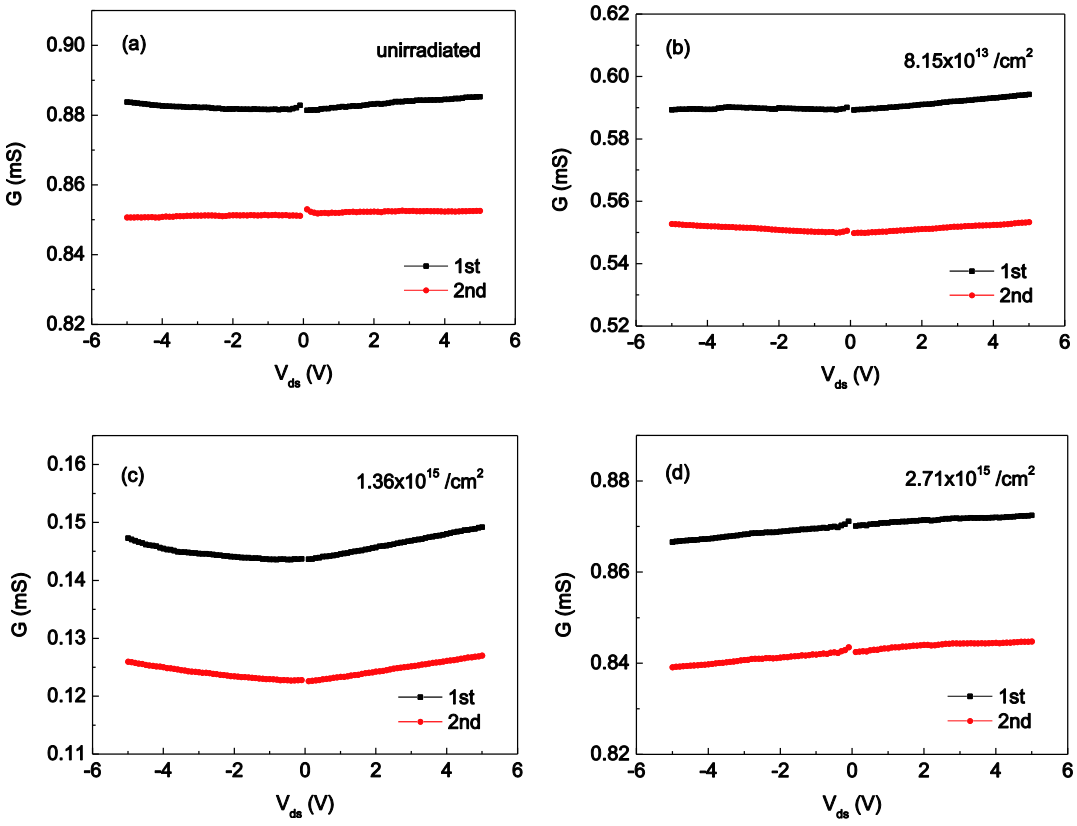

Figure 5.16 The conductance as a function of V_{ds} for unirradiated and irradiated graphene in twice measurements (black one first and red one second) (a) unirradiated (b) 2.04 ×10^{13} /cm^2, (c) 1.36 ×10^{15} /cm^2 and (d) 2.71 ×10^{15} /cm^2.

Figure 5.16 (a)-(d) shows the conductance as a function of drain to source voltage (V_{ds}) for unirradiated and irradiated graphene in twice measurements. The time difference between these two measurements was five minutes and sweeping range of V_{ds} was from -5 V to 5V. It can be seen that for graphene irradiated at the dose density of 8.15 ×10^{13} /cm^2, the conductance in the first and second measurement were around 0.58 mS and 0.55 mS which indicate the stable state of conductance in graphene after e-beam irradiation. When the dose density increases to 1.36 × 10^{15} /cm^2 and 2.71 ×10^{15} /cm^2, the conductance also shows a stable state which suggests that e-

beam irradiation leads to the modification of structure and Fermi level of graphene [9] [17-19], and it is hard to be recovered by applying drain-to-source voltage.

5.6 Comparison

Here, the irradiation influence on structural and transport properties of graphene grown on SiO_2 substrate prepared by CVD method and graphene grown on SiC substrate were compared, as shown in table 5.9.

Table 5.9 Comparison of irradiation influence on structural and transport properties of graphene prepared by CVD method and graphene grown on SiC substrate.

	Graphene grown on SiO_2 substrate prepared by CVD method	Graphene grown on SiC substrate by sublimation
X-ray photoelectron spectroscopy	With increasing the dose, the composition of C-C sp^2 bond decreases, while that of C-C (H) sp^3 bond and C-C=O bond increases.	With increasing the dose, the composition of graphene component decreases, while that of SiC component increases with the dose.
Raman spectroscopy	Blue-shift of G and 2D peak Significant D peak Band width of 2D peak increases	Red-shift of G and 2D Very weak D peak Band width of 2D peak increases
Electrical conductance	Non-monotonic dependence on dose hole doping, defect scattering	Non-monotonic dependence on dose electron doping, strain and defect scattering

In the two graphene samples, both the composition of C-C sp^2 bond shows decrease dependence on the irradiation dose density. For the graphene grown on SiO_2 substrate prepared by CVD method, the composition of C-C (H) sp^3 and C-C=O bond shows monotonic increase dependence on the dose density, which suggests oxidization and hole doping in graphene prepared by CVD method results from the decomposition of PMMA residues. While for graphene grown on SiC substrate by sublimation, the composition of SiC component shows an increase with dose density, this indicates the progressive local amorphization of graphene and strain released after irradiation. In the Raman spectra, blue shifts of G and 2D peaks were observed in graphene grown on SiO_2 substrate prepared by CVD method, a significant D peak appeared and the bandwidth of 2D band increases with the dose density. While for graphene

grown on SiC substrate, red-shift of G and 2D peaks were observed, the D peak is very weak and the bandwidth of 2D peak increases with the dose. Both the electrical conductance of these two types of graphene show non-monotonic dependence on dose density. The transport properties of graphene grown on SiO_2 by CVD method are dominated by defect scattering and hole doping, while that of graphene on SiC substrate are controlled by electron doping, strain and defect scattering. The comparison between the influence caused by irradiation on these two types of graphene exhibits the evolution of the structure and its relationship with the transport properties, which can be applied in the design of novel graphene based memory and transistor.

5.7 Conclusion

In this chapter, electron beam irradiation was performed on graphene grown on SiC substrate to modulate the structural and electrical properties. The frequencies of G and 2D peaks show red-shits dependence on the dose density, and an increase of the bandwidth of the 2D peak was observed, which are related to interaction between graphene and buffer layer or bridging modification between graphene and SiC substrate induced by irradiation. The strain released after irradiation may also contribute to the behavior. Besides, the electron doping results from electron beam irradiation may also lead to the red-shift of 2D peak. Furthermore, the electrical conductance measured shows a non-monotonic dependence on the dose density which is related to the competitive effects of strain, electron doping and defect scattering. In summary, the modification of structural properties of graphene after irradiation and its relationship with the transport properties are demonstrated, which can be applied in graphene-based memory and logic devices, transistors and integrated circuits.

References

(1) Norimatsu, W.; Kusunoki, M. Structural features of epitaxial graphene on SiC {0001} surfaces. *J. Phys. D: Appl. Phys.* **2014**, *47*(9), 094017.

(2) Norimatsu, W.; Kusunoki, M. Epitaxial graphene on SiC {0001}: advances and perspectives. *Phys. Chem. Chem. Phys.* **2014**, *16*(8), 3501.

(3) Emtsev, K. V.; Speck, F.; Seyller, T.; Ley, L.; Riley, J. D. Interaction, growth, and ordering of epitaxial graphene on SiC {0001} surfaces: A comparative photoelectron spectroscopy study. *Phys. Rev. B.* **2008**, *77*(15), 155303.

(4) Mathieu, C.; Lalmi, B.; Menteş, T. O.; Pallecchi, E.; Locatelli, A.; Latil, S.; Ouerghi, A. Effect of oxygen adsorption on the local properties of epitaxial graphene on SiC (0001). *Phys. Rev. B.* **2012**, *86*(3), 035435.

(5) Pallecchi, E.; Ridene, M.; Kazazis, D.; Mathieu, C.; Schopfer, F.; Poirier, W.; Ouerghi, A. Observation of the quantum Hall effect in epitaxial graphene on SiC (0001) with oxygen adsorption. *Appl. Phys. Lett.* **2012**, *100*(25), 253109.

(6) Coletti, C.; Riedl, C.; Lee, D. S.; Krauss, B.; Patthey, L.; von Klitzing, K.; Starke, U. Charge neutrality and band-gap tuning of epitaxial graphene on SiC by molecular doping. *Phys. Rev. B.* **2010**, *81*(23), 235401.

(7) Riedl, C.; Coletti, C.; Iwasaki, T.; Zakharov, A. A.; Starke, U. Quasi-free-standing epitaxial graphene on SiC obtained by hydrogen intercalation. *Phys. Rev. Lett. 103*(24), **2009**, 246804.

(8) Velez-Fort, E.; Mathieu, C.; Pallecchi, E.; Pigneur, M.; Silly, M. G.; Belkhou, R.; Ouerghi, A. Epitaxial graphene on 4H-SiC (0001) grown under nitrogen flux: Evidence of low nitrogen doping and high charge transfer. *ACS Nano.* **2012**, *6*(12), 10893.

(9) Tapaszto, L.; Dobrik, G.; Nemes-Incze, P.; Vertesy, G.; Lambin, P.; Biró, L. P. Tuning the electronic structure of graphene by ion irradiation. *Phys. Rev. B.* **2008**, *78*(23), 233407.

(10) Nair, R. R.; Ren, W.; Jalil, R.; Riaz, I.; Kravets, V. G.; Britnell, L.; Geim, A. K. Fluorographene: A Two-Dimensional Counterpart of Teflon. *Small*, **2010**, *6*(24), 2877.

(11) Krasheninnikov, A. V.; Nordlund, K. Ion and electron irradiation-induced effects in nanostructured materials. *J. Appl. Phys.* **2010**, *107*(7), 071301.

(12) Jee, H. G.; Jin, K. H.; Han, J. H.; Hwang, H. N.; Jhi, S. H.; Kim, Y. D.; Hwang, C. C. Controlling the self-doping of epitaxial graphene on SiC via Ar ion treatment. *Phys. Rev. B.* **2011**, *84*(7), 075457.

(13) Prével, B.; Benoit, J. M.; Bardotti, L.; Médinon, P.; Mayumi Sato, A.; Ouerghi, A.; Gierak, J. Local ion irradiation of thin graphene films grown on SiC substrates. *Microelectronic Eng.* **2012**, *98*, 206.

(14) Prével, B.; Benoit, J. M.; Bardotti, L.; Médinon, P.; Ouerghi, A.; Lucot, D.; Gierak, J. Nanostructuring graphene on SiC by focused ion beam: Effect of the ion fluence. *Appl. Phys. Lett.* **2011**, *99*(8), 083116.

(15) Huang, Q.; Chen, X.; Liu, J.; Wang, W.; Wang, G.; Wang, W.; Guo, L. Epitaxial graphene on 4H-SiC by pulsed electron irradiation. *Chem. Commun.* **2010**, *46*(27), 4917.

(16) Go, H.; Kwak, J.; Jeon, Y.; Kim, S. D.; Lee, B. C.; Kang, H. S.; Park, K. Low-temperature formation of epitaxial graphene on 6H-SiC induced by continuous electron beam irradiation. *Appl. Phys. Lett.* **2012**, *101*(9), 092105.

(17) Qing-Song, H.; Li-Wei, G.; Wen-Jun, W.; Gang, W.; Wan-Yan, W.; Yu-Ping, J.; Xiao-Long, C. Raman Spectrum of Epitaxial Graphene on SiC (0001) by Pulsed Electron Irradiation. *Chinese Phys. Lett.* **2010**, *27*(4), 046803.

(18) Zhi, Z.; Ying, H.; Xin-Yan, S.; Xing-Hua, L. Raman Spectrum of Epitaxial Graphene Grown on Ion Beam Illuminated 6H-SiC (0001). *Chinese Phys. Lett.* **2014**, *31*(11), 116801.

(19) Kim, K. J.; Choi, J.; Lee, H.; Lee, H. K.; Kang, T. H.; Han, Y. H.; Kim, B. Effects of 1 MeV electron beam irradiation on multilayer graphene grown on 6H-SiC (0001). *J. Phys. Chem. C.* **2008**, *112*(34), 13062.

(20) Ouerghi, A.; Silly, M. G.; Marangolo, M.; Mathieu, C.; Eddrief, M.; Picher, M.; Sirotti, F.; El Moussaoui, S.; Belkhou, R. Large-Area and High-Quality Epitaxial Graphene on off-Axis SiC Wafers. *ACS Nano* **2012**, *6*, 6075.

(21) Wong, S. L.; Huang, H.; Wang, Y.; Cao, L.; Qi, D.; Santoso, I.; Wee, A. T. S. Quasi-free-standing epitaxial graphene on SiC (0001) by fluorine intercalation from a molecular source. *ACS Nano*. **2011**, *5*(9), 7662.

(22) Coletti, C.; Emtsev, K. V; Zakharov, A. A.; Ouisse, T.; Chaussende, D.; Starke, U. Large Area Quasi-Free Standing Monolayer Graphene on 3C-SiC(111). *Appl. Phys. Lett.* **2011**, *99*, 081904.

(23) Robinson, J. T.; Burgess, J. S.; Junkermeier, C. E.; Badescu, S. C.; Reinecke, T. L.; Perkins, F. K.; Snow, E. S. Properties of fluorinated graphene films. *Nano Lett*. **2010**, *10*(8), 3001.

(24) Ni, Z. H.; Chen, W.; Fan, X. F.; Kuo, J. L.; Yu, T.; Wee, A. T. S.; Shen, Z. X. Raman spectroscopy of epitaxial graphene on a SiC substrate. *Phys. Rev. B.* **2008**, *77*(11), 115416.

(25) Ferralis, N.; Maboudian, R.; Carraro, C. Evidence of structural strain in epitaxial graphene layers on 6H-SiC (0001). *Phys. Rev. Lett.* **2008**, *101*(15), 156801.

(26) Basko, D. M.; Piscanec, S.; Ferrari, A. C. Electron-electron interactions and doping dependence of the two-phonon Raman intensity in graphene. *Phys. Rev. B.* **2009**, *80*(16), 165413.

(27) Casiraghi, C.; Pisana, S.; Novoselov, K. S.; Geim, A. K.; Ferrari, A. C. Raman fingerprint of charged impurities in graphene. *Appl. Phys. Lett.* **2007**, *91*, 032102.

(28) Childres, I.; Jauregui, L. A.; Foxe, M.; Tian, J.; Jalilian, R.; Jovanovic, I.; Chen, Y. P. Effect of electron-beam irradiation on graphene field effect devices. *Appl. Phys. Lett.* **2010**, *97*(17), 173109.

(29) Das, A.; Pisana, S.; Chakraborty, B.; Piscanec, S.; Saha, S. K.; Waghmare, U. V.; Novoselov, K. S.; Krishnamurthy, H. R.; Geim, A. K.; Ferrari, A. C.; et al. Monitoring dopants by Raman scattering in an electrochemically top-gated graphene transistor. *Nat. Nanotech.* **2008**, *3*, 210.

(30) Chen, J. H.; Cullen, W. G.; Jang, C.; Fuhrer, M. S.; Williams, E. D. Defect scattering in graphene. *Phys. Rev. Lett.* **2009**, *102*, 680501.

(31) Guo, B.; Liu, Q.; Chen, E.; Zhu, H.; Fang, L.; Gong, J. R. Controllable N-doping of graphene. *Nano Lett.* **2010**, *10*, 4975.

(32) Fu, X. W.; Liao, Z. M.; Zhou, J. X.; Zhou, Y. B.; Wu, H. C.; Zhang, R.; Yu, D. Strain dependent resistance in chemical vapor deposition grown graphene. *Appl. Phys. Lett.* **2011**, *99*(21), 213107.

(33) Ni, Z. H.; Yu, T.; Lu, Y. H.; Wang, Y. Y.; Feng, Y. P.; Shen, Z. X. Uniaxial strain on graphene: Raman spectroscopy study and band-gap opening. *ACS Nano*. **2008**, *2*(11), 2301.

(34) Kamins, T. I.; Rose, P. H. Electron-beam annealing of ion-implantation damage in integrated circuit devices. *J. Appl. Phys.* **1979**, 50(3), 1308.

(35) Greenwald, A. C.; Kirkpatrick, A. R.; Little, R. G. Minnucci, J. A. Pulsed-electron-beam annealing of ion-implantation damage. *J. Appl. Phys.* **1979**, 50(2), 783.

Chapter VI Conclusions

In this thesis, the influence of irradiation on structural and transport properties of graphene were investigated, which shows highly potential application in graphene-based memory and logic devices, transistors and integrated circuits. Ion irradiation and electron irradiation were both employed, and two types of graphene were used, the first one was graphene grown on Cu foils by CVD method and then transferred to SiO_2 substrate, while the other one was epitaxial graphene grown on SiC substrate by sublimation.

Helium ion irradiation was performed on graphene grown on SiO_2 substrate by CVD method, meanwhile vacuum annealing was used to restore the damage caused by irradiation. A reversible charge transfer doping effect in CVD graphene due to reactions with polymethyl methacrylate (PMMA) residues was observed. XPS results show that the composition ratios of sp^3 hybrid C–C (H), C−C=O and C−O−C (H) bonds in graphene increase after irradiation while they decrease after annealing, which indicates that chemical bonds between functional groups in PMMA residues and graphene could be formed due to He^+ ion irradiation, and that the desorption of functional groups from graphene is dominant during the vacuum annealing process. Both the G and 2D bands in the Raman spectra exhibit blue-shift after irradiation. The intensity ratio of the D peak to the G peak increases a lot as the dose density is larger than $1.2 \times 10^{13}\,He^+/cm^2$. It suggests that before the formation of large amount of defects, interaction between graphene and PMMA residues leads to hole doping in graphene. By annealing the irradiated graphene in vacuum, red-shift of the G and 2D bands were observed, indicating the charge-transfer doping can be partially restored. This behavior results from the reduction of hole doping which is caused by the desorption of functional groups in graphene. The electrical conductance of graphene shows a similar non-monotonic dependence on the dose density as the Raman band shift, and the trend remains after annealing, which indicates the doping also involves irreversible effect. The electronic hysteresis behavior becomes more obvious when the graphene irradiated at larger dose density, which suggests the competitive influence of charge trapping and tunneling effect. The resistance hysteresis loops were also measured under perpendicular and in-plane magnetic field, which shows the higher perpendicular magnetic field can enhance the hysteresis behavior.

Electron beam irradiation was performed on graphene epitaxial graphene grown on SiC substrate by sublimation. XPS results show that a large number of C-C sp^2 bonds were broken after high dose irradiation, which indicates modification of the structure of graphene. The frequencies of G and 2D peaks show red-shits dependence on the dose density, and an increase of the bandwidth of the 2D peak was observed, which are related to the progressive local amorphization of graphene induced by irradiation. The strain released after irradiation may also contribute to the behavior. Besides, the modification of n-type doping results from electron beam irradiation may also lead to the red-shift of 2D peak. The intensity ratio of 2D peak to SiC peak and electrical conductance of graphene show a non-monotonic dependence on the irradiation dose, which is attributed to the competitive effect of local progressive amorphization, strain and electron doping.

These works show a full investigation of the modification of structural properties of graphene after irradiation and its relationship with the transport properties, which provides convenient and efficient method to modulate the properties of graphene that can be applied in graphene-based memory and logic devices, transistors and integrated circuits.

List of Publications

(1) Deng, C. X.; Lin, W. W.; Agnus, G.; Dragoe, D.; Pierucci, D.; Ouerghi, A.; Zhao, W. S. Reversible Charge-Transfer Doping in Graphene due to Reaction with Polymer Residues. *J. Phys. Chem. C.* **2014**, *118*(25), 13890.

(2) Deng, C. X.; Lin, W. W.; Eimer, S.; Ravelosona, D.; Chappert, C.; Zhao, W. S. Raman Spectroscopy Study of Low Energy He Ion Irradiation Effect in Graphene Transferred onto SiO_2. *IEEE International Conference on Nanotechnology*. **2013**, Beijing, China.

Conferences

(1) The 13th edition of Trends in Nanotechnology International Conference (TNT2012).

(2) Journées Nationales du Réseau Doctoral en Micro-nanoélectronique (JNRDM 2014).

Summer School

(1) The 6th IEEE Magnetics Society Summer School.

(2) School on Science Management for Scientist and Engineers (SOSMSE) 2013.

Acknowledgements

It is my great pleasure to thank every people who made this thesis possible.

First, I am highly grateful to my supervisor Prof. Claude Chappert and Weisheng Zhao for giving me the opportunity to study PhD degree in Paris-Sud University. I would appreciate Prof. Chappert for spending the valuable time revising the abstract and writing the recommendation letter when I applied the summer school in 2013. As Prof. is very busy with various affairs, Prof. Zhao took charge of my study mostly and I am greatly thankful for his kindly and careful guidance. In 2011, Professor Zhao held an attractive lecture in Sun Yat-sen Univeristy (where I gained the master degree) and made me have lots of interests in MRAM and spinelectronics. After communicating with him by email, we decided to study the hot material graphene and novel graphene based memory and logic devices, which is a cutting-edge topic recently. During the last three and a half years, his inspiring and valuable guidance encouraged me at every stage of my research work, and I am also impressed by his optimistic, active and enthusiastic personality. We spent much time on discussing and planning for the experiments, which contributed much to my first paper published in the Journal of Physical Chemistry C. Also, he helped me to attend many international conferences (TNT 2012 and JNRDM 2014) and summer schools (6^{th} IEEE Magnetics summer school and SOSMSE), where I discussed with some professors, post-docs and PhD students and learned much knowledge about graphene and other interesting topics.

Second, I would like to give special thanks to Dr. Weiwei Lin, a postdoctoral researcher at Johns Hopkins University now. Although I had some research experience before, I was completely new at the field of graphene. Thanks to the kind and selfless help from Dr. Weiwei Lin on reading paper and understanding the basic principle of graphene and fabrication method. We spent much time doing experiments together and discussed the details of the phenomena we observed. For the two papers published, he also made much contribution to the revision and questions put forward by the reviewers. And I would like to thank my colleagues in IEF: Sylvain Eimer, Ivanka Barisic, Guillaume Agnus, and Diana Dragoe. Sylvain Eimer and Ivanka Barisic helped us perform the helium ion irradiation and vacuum annealing; Guillaume Agnus helped us perform atomic force microscopy and taught me to operate the transport measurement platform; Diana Dragoe spent much time on measuring the X-ray spectroscopy and gave us very useful

information about the chemical situation of graphene after irradiation and annealing. I would also like to thank Prof. Abdelkarim Ouerghi, Bayle Fabien and Debora Pierucci. Prof. Abdelkarim Ouerghi gave us many valuable advices on revision of the paper. Bayle Fabien and Debora Pierucci helped us perform the electron beam irradiation on graphene grown on SiC substrate and measure the Raman spectra of graphene samples after irradiation respectively. Although we did not publish journal paper about irradiation influence on graphene grown on SiC substrate, chapter V were composed of these results, which is of much importance to the final version of this thesis. I would like to thank Dafiné, who gave me help and advices when I wrote the manuscript. I gratefully thank Jiaqi Zhou and You Wang, who spent much time on revising the thesis. This work was supported partly by the French National Center for Scientific Research (CNRS)-G3N COSIGN project. I would like to thank the French National Research Agency (ANR) DIPMEM project, RTRA, C'Nano Ile-de-France and LABEX NanoSaclay for funding. I would like to deeply thank the Chinese government scholarship schemes program (CSC) for supporting the living expenses during my PhD study. Also, I thank C. Chaleil (DSM/IRAMIS/SPEC, CEA-Saclay) for the use of Raman spectroscopy and X. Y. Lin (Tsinghua University) for his fruitful discussion.

I would like to thank colleagues in IEF: Prof. Jacques-Olivier Klein, Djaafar Chabi, Nicolas Vernier, Na Lei, Liza Herrera Diez, Nicolas Locatelli, Joseph S. Friedman, Karin Garcia, Damien Querlioz, Thibaut Devolder, Kim Joo-Von, and Jean-Paul Adam. It was a pleasure to work, play basketball and hang out with them. I would like to thank Yayha Lakys, who gave me much help when I arrived in Paris in 2011.

Naturally I thank all Chinese friends: Qi An, Yu Zhang, Zhaohao Wang, Yue Zhang, Erya Deng, Li Su, Kang Wang, etc. It is lucky to meet you all and we spent happy time together in the last several years. Especially, I thanks to my friend Yueyuan Gao, who gave me much help when I was ill. Meanwhile, I greatly thank my landlord: Christian Angé and his family, who provided wonderful living conditions so that I can focus on my PhD study.

Finally, I would like to give grateful thanks to my family, my father, mother, uncles, aunts, brothers and sisters, who always support me whether I am, succeed or lost. It is very pity that my grandparents have passed away in the last few years, and this thesis is dedicated to them.

Résumé en français

R.1 Introduction

Depuis l'invention du premier transistor de silicium en 1947, la taille a réduit de façon exponentielle et le nombre de transistors sur une puce a énormément augmenté (loi de Moore) il y a plus de 60 ans. Comme la puce devient de plus en plus complexe, les obstacles des procédés de lithographie seront présents, tels que les motifs multiples et la lithographie par ultraviolets extrêmes (EUV). En 2004, le premier graphène matérielle 2D a été fabriquée par Andre Geim et Konstantin. La structure en nid d'abeille notamment à motifs avec sp2 liés atomes de carbone apporte au graphène d'excellentes propriétés électriques, optiques, mécaniques et thermiques, etc., qui rend le graphène comme le candidat idéal appliqué dans le transistor ou les circuits électroniques.

R. 1.1 Matériaux à base de carbone

Le carbone est l'élément chimique symbolisé par C et numérotée six dans le tableau périodique. Les quatre électrons dans la couche de valence la plus externe de l'atome de carbone peuvent former une large gamme de liaisons covalentes avec d'autres atomes, ainsi variété de composés sont formés sur la base de ces liaisons chimiques. En outre, le carbone peut se lier avec lui-même dans au moins trois façons différentes: liaison simple, doubles liaisons et triples liaisons, et former trois grandes allotropies de carbone-le diamant, le graphite et les fullerènes.

R. 1.2 Le Graphène

R. 1.2.1 Structure réseau cristallin

Le graphène idéal à une seule couche est considérée comme l'épaisse d'un atomique feuille de planificateur d'atomes de carbone densément emballé dans nid d'abeille treillis (Figure R.1a). Chaque atome de carbone dans le graphène est lié à trois autres atomes de carbone par des liaisons C-C hybrides sp^2 et les quatrièmes électrons de valence dans le reste p_z-orbital qui est perpendiculaire au plan de graphène. La zone grise présente la cellule primitive unitaire de graphène avec l'unité réseau vecteurs $\vec{a}_1$ et $\vec{a}_2$, hère $\vec{a}_1 = \frac{a}{2}(3, \sqrt{3}), \vec{a}_2 = \frac{a}{2}(3, -\sqrt{3})$, a est le paramètre de maille ~ 1,42 Å. La zone de Brillouin de graphène est présentée dans la figure R.1b,

et les vecteurs du réseau réciproque sont $\vec{G}_1 = \frac{2\pi}{3a}(1, \sqrt{3})$ and $\vec{G}_2 = \frac{2\pi}{3a}(1, -\sqrt{3})$. Dans l'espace des moments, les positions des coins sont donnés par $\vec{K} = \frac{2\pi}{3a}\left(1, \frac{1}{\sqrt{3}}\right)$ et $\overrightarrow{K'} = \frac{2\pi}{3a}\left(1, -\frac{1}{\sqrt{3}}\right)$.

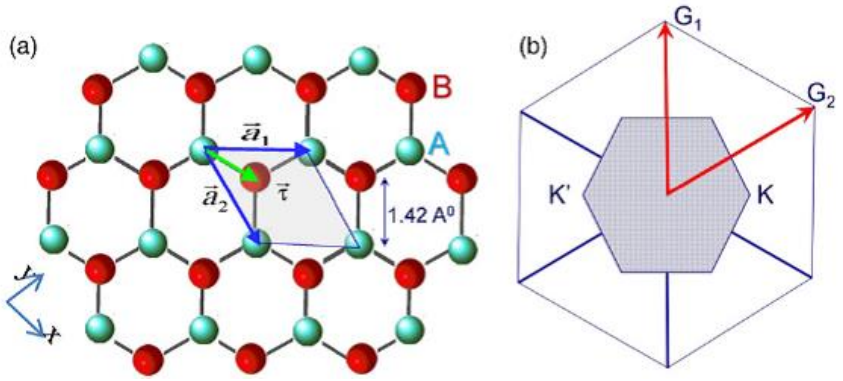

Figure R.1 (a) La structure de réseau de graphène. Les deux sous-réseaux triangulaires sont indiqués par des couleurs rouges et vertes. La maille élémentaire primitif est représentée par la zone grisée avec l'unité de treillis vecteurs $\vec{a}_1$ et $\vec{a}_2$. (b) Zone de Brillouin de graphène. $\vec{G}_1$ et $\vec{G}_2$sont des vecteurs du réseau réciproque.

R.1.2.2 La structure de bande et les propriétés électroniques

Les bandes d'énergie provenant de cette approche hamiltonien peut être décrite par l'équation:

$$E_{\pm}(\boldsymbol{k}) = \pm t\sqrt{1 + \cos^2\left(\frac{k_y a}{2}\right) + 4\cos\left(\frac{\sqrt{3}}{2}k_x a\right)\cos\frac{k_y a}{2}}, \qquad (1)$$

Ici la bande de conduction et la bande de valeur sont indiqués par signe plus $E_+(\boldsymbol{k})$ et le signe moins $E_-(\boldsymbol{k})$ respectivement. C'est clair d'observer que la structure de bande d'énergie est symétrique près de la zone d'énergie zéro. De plus, la relation de dispersion linéaire entre E_k et $\boldsymbol{k}$ près du point de Dirac donne lieu à des propriétés particulières de graphène. La plus haute mobilité rapportée près de 200,000 $cm^2\ V^{-1}\ s^{-1}$ qui a été mesurée à basse température sur le graphène suspendu. L'effet demi-entier anormal de Hall quantique (EHQ) a également été observé dans le graphène.

R.1.2.3 Transport Spin

Les interactions de couplage spin-orbite et hyperfins faibles conduisent à la longue durée de vie de spin des électrons de spins. Combiné avec la grande mobilité des électrons dans le graphène, il est considéré d'avoir un spin avec grand longueur de relaxation dans le dispositif électronique de spin à base de graphène. La plus longue durée de vie de spin de 6,2 ns a été observée dans le dispositif bicouche graphène (BLG) de filage à 20K. La plus grande longueur de relaxation de spin (λs) de 12 µm ont été observées dans le dispositif de transport de spin graphène sur substrat SiO_2 couverte par du nitrure de bore hexagonal (BN).

R. 1.3 Préparation du graphène

R. 1.3.1 Exfoliation

Exfoliation mécanique est une des méthodes les plus utilisées pour fabriquer des échantillons de graphène. Utilisation du ruban adhésif, de minces couches de graphite pyrolytique hautement orienté (HOPG) ont été clivés avec le processus de pelage répété et jusqu'à obtenir la couche unique, des échantillons de bicouche ou multicouche graphène nécessaires. Le graphène exfolié montre de haute qualité avec peu de défauts contenus, ce qui conduit à des propriétés électroniques extraordinaires pour la recherche. Exfoliation mécanique est une méthode de faible coût et aucun équipement spécial n'est nécessaire, tandis que la difficulté d'obtenir une série de films de graphène identiques limite cette méthode pour la production à grande échelle.

R. 1.3.2 Dépôt en phase vapeur chimique

Habituellement, le graphène a été déposé sur le substrat métallique par un procédé de CVD et ensuite transférée à un autre substrat. Spécialement, le graphène cultivé sur Cu lame expositions hautement continue aux joints de grains, à faible solubilité du carbone et un bon contrôle de couches de graphène. Généralement, il existe deux méthodes développées pour transférer le graphène comme cultivés sur Cu lame sur des substrats cibles, le processus de transfert PMMA-assistée est utilisé pour préparer graphène à petite taille (centimétrique), tandis que la méthode de transfert roll-to-roll peut produire graphène en grand format (jusqu'à 30 pouces). Le graphène sur des feuilles de cuivre a été revêtue avec le PMMA et ensuite flotter en solution aqueuse, après que les feuilles ont été enlevées de Cu, le graphène a été transféré sur le substrat SiO_2/Si. Comme

pour le procédé de transfert assisté PMMA, une pellicule de polymère est collée à la surface de graphène, et le mettre dans une solution de persulfate d'ammonium pour enlever les feuilles de cuivre. En fin de compte, le support de polymère a été retiré et graphène est transféré sur le substrat de cible. Il est intéressant de souligner que les résidus de PMMA sur la surface de graphène sont difficiles à être complètement supprimé. Cela conduira à dopage chimique dans le graphène et modifier ses propriétés.

R. 1.3.3 Graphène épitaxiale sur carbure de silicium

Graphène épitaxiale peut être facilement formée sur carbure de silicium en chauffant directement le substrat de SiC à une température élevée sous vide ou dans une atmosphère de gaz inerte, puis les atomes de silicium peut se sublimer à partir du substrat, et les atomes de carbone restants peuvent former le graphène épitaxie spontanément la surface du substrat de SiC. Monocristallin 6H-SiC et 4H-SiC sont tous les deux utilisés pour préparer graphène sur la surface du substrat. Traditionnellement, cette méthode peut être classé en deux types: graphène sur Si visage et graphène cultivé sur C surface. Sur la surface de terminaison Si, le graphène montre un bon contrôle de l'épaisseur, haute homogène et présente de bonnes propriétés de transport. Mais il existe une couche de carbone tampon entre graphène et SiC. Alors que sur la surface de terminaison C, le graphène a tendance à former la structure multicouche, et les couches ne sont pas homogènes. En outre, l'effet de sublimation de sur-axe et hors axe substrats de SiC conduit à la qualité différente des feuilles de graphène. Le substrat SiC dans l'axe présent beaucoup d'effet de l'étape de trousseau, et la formation de couches de graphène continues sont empêchés. Bien que le substrat de SiC hors-axe contient beaucoup moins d'étapes et l'effet de trousseau est réduite.

R. 1.3.4 Le graphène sur un substrat de nitrure de bore

Le nitrure de bore hexagonal est un isomorphe de graphite isolant et présente structure réticulaire en nid d'abeilles occupé avec des atomes de bore et d'azote, la constante de maille est de 1,8% plus longue que celle de graphène. L'énergie différent des atomes du bore et de l'azote conduit à grande largeur de bande interdite de 5,97 eV et 1,7 % mésappariement avec du graphite. En outre, la surface ultra - plate de h -BN pourrait supprimer l'ondulation du graphène, et les résultats de liaison ioniques dans liaisons pendantes et les pièges de charge presque libre, ces propriétés uniques construisent h-BN comme un substrat idéal pour soutenir le graphène. Cette méthode est

adaptée pour la recherche en laboratoire qui poursuit la mobilité d'enregistrement et de nouveaux phénomènes physiques. On a obtenu les plus hautes mobilités porteuse 500,000 $cm^2 V^{-1} s^{-1}$ de graphène sur h-BN, et l'effet Hall Quantique fractionnaire anomal a également été observé.

R. 1.4 Modulation des propriétés du graphène

Les études de modulation des propriétés de graphène ont attiré beaucoup plus d'attention au cours des dernières années. Plusieurs types de procédés ont été employés, par exemple: le champ électrique, électrochimique, le dopage chimique, l'irradiation et l'ingénierie d'interface. Le couplage d'électron-phonon réglable de graphène a été observé dans les spectres de Raman en appliquant un champ électrique externe. Le graphène décoré de palladium préparé par un procédé électrochimique révèle la diminution de la résistance maximale et sensible à différentes atmosphères de gaz. Le graphène fabriqué sur différents substrats montre l'effet de l'ingénierie. Les spectres Raman exposent une variation significative de la position, l'intensité et la largeur de bande. Le niveau de Fermi peut aussi être contrôlé dans la plage de -130 mV à 90 mV. Dans cette thèse, l'irradiation d'ions induites par dopage chimique a été observé dans le graphène sur un substrat de SiO_2, et l'influence de l'irradiation par faisceau d'électrons sur le graphène cultivés sur substrat de SiC a également été étudiée.

R.2 Méthodes Expérimentales

R.2.1 Irradiation

L'irradiation implique le processus que particules énergétiques interagissent avec les matériaux cibles, qui entraîne la modification de la structure, et en outre module les propriétés électriques, chimiques, optiques, etc. Il fournit un outil utile pour étudier les propriétés de base ou décorer la surface des matériaux cibles. Par ailleurs, cette méthode peut être utilisée pour développer divers types de fonctions pour des applications particulières. Selon le type de niveau d'énergie et la source, l'effet de l'irradiation est différent et peut être appliqué dans différents domaines. L'implantation ionique est principalement utilisé pour introduire le dopage contrôlable dans un substrat et de moduler les propriétés électroniques. L'irradiation des aliments est une technologie qui est largement utilisé pour réduire ou détruire les microorganismes pathogènes, les bactéries et les insectes, et d'améliorer ainsi la qualité et la durée de vie de plus en plus des aliments. Dans l'agriculture, l'irradiation permet de développer de nouveaux produits et d'améliorer la production

des cultures. Dans la zone de la médecine, l'irradiation est utilisée pour le diagnostic, la radiothérapie et la stérilisation. Dans cette thèse, la modulation des propriétés structurelles et de transport du graphène a été étudiée par l'ion et l'irradiation d'électrons, en attendant recuit fournit une méthode pratique pour restaurer ces propriétés. Les résultats observés indiquent application hautement potentielle dans des dispositifs de mémoire et de logique, transistors et des circuits intégrés à base de graphène.

R.2.1.1 Ion Irradiation

L'irradiation d'ion est une de la technologie la plus utilisée pour modifier les propriétés de matériau cible. Selon la masse des ions, les ions utilisés dans l'irradiation sont divisés en deux catégories: les ions lourds et les ions légers. Habituellement, le H, He et parfois ions Li sont considérés comme des ions légers, tandis que les autres ions d'éléments chimiques sont classés comme des ions lourds, tels que C, N et ions Ne, etc. Un autre facteur important qui influe sur l'effet irradiation est de l'énergie, normalement l'énergie des ions inférieure à 30 keV est appelée basse énergie, tandis que l'énergie supérieure à 30 keV et atteindre parfois MeV et même GeV est considérée comme haute énergie. Aussi la dose joue un rôle crucial sur l'effet de l'irradiation. Irradiation à faible dose conduit à une petite quantité de défauts formés dans le matériau de la cible et effectue une modification mineure des propriétés. Le moyen d'irradiation à forte dose un certain nombre d'ions frappent la même zone une fois et se traduit par le changement majeur de la structure du matériau de cible. Dans cette thèse, faible consommation d'énergie de 5,4 keV irradiation ionique He^+ a été réalisée pour adapter les propriétés du graphène cultivés substrat SiO2 par la méthode CVD. La source d'ionisation Penning ou Philips Gauge (PIG) a été utilisée pour créer des ions He^+ dans nos expériences. Penning ionisation est un processus de collision atomique fondamentale qui implique la réaction photochimique entre excité atome A* (A a absorbé un photon) avec un atome cible B, conduit à la formation des atomes excités A, cation B+ et d'un électron e-. En même temps, le processus se produit dans l'état où l'énergie des métastables atomes A est supérieure à l'énergie d'ionisation de l'atome B.

$$A^* + B \rightarrow A + B^+ + e^- \qquad (2)$$

Typiquement, une source de Penning est constitué de fer annulaire de la cathode (ou deux cathodes se faisant face), l'anode en acier inoxydable, et le samarium cobalt aimant permanent.

R.2.1.2 Electron Irradiation

L'irradiation d'électrons est un procédé qui comprend l'accélération des électrons à une certaine énergie et bombarde le matériau de cible. Comme la masse de l'électron est beaucoup plus léger que l'ion, le résultat de dommages causés par une irradiation par faisceau d'électrons est moins nocif que l'irradiation d'ions. En outre, l'irradiation d'électrons n'entraîne pas de dopage chimique dans le graphène par rapport à une irradiation d'ions. Différentes approches peuvent être utilisées pour effectuer l'irradiation d'électrons, telles que la microscopie électronique à transmission (TEM), microscopie électronique à balayage (MEB) et des installations spécifiques de haute énergie, etc. Dans nos expériences, le microscope électronique SEM FEG Philips XL30S balayage (MEB) a été utilisé à irradier le graphène épitaxiale développé sur carbure de silicium. Le faisceau d'électrons est émis à partir du canon aux électrons, ensuite la lentille et bobines de déviation électromagnétiques sont utilisées pour contrôler le trajet de déplacement des électrons et atteindre le graphène sur la platine porte-échantillon.

R.2.2 Recuit

Recuit se réfère au processus de traitement thermique qui vise à soulager le stress, augmentation de ductilité et de la douceur, l'homogénéisation et la recristallisation, etc. Il est largement utilisé dans la métallurgie et la science des matériaux. Typiquement, un processus de recuit complète se compose de trois étapes: chauffage de l'échantillon à la température désirée, puis de maintien à cette température pendant suffisamment de temps, à la fin, refroidissement de l'échantillon à une certaine température (généralement de la température ambiante). Les taux de chauffage, la température de maintien, le temps de recuit et taux de refroidissement sont les paramètres les plus importants qui influencent l'effet de recuit. Récemment, le recuit est couramment utilisé pour éliminer la contamination et d'améliorer la propreté de la surface de graphène, quant à la tension entre le substrat et le graphène peut être modulée par ce procédé de traitement thermique.

R.2.3 Caractérisation Structurale

R.2.3.1 Spectroscopie Raman

Spectroscopie Raman est une technologie spectroscopique basée sur la diffusion inélastique ou Raman Effet, et couramment utilisée pour étudier les mouvements moléculaires, en particulier les transitions en basse fréquence de vibration, de rotation et d'autres. Un faisceau de lumière monochromatique (généralement laser) irradie l'échantillon et provoque l'interaction entre les photons et les molécules qui se traduisent par des changements de fréquence de la lumière incidente, qui est appelé diffusion inélastique ou Raman effet. Typiquement, un système Raman est constitué de quatre composantes principales: source de lumière (laser), le système d'irradiation et de l'optique de collecte de lumière, filtre d'émission ou d'un spectrophotomètre, et des détecteurs (Charge Coupled Device (CCD) ou photomultiplicateur (PMT)). Dans le graphène, la spectroscopie Raman est habituellement utilisée pour évaluer la qualité de l'échantillon de graphène, tels que le nombre et l'orientation des couches, les défauts et Type bord. Plus important encore, la spectroscopie Raman présente un outil puissant pour comprendre l'effet du champ électrique et magnétique, dopage chimique, et le contraint dans le graphène, et fournit des informations sur la façon de moduler les propriétés du graphène. La caractéristique la plus importante de spectres Raman du graphène vierge est le pic G et 2D, pour le graphène avec des défauts, le pic de D et parfois pic D ' sont observées dans les spectres Raman. Le G bande qui est d'environ 1580 cm^{-1}, résulte de la vibration dans le plan de sp^2 liés C atomes et doublement dégénère (E_{2g}) mode de phonons au centre de la zone de Brillouin. Le pic de D (environ 1350 cm^{-1}) est lié aux modes de cycles à six atomes de respiration et est activé par défaut dans le graphène. Il vient du phonon autour du point de la zone de Brillouin K et est activé par double résonance. La bande de 2D (environ 2700 cm^{-1}) est le deuxième ordre de D de pointe, les résultats de la dispersion intravalley de deux phonons dans la dynamique inverse, et la fréquence est deux fois d'un phonon D pic le intravalley de défaut assistée.

R.2.3.2 X-ray Spectroscopie Photoélectronique

Spectroscopie de photoélectrons X (XPS), aussi connu comme spectroscopie électronique pour analyse chimique (ESCA), est une technique d'analyse de surface largement utilisée pour étudier la composition élémentaire et de l'état chimique sur la surface du matériau. Le photon de la lumière incidente interagit avec l'électron orbital et transfère l'énergie d'électrons, puis provoque l'émission d'un électron orbital de l'atome, ce procédé est appelé émission photoélectrique et la technique XPS est basé sur cet effet. Un instrument XPS commerciale est généralement composé

de source de rayons X, la chambre d'introduction d'échantillon, un système ultravide (UHV), une lentille de collecte d'électrons, l'analyseur d'énergie, le système de détecteur d'électrons, le système commandé par ordinateur et d'autres composants supplémentaires. Dans cette thèse, XPS a été utilisée pour étudier la composition élémentaire de graphène préparé par CVD et que, après l'irradiation et recuit, le changement de la concentration de l'élément de carbone et de l'oxygène sur la surface de graphène a fourni des preuves puissantes pour l'irradiation induite par le dopage chimique puis réduite par recuit.

R.2.3.3 La Microscopie à Force Atomique

La microscopie à force atomique est un type de microscopie à sonde de balayage (SPM) qui sert à former une image topographique surface en trois dimensions (3D) et déterminer la rugosité de la surface. Cette technique fait usage de la force atomique entre la pointe de sonde et l'échantillon et la forme de l'image à résolution atomique de la surface de l'échantillon. Typiquement, un instrument de l'AFM est composé d'un faisceau laser, de consoles, pointe, scanner piézoélectriques, détecteur de photodiode et le contrôleur de l'ordinateur. La pointe de la sonde est placée sur l'extrémité d'un cantilever, et la force entre la surface de la pointe et la surface de l'échantillon conduit à la déflexion du cantilever. Ainsi, la force mesurée est déterminée par la constante de ressort du bras de levier, de la distance entre la pointe et la surface de l'échantillon. Dans cette thèse, l'AFM en mode taraudage a été réalisée en vierge, irradié graphène et que, après recuit, la rugosité obtenu montre le graphène devient plus propre après l'irradiation et de recuit.

R.2.4 Propriétés de Transport

R.2.4.1 Propriétés électriques

Les propriétés électriques du graphène après irradiation ont été mesurées par Keithley 2400 connecté à une station de la sonde de micromanipulateur, et la méthode à deux sondes a été employé pendant les mesures. Toutes les mesures ont été effectuées en atmosphère ambiante.

R.2.4.2 Magnétorésistance

Les électro-aimants sont alimentés par la puissance qui est sous le contrôle du SR830 amplificateur de verrouillage dans le mode de sortie en courant continu. Le Keithley 2400 est utilisé pour des signaux de courant ou de tension d'entrée à travers les ports d'entrée du

connecteur. Avec un capteur placé sur le centre de l'électro-aimant, le champ magnétique généré peut être mesurée par le voltmètre HP 34902. Dans cette thèse, la magnétorésistance du graphène a été mesurée en appliquant divers drain à courant de source (I_{ds}).

R.3 Influence de basse énergie des ions He^+ irradiation sur les propriétés structurelles de graphène

R.3.1 Low Energy ions He^+ irradiation

La faible énergie des ions He^+ irradiation a été effectuée dans les échantillons de graphène à température ambiante (RT) dans un système à vide élevé avec une pression de base de 2×10^{-7} mbar et une pression de fonctionnement de 1×10^{-6} mbar. L'irradiation est d'une grande homogénéité et une faible divergence dans une zone de 2×2 cm^2. Une tranche du graphène a été coupée à plusieurs pièces dans 5 mm × 5 mm de taille. Ils ont été irradiés avec He^+ énergie des ions de 5,4 keV et la densité de dose allant de 4×10^{12} He^+/cm^2 à $2,5 \times 10^{13}$ He + / cm^2. La durée d'irradiation est d'environ 1 s pour le dosage de 10^{13} He^+/cm^2.

R.3.2 X-ray Spectroscopie Photoélectronique

Figure R.2 (a) montre la micrographie optique du graphène de PMMA transféré, où les résidus de PMMA (bleu) sur la surface de graphène peuvent être observés. Figure R.2 (b) montre les relevés XPS de l'échantillon non irradié de graphène, le graphène à la dose de $2,5 \times 10^{13}$ He^+/ cm^2 et que recuit après la dose de $2,5 \times 10^{13}$ He^+/cm^2. Seuls les pics O1s, C1s, Si2s et Si2p ont été détectés dans les enquêtes de XPS, qui suggèrent qu'il n'y a pas d'autres impuretés ont été introduits dans le graphène au cours des processus d'irradiation et de recuit. Comme montré dans le tableau R.1, le rapport atomique C diminue après l'irradiation, tandis que les deux rapports de Si et O augmentent. Comportements similaires sont observés que les échantillons sont recuits après l'irradiation. Après la dose de $2,5 \times 10^{13}$ He^+/cm^2 et recuit, le rapport C atomique diminue de 10,5±0,2%. Il indique la quantité de résidus de PMMA diminue à la fois l'irradiation et après recuit. Figures R. 2 (c) et 2 (d) spectres noyau de niveau C 1s spectacle et de 1 O des échantillons de graphène, respectivement. L'énergie et la surface du pic rapport de liaison de C 1s composants n'est répertorié dans le tableau 2. Pour l'échantillon de graphène à la dose de $2,5 \times 10^{13}$ He^+/cm^2, le rapport de surface de sp^2 hybride de liaison C-C (284,3 eV) diminue tandis que celui de

hybride sp^3 de C-C(H) liaison C-C=O et C-O-C(H) des groupes augmente. Il indique que l'irradiation conduit à l'oxydation de graphène à partir des groupes fonctionnels dans les résidus de PMMA. Après le recuit de l'échantillon irradié, le rapport de surface de sp^2 hybrides de liaison

Table R.1 Proportions en atomes de Si, C et O dans l'échantillon non irradié de graphène, le graphène irradiées à la dose de 2,5 $\times 10^{13}$ He^+/cm^2 et que recuites après la dose de 2,5 $\times 10^{13}$ He^+/cm^2.

	Rapport atomique de Si (%)	Rapport atomique de C (%)	Rapport atomique de O (%)
non irradié	23.6 ±0.1	36.0 ±0.2	40.4 ±0.1
2.5 $\times 10^{13}$ /cm^2	27.2 ±2.9	23.9 ±3.6	48.9 ±2.8
recuit	33.4 ±0.1	10.5 ±0.2	56.1 ±0.2

Table R.2 Energie reliure et de rapport de surface de composants en C 1s graphène non irradié, le graphène à la dose de 2,5 $\times 10^{13}$ He^+/cm^2 et que recuit après la dose de 2,5 $\times 10^{13}$ He^+/cm^2.

		C1	**C2**	**C3**	**C4**	**C5**
non irradié	Reliure énergie (eV)	284.6 ±0.1	285.0 ±0.1	285.7 ±0.1	286.7 ±0.1	289.1 ±0.1
	Rapport de surface (%)	53.2 ±2.1	17.2 ±2.1	8.9 ±1.7	10.5 ±1.9	10.2 ±0.3
2.5 $\times 10^{13}$ /cm^2	Reliure énergie (eV)	284.3 ±0.1	285.0 ±0.1	285.7 ±0.1	286.7 ±0.1	289.0 ±0.1
	Rapport de surface (%)	24.4 ±3.8	29.0 ±6.3	26.7 ±1.7	14.9 ±2.6	4.9 ±1.9
2.5 $\times 10^{13}$ /cm^2 recuit	Reliure énergie (eV)	284.3 ±0.1	285.0 ±0.1	285.7 ±0.1	286.7 ±0.1	
	Rapport de surface (%)	64.1 ±2	20.8 ±2	6.3 ±0.6	8.8 ±0.3	

C-C augmente alors que celui de sp^3 hybride de C-C(H) liaison C-C=O et C-O-C(H) des groupes diminue. Il suggère que l'irradiation induite par oxydation dans le graphène est réduite par recuit. Le rapport de surface de O-C=O liaison diminue après irradiation et disparaît presque après recuit, qui peut être lié à la décomposition des groupes fonctionnels carboxyle et méthyl dans les résidus

de PMMA. Sur la figure R.2 (d), l'augmentation des 1 O signaux du SiO_x (532,7 ± 0,1 eV) indique également la diminution de la quantité des résidus PMMA.

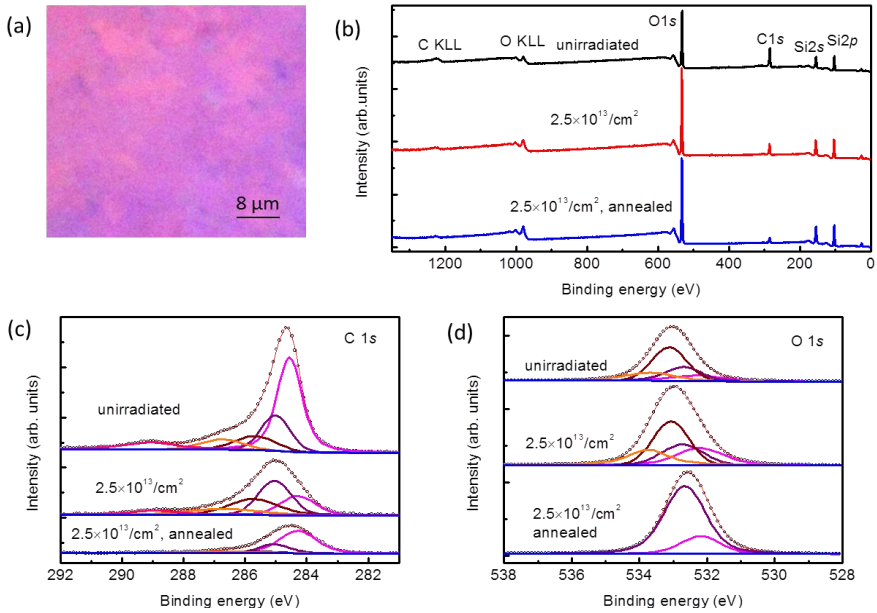

Figure R.2 (a) Micrographie optique de PMMA transféré CVD graphène sur substrat Si/SiO_2. (b) Enquêtes XPS (c), (d) C 1s et O niveau de base 1s spectres des graphène non irradié, le graphène à la dose de 2,5 × 10^{13} He^+/cm^2 et que recuit après la dose de 2,5 × 10^{13} He^+/cm^2.

R.3.3 Spectroscopie Raman

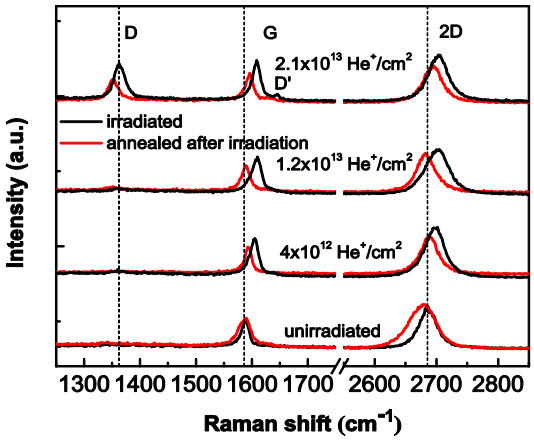

Figure R.3 Evolution des spectres Raman du graphène, graphène irradiés et irradiés (lignes noires) avec différentes densités de dose après recuit (lignes rouges).

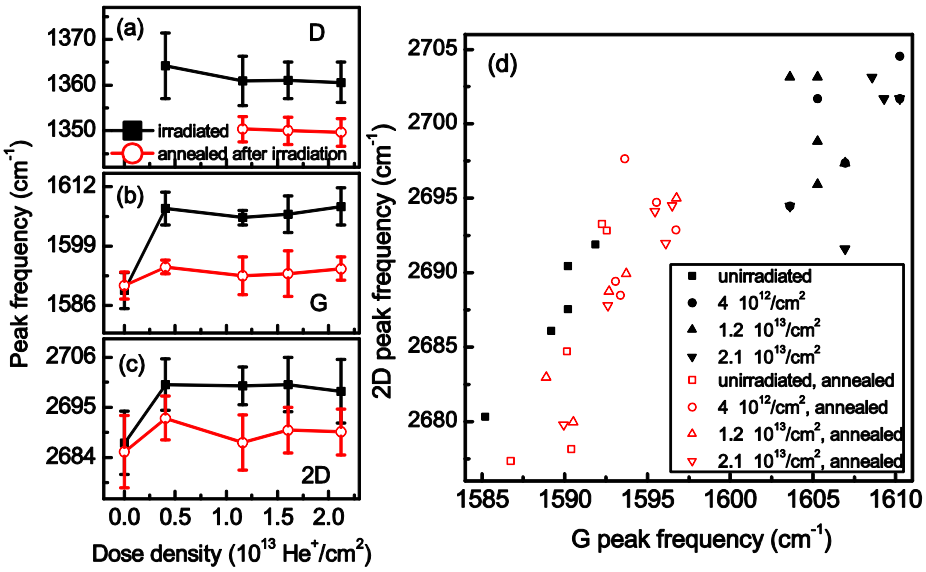

Figure R.4 Dépendances de densité de la dose des fréquences de (a) pic de D, (b) et le pic G (c) 2D pour le graphène irradié (solide noir) et le graphène recuit après irradiation (rouge ouverte).

Comme montré dans la Figure R.3, les pics intravalley G de la bande à ~ 1590 cm^{-1} pour le graphène non irradié. Le pic de D à ~ 1362 cm^{-1} augmente de manière significative pour la densité de dose de 2,1 × 10^{13} He^{+}/cm^{2}, et le pic D'apparu vers 1640 cm^{-1} correspond à une intravalley processus à des phonons dans les défauts assistés de graphène. La bande 2D autour ~ 2690 cm^{-1} est le deuxième ordre de la bande de D. On peut voir le comportement de bande décalage de la Figure R.3 après irradiation et recuit. Comme montré dans la R.4, le bleu-décalage de bande du G a été observé, qui peut être due à la fois électronique et le trou le dopage dans le graphène, tandis que le bleu-shift dans la bande 2D peut être causé par trou dopage. Il suggère que le trou dopage est une contribution importante aux décalages bleus observés dans les deux groupes G et 2D en raison de couplage électron-phonon. Comme montré dans les résultats de l'XPS, le groupe fonctionnel carboxyle résiduel de PMMA résidus sur la surface de graphène peut être la source principale de trou dopage. Les liaisons chimiques entre des groupes fonctionnels de résidus PMMA et graphène pourraient être formés en raison de l'irradiation d'ions, qui conduit à dopage dans le trou graphène. L'absorption d'oxygène et de H_2O dans le graphène après irradiation peut à petite contribution à trou dopage. Après le recuit du graphène irradié, le D, des bandes G et 2D dans les spectres Raman retour vers fréquence inférieure. Les rouges-quarts des deux bandes G et 2D du graphène irradié après recuit sont liées à la réduction des frais de transfert de dopage dans le graphène. Comme les résultats XPS montrent, les résultats de recuit

dans la décomposition des groupes fonctionnels carboxyle et méthoxy. Il suggère que les obligations d'irradiation induite entre les groupes fonctionnels à partir de résidus de PMMA et graphène peuvent être brisées après recuit. La désorption de groupes fonctionnels de graphène est dominante pendant le processus de recuit sous vide, ce qui conduit à la réduction du dopage trou et décalage vers le rouge dans des bandes Raman. Il faut remarquer que les comportements non-monotones pour les deux fréquences G et 2D bande restent après recuit. Il indique que l'irradiation d'ions conduit également à l'effet irréversible dans le graphène, c'est à dire l'effet de dopage est partiellement réversible.

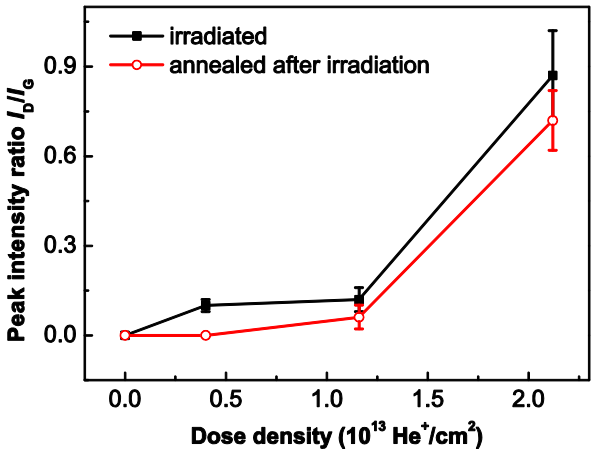

Figure R.5 Dependences of the intensity ratio of the D peak to the G peak (I_D/I_G) on dose density of the irradiated graphene (black solid) and the graphene annealed after irradiation (red open).

Comme la Figure R.5 montre, avant le recuit, le rapport I_D/I_G est inférieur à 0,1 comme le dosage est inférieur à $1,2 \times 10^{13}$ He^+/cm^2, qui indique peu de défauts de graphène. Le rapport I_D/I_G augmente beaucoup lors que le dosage est supérieure à $1,2 \times 10^{13}$ He^+/cm^2, qui indique l'augmentation de la quantité de défauts. L'augmentation du taux de I_D/I_G indique les moyennes entre les défauts de distance diminue. Pour la densité de la dose de $2,1 \times 10^{13}$ He^+/cm^2, le rapport de I_D/I_G est d'environ 0,87, et la distance moyenne inter-défaut est d'environ 20 nm. Après recuit, les ratios I_D/I_G de la diminution de graphène irradié. Pour la densité de la dose de $2,1 \times 10^{13}$ He^+/cm^2, le rapport de I_D/I_G est d'environ 0,72 après le recuit, et la distance moyenne inter- défaut calculée est environ 26,7 nm, qui est supérieure à celle avant le recuit. Il indique que la quantité de défauts diminue après recuit.

L'influence de l'irradiation et le processus de recuit a également été étudiée. Un échantillon de graphène a été irradié à la densité de la dose de 2,1 × 10^{13} He^+/cm^2 et ensuite recuit à 300 ℃ pendant 1 h. Tandis que l'autre a été traité par un procédé d'inversion, irradié à la densité de la dose de 2,1 × 10^{13} He^+/cm^2 et ensuite recuit à 300 ℃ pendant 1 h. Il n'y a pas de différence significative entre les spectres Raman des deux échantillons de graphène. Ces résultats fournissent la preuve que les effets de l'irradiation et de recuit ont une faible relation avec les processus. L'irradiation à dose élevée à la densité de la dose de 1 × 10^{14} He^+/cm^2 et 1 × 10^{15} He^+/cm^2 a également été effectuée sur le graphène, respectivement. Les résultats indiquent que le graphène a été largement détruite après être irradié à la densité de la dose au-dessus de la dose de × 10^{14} He^+/cm^2, la structure a été totalement changée et il y avait quelques graphène restés sur le substrat SiO_2/Si.

R.3.4 Microscopie à Force Atomique

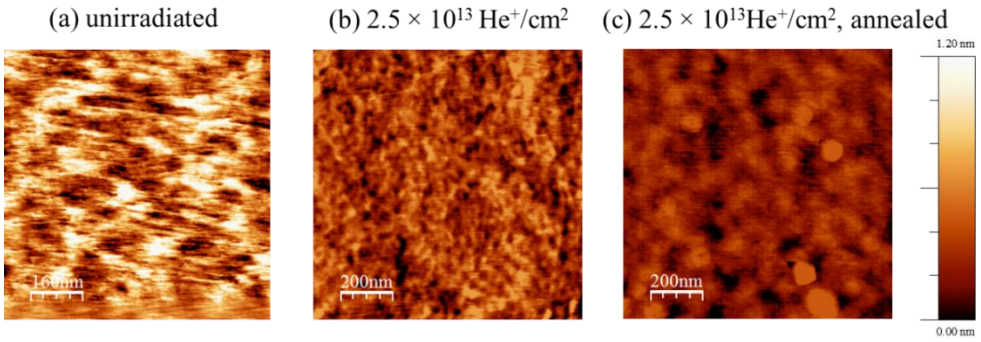

Figure R.6 AFM images du graphène non irradié, le graphène à la dose de 2,5 × 10^{13} He^+/cm^2 et que recuit après la dose de 2,5 × 10^{13} He^+/cm^2.

La moyenne quadratique rugosité (RMS) de la surface de l'échantillon pour le graphène non irradié, le graphène à la dose de 2,5 × 10^{13} He^+/cm^2 et que recuit après l'irradiation sont 0,35 ± 0,17 nm, 0,20 ± 0,07 nm et 0,15 ± 0,05 nm respectivement. Il indique que l'irradiation ne provoque pas la surface rugueuse et la morphologie de surface devient lisse après recuit. La tache noire avec une hauteur zéro en images AFM (Figure R.6) des échantillons de graphène irradiées et recuits peut indiquer la présence de défauts dans le graphène. Compte tenu de la diminution de la quantité de carbone dans XPS, les résultats de l'AFM confirment que les résidus de PMMA sur la surface sont essentiellement éliminés après l'irradiation et recuit, qui conduit à lisser la morphologie de surface.

R.4 Influence de basse énergie des ions He^+ irradiation sur les propriétés de transport du graphène

R.4.1 Conductance électrique

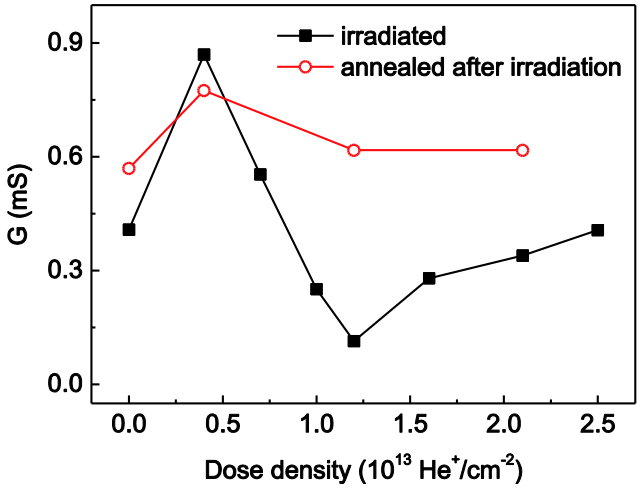

Figure R.7 Dépendances de densité de dose de conductance électrique du graphène irradié (carrés pleins) et ce recuit après irradiation (cercles ouverts) sous une tension drain-source de 0,1 V sans déclenchement.

Comme montré dans la Figure R.7, la conductance électrique montre dépendance non-mono tonique sur la densité de dose, qui reste après le recuit. Ce comportement est lié aux effets concurrentiels de concentration de porteurs, la mobilité et la diffusion de défaut. L'irradiation d'ions He^+ provoque la décomposition des résidus de PMMA et les résultats dans le trou dopage dans le graphène, qui conduit à l'augmentation de conductance à la densité de la dose de 4,0 × 10^{13} He^+/cm^2. En augmentant la densité de la dose de 1,2 × 10^{13} He^+/cm^2, la quantité de défauts et les troubles formées dans l'augmentation de graphène, qui conduisent à la diminution de la mobilité et améliore l'effet de diffusion de défauts, ce résultat dans la diminution de la conductance du graphène. Alors que continuer à augmenter la densité de la dose à 2,5 × 10^{13} He^+/cm^2, le dopage de trou dans le graphène devient plus important et les résultats dans l'augmentation de la conductance du graphène. Comme montré dans la figure R.3, le pic augmente considérablement D à la densité de la dose de 2,1 × 10^{13} He^+/cm^2, cela est lié à plus d'impuretés tels que O et H atomes ont été introduits dans le graphène à travers le trou dopage par l'irradiation.

R.4.2 Hystérésis électronique

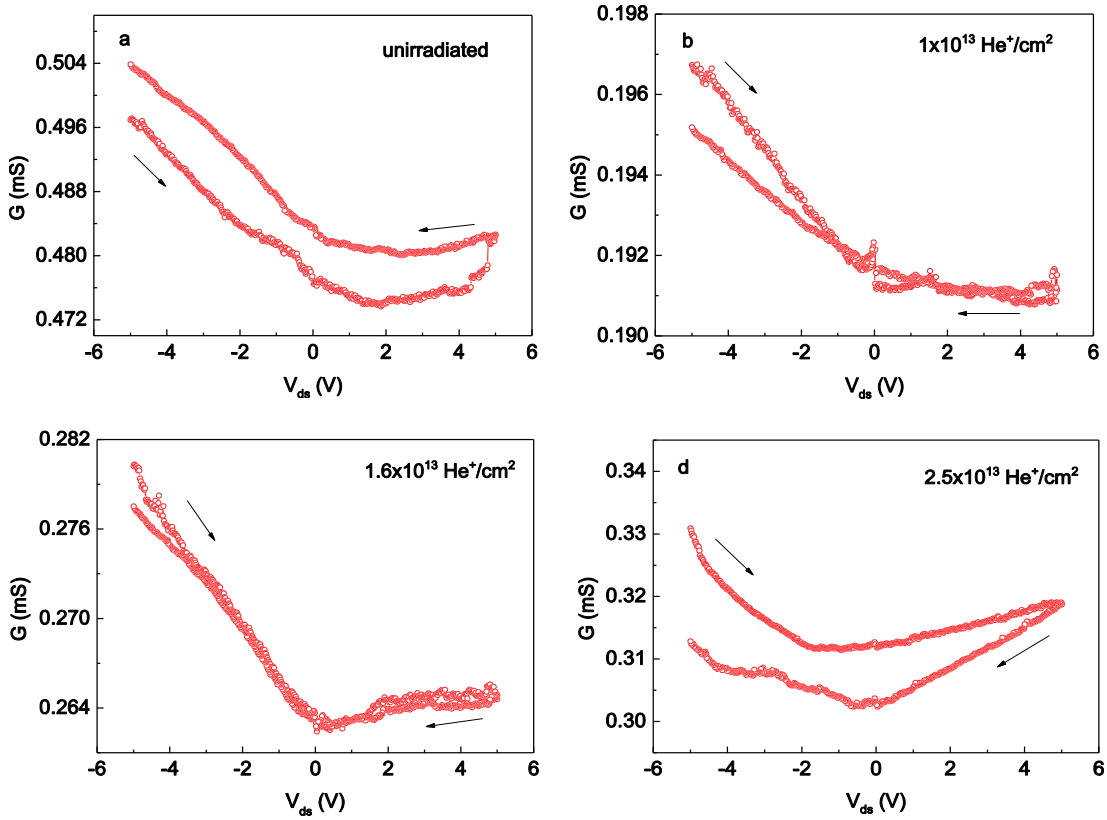

Figure R.8 La conductance en fonction de la tension drain-source (a) graphène non irradié et graphène irradié avec de différentes densités de dose (b) 1×10^{13} He^+/cm^2 (c) $1{,}6 \times 10^{13}$ He^+/cm^2 (d) $2{,}5 \times 10^{13}$ He^+/cm^2. En avant et en arrière direction de balayage sont indiquées par les flèches noires.

Comme montré dans la Figure R.8, le comportement d'hystérésis électronique affaibli d'abord, puis augmente, après l'augmentation de la densité de la dose. Pour le graphène non irradié, l'accusation processus de piégeage se produisant à l'interface joue le rôle le plus important sur le comportement d'hystérésis, alors que la recharge capacitif et réaction redox interfaciale montrent beaucoup moins de contribution à ce phénomène de transfert de charge. Le tunnel peut également se produire en raison des défauts initiaux résultent du processus de Fabrication. Bien irradier graphène à la densité de la dose de 1×10^{13} He^+/cm^2 et $1{,}6 \times 10^{13}$ He^+/cm^2, un petit nombre de défauts formés dans graphène, et induire effet tunnel entre les sites de défauts. Pendant ce temps, les résultats d'irradiation d'ions He^+ dans la décomposition des résidus de PMMA sur la surface de graphène et induit le dopage chimique en graphène, qui augmente encore la densité des défauts et impuretés, ainsi l'effet tunnel devient plus prononcé. Les atomes H et O à partir de

résidus de PMMA peuvent également contribuer à la réaction redox interfaciale. Sous faible irradiation dose, les deux principaux mécanismes: effet tunnel et de piégeage de charge en concurrence avec l'autre, ce qui entraîne dans le comportement d'hystérésis affaiblie. Après l'augmentation de la densité de la dose de $2,5 \times 10^{13}$ He^{+}/cm^{2}, un grand nombre de défauts formés et plusieurs impuretés dopées dans le graphène, qui rend l'effet tunnel jouer un rôle prépondérant sur le comportement d'hystérésis. De cette façon, l'influence de piégeage de charge est réduite, et le comportement plus significatif d'hystérésis électronique apparaît. Après recuit de la graphène irradié à la densité de la dose de 1×10^{13} He^{+}/cm^{2} à 300 ℃ pendant 1 h, comportement d'hystérésis supprimé de ce dispositif électronique de graphène a été observée. Ceci est lié à la réduction de niveau de dopage dans le graphène qui provient de la décomposition des résidus de PMMA, pendant ce temps, le recuit de restauration des défauts cristallins de graphène et réduit les pièges de charges sur le substrat SiO_2.

R.4.2.1 Taux de Balayage

Le comportement d'hystérésis électronique suit également une trajectoire de affaibli puis renforcé avec la diminution du taux de balayage. Lorsque le temps d'attente est de 50 ms, le piégeage de charge et le résultat d' effet tunnel dans le comportement d'hystérésis avec ΔV_{ds} de 0.1V, tandis que d'augmenter le temps d'attente pour 100 ms et 200 ms, la réaction redox interfaciale rivaliser avec la charge effet de piégeage, et conduire à un comportement d'hystérésis plus faible, en continuant à augmenter le temps d'attente de 500 ms, la réaction d'oxydo-réduction interfaciale présente plus d'influence que le piégeage de charge et un comportement d'hystérésis plus marqué électronique s'affiche.

R.4.2.2 Hystérésis électronique sous champ magnétique

L'hystérésis électronique de graphène non irradié sous champ magnétique différente a été mesurée, comme montré dans la Figure R.9. Le V_{ds} balaie de -1 V à 1 V, puis de nouveau à -1 V, étape de balayage est de 0,01 V, champ magnétique perpendiculaire externe (μ_0Hz) de 0,2 T, 0,4 T, 0,6 T, 0,8 T et T 1 ont été appliqués sur le dispositif de graphène non irradié. La différence de la résistance maximale (ΔR_{max}) dans la direction de balayage avant et en arrière V_{ds} montre une tendance d'augmentation avec le champ magnétique perpendiculaire. Cela peut être en raison du changement de la direction du mouvement des électrons ou des trous dans le graphène, qui

provient de la force de Lorenz tout un champ magnétique perpendiculaire externe est appliqué sur l'appareil, et les résultats dans le comportement de résistance d'hystérésis plus évident dans le graphène non irradié. En outre, nous avons également mesuré la dépendance Vds sur la résistance du graphène non irradié sous différent champ magnétique dans le plan et boucle d'hystérésis faible a été observée. Cela peut être même liée à la direction du champ magnétique dans le plan et le mouvement du support, ainsi la force de Lorenz est zéro et n'a pas d'influence sur le support, puis conduit à un comportement d'hystérésis électronique plus faible. Pour le graphène irradié à la densité de la dose de 2×10^{13} He^{+}/cm^{2}, le comportement d'hystérésis électronique ne montre pas d'amélioration évidente après application d'un champ magnétique perpendiculaire externe. Après avoir effectué l'irradiation sur le graphène, les atomes C, H et O provenant de la décomposition des résidus PMMA vont interagir avec les atomes de carbone dans le graphène, puis plus de défauts et d'impuretés seront formés dans le graphène, donc l'effet tunnel devient plus important. Bien que le champ magnétique perpendiculaire externe exerce une force de Lorenz sur les supports dans le graphène et change la direction de mouvement, tandis que du fait du grand nombre de défauts et d'impuretés, l'influence du champ magnétique est affaibli et conduit à des comportements électroniques d'hystérésis qui ne montre pas de changement évident lors de l'application du champ magnétique perpendiculaire.

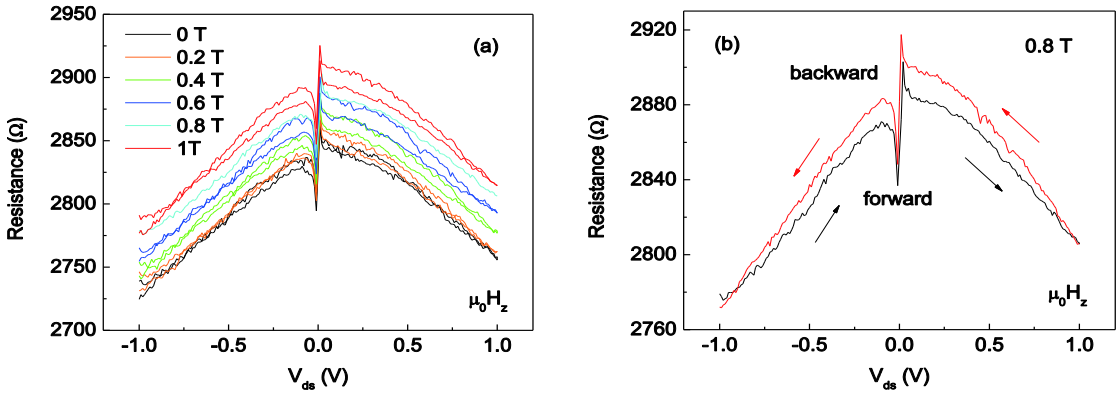

Figure R.9 (a) Le comportement de résistance d'hystérésis du graphène non irradié en fonction de Vds sous différents champs magnétiques perpendiculaires (b) Le détail de processus de comportement d'hystérésis du graphène non irradié mesurée sous 0,8 T champ magnétique perpendiculaire.

R.4.3 Magnétorésistance

La magnétorésistance du graphène non irradié montre faible dépendance à l'égard champ magnétique perpendiculaire et le drain au courant de la source à l'ordre de milliampères. Cela peut être lié à une faible distribution de charge homogène dans le graphène non irradié.

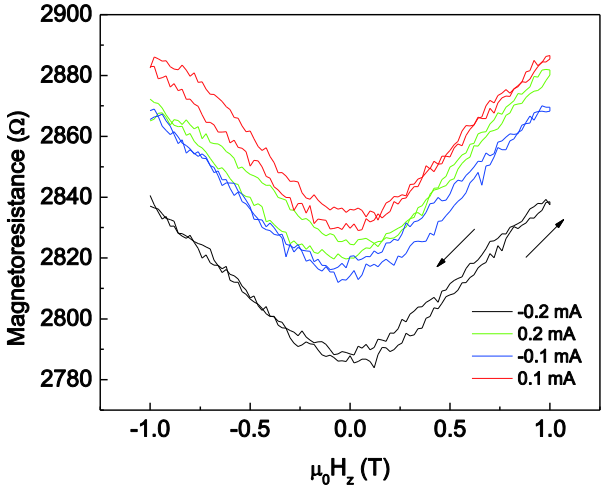

Figure R.10 La magnétorésistance de graphène non irradié en fonction du champ magnétique perpendiculaire à titre de vidange autre courant de source (I_{ds}).

R.5 Influence de l'irradiation par faisceau d'électrons sur les propriétés structurelles et Transport de graphène cultivés sur SiC Substrat

R.5.1 Irradiation par faisceau d'électrons

L'irradiation d'électrons a été effectuée par Philips sous FEG SEM degré de 8,6 × 10^{-6} mbar de vide, l'énergie des électrons est de 30 keV et le courant est de 16 nA. Le grossissement de 36 × a été utilisé, et a conduit à la plus grande zone irradiée de 3,4 × 2,6 mm^2. Tant faible dose et une irradiation à haute dose à l'ordre de $10^{13}/cm^2$ et $10^{16}/cm^2$ ont été réalisées sur le graphène cultivés sur substrat SiC.

R.5.2 X-ray Spectroscopie Photoélectronique

Comme montré dans la Figure R.11, C1s, O1s, Si2s et Si2p pics ont été détectés dans les enquêtes XPS. F1s pic a également été observée dans l'enquête, cela peut être dû au fait que substrat SiC a été nettoyé par une solution de HF pendant les processus de fabrication. Les ratios de Si, C et O atomes ne montrent pas de changement significatif après une faible dose et une

irradiation à forte dose (tableau R.3). Comme il n'y a pas de résidus de PMMA restés sur la surface du graphène, l'irradiation de la dose n'a pas entraîné de réaction chimique complexe dans le graphène cultivés sur substrat SiC. L'augmentation légère du ratio atomes O peut être liée à l'adsorption de plusieurs molécules d'O_2 et H_2O lorsqu'elle est exposée à l'environnement ambiant de l'air après l'irradiation.

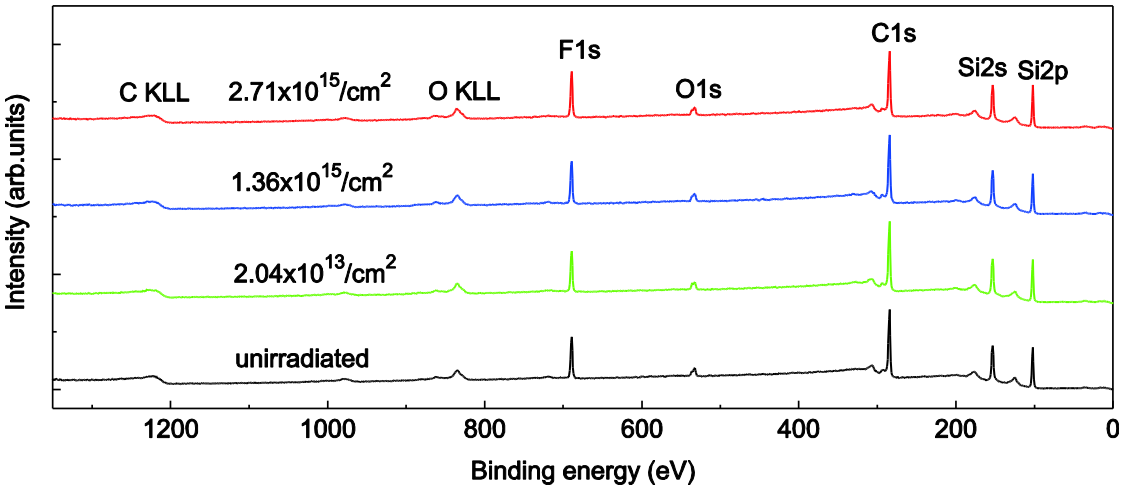

Figure R.11 Enquêtes XPS de graphène non irradié, le graphène irradié à la dose de 2.04 $\times 10^{13}/cm^2$, 1.36 $\times 10^{15}/cm^2$ et 2.71 $\times 10^{15}/cm^2$.

Table R.3 Ratios Atom de Si, C et O dans les échantillons de graphène ionisés et non ionisés.

	Rapport atomique de Si (%)	Rapport atomique de C (%)	Rapport atomique de O (%)
non irradié	30.3 ±0.2	60.9 ±0.3	8.8 ±0.1
2.04 $\times 10^{13}$ /cm^2	29.7 ±0.9	61.4 ±1.2	8.8 ±0.3
1.36 $\times 10^{15}$ /cm^2	29.1 ±2.1	61.4 ±2.7	9.5 ±0.3
2.71 $\times 10^{15}$ /cm^2	29.2 ±2.4	60.7 ±2.1	10.1 ±0.7

Comme montré dans la Figure R.12, l'intensité de liaison sp^2 C-C diminue évidemment après irradiation à forte dose, tandis que l'intensité de la liaison Si-C obligataire augmente beaucoup. C'est un gage de dose d'irradiation conduit à la rupture de la liaison sp^2 C-C dans le graphène, et plus encore emprunt Si-C formé dans le graphène. En outre, les liaisons pendantes C résultent de l'irradiation interagir avec les atomes de Si dans le substrat, donc plusieurs liaisons C-Si sont formées. Comme montré dans le tableau R.4, avec l'augmentation de la dose, la composition de

liaison C-C sp^2 diminue. Le rapport de surface de liaison Si-C montre une augmentation monotone par rapport à la dose non irradié et irradié graphène bas, passant de 24,1 % à environ 23,3 % et atteindre environ 38,8 % et 39,2 % à la fin. Ces résultats suggèrent en outre que l'irradiation à dose élevée rompt la structure cristalline de graphène, les liaisons C-C sp^2 sont brisées et forment la liaison Si-C, tandis que l'irradiation à faible dose permet une récupération de la structure de graphène.

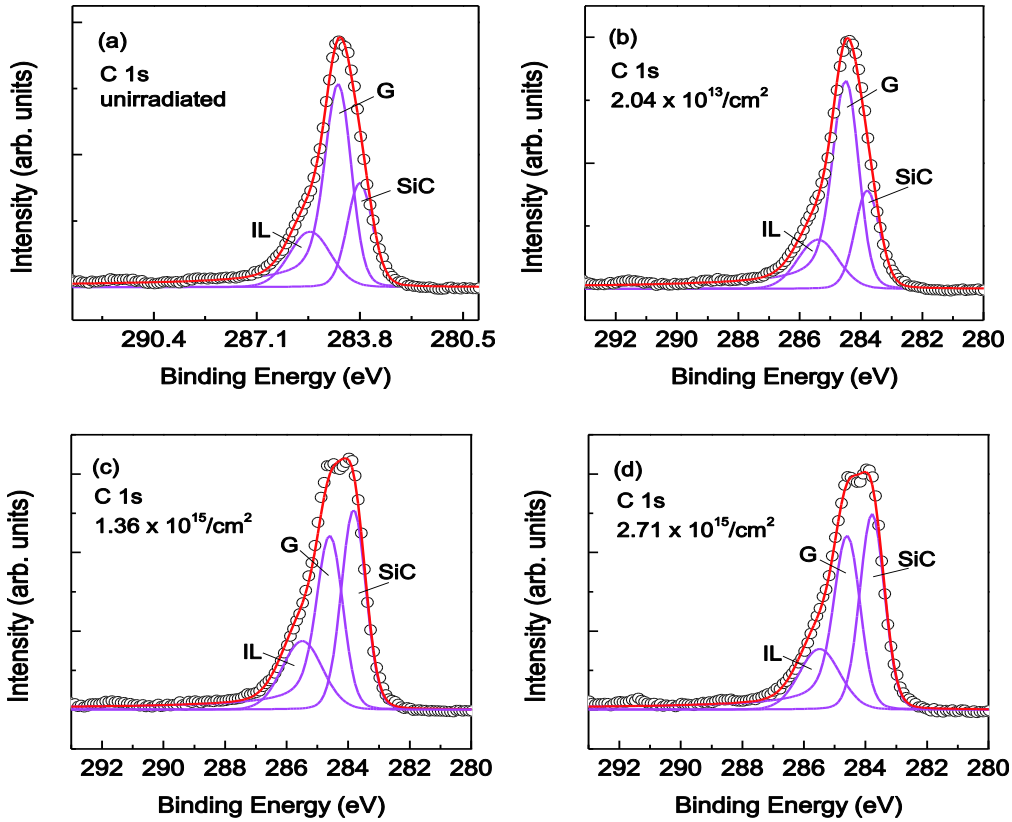

Figure R.12 XPS C niveau de base 1s spectres du graphène non irradié, le graphène irradié à la dose de $2.04 \times 10^{13}/cm^2$, $1.36 \times 10^{15}/cm^2$ et $2.71 \times 10^{15}/cm^2$.

Comme montré dans la Figure R.13, l'intensité de la liaison Si-C diminue après irradiation à faible dose, tandis qu'elle augmente beaucoup après l'irradiation à dose élevée de $1,36 \times 10^{15}$ /cm^2 et $2,71 \times 10^{15}$ /cm^2. L'intensité de la liaison Si-F montre la dépendance inverse de la densité de la dose, elle augmente après l'irradiation à faible dose, puis décroît après l'irradiation à forte dose. Ceci indique qu'un certain nombre d'atomes de F interagissent avec des atomes de Si dans le substrat après l'irradiation à faible dose. Bien à l'irradiation à haute dose, les interactions entre F et Si atomes sont supprimées, puis plusieurs liaisons Si-C sont formées.

Table R.4 Reliure énergie et de rapport de surface de composants en C 1s non irradié et le graphène graphène irradié à la densité de la dose de $2.04 \times 10^{13}/cm^2$, $1.36 \times 10^{15}/cm^2$ et $2.71 \times 10^{15}/cm^2$.

		SiC	**G**	**IL**
non irradié	Reliure énergie (eV)	283.8±0.1	284.4±0.1	285.4±0.1
	Rapport de surface (%)	24.1±1.8	55.4±2.2	20.5±2.9
2.04×10^{13} /cm^2	Reliure énergie (eV)	283.8±0.1	284.4±0.1	285.4±0.1
	Rapport de surface (%)	23.3±2.2	58.0±2.7	18.7±2.3
1.36×10^{15} /cm^2	Reliure énergie (eV)	283.8±0.1	284.5±0.1	285.5±0.1
	Rapport de surface (%)	38.8±3.1	39.8±3.4	21.4±3.1
2.71×10^{15} /cm^2	Reliure énergie (eV)	283.8±0.1	284.5±0.1	285.5±0.1
	Rapport de surface (%)	39.2±3.5	40.8±3.9	20.0±2.8

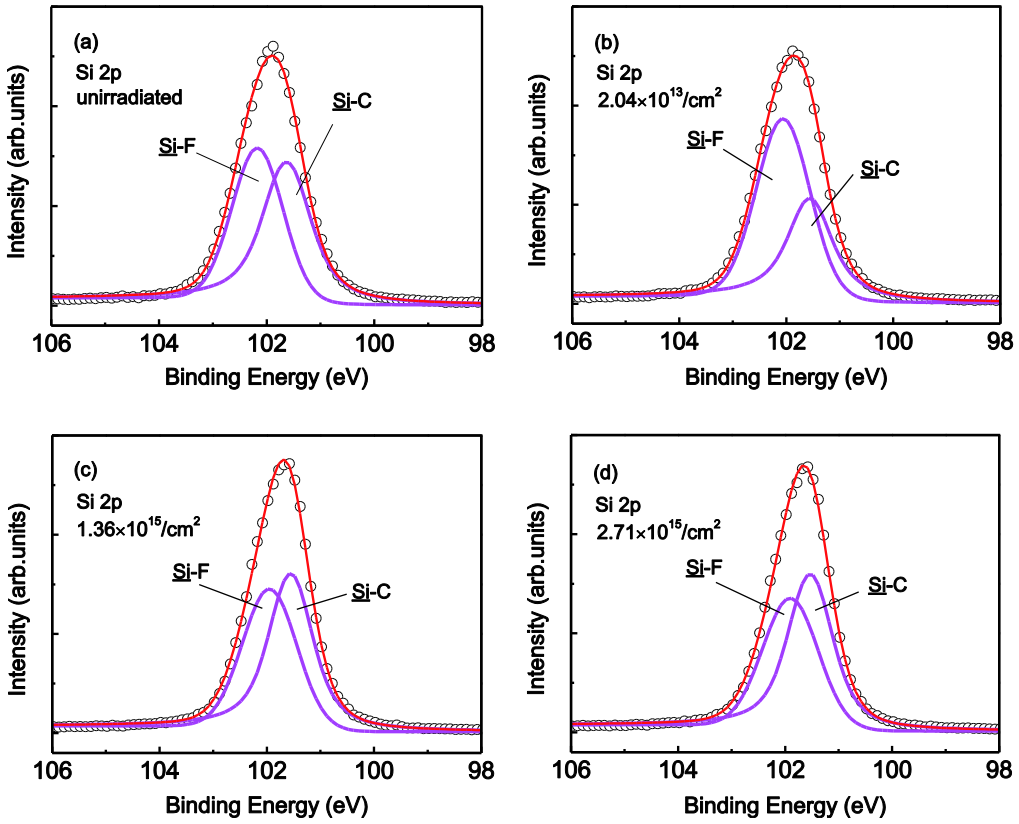

Figure R.13 XPS Si noyau niveau 2p spectres du graphène non irradié, le graphène irradié à la dose de $2.04 \times 10^{13}/cm^2$, $1.36 \times 10^{15}/cm^2$ et $2.71 \times 10^{15}/cm^2$.

R.5.3 Spectroscopie Raman

Comme montré dans la Figure R.14, pour le graphène non irradié, les pics G et 2D localisent autour des 1595.7 cm^{-1} et 2727.3 cm^{-1}. Il est intéressant de souligner que le pic 2D montre un changement élevé de ~ 40 cm^{-1} par rapport à 1580 cm^{-1} du graphène exfolié. Ceci est lié à une contrainte de compression uniforme dans le graphène épitaxiale sur SiC. Les deux autres pics qui sont d'environ 1516,6 cm^{-1} et 1708,7 cm^{-1} proviennent du substrat de SiC. Ces deux pics de SiC ont une large bande passante et les positions sont à proximité de la pointe G, ainsi chevauchement des trois pics observés dans le spectre Raman. La couche tampon sous le film de graphène contribue également aux courbes de Raman se chevauchent. Comme montré dans la Figure R.15, le comportement de décalage vers le rouge de pic G a été observé.

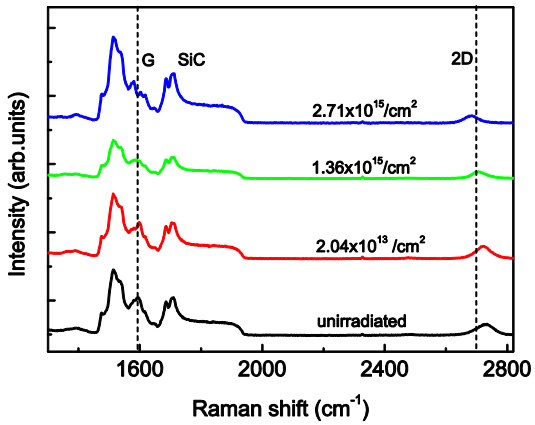

Figure R.14 Evolution des spectres Raman de graphène non irradié et irradié graphène avec différentes densités de dose: 2.04 $\times 10^{13}$ /cm^2, 1.36 $\times 10^{15}$ /cm^2 and 2.71 $\times 10^{15}$ /cm^2.

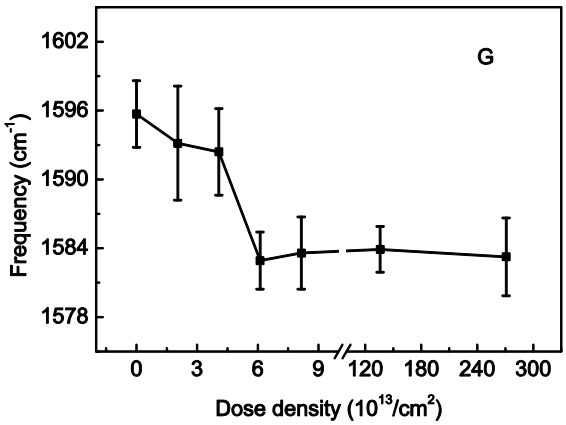

Figure R.15 Dose dépendance de la densité de la fréquence du pic G pour le graphène non irradié et irradié avec différentes densités de dose.

Comme le pic G dans le spectre Raman provient de la vibration dans le plan de sp^2 liés atomes de C et doublement dégénérée (E_{2g}) Mode de phonons au centre de zone de Brillouin, l'irradiation par faisceau d'électrons rompt les liaisons C-C sp^2 dans le graphène, et induire l'interaction entre graphène et le substrat SiC. En attendant, la composition de la liaison Si-C augmente avec la dose, c'est lié à l'irradiation faisceau d'électrons conduisant à la modification de pontage entre les feuilles de graphène et le substrat en SiC, qui contribue au décalage vers le rouge de pic G. Ces résultats indiquent l'amorphisation locale progressive de graphène. De plus, la souche locale libérée après l'irradiation par un faisceau d'électrons peut également contribuer à la

rétrogradation de pic G. Pour le décalage vers le rouge de pic 2D (figure R.16), à l'exception du mécanisme mentionné ci-dessus, les résultats de dopage d'électrons par l'irradiation par faisceau d'électrons conduit aussi à ce comportement.

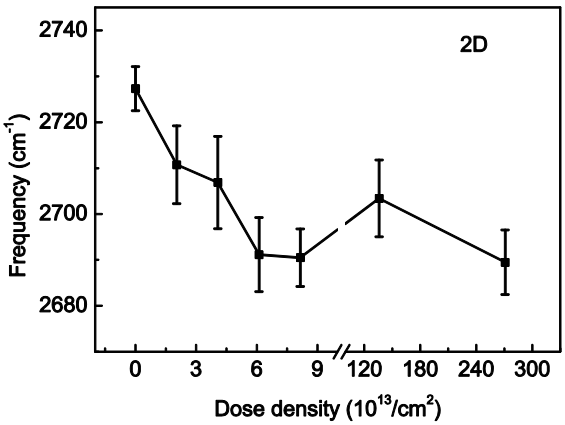

Figure R.16 Dose dépendance de la densité de la fréquence de pic 2D pour le graphène graphène non irradié et irradié avec différentes densités de dose.

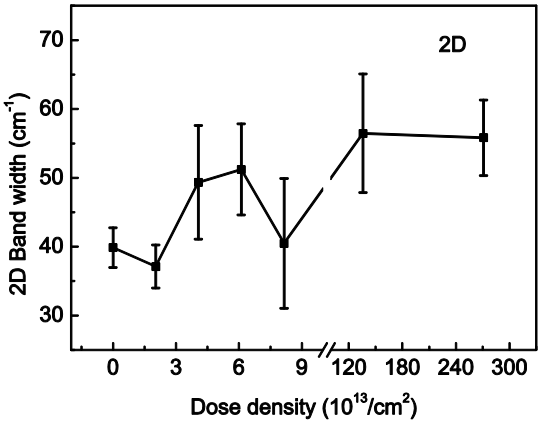

Figure R.17 Dépendances de dose de la largeur de bande de graphène 2D de pointe pour non irradié et irradié

Comme montré dans la R.17, la largeur de bande 2D montre une dépendance croissante de la densité de la dose. Ceci est lié à l'armature de l'irradiation de l'interaction entre le substrat en SiC et le graphène, conduisant ainsi à une amorphisation locale progressive de graphène. La souche libérée après l'irradiation peut également contribuer à ce comportement.

R.5.3 Propriétés de Transport

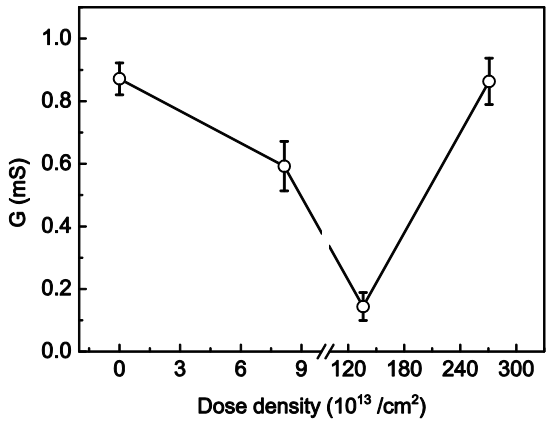

Figure R.18 Dépendances de densité de dose de conductance électrique dans le graphène non irradié et irradié sous une tension drain-source de 0.1 V sans déclenchement.

Similaires aux résultats dans le chapitre IV, une dépendance non- monotone de la conductance de la densité de la dose a été observée (Figure R.18), qui est en relation avec les effets compétitifs de concentration de porteurs, de la mobilité et de la diffusion des défauts. La souche de graphène entraîne une modification de structure et influencer davantage la conductance électrique. Les résultats de dopage d'électrons à partir de l'irradiation par faisceau d'électrons peuvent modifier la concentration de porteur et de la mobilité. Pendant ce temps, la petite quantité de défauts ou de troubles formées dans graphène par l'irradiation conduisent à la diffusion de défauts. A la densité de la dose de 8,15 $\times 10^{13}$ /cm^2 et 1,36 $\times 10^{15}$ /cm^2, et la souche défaut diffusion joue un rôle plus important et se traduit par la diminution de la conductance. Bien que continuer à augmenter la densité de la dose à 2,71 $\times 10^{15}$ /cm^2, l'effet de dopage d'électrons devient plus important et conduit à l'augmentation de la conductance.

R.5.4 Comparaison

Table R.5 Comparaison de l'influence de l'irradiation sur les propriétés structurelles et de transport du graphène préparés par procédé CVD et graphène cultivés sur substrat SiC.

	Le graphène cultivé sur substrat de SiO_2 préparé par CVD	Graphène cultivé sur susbatrate SiC par sublimation
X-ray Spectroscopie Photoélectronique	Avec l'augmentation de la dose, la composition de liaison C-C sp^2 diminue, tandis que celle de C-C (H) obligataires sp^3 et C-C=O obligations augmente.	Avec l'augmentation de la dose, la composition de liaison C-C sp^2 diminue, tandis que celle de la liaison Si-C augmente avec la dose.
Spectroscopie Raman	Blue- changement de G et 2D de pointe Pic significatif D Largeur de bande de 2D pic augmente	Décalage vers le rouge de G et 2D Très faible pic D Largeur de bande de 2D pic augmente
Conductance électrique	La dépendance non-monotone de la dose, trou dopage, la diffusion de défaut	La dépendance non-monotone de la dose, dopage d'électrons, la souche et la diffusion de défaut

Ici, l'influence de l'irradiation sur les propriétés structurelles et de transport du graphène cultivés sur substrat SiO_2 préparé par procédé CVD et graphène cultivés sur substrat SiC ont été comparés, comme indiqué dans le tableau 5.9. Tant la composition de liaison C-C sp^2 montre la dépendance à la diminution de la densité de la dose d'irradiation. Pour le graphène cultivé sur un substrat de SiO_2 préparée par un procédé CVD, la composition de C-C(H) sp^3 et C-C=O liaison montre augmentation monotone en fonction de la densité de la dose, qui suggère l'oxydation et le trou dopage dans le graphène préparé par procédé CVD résultats de la décomposition des résidus de PMMA. Alors que pour le graphène cultivé sur substrat de SiC par sublimation, la composition de liaison Si-C montre une augmentation monotone de la densité de la dose, qui indique l'amorphisation locale progressive de graphène et souche publié après irradiation. Dans les spectres Raman, des changements bleus de G et 2D pics ont été observés dans le graphène cultivé sur substrat SiO_2 préparé par un procédé CVD, un pic significatif a apparu D et la largeur de bande de la bande 2D augmente avec la densité de la dose. Alors que pour le graphène cultivé sur substrat de SiC, décalages vers le rouge de G et 2D pics ont été observés, le pic D est très faible et la largeur de bande de pic 2D augmente avec la dose. Tant la conductance électrique de ces

deux types de graphène montre la dépendance non-monotone de la densité de la dose. Les propriétés de transport du graphène cultivé sur SiO_2 par la méthode CVD sont dominées par diffusion de défaut et le trou dopage, tandis que ceux de graphène sur substrat SiC sont contrôlés par le dopage d'électrons, la souche et la diffusion de défaut. La comparaison entre l'influence provoquée par l'irradiation sur ces deux types de graphène présente l'évolution de la structure et sa relation avec les propriétés de transport, qui peuvent être appliquées à la conception du roman graphène basé sur la mémoire et le transistor.

R.6 Conclusions

Dans cette thèse, l'influence de l'irradiation sur les propriétés structurelles et de transport du graphène ont été étudiées, qui montre l'application hautement potentielle en mémoire et les dispositifs logiques, transistors et des circuits intégrés à base de graphène. L'irradiation d'ion et l'irradiation d'électrons ont été tous les deux employées, et deux types de graphène ont été utilisés, le premier était graphène cultivé sur des feuilles de Cu par procédé CVD, puis transféré au substrat SiO_2, tandis que l'autre était graphène épitaxiale cultivé sur substrat SiC par sublimation.

L'irradiation d'ions hélium a été réalisée sur le graphène cultivé sur SiO_2 substrat par CVD, quant à vide recuit a été utilisé pour réparer les dommages causés par l'irradiation. Un effet de dopant de transfert de charge réversible dans graphène CVD grâce à des réactions avec poly méthacrylate de méthyle (PMMA) résidus a été observé. L'irradiation par faisceau d'électrons a été effectuée sur le graphène épitaxiale cultivé sur substrat SiC par sublimation. Les fréquences de G et 2D pics montrent la dépendance rouge-chie de la densité de la dose, et une augmentation de la largeur de bande du pic 2D a été observée, qui sont liés à l'interaction entre le graphène et la couche tampon ou la modification de pontage entre graphène et le substrat SiC induite par irradiation. La souche libérée après irradiation peut également contribuer au comportement. En outre, les résultats de dopage d'électrons par irradiation par faisceau d'électrons peuvent également conduire au décalage vers le rouge de pic 2D.